Numerical Field Simulations of Composite Material

Dissertation

zur Erlangung des Grades

des Doktors der Naturwissenschaften

der Naturwissenschaftlich-Technischen Fakultät

der Universität des Saarlandes

von

Tobias Rafael Weber

Saarbrücken
2020

Tag des Kolloquiums:	06.08.2020
Dekan:	Prof. Dr. Guido Kickelbick
1. Gutachter:	Prof. Dr. Rolf Pelster
2. Gutachter:	Prof. Dr. techn. Romanus Dyczij-Edlinger
Vorsitz:	Prof. Dr. Christian Wagner
Akad. Mitarbeiter:	Dr.-Ing. Andreas Tschöpe

Abstract

In the following work, results are presented which increase the understanding of the properties of composite material consisting of a non-magnetic matrix and ferromagnetic, spherical inclusions which fulfill the conditions of a homogeneous effective medium. Especially, we are interested in the shift of the ferromagnetic resonance frequency and the effective permeability tensor in dependence of the material properties and the microstructure of the composite. For generating the data of interest, various numerical simulation methods, including calculation of the static orientation of the magnetic moments, modelling of the of waveguide-based transmission and reflection experiments and corresponding evaluation methods, are used.

With the methods at hand, we are able to analyze as well composite bulk material as finite samples and consider different kinds of inclusion arrangements from simple cubic lattices to random insertion. One of the main tasks during this work was to find possibilites to produce results with low inclusion numbers, to which we are restricted due to high memory consumptions in the high-frequency simulations, which also coincide with the large system limit. Even if we come up against limits due to finite memory resources leading to artifacts, we identify and isolate different, counteracting effects which cause a shifting of the ferromagnetic resonance frequency.

Kurzdarstellung

In der vorliegenden Arbeit werden Ergebnisse präsentiert, die das Verständnis von Eigenschaften von Kompositmaterialien erhöhen, die aus einer nichtmagnetischen Matrix und ferromagnetischen, kugelförmigen Inklusionen bestehen, die die Bedingungen des homogenen effektiven Mediums erfüllen. Besonderes Interesse gilt dabei der Verschiebung der ferromagnetischen Resonanz und dem effektiven Permeabilitätstensors in Abhängigkeit der Materialeigenschaften und der Mikrostruktur des Komposits. Für die Untersuchung werden zahlreiche Simulationsmethoden zur Berechnung der statischen Orientierung der magnetischen Momente, zur Modellierung der wellenleitergestützten Transmissions- und Reflexionsexperimente und entsprechende Auswertemethoden eingesetzt.

Mit den zur Verfügung stehenden Methoden können sowohl unendlich ausgedehnte als auch endliche Kompositproben und verschiedene Anordnungen der Inklusionen, vom einfach kubischen Gitter bis zum zufälligen Einwurf, untersucht werden. Eine der Hauptaufgaben dieser Arbeit war es, Möglichkeiten zu finden, um mit geringen Inklusionszahlen, auf die wir in den Hochfrequenzsimulationen aufgrund deren hohen Speicherverbrauchs beschränkt sind, Ergebnisse zu produzieren, die auch für den Grenzfall großer Systeme gelten. Obwohl wir dabei auf Grenzen und daraus resultierende Artefakte stoßen, isolieren wir verschiedene, sich entgegenwirkende Effekte, die eine Verschiebung der ferromagnetischen Resonanzfrequenz verursachen.

Nomenclature of the Magnetic Field Magnitudes

In the presentation of the results gained during this work (see chapters 4 and 5), the following nomenclature is used:

- H_{inc}: Internal magnetic bias of inclusions, which is an input parameter of the simulations. Does not respect dipole interactions.
- H_{dip}: Dipole field acting on one regarded inclusion caused by the surrounding inclusions. Calculated in the static simulations.
- H_{inc}^{dip}: Internal magnetic bias of inclusions when dipolar interaction is included. Consequently,

$$H_{inc}^{dip} = H_{inc} + H_{dip}. \tag{1}$$

- M_s^{inc}: Saturation magnetization of the inclusions, also an input parameter of the simulations.
- M_{eff}: Effective magnetization of the composite sample.
- H_{eff}: Effective field in the composite. Corresponds to the mean value of the field magnitudes in the sample

$$H_{eff} = \langle H(\mathbf{x}) \rangle = \frac{1}{V} \int_V H(\mathbf{x}) \mathrm{d}V \tag{2}$$

According to demagnetization theory (see equation 1.153), this magnitude is connected with H_{inc} of one spherical inclusion in a medium with magnetization M_{eff} via

$$H_{inc} = H_{eff} - \frac{M_s^{inc} - M_{eff}}{3}. \tag{3}$$

- H_{eff}^{loc}: Effective local field at the place of one regarded inclusion in the composite and determining the resonance frequency of this inclusions via $\nu_0 = \gamma H_{eff}^{loc}$. When we take into account spatial dipolar interactions between the inclusions, $H_{eff}^{loc} \neq H_{eff}$ is valid, in general. Contrary, in the simulations without dipolar interactions every inclusion is exposed to $H_{eff}^{loc} = H_{eff}$. The differences between the field magnitudes H_{eff}^{loc} and H_{eff} are schematically sketched in figure 1.

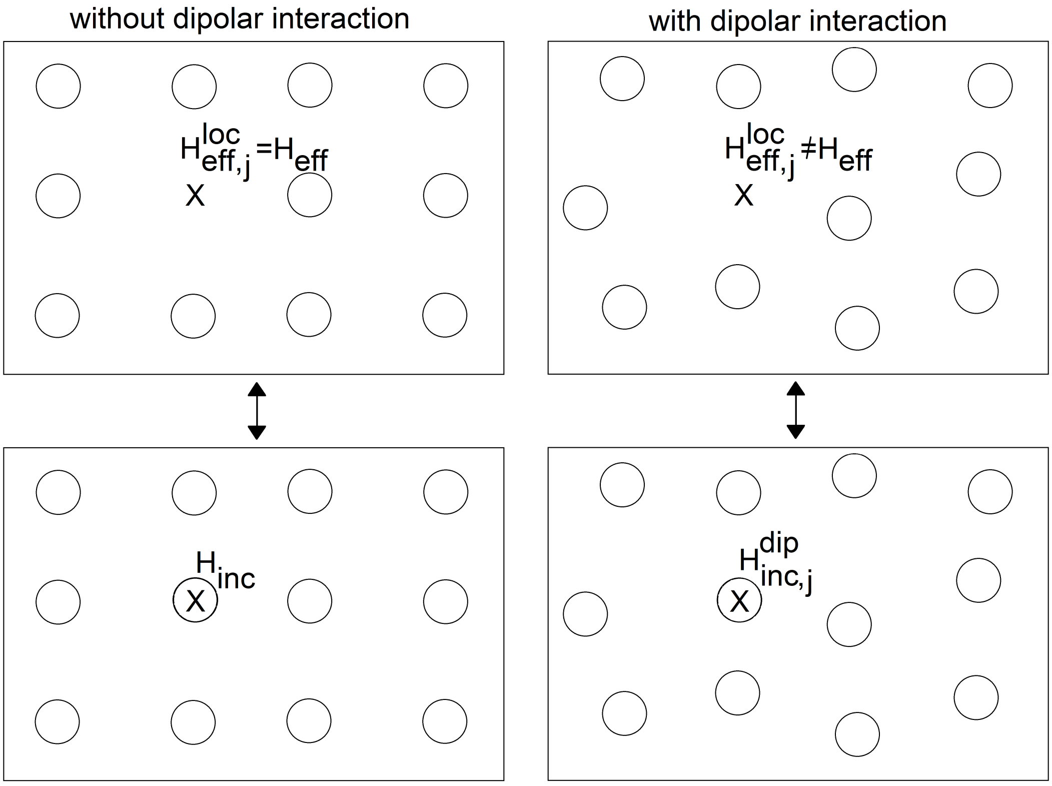

FIGURE 1 – *In the case when inclusions are placed on a simple cubic lattice, dipolar interactions can be neglected (see section 4.2.1), meaning that every inclusion is exposed to the same effective field H_{eff} (top left picture). When microstructure is generated randomly, local fields at the places of the inclusions fluctuate, as shown in the top right picture. Here, H^{loc}_{eff} is the superposition of H_{eff} and dipolar fields resulting from all surrounding inclusions. H^{loc}_{eff}* ***is not the internal magnetic field in the particle, but the field which would arise at the point of the inclusion's center when no particle would be placed at this point as indicated by the missing circles in the top pictures, which are included in the lower ones.***

In an analog manner as in equation 3, we can write

$$H^{dip}_{inc} = H^{loc}_{eff} - \frac{M^{inc}_s - M_{eff}}{3}. \tag{4}$$

in order to relate the internal magnetic field in the inclusion with the local field in the matrix when dipolar interactions are respected. Further discussion of the field magnitudes of H_{eff} and H^{loc}_{eff} can be found in context of figure 4.103.

- With regard to our simulation sequences, we distinguish:
    1. $H_{inc} = const.$ in which the internal magnetic bias of the inclusions is kept constant for every filling factor. This is easily realized in the simulations because H_{inc} is an input parameter.
    2. $H_{eff} = const.$ in which the effective field in the sample should take the same values for different volume fractions of inclusions.

Regarding equation 3 and setting $H_{eff} = H_{inc} + \frac{M^{inc}_s}{3}$, as it is the case for one isolated sphere in a non-magnetic environment (see further discussions in context of equation 4.22), when keeping this magnitude constant, both cases differ for different filling factors by the term of $\pm\frac{M_{eff}}{3}$.

- H_{ext}: Externally applied magnetic field acting on the sample. In case of infinite samples, $H_{ext} = H_{eff}$ is fulfilled. Accordingly, the case of constant effective fields in an infinitely extended device for different filling factors corresponds to an externally applied field maintaining the same values for different samples.

Contents

Introduction

Magnetic materials are used in a large variety of applications, as the interaction with high-frequency electromagnetic fields in inductors, microwave filters or radar absorbers. These instruments require special material properties at certain frequencies in order to fulfill the tasks of interest [1–5]. Within this context, composite materials consisting of different magnetic or non-magnetic components promise to be powerful tools in order to tune the material behavior as desired. Accordingly, the understanding of the developing of the properties of these materials is of great interest for the purpose of efficiently engineering modern composite materials [6]. In this context, many analytic effective medium theories have been developed in which the heterogeneous composite is treated as a homogeneous material whose properties should be determined in dependence of the components' properties and the internal microstructure. These theories can be applied if the included components in the composite are small compared to the wavelength of the incident electromagnetic wave, which is unproblematically to fulfill for microwave frequencies [7, 8]. Accordingly, the field fluctuations in the composite material are treated in a mean field approximation.

In this work, we want to gain further knowledge on the formation of one of the composite's effective properties, the tensorial effective permeability in the vicinity of the ferromagnetic resonance. For that purpose, we use simulation methods, which do not disregard the spatial inhomogeneities, in contrast to analytic theories. Especially, we are interested in the behavior of the ferromagnetic resonance frequency for different composite systems in comparison to homogeneous bulk materials. In order to analyze this issue, we regard composites which consist of a non-magnetic matrix with spherical, ferromagnetic inclusions with material properties in the value range of ferrites. Within this, the mathematical description of the tensorial magnetic permeability of the inclusions is done according to Polder's model [9], meaning the inclusions to be fully magnetized by an externally applied magnetic field.

The work at hand is structured in the following manner: In the first chapter we present the theorical basics with regard to the propagation of electromagnetic waves, magnetism of matter and the already mentioned effective medium theories, which represent the fundamental knowledge for all further considerations. Following this, we reproduce current results from modern works, in which common effective medium theories are refined with regard to the topic of tensorial permeabilities of composites in the vicinity of the ferromagnetic resonance. By this, we want to give an overview on the state of the art and outline the motivation for this work. In chapter 3, the methods used in the examinations are explained. Within this, we regard transmission and reflection experiments, which are performed in silico in our case, and the corresponding evaluation methods in dependence of the properties of the device under test. Furthermore, we describe the simulation techniques we perform in order to reproduce experimental set-ups, i. e. the finite element method, model order reduction methods, the commercial *High Frequency Structure Simulator* by *Ansys* and a numerical computing method in order to include dipolar interaction between the magnetic moments of the inclusions. Afterwards, examinations start in which bulk materials under different conditions with regard to the microstructure of the devices are analyzed. Here, we first have to do some previous considerations in order to prove the reliability of the methods at hand before we choose composites with inclusions on a simple cubic lattice as a simple as possible starting point. By this, we can draw first conclusions which are helpful for the understanding of the results of the following sections in which more complicated microstructures are analyzed. In chapter 5, we also take into account boundary effects in order to analyze finite samples in our simulations and examine the influence of the variation of the inclusion density.

Chapter 1

Fundamental Knowledge

In this chapter, the fundamental knowledge is presented, which is necessary in order to understand the phenomena of interest and the background of the used methods in the present work. Beginning with the propagation of electromagnetic waves and the governing equations in section 1.1, the differences between propagating waves without spatial restrictions (1.1.1) or in rectangular and parallel plate waveguides (1.1.2), respectively, are highlighted.
This is continued by section 1.2 which deals with various properties of different materials in static or high-frequency fields. The materials of interest in this work are not homogeneous, but composites consisting of a surrounding matrix of one material and dispersed inclusions of another with different properties. Because these spherical inclusions have a diameter small enough so that effective medium conditions are fullfilled, we also have to deal with basic effective medium theories which are presented in section 1.3.

1.1 Propagation of Electromagnetic Waves

1.1.1 Free Space Propagation in Vacuum

In the following, the derivation and solution of the wave equation for electromagnetic waves is presented as it can be found in many different textbooks as [10], for example. The starting point for this are the *Maxwell equations* which are given below in their differential formulation:

$$\boldsymbol{\nabla} \cdot \mathbf{D} = \rho \text{ (Gauss's law)} \tag{1.1}$$

$$\boldsymbol{\nabla} \times \mathbf{H} - \frac{\partial}{\partial t}\mathbf{D} = \mathbf{j} \text{ (Ampère's circuital law)} \tag{1.2}$$

$$\boldsymbol{\nabla} \cdot \mathbf{B} = 0 \text{ (Gauss's law for magnetism)} \tag{1.3}$$

$$\boldsymbol{\nabla} \times \mathbf{E} + \frac{\partial}{\partial t}\mathbf{B} = \mathbf{0} \text{ (Faraday's law of induction)} \tag{1.4}$$

in which

$$\boldsymbol{\nabla} = \begin{pmatrix} \frac{\partial}{\partial_x} \\ \frac{\partial}{\partial_y} \\ \frac{\partial}{\partial_z} \end{pmatrix}$$

denotes the nabla operator, **D** the electric displacement field, ρ the free charge density, **H** the magnetic field, **j** the free current density, **B** the magnetic flux density and **E** the electric field. Moreover, $\frac{\partial}{\partial t}$ labels the partial time derivative.

Hereafter, we consider a region without currents and free charge carriers (meaning $\rho = 0$ and $\mathbf{j} = \mathbf{0}$), as in a vacuum, and use the relations

$$\mathbf{D} = \varepsilon_0 \varepsilon_r \mathbf{E} = \varepsilon \mathbf{E} \quad \text{and} \quad \mathbf{B} = \mu_0 \mu_r \mathbf{H} = \mu \mathbf{H} \tag{1.5}$$

with the vacuum permittivity $\varepsilon_0 = 8.854 \cdot 10^{-12} \, \frac{\mathrm{A^2 s^4}}{\mathrm{kg\ m^3}}$, vacuum permeability $\mu_0 = 1.257 \cdot 10^{-6} \, \frac{\mathrm{kg\ m}}{\mathrm{A^2 s^2}}$ and the dimensionless material dependent relative permittivity/permeability ε_r, μ_r, which both equal one in vacuum. Consequently, equation 1.2 can be written as

$$\boldsymbol{\nabla} \times \mathbf{B} = \mu_0 \varepsilon_0 \frac{\partial}{\partial t} \mathbf{E}. \tag{1.6}$$

Moreover, equation 1.1 becomes

$$\boldsymbol{\nabla} \cdot \mathbf{E} = 0. \tag{1.7}$$

Taking the curl of equation 1.4 by applying $\boldsymbol{\nabla}\times$ and using 1.6 delivers

$$\boldsymbol{\nabla} \times (\boldsymbol{\nabla} \times \mathbf{E}) = -\frac{\partial}{\partial t} (\boldsymbol{\nabla} \times \mathbf{B}) \tag{1.8}$$

$$= -\mu_0 \varepsilon_0 \frac{\partial^2}{\partial t^2} \mathbf{E}. \tag{1.9}$$

The left side of this equation can be simplified through a well-known vector calculus identity for the curl of the curl

$$\boldsymbol{\nabla} \times (\boldsymbol{\nabla} \times \mathbf{E}) = \boldsymbol{\nabla}(\boldsymbol{\nabla} \cdot \mathbf{E}) - \boldsymbol{\nabla}^2 \mathbf{E}. \tag{1.10}$$

Remembering equation 1.7, we finally find

$$\boldsymbol{\nabla}^2 \mathbf{E} = \mu_0 \varepsilon_0 \frac{\partial^2}{\partial t^2} \mathbf{E} \tag{1.11}$$

By this, we calculated the wave equation for **E** which can be derived for **B** in a very similiar way. For example, the solution of 1.11 can be calculated as

$$E_x(z,t) = E_0 \sin(\omega t - kz) \ , \quad E_y = 0 \quad \text{and} \quad E_z = 0 \tag{1.12}$$

with the electric field amplitude E_0, the angular frequency $\omega = 2\pi f$, the wavenumber $k = \frac{2\pi}{\lambda}$ and $\lambda \cdot \nu = \frac{\omega}{k} = c$. Here, ν denotes the frequency of the electromagnetic wave, λ its wavelength and $c = \frac{1}{\sqrt{\varepsilon_0 \mu_0}}$ its propagation velocity - the speed of light in vacuum.

According to 1.4, the **B**-field in this case can be computed via the resulting differential equation

$$\frac{\partial \mathbf{B}}{\partial t} = E_0 k \cos\left(\omega t - kz\right) \mathbf{y} \tag{1.13}$$

with the unity vector in y-direction $\mathbf{y}$. A solution to this problem can be found in

$$B_x = 0, \quad B_y(z,t) = \frac{E_0}{c} \sin\left(\omega t - kz\right), \quad \text{and} \quad B_z = 0. \tag{1.14}$$

Consequently, both fields oscillate with the same phase and perpendicular to each other and to the direction of propagation, which is the z-direction in this case. The propagation is schematically drawn in figure 1.1. Moreover, it can be seen, that the field amplitudes are connected via

$$B_0 = \frac{E_0}{c} = E_0 \sqrt{\mu_0 \varepsilon_0} \tag{1.15}$$

$$\Leftrightarrow H_0 = \sqrt{\frac{\varepsilon_0}{\mu_0}} E_0. \tag{1.16}$$

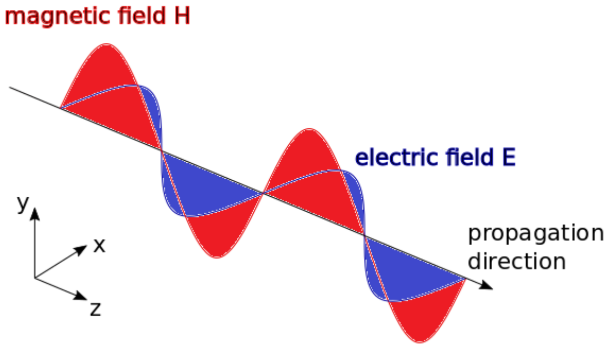

FIGURE 1.1 – *Schematic sketch of the free propagation of electromagnetic waves. The magnetic field component is drawn in red and oscillates in y-direction, while the blue line represents the electric field component oscillating in x-direction. The wave propagates along the z-axis.*

1.1.2 Spatial Restrictions: Propagation in Waveguides

The above obtained propagation properties are not maintained when space is restricted, as by the two different types of waveguides regarded in the following. These waveguides are hollow tubes with a cross section that is constant along the direction of propagation while their walls are supposed to have an infinite conductivity in theory. Experimentally, this is well realized by choosing high-conductive materials for the waveguide walls, as metals. As a consequence, special boundary conditions are imposed on the solutions of the Maxwell equations, resulting in new propagation phenomena which will be analyzed in detail in the following sections for rectangular and parallel plate waveguides, respectively. Before, we regard the propagation of waves in conducting media for the purpose of understanding the roots of the imposed boundary conditions.

The underlying textbooks for the following sections were [11–14], but issues given here can also be found in many further works dealing with guided waves.

1.1.2.1 Propagation in Conducting Materials

In real applications, the waveguide walls are made of high-conductive metals. Therefore, it is justified to suppose them to have infinite conductivity for theoretical issues. In order to understand the physical consequences of the spatial restriction by conducting walls, we have to derive the wave equation for the propagation in conducting media. Contrary to the previous case, we have

$$\mathbf{j} = \boldsymbol{\sigma}\mathbf{E} \neq \mathbf{0} \tag{1.17}$$

with the material dependent conductivity $\boldsymbol{\sigma}$, which is a tensorial quantity, in general. Moreover, the relative permittivity ε_r and relative permeability μ_r of the regarded medium can be different from one. An analog derivation of the wave equation as in section 1.1.1 now delivers

$$\boldsymbol{\nabla}^2\mathbf{E} = \mu\varepsilon\frac{\partial^2}{\partial t^2}\mathbf{E} + \mu\boldsymbol{\sigma}\frac{\partial}{\partial t}\mathbf{E} \tag{1.18}$$

in which the additional damping term $\mu\boldsymbol{\sigma}\frac{\partial}{\partial t}\mathbf{E}$ occurs. An exemplaric solution is given by

$$E_x(z,t) = E_0 \exp\left(-\frac{\alpha}{2}z\right)\sin(\omega t - kz)\ , \quad E_y(t) = 0 \quad \text{and} \quad E_z(t) = 0 \tag{1.19}$$

with the damping parameter

$$\alpha = \sqrt{\frac{2\sigma\omega}{\varepsilon c^2}}. \tag{1.20}$$

Obviously, the penetration depth $\delta = \frac{1}{\alpha}$ in the limiting case $\sigma \to \infty$ is zero, meaning the electrical field component to vanish in the walls of the waveguide. The important consequences for wave propagation are presented in the following.

1.1.2.2 TEM, TE and TM Modes

We regard waves propagating in $z-$direction through waveguides with constant cross sections in the $x-y-$plane and perfectly conducting walls. Furthermore, we assume time-harmonic fields according to $\mathbf{E},\mathbf{H} \propto \exp(-i\omega t)$, but dispense with this term for the sake of clarity. Choosing a general ansatz, splitting $z-$dependence and separating fields into transverse $(\mathbf{e},\mathbf{h})$ and longitudinal components (e_z, h_z), we can write

$$\mathbf{E}(x,y,z) = \{\mathbf{e}(x,y) + \mathbf{z}e_z(x,y)\}\exp(-i\beta z) \tag{1.21}$$

$$\mathbf{H}(x,y,z) = \{\mathbf{h}(x,y) + \mathbf{z}h_z(x,y)\}\exp(-i\beta z) \tag{1.22}$$

where $\mathbf{z}$ denotes unity vector in $z-$direction and β is the propagation constant. In free space propagation $\beta = k = \frac{2\pi}{\lambda}$ is valid, but as we will see, this relation does not always hold and depends on the regarded boundary conditions. Applying equations 1.2 and 1.4 in a current-free environment $(\mathbf{j} = \mathbf{0})$ and replacing $\mathbf{B} = \mu\mathbf{H}$ and $\mathbf{D} = \varepsilon\mathbf{E}$, we find the two relations

$$\nabla \times \mathbf{E} = -i\omega\mu\mathbf{H} \tag{1.23}$$
$$\nabla \times \mathbf{H} = -i\omega\varepsilon\mathbf{E}, \tag{1.24}$$

which deliver six scalar, partial differential equations for the six vector components E_x, E_y, E_z, H_x, H_y and H_z:

$$\frac{\partial E_z}{\partial y} + i\beta E_y = -i\omega\mu H_x \tag{1.25}$$
$$-\frac{\partial E_z}{\partial x} - i\beta E_x = -i\omega\mu H_y \tag{1.26}$$
$$\frac{\partial E_y}{\partial x} - \frac{\partial E_x}{\partial y} = -i\omega\mu H_z \tag{1.27}$$
$$\frac{\partial H_z}{\partial y} + i\beta H_y = i\omega\varepsilon E_x \tag{1.28}$$
$$-\frac{\partial H_z}{\partial x} - i\beta H_x = i\omega\varepsilon E_y \tag{1.29}$$
$$\frac{\partial H_y}{\partial x} - \frac{\partial H_x}{\partial y} = i\omega\varepsilon E_z. \tag{1.30}$$

Eliminating E_y in 1.25 by inserting 1.29, E_x in 1.26 by inserting 1.28 and vice versa for H_y in 1.28 and H_x in 1.29, leads to four equations for the transverse components

$$E_x = -\frac{i}{k_c^2}\left(\beta\frac{\partial E_z}{\partial x} + \omega\mu\frac{\partial H_z}{\partial y}\right) \tag{1.31}$$
$$E_y = \frac{i}{k_c^2}\left(-\beta\frac{\partial E_z}{\partial y} + \omega\mu\frac{\partial H_z}{\partial x}\right) \tag{1.32}$$
$$H_x = \frac{i}{k_c^2}\left(\omega\varepsilon\frac{\partial E_z}{\partial y} - \beta\frac{\partial H_z}{\partial x}\right) \tag{1.33}$$
$$H_y = -\frac{i}{k_c^2}\left(\omega\varepsilon\frac{\partial E_z}{\partial x} + \beta\frac{\partial H_z}{\partial y}\right). \tag{1.34}$$

Here, cut-off wavenumber $k_c^2 = k_m^2 - \beta^2$ was introduced, where $k_m = k_0\sqrt{\varepsilon_r\mu_r}$ is the wavenumber in the material filling the waveguide and k_0 the same for vacuum. So far, only general considerations have been done, but now we will have a deeper look at the different forms in which waves can propagate in the guides. These forms are called modes and are characterized by their individual field patterns. One can distinguish between

- transverse electromagnetic modes (TEM)
- transverse electric modes (TE)
- transverse magnetic modes (TM).

By definition, TEM modes are characterized by the condition $E_z = H_z = 0$, meaning fields to be restricted to oscillate transversly to propagation along $z-$axis. Accordingly, TE-modes fulfill only $E_z = 0$, while $H_z \neq 0$ and vice versa, $H_z = 0$ and $E_z \neq 0$ applies for TM-modes. In the following, the modes arising in rectangular and parallel plate waveguides are analyzed.

1.1.2.3 Rectangular Waveguide

As suggested by its name, this waveguide has a rectangular cross section with the dimensions a and b, whereby a denotes the longer edge, as shown in figure 1.2. Conditioned by this geometry, this waveguide can support TE and TM, but not TEM modes. In this case, the first arising mode is of TE-type, reducing equations 1.31-1.34 to

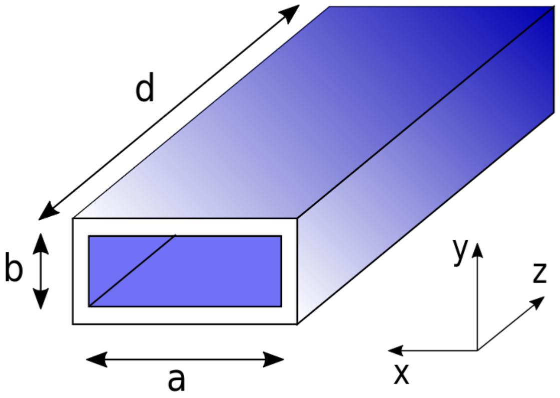

FIGURE 1.2 – *A rectangular waveguide with the inner dimensions a and b and a length of d.*

$$E_x = -\frac{i}{k_c^2}\omega\mu\frac{\partial H_z}{\partial y} \tag{1.35}$$

$$E_y = \frac{i}{k_c^2}\omega\mu\frac{\partial H_z}{\partial x} \tag{1.36}$$

$$H_x = -\frac{i}{k_c^2}\beta\frac{\partial H_z}{\partial x} \tag{1.37}$$

$$H_y = -\frac{i}{k_c^2}\beta\frac{\partial H_z}{\partial y}. \tag{1.38}$$

In order to solve these equations, one needs further information on H_z which can be drawn from *Helmholtz wave equation*, which is actually the same as 1.11 applied on H_z

$$\left(\frac{\partial^2}{\partial x^2} + \frac{\partial^2}{\partial y^2} + \frac{\partial^2}{\partial z^2} + \beta^2\right) H_z = 0. \tag{1.39}$$

Separating $H_z(x,y,z) = h_z(x,y)\exp(-ik_m z)$ for the purpose of splitting its $z-$dependence and using $k_c^2 = k_m^2 - \beta^2$, one finds

$$\left(\frac{\partial^2}{\partial x^2} + \frac{\partial^2}{\partial y^2} - k_c^2\right) h_z = 0. \tag{1.40}$$

Now, one can choose the following separation ansatz

$$\begin{aligned} h_z(x,y) &= h_z^x(x) h_z^y(y) \\ &= \left(A\cos\left(k_x x\right) + B\sin\left(k_x x\right)\right)\left(C\cos\left(k_y y\right) + D\sin\left(k_y y\right)\right) \end{aligned} \tag{1.41}$$

under the boundary conditions for the electric field components (see section 1.1.2.1)

$$E_x = 0 \quad \text{at} \quad y = 0 \quad \text{and} \quad y = b \tag{1.42}$$

$$E_y = 0 \quad \text{at} \quad x = 0 \quad \text{and} \quad x = a. \tag{1.43}$$

Since we are looking for a solution for the magnetic field, but only know boundary conditions for the electric components, we have to use 1.35 and 1.36 to find

$$E_x = -\frac{i}{k_c^2}\omega\mu k_y \left(A\cos\left(k_x x\right) + B\sin\left(k_x x\right)\right)\left(-C\sin\left(k_y y\right) + D\cos\left(k_y y\right)\right) \tag{1.44}$$

$$E_y = \frac{i}{k_c^2}\omega\mu k_x \left(-A\sin\left(k_x x\right) + B\cos\left(k_x x\right)\right)\left(C\cos\left(k_y y\right) + D\sin\left(k_y y\right)\right). \tag{1.45}$$

By this, the relations

$$B = 0, \quad D = 0, \; k_x = \frac{\pi n}{a} \quad \text{and} \quad k_y = \frac{\pi m}{b} \tag{1.46}$$

with $n, m \in \mathbb{N}$, denoting different modes, can be obtained. Accordingly, this leads to the solution for the magnetic field

$$h_z^{n,m}(x,y) = A_{n,m}\cos\left(\frac{\pi n}{a}x\right)\cos\left(\frac{\pi m}{b}y\right) \tag{1.47}$$

with the arbitrary amplitude $A_{n,m}$. Applying equation 1.40 on this solution, we obtain

$$k_c^2 = k_x^2 + k_y^2. \tag{1.48}$$

This yields the very important dispersion relation for $\mathrm{TE}_{n,m}$ modes in the rectangular waveguide

$$\beta^{n,m} = \sqrt{k_m^2 - k_c^2} = \sqrt{k_m^2 - \left(\frac{\pi n}{a}\right)^2 - \left(\frac{\pi m}{b}\right)^2}. \tag{1.49}$$

Obviously, this expression becomes purely imaginary if $k_m < k_c$, meaning that waves entering the waveguide will decay exponentially and do not propagate. The corresponding cut-off frequency is given by

$$\nu_c^{n,m} = \frac{k_c}{2\pi\sqrt{\mu\varepsilon}} = \frac{1}{2\pi\sqrt{\mu\varepsilon}}\sqrt{\left(\frac{\pi n}{a}\right)^2 + \left(\frac{\pi m}{b}\right)^2} \tag{1.50}$$

and the associated wavelength by

$$\lambda_c^{n,m} = \frac{c}{f_c^{n,m}} = \frac{2}{\sqrt{\left(\frac{n}{a}\right)^2 + \left(\frac{m}{b}\right)^2}}. \tag{1.51}$$

In order to analyze devices in waveguides, it is necessary that only one mode is able to propagate while all others are damped. So, the mode with the lowest cut-off frequency is of special interest. In case $a > b$, the dominant TE mode is defined by $n = 1$ and $m = 0$, leading to

$$\nu_c^{1,0} = \frac{1}{2a\sqrt{\mu\varepsilon}}. \tag{1.52}$$

Considering a so-called X-band rectangular waveguide with the dimensions $a = 2.286$ cm and $b = 1.016$ cm, a cut-off frequency for the dominant mode of $\nu_c^{1,0} = 6.56$ GHz results. The second mode is able to propagate at frequencies above $\nu_c^{2,0} = 13.12$ GHz. Accordingly, this waveguide can be used for measurements between these two frequencies, while it is recommended to limit to the range of $8 - 12$ GHz.
Below the cut-off frequencies for different modes, the above given concepts also deliver the related field patterns. From 1.47, we conclude

$$H_z^{n,m}(x, y, z) = A_{n,m} \cos\left(\frac{\pi n}{a} x\right) \; \cos\left(\frac{\pi m}{b} y\right) \; \exp\left(-i\beta z\right). \tag{1.53}$$

The usage of 1.35-1.38 delivers the remaining field components

$$E_x^{n,m}(x, y, z) = A_{n,m} \frac{i\omega\mu m\pi}{k_c^2 b} \cos\left(\frac{\pi n}{a} x\right) \; \sin\left(\frac{\pi m}{b} y\right) \; \exp\left(-i\beta z\right) \tag{1.54}$$

$$E_y^{n,m}(x, y, z) = -A_{n,m} \frac{i\omega\mu n\pi}{k_c^2 a} \sin\left(\frac{\pi n}{a} x\right) \; \cos\left(\frac{\pi m}{b} y\right) \; \exp\left(-i\beta z\right) \tag{1.55}$$

$$H_x^{n,m}(x, y, z) = A_{n,m} \frac{i\beta n\pi}{k_c^2 a} \sin\left(\frac{\pi n}{a} x\right) \; \cos\left(\frac{\pi m}{b} y\right) \; \exp\left(-i\beta z\right) \tag{1.56}$$

$$H_y^{n,m}(x, y, z) = A_{n,m} \frac{i\beta m\pi}{k_c^2 b} \cos\left(\frac{\pi n}{a} x\right) \; \sin\left(\frac{\pi m}{b} y\right) \; \exp\left(-i\beta z\right). \tag{1.57}$$

For the dominant $\mathrm{TE}_{1,0}$ mode, these fields are shown in picture 1.3.

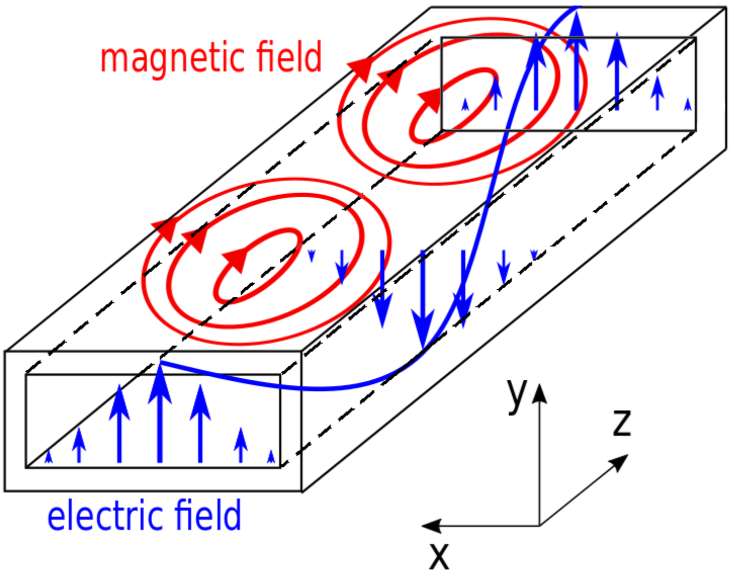

FIGURE 1.3 – *The* **E** *(blue) and* **H** *(red) pattern of the* $TE_{1,0}$ *mode in a rectangular waveguide. While* **E** *only oscillates in* $y-$*direction, the field lines of* **H** *draw circles in the* $x-z-$*plane.*

Repeating the above calculations for TM modes, one finds the same dispersion relation (1.49) and cut-off behavior (1.50) as for TE modes. An analysis of the field patterns shows the first TM mode to be defined by $n = m = 1$.

1.1.2.4 Parallel Plate Waveguide

The second type of waveguides of interest is the parallel plate waveguide. It consists of two parallely fixed, conducting plates with a constant distance b in $y-$direction, but infinite extension in $x-$direction (see figure 1.4). One consequence of this changed

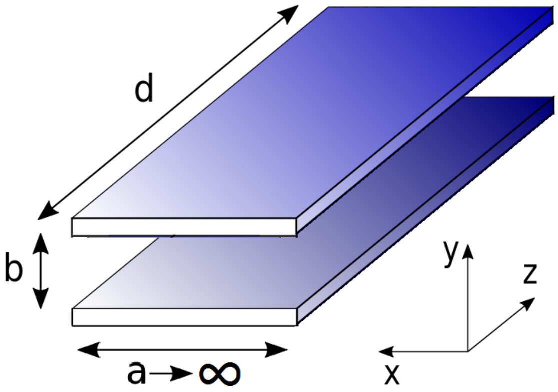

FIGURE 1.4 – *Parallel plate guides consist of two opposing conducting plates in a distance* b *and infinite extension perpendicular to propagation direction. It can be seen as a rectangular waveguide in the limiting case* $a \to \infty$.

geometry compared to the previous case is that the dominant mode is now of TEM type, accordingly fulfilling $H_z = E_z = 0$ when propagation follows $z-$direction. Including this and taking additionally the limit of $a \to \infty$, the same procedure as in the previous section can be repeated in order to gain insight in the cut-off behavior.
Again regarding equations 1.31-1.34 and applying $H_z = E_z = 0$, it directly becomes clear that either no fields appear inside the waveguide or k_c has to approach zero in order to find solutions. Although these solutions are indetermined at this point, we can already conclude that

$$k_c^2 = k_m^2 - \beta^2 = 0 \tag{1.58}$$

$$\Leftrightarrow \ \beta = k_m = \omega\sqrt{\mu\varepsilon} \tag{1.59}$$

and that the dominant mode arises already with frequency $\nu_c \to 0$ GHz. Further insight into the topic of field patterns, can be gained by analyzing *Laplace's equation* for the electrostatic potential Φ inside the waveguide

$$\boldsymbol{\nabla}^2\Phi(x, y, z) = 0. \tag{1.60}$$

In the present case, we can reduce this equation to

$$\frac{\partial^2}{\partial y^2}\Phi(y) = 0. \tag{1.61}$$

By this approach, the system is treated as a static plate capacitor, which is actually correct because of the infinite extension in $x-$direction, implying no boundary conditions on the guided waves, and because of the splitting of the $z-$dependence by the separation ansatz with a factor of $\exp(-i\beta z)$. Accordingly, the boundary conditions in $y-$direction are defined by

$$|\Phi(y = 0) - \Phi(y = b)| = V \tag{1.62}$$

with the voltage V between the two plates. Choosing $\Phi(y = 0) = 0$, we can find a solution Φ by

$$\Phi(y) = V\frac{y}{b}, \tag{1.63}$$

which delivers the transverse electric field by applying the definition of the potential

$$\mathbf{e}(x, y) = -\boldsymbol{\nabla_t}\Phi = -\frac{V}{b}\mathbf{y}. \tag{1.64}$$

Within this,

$$\boldsymbol{\nabla_t} = \begin{pmatrix} \frac{\partial}{\partial x} \\ \frac{\partial}{\partial y} \end{pmatrix} \tag{1.65}$$

denotes the transverse nabla operator. Consequently, the total electric field is given by

$$\mathbf{E} = \mathbf{e}(x,y)\exp(-i\beta z) = -\frac{V}{b}\exp(-ik_m z)\mathbf{y}, \tag{1.66}$$

in which we also used the result for the propagation constant $k_m = \beta$. Once again, the magnetic component can be found by applying equation 1.23:

$$\mathbf{H} = \frac{k_m}{\omega\mu}\frac{V}{b}\exp(-ik_m z)\mathbf{x}. \tag{1.67}$$

Hence, it becomes clear that both field components oscillate in only one direction. The corresponding field patterns for $\mathbf{E}$ and $\mathbf{H}$ of this dominant TEM mode in the parallel plate waveguide are shown in figure 1.5.

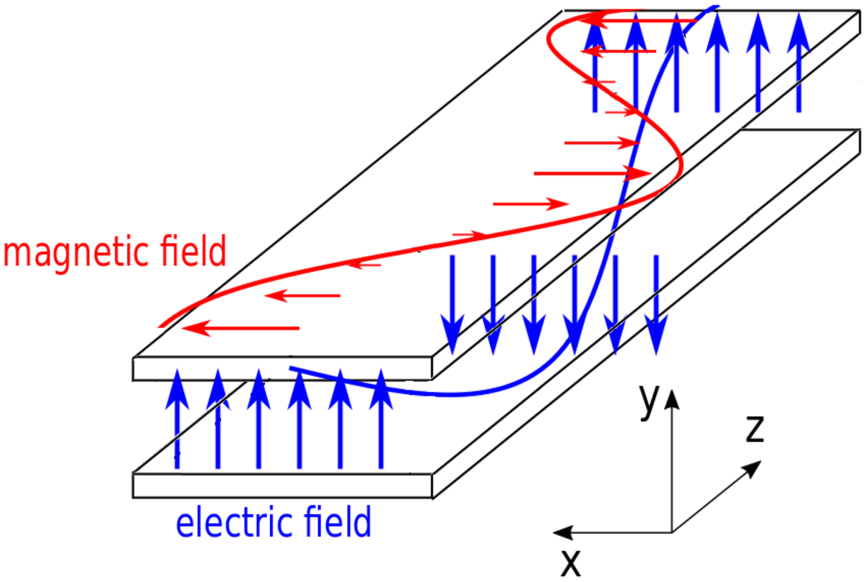

Figure 1.5 – *The* $\mathbf{E}$ *(blue) and* $\mathbf{H}$ *(red) pattern of the TEM mode in a parallel plate waveguide. Both fields' oscillations are restricted to only one direction: field lines of* $\mathbf{E}$ *follow* $y-$*direction, while* $\mathbf{H}$ *oscillates in* $x-$*direction.*

1.1.3 Transmission and Reflection of Electromagnetic Waves

The transmission and reflection of electromagnetic waves plays an important role for the simulations and the evaluations performed in this work. For this reason, the underlying continuity conditions for the fields will be derived in this section. At this point, we restrict to the conditions for the components of $\mathbf{E}$ and $\mathbf{H}$, which are parallely orientated to the reflecting and transmitting surface, because these are sufficient in order to understand the origin of the later used scattering parameters ($S-$Parameters). Additionally, the continuity condition for the normal component of $\mathbf{B}$ will be analyzed in 1.2.1. In this section, we refer to calculations which can be found in many textbooks as [15] or [16], for example.

Considering the electric field component $\mathbf{E}$, we again regard equation 1.4

$$\nabla \times \mathbf{E} = -\frac{\partial}{\partial t}\mathbf{B} \tag{1.68}$$

and use *Stoke's theorem* for a vector field $\mathbf{F}$

$$\int_A (\nabla \times \mathbf{F})\,\mathrm{d}\mathbf{A}' = \oint_{\partial A} \mathbf{F}\mathrm{d}\mathbf{l} \tag{1.69}$$

where ∂A denotes the border of area A, leading to

$$\int_A (\nabla \times \mathbf{E})\,\mathrm{d}\mathbf{A}' = \oint_{\partial A} \mathbf{E}\mathrm{d}\mathbf{l} \tag{1.70}$$

$$= -\int_A \frac{\partial}{\partial t}\mathbf{B}\mathrm{d}\mathbf{A}'. \tag{1.71}$$

Now, we regard the boundary between two different media and define a rectangular area with edge lengths h and b as shown in figure 1.6.

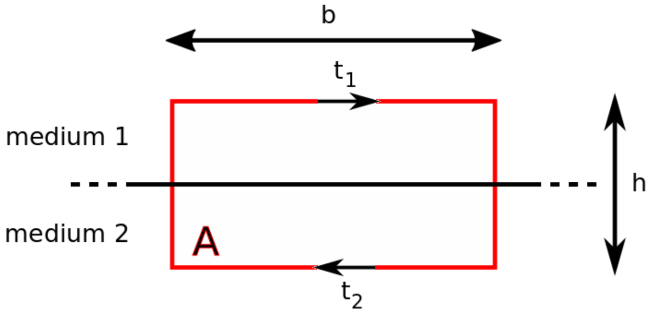

FIGURE 1.6 – *The border line between two different media is considered in order to gain insight into the boundary conditions of the magnetic field. The red line indicates area A along whose edges $\mathbf{E}$ and $\mathbf{H}$ are integrated. $\mathbf{t_1}$ and $\mathbf{t_2}$ denote unity vectors parallely orientated to the regarded border line.*

Considering the limiting case of $h \to 0$, the border integral reduces to the both edges parallel to the boundary:

$$\oint_{\partial A} \mathbf{E}\mathrm{d}\mathbf{l} = \mathbf{E_1 t_1}b + \mathbf{E_2 t_2}b \tag{1.72}$$

$$= -\int_A \frac{\partial}{\partial t}\mathbf{B}\mathrm{d}\mathbf{A}' \tag{1.73}$$

$$= 0. \tag{1.74}$$

Therein, the last integral becomes zero because the so defined area A vanishes in the considered case. Accordingly, we can conclude

$$\mathbf{E_1 t_1}b + \mathbf{E_2 t_2}b = 0 \tag{1.75}$$

$$\Leftrightarrow \mathbf{E_{1,t}}b - \mathbf{E_{2,t}}b = 0 \tag{1.76}$$

$$\Leftrightarrow \mathbf{E_{1,t}} = \mathbf{E_{2,t}} \tag{1.77}$$

because of $\mathbf{t_1} = -\mathbf{t_2}$. Following this, the parallel component of the electric field $\mathbf{E_t}$ is continuous at such a boundary.

Analogically, we can derive the boundary condition for the magnetic field $\mathbf{H}$ by regarding equation 1.2 in the absence of a current $\mathbf{j}$ (which will be the case because we restrict to non-conducting samples in our examinations):

$$\boldsymbol{\nabla} \times \mathbf{H} = \frac{\partial}{\partial t}\mathbf{D}. \tag{1.78}$$

Repeating the previous considerations and computations, we find:

$$\begin{aligned}
\oint_{\partial A} \mathbf{H}\mathrm{d}\mathbf{l} &= \mathbf{H_1}\mathbf{t_1}b + \mathbf{H_2}\mathbf{t_2}b && (1.79)\\
&= -\int_A \frac{\mathrm{d}}{\mathrm{d}t}\mathbf{D}\mathrm{d}\mathbf{A}' && (1.80)\\
&= 0. && (1.81)
\end{aligned}$$

Consequently, we find in the limiting case $h \to 0$

$$\begin{aligned}
&\mathbf{H_1}\mathbf{t_1}b + \mathbf{H_2}\mathbf{t_2}b = 0 && (1.82)\\
\Leftrightarrow\ &\mathbf{H}_{\mathbf{1},\mathbf{t}}b - \mathbf{H}_{\mathbf{2},\mathbf{t}}b = 0 && (1.83)\\
\Leftrightarrow\ &\mathbf{H}_{\mathbf{1},\mathbf{t}} = \mathbf{H}_{\mathbf{2},\mathbf{t}} && (1.84)
\end{aligned}$$

meaning the parallel component of $\mathbf{H}$ to be continuous, too. With this knowledge, we can calculate the reflection and transmission of an electromagnetic wave orthogonally impinging the boundary between two media. For simplicity, we regard the first medium as vacuum (see figure 1.7). Therein, fields are given by

$$\begin{aligned}
\mathbf{E_i} &= E_i \exp(-ik_i z)\mathbf{x} && (1.85)\\
\mathbf{E_r} &= E_r \exp(-ik_r z)\mathbf{x} && (1.86)\\
&= E_r \exp(ik_i z)\mathbf{x} && (1.87)\\
\mathbf{E_t} &= E_t \exp(-ik_t z)\mathbf{x} && (1.88)\\
\mathbf{H_i} &= H_i \exp(-ik_i z)\mathbf{y} && (1.89)\\
&= \sqrt{\frac{\varepsilon_0}{\mu_0}} E_i \exp(-ik_i z)\mathbf{y} && (1.90)\\
\mathbf{H_r} &= H_r \exp(-ik_r z)\mathbf{y} && (1.91)\\
&= H_r \exp(ik_i z)\mathbf{y} && (1.92)\\
&= -\sqrt{\frac{\varepsilon_0}{\mu_0}} E_r \exp(ik_i z)\mathbf{y} && (1.93)\\
\mathbf{H_t} &= H_t \exp(-ik_t z)\mathbf{y} && (1.94)\\
&= \sqrt{\frac{\varepsilon}{\mu}} E_t \exp(-ik_t z)\mathbf{y}. && (1.95)
\end{aligned}$$

Note that equation 1.16 was used in order to replace magnetic field amplitudes. Because both fields parallely oscillate to the border in case of free or TEM waves, we can use

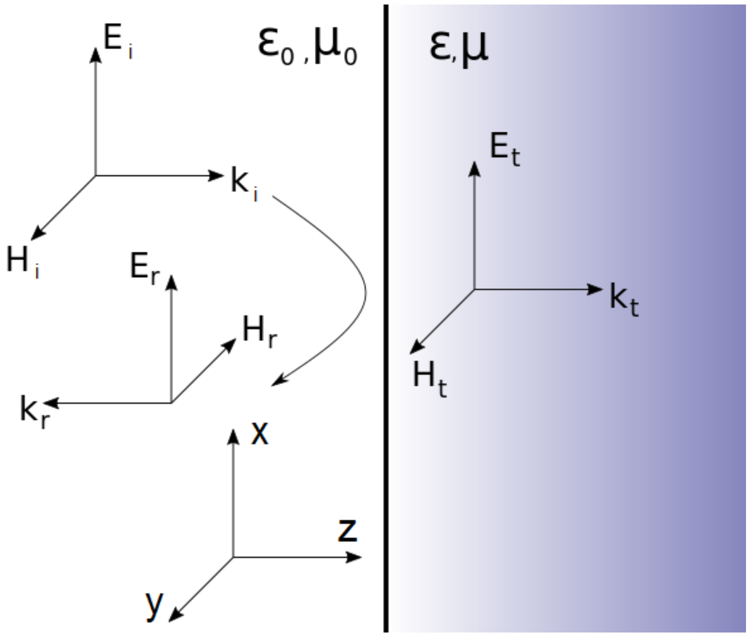

FIGURE 1.7 – *An electromagnetic wave impinges the transition from vacuum to another medium with permittivity ε and permeability μ and is partly reflected and transmitted. Index i denotes the incident wave, r the reflected and t the transmitted parts of it. Due to the reversal of propagation direction $\mathbf{k_e} = -\mathbf{k_r}$ through reflection, also the direction of the magnetic component changes.*

the above derived continuity of the tangential components and conclude

$$E_i + E_r = E_t \tag{1.96}$$

and

$$H_i + H_r = H_t. \tag{1.97}$$

Inserting magnetic field expressions 1.90, 1.93 and 1.95 in 1.97 and respecting $\varepsilon = \varepsilon_r\ \varepsilon_0$ and $\mu = \mu_r\ \mu_0$, leads to

$$E_i\sqrt{\frac{\varepsilon_0}{\mu_0}} - E_r\sqrt{\frac{\varepsilon_0}{\mu_0}} = E_t\sqrt{\frac{\varepsilon_r\varepsilon_0}{\mu_r\mu_0}} \tag{1.98}$$

$$\Leftrightarrow\ E_t = \sqrt{\frac{\mu_r}{\varepsilon_r}}(E_i - E_r). \tag{1.99}$$

Now, using equation 1.96, we find

$$E_t = \sqrt{\frac{\mu_r}{\varepsilon_r}}(E_i - E_t + E_i) \tag{1.100}$$

$$\Leftrightarrow\ E_t = \underbrace{\frac{2}{1+\sqrt{\frac{\varepsilon_r}{\mu_r}}}}_{=:t} E_i \tag{1.101}$$

in which we can define the transmission coefficient t. Again using equation 1.96, we find

$$E_r = E_t - E_i = \underbrace{(t-1)}_{r} E_i \tag{1.102}$$

leading to the reflection coefficient

$$r = t - 1 = \frac{2}{1+\sqrt{\frac{\varepsilon_r}{\mu_r}}} - 1 = \frac{1-\sqrt{\frac{\varepsilon_r}{\mu_r}}}{1+\sqrt{\frac{\varepsilon_r}{\mu_r}}}. \tag{1.103}$$

Now, we can regard the transmission and reflection behavior of an electromagnetic wave with a given amplitude A passing through a finite sample with permittivity ε and permeability μ: At the first border, a fraction $r \cdot A$ is reflected while $t \cdot A = (1+r)A$ is transmitted. Then, the transmitted wave has to cross the sample, leading to an additional phase factor of $a = \exp(-ik_m d)$ with the wave number in the device material k_m and a sample length of d. Reaching the rear boundary of the sample, transmission and reflection occurs again, but now from test material to vacuum, changing the reflection $r \to -r$ and transmission coefficient $(1+r) \to (1-r)$. Subsequently, the reflected signal travels back whereby the factor of a occurs again. Although propagation direction changes through reflection, leading to $k_m \to -k_m$, factor a remains the same because the travelled path also changes from $d \to -d$. Afterwards, the wave hits the first boundary, being transmitted and reflected again and so on. This process of multiple reflection is illustrated in picture 1.8. The total parts of the wave which are reflected and transmitted are called scattering parameters and are calculated in the following. Summing up the parts leaving the sample in the direction of incidence and

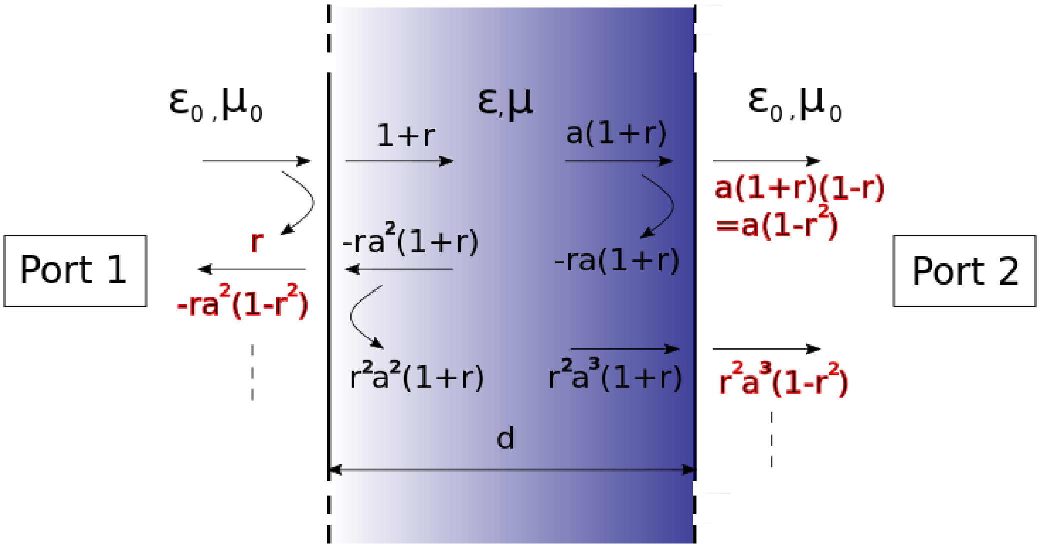

FIGURE 1.8 – *An incident electromagnetic wave arriving from port 1 hits a finite sample. In this process, the wave will be reflected and transmitted infinite times. The fractions of the incident amplitude leaving the sample to port 1 or 2, respectively, are written in red.*

travelling to port 1 again, we find

$$S_{11} = \frac{E_r}{E_i} = r - ra^2(1-r^2) - r^3a^4(1-r^2) - ... \tag{1.104}$$
$$= r \cdot \Big(1 - a^2(1-r^2) - r^2a^2(a^2(1-r^2)) - ...\Big) \tag{1.105}$$
$$= r \cdot \left(1 - (1-r^2)a^2 \underbrace{(1 + r^2a^2 + r^4a^4 + ...)}_{\sum_{i=0}^{\infty}(r^2a^2)^i}\right) \tag{1.106}$$
$$= r \cdot \left(1 - (1-r^2)a^2 \frac{1}{1-r^2a^2}\right) \tag{1.107}$$
$$= \frac{(1-a^2)r}{1-r^2a^2} \tag{1.108}$$

where we used the sum formula for infinite geometric series

$$\sum_{i=0}^{\infty} a_0 q^k = \frac{a_0}{1-q}. \tag{1.109}$$

Analogically, we calculate the fraction of the incident signal which passes the sample and is measured at port 2

$$S_{21} = \frac{E_t}{E_i} = a(1-r^2) + r^2a^3(1-r^2) + r^4a^5(1-r^2) + ... \tag{1.110}$$
$$= a \cdot \Big((1-r^2) + r^2a^2(1-r^2) + r^4a^4(1-r^2) + ...\Big) \tag{1.111}$$
$$= a(1-r^2)\left(\underbrace{1 + r^2a^2 + r^4a^4 + ...}_{\sum_{i=0}^{\infty}(r^2a^2)^i}\right) \tag{1.112}$$
$$= \frac{(1-r^2)a}{1-r^2a^2}. \tag{1.113}$$

Within this, it has to be noted that a correction of the measured $S-$parameters at the ports is necessary. In case that the air-filled distance between sample boundary and port amounts l in propagation direction, an additional phase factor has to be taken into account, which will be discussed in detail in section 3.1. There are two more $S-$parameters, S_{22} and S_{12}, for which the direction of propagation is changed, that means the wave to be arised at port 2. In the case of reciprocal devices, $S_{12} = S_{21}$ is valid, while both values differ for non-reciprocal set-ups. Contrary, $S_{11} = S_{22}$ is true in both cases. Due to energy conservation,

$$|S_{11}|^2 + |S_{21}|^2 = |S_{22}|^2 + |S_{12}|^2 = 1 \tag{1.114}$$

is always true in dissipation-free samples. In the case that the sample is hit by an electromagnetic wave in a waveguide, we have to respect the influence of the dominating mode by choosing the right dispersion relation $\beta^{n,m}$ instead of k_m in the phase factor $a = \exp(-i\beta^{n,m}d)$. Generally, the $S-$parameters are complex values.

1.2 Magnetism of Matter

In this work, the previously discussed wave phenomena will be used as a tool in order to gain insight into the behavior of composites in static and high-frequent magnetic fields, which is described by the magnetic susceptibility $\boldsymbol{\chi}$ or the related permeability $\boldsymbol{\mu}$. Accordingly, a deeper look into the topic of magnetism of matter is necessary and will be delivered in the following section. For that purpose, we will discuss magnetostatic phenomena at first, before dealing with the ferromagnetic resonance, which will be the main topic of the present work. The basic issues discussed in the following are drawn from textbooks specialized on magnetism [17, 18].

1.2.1 Matter in Static Magnetic Fields

If a material consists of atoms or molecules carrying a magnetic dipole moment $\mathbf{p_m}$, interaction occurs when it is exposed to an externally applied magnetic field $\mathbf{H}$. The sum over all of these n microscopic dipole moments divided by the filled volume is called magnetization

$$\mathbf{M} = \frac{1}{V}\sum_{i=1}^{n} \mathbf{p_{m,i}}. \tag{1.115}$$

The two fields $\mathbf{H}$ and $\mathbf{M}$ are connected to each other by the magnetic susceptibility $\boldsymbol{\chi}$ via

$$\mathbf{M} = \boldsymbol{\chi}\mathbf{H}. \tag{1.116}$$

In general, $\boldsymbol{\chi}$ is a tensorial quantity, but in many cases, it reduces to scalar values. Moreover, flux density $\mathbf{B}$ is needed in order to describe magnetic phenomena properly. These three regarded fields fulfill the relations

$$\begin{aligned} \mathbf{B} &= \mu_0 \left(\mathbf{H} + \mathbf{M}\right) && (1.117)\\ &= \mu_0 \left(\mathbf{H} + \boldsymbol{\chi}\mathbf{H}\right) && (1.118)\\ &= \mu_0 \left(\mathbf{I} + \boldsymbol{\chi}\right)\mathbf{H} && (1.119)\\ &= \mu_0 \boldsymbol{\mu_r}\mathbf{H} && (1.120)\\ &= \boldsymbol{\mu}\mathbf{H}. && (1.121) \end{aligned}$$

By this, we showed the connection between the relative permeability $\boldsymbol{\mu_r} = \mathbf{I} + \boldsymbol{\chi}$ and the susceptibility, in which $\mathbf{I}$ denotes the unity matrix. As these relations are caused by the dipole moments on an atomic scale, we want to focus on the dipoles' origin in the following. As a starting point for that purpose, we regard an infinite long conducting cylinder of radius r with a current density of $\mathbf{j}$ flowing in it, with the goal of calculating the caused flux density $\mathbf{B}$ (figure 1.9). Assuming a time-independent electric field and using $\mathbf{B} = \mu_0\mathbf{H}$, equation 1.2 can be written as

$$\boldsymbol{\nabla} \times \mathbf{B} = \mu_0 \mathbf{j}. \tag{1.122}$$

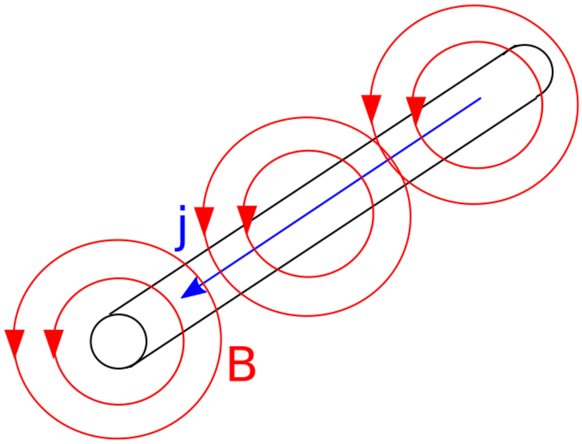

FIGURE 1.9 – *A current in a cylindrical conductor causes a radial symmetric magnetix flux around itself.*

Integrating both sides of this equation over a circular area S of radius R with its center in the center of the cylinder's cross section and its normal vector parallel to $\mathbf{j}$, we obtain

$$\int_S (\boldsymbol{\nabla} \times \mathbf{B})\, \mathrm{d}\mathbf{S}' = \int_S \mu_0 \mathbf{j} \mathrm{d}\mathbf{S}' = \mu_0 I \tag{1.123}$$

with the strength of the electric current I. Remembering Stoke's theorem (1.69), we can conclude

$$\oint_{\partial S} \mathbf{B} \mathrm{d}\mathbf{l} = \mu_0 I. \tag{1.124}$$

As a consequence of equation 1.122, $\mathbf{B}\mathrm{d}\mathbf{l}$ is constant along ∂S, leading to

$$\mathbf{B} = \frac{\mu_0 I}{2\pi R} \mathbf{e}_l \quad \Leftrightarrow \quad \mathbf{H} = \frac{I}{2\pi R} \mathbf{e}_l \tag{1.125}$$

with the angular coordinate unity vector $\mathbf{e}_l$.
Due to our interest in the atomic origin of magnetization, we have to the modify this situation and regard a conducting wire bent to a closed loop, comparable to electrons orbiting the nucleus. In this case, we need the *Biot-Savart law*, which is derived from Maxwell equations, in order to calculate the resulting magnetic field:

$$\mathrm{d}\mathbf{B} = -\frac{\mu_0}{4\pi} \frac{\mathbf{r} \times \mathbf{j}}{r^3} \mathrm{d}V. \tag{1.126}$$

This formular describes the magnetic flux density at the origin when a volume of $\mathrm{d}V$ at point $\mathbf{r}$ carries a current density of $\mathbf{j}$. Replacing $\mathrm{d}V = \mathbf{a}\mathrm{d}\mathbf{l}$ with the area normal vector $\mathbf{a}$ and the length element $\mathrm{d}\mathbf{l}$ and additionally using $I = \mathbf{j}\mathbf{a}$, the above law becomes

$$\mathrm{d}\mathbf{B} = -\frac{\mu_0}{4\pi} I \frac{\mathbf{r} \times \mathrm{d}\mathbf{l}}{r^3}. \tag{1.127}$$

Regarding the field in the center of a circular loop of radius r with a current flowing in it, the infinitesimal length element can be expressed by the radius and an incremental angle dθ via (see figure 1.10)

$$\mathrm{d}\mathbf{l} = r\mathrm{d}\theta\mathbf{e}_{\mathbf{l}}. \tag{1.128}$$

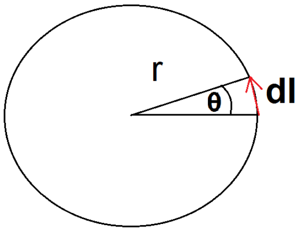

FIGURE 1.10 – *The length element* d**l** *of a circle with radius* r.

By definition, $\mathbf{e}_{\mathbf{l}}$ and $\mathbf{r}$ are orthogonal to each other. It follows

$$\mathrm{d}\mathbf{B} = -\frac{\mu_0 I}{4\pi}\frac{r^2\mathrm{d}\theta}{r^3}\mathbf{e}_{\mathbf{B}} \tag{1.129}$$

$$= -\frac{\mu_0}{4\pi}I\frac{\mathrm{d}\theta}{r}\mathbf{e}_{\mathbf{B}} \tag{1.130}$$

where $\mathbf{r} \times \mathbf{e}_{\mathbf{l}} = r\mathbf{e}_{\mathbf{B}}$. Then, integrating over the whole loop leads to

$$\mathbf{B} = -\frac{\mu_0 I}{2r}\mathbf{e}_{\mathbf{B}} \quad \Leftrightarrow \quad \mathbf{H} = -\frac{I}{2r}\mathbf{e}_{\mathbf{B}}. \tag{1.131}$$

In summary, we find the magnetic field caused by a circular current, which could also result from electrons circling around an atomic core. For the purpose of drawing further conclusions on the magnetic moments $\mathbf{p_m}$, we now regard a line of N of such circular currents as in a solenoid (figure 1.11). Repeating the previous calculations for this case, we obtain

$$\oint_{\partial S}\mathbf{B}\mathrm{d}\mathbf{l} = \mu_0\int_S \mathbf{j}\mathrm{d}\mathbf{S}' = \mu_0 n I. \tag{1.132}$$

Therein, the integration path is chosen as rectangular and containing parts of n loops. Evaluating the left-hand side of equation 1.132 and considering the case of $n, N \to \infty$, while $n < N$, we observe the field B_{in} inside the solenoid to be constant and parallel to the chosen integration path, while the field outside disappears. Moreover, the contributions of the left and right edge of the integration path become zero because field lines are perpendicular to it, leading to a zero-valued scalar product. Finally, we conclude from equation 1.132

$$B_{in}d = \mu_0 n I \tag{1.133}$$

$$\Leftrightarrow B_{in} = \mu_0\frac{n}{d}I \Leftrightarrow H_{in} = \frac{n}{d}I. \tag{1.134}$$

Now, we can compare this outcome with the magnetic field arising from microscopic atomic currents in case that there is no external field applied ($\mathbf{H} = 0$). Then, the

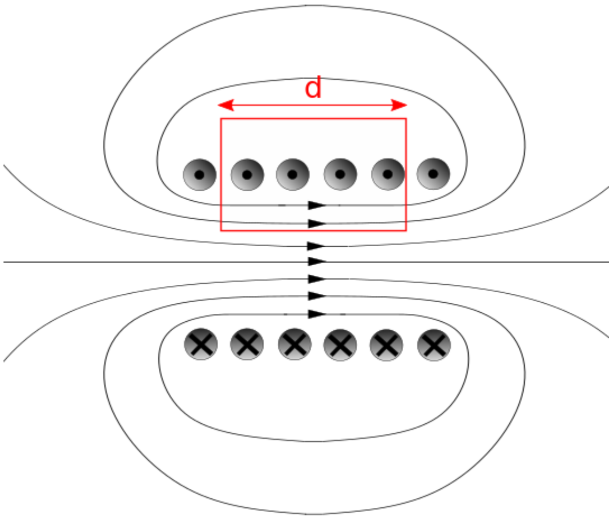

FIGURE 1.11 – *The magnetic field of a solenoid consisting of $N = 6$ turns. The red line marks an exemplary integration path which is used in calculations, in this case including $n = 4$ currents.*

equivalence of

$$\begin{aligned} B &= \mu_0(H + M) && (1.135) \\ &= \mu_0 M && (1.136) \\ &= \mu_0 \frac{n}{d} I && (1.137) \end{aligned}$$

shows that, on the one hand, magnetization can be calculated as

$$M = \frac{n}{d} I \tag{1.138}$$

and, on the other hand, via the definition

$$\begin{aligned} M &= \frac{n}{V} p_m && (1.139) \\ &= \frac{n}{Ad} p_m. && (1.140) \end{aligned}$$

Here, V is the total volume of the regarded line of atoms and A the area which is circulated by one microscopic current. Consequently,

$$p_m = IA, \tag{1.141}$$

suggesting the magnetic moments to have their origin in microscopic atomic currents. Regarding a hydrogen atom in the Bohr model, we can calculate the current caused by a single electron orbiting the core by

$$I = \frac{ev}{2\pi r_0} \tag{1.142}$$

with the elementary charge e, tangential speed v and the radius of the first Bohr orbit r_0. Inserting the corresponding angular moment $L = mr_0v$, we find

$$I = \frac{e}{2m\pi r_0^2} L \tag{1.143}$$

$$\Rightarrow p_m = \frac{e}{2m\pi r_0^2} L\pi r_0^2 \tag{1.144}$$

$$= \frac{e}{2m} L. \tag{1.145}$$

Inserting the minimal value for $L = \hbar$, which is given by the reduced Planck constant, we obtain the Bohr magneton

$$\mu_B = \frac{e}{2m}\hbar = 9.27 \cdot 10^{-24} \text{ Am}^2. \tag{1.146}$$

Considering the arrangement of the atomic magnetic moments in solids in absence of an external field, two different cases are possible. Firstly, the moments could be randomly oriented without interacting with each other, leading to an overall magnetization of $\sum \mathbf{p_m} = \mathbf{0}$ in the solid. Only when an external field is applied, moments align and a non-vanishing magnetization is observed. In case that moments enforce the external field, this material is called paramagnetic. Oppositely, a material with magnetic moments counteracting to an outer field is a diamagnet.
Secondly, there can be an interaction between the atomic magnetic dipole moments, leading to $\sum \mathbf{p_m} \neq \mathbf{0}$ in general, even without an external magnetic bias. This phenomena is called ferromagnetism, which will be treated in the next section.
Additionally to the previous enlisted types of magnetism, there are also antiferromagnetism and ferrimagnetism, which are not of interest in this work and are only mentioned for the sake of completeness.
When analyzing the behavior of finite samples, we have to take care on an additional effect appearing on the surface of magnetic materials. For gaining insight into this issue, we regard the boundary between two media and use Maxwell's equation 1.3

$$\boldsymbol{\nabla} \cdot \mathbf{B} = 0$$

and *Gauss's theorem* for a vector field $\mathbf{F}$

$$\int_V (\boldsymbol{\nabla} \cdot \mathbf{F})\, \mathrm{d}V' = \oint_S \mathbf{F} \cdot \mathbf{n}\mathrm{d}S \tag{1.147}$$

where S denotes the surface of volume V and $\mathbf{n}$ the corresponding unity normal vector. These equations deliver

$$\int_V (\boldsymbol{\nabla} \cdot \mathbf{B})\, \mathrm{d}V' = \oint_S \mathbf{B} \cdot \mathbf{n}\mathrm{d}S = 0. \tag{1.148}$$

For our purpose, we define a box with height h and base area S, containing a part of the boundary surface as shown in figure 1.12. By considering the limiting case of $h \to 0$, we are able to gain insight into the boundary conditions of the magnetic flux

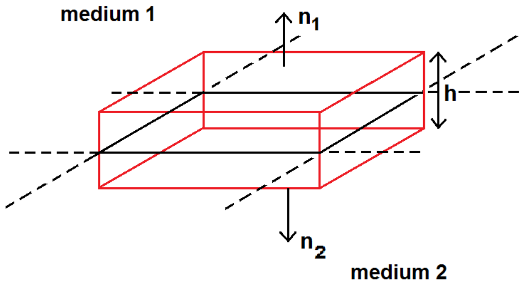

FIGURE 1.12 – *The boundary area between two different media, indicated by black lines, is considered in order to gain insight into the boundary conditions of the magnetic flux density. The red box is used as integration volume for the divergence of* $\mathbf{B}$.

density. In this case, equation 1.148 becomes

$$\mathbf{B_1 n_1} S + \mathbf{B_2 n_2} S = 0 \tag{1.149}$$

where $\mathbf{n_1} = -\mathbf{n_2}$ denote the normal vectors on the two surfaces of the considered box and $\mathbf{B_1}$ and $\mathbf{B_2}$ the flux densities in both media. Accordingly, one finds

$$(\mathbf{B_1} - \mathbf{B_2})\mathbf{n} = 0 \tag{1.150}$$

$$\Leftrightarrow \quad (\mathbf{H_1} - \mathbf{H_2})\mathbf{n} = (\mathbf{M_2} - \mathbf{M_1})\mathbf{n} \tag{1.151}$$

yielding that the normal component of the flux density $\mathbf{B}$ is continous at the boundary between two media, while the normal component of the magnetic field $\mathbf{H}$ shows a discontinuity when the magnetizations of the two media distinguish from each other. Considering an infinite magnetized plate with a magnetization $\mathbf{M_1}$ parallel to normal surface vector $\mathbf{n}$ and surrounded by a medium with an also parallely aligned magnetization $\mathbf{M_2}$ and a magnetic field $\mathbf{H_2}$, we find for the magnetic field inside the plate

$$\mathbf{H_1} = \mathbf{H_2} - (\mathbf{M_1} - \mathbf{M_2}). \tag{1.152}$$

More generally spoken, regarding an arbitrarily shaped magnetized device surrounded by magnetic material, one can define the demagnetization tensor $\mathbf{N}$, which fulfills

$$\mathbf{H_1} = \mathbf{H_2} - \mathbf{N}(\mathbf{M_1} - \mathbf{M_2}). \tag{1.153}$$

In case of ellipsoid samples, $\mathbf{N}$ becomes exact and diagonal, where diagonal components satisfy $n_x + n_y + n_z = 1$. Due to rotational symmetry, $n_x = n_y = n_z = \frac{1}{3}$ is valid for spheres.

1.2.2 Ferromagnetism

Ferromagnetism and especially the effect of ferromagnetic resonance are of great interest in this thesis. Accordingly, deeper insight into these topics are given in the following.

As mentioned before, an interaction between the atomic dipole moments occurs in ferromagnets, giving them the ability to align even without the influence of external fields, leading to non-vanishing magnetizations, in general. When additionally applying and increasing a static magnetic field, the value of magnetization also arises and approaches a maximum value which is called saturation magnetization M_s. This saturation magnetization is reached when the outer field is strong enough to align all magnetic moments strictly parallel to themselves. The therefore required value of the external field is called saturation field H_{sat}. Again reducing the strength of the external field, magnetization also decreases due to thermal fluctuations which disturb the perfect alignment. When external field reaches zero, a magnetization remains, which is typically for ferromagnetic materials and is called remanence M_r, for which $M_r < M_s$ is valid. Inverting the direction of the outer field and increasing its magnitude again, magnetization vanishes at a non-zero field which is called coercivity H_{ci} before approaching the value of $-M_s$. These behavior can be pictured in a ferromagnetic hysteresis loop, shown in figure 1.13.

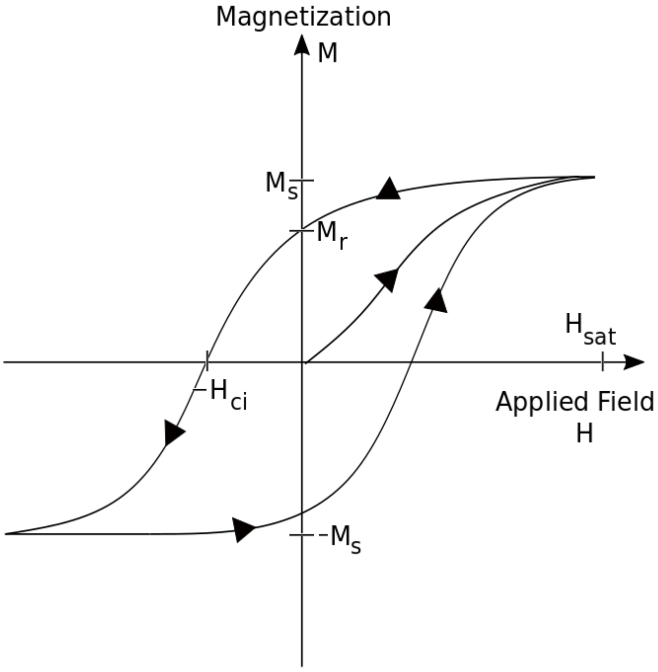

Figure 1.13 – *A typical hysteresis loop for a ferromagnet, where magnetization of a sample is plotted in dependence of the applied external field. Curve starts in the demagnetized state ($M = 0$). The quantities of saturation magnetization M_s, saturation field H_{sat}, remanence M_r and coercitivity H_{ci} are marked in the picture.*

As already mentioned, thermal fluctuations disturb the alignment of magnetic moments. Consequently, such hysteresis loops are also temperature dependent and especially saturation magnetization is influenced by thermal energies. When examining the hysteresis loop of a given device at different temperatures, it is observed that higher temperatures reduce saturation magnetization until it disappears at a special value called Curie temperature T_c. Above this temperature, the material behaves like a paramagnet due to the increasing influence of thermal perturbations on the magnetic interaction between the atomic moments which prevents them from aligning. The typical relation between Curie temperature and saturation magnetization is shown in figure 1.14.

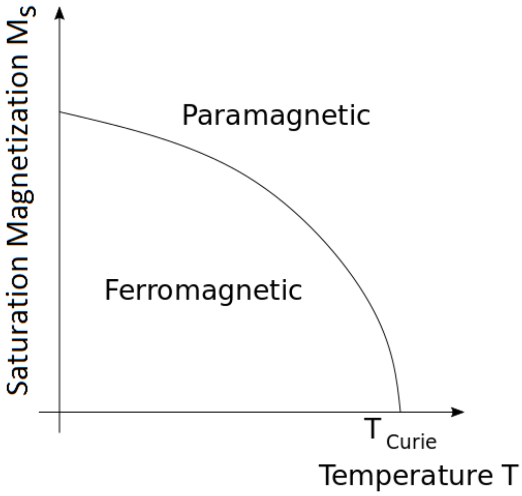

Figure 1.14 – *Saturation magnetization M_s decreases with increasing temperature due to disturbing thermal fluctuations. The Curie temperature T_{Curie} denotes the point in which M_s vanishes. The paramagnetic and ferromagnetic phases are separated by this curve.*

A further important phenomena, which is the main topic of this work, is the ferromagnetic resonance appearing when a ferromagnetic device is brought into an externally applied static magnetic field $\mathbf{H_{ext}}$, while a high-frequent electromagnetic wave $\mathbf{h}(t)$ oscillates perpendicularly to it. This composition causes a precessive motion of the single dipole moments (see figure 1.15), whose consequences will be derived in the following.

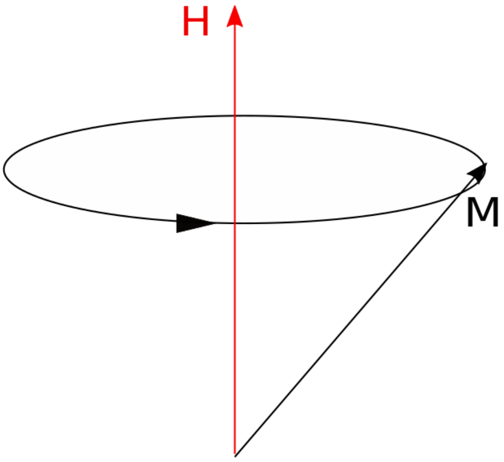

Figure 1.15 – *The precessive motion of the magnetization vector $\mathbf{M}$ around the static magnetic field $\mathbf{H_{ext}}$.*

We assume the static field to be applied in $z-$direction as

$$\mathbf{H_{ext}} = \begin{pmatrix} 0 \\ 0 \\ H_{ext} \end{pmatrix}, \tag{1.154}$$

$$\tag{1.155}$$

while the magnetic component of the high-frequent wave oscillates in $x-y-$plane (as the magnetic component of a $TE_{1,0}$ mode in a rectangular waveguide with propagation in $x-$ or $y-$direction)

$$\mathbf{h}(t) = \begin{pmatrix} h_x \\ h_y \\ 0 \end{pmatrix}. \tag{1.156}$$

Within this, we assume the static field to be large enough in order to fully magnetize the device unter test, meaning $H_{ext} > H_{sat}$ and, furthermore, $H_{ext} \gg h_x, h_y$. Additionally, the high-frequent magnetic components are time-harmonic, i. e. $h_x, h_y \propto \exp(-i\omega t)$ with the angular frequency ω.
The total magnetic field $\mathbf{H_{tot}}$ inside a ferromagnetic device under test is also influenced by a demagnetization field (see section 1.2)

$$\mathbf{H_{dem}} = -\mathbf{NM} \tag{1.157}$$

with the magnetization $\mathbf{M}$, which can be assumed to be static along $z-$direction, while its $x-$ and $y-$components should be time-harmonic as the incoming magnetic signal, $m_x, m_y \propto \exp(-i\omega t)$. Assuming an ellipsoidal sample, we can write

$$\mathbf{H_{tot}} = \mathbf{H_{ext}} + \mathbf{H_{dem}} + \mathbf{h} = \begin{pmatrix} h_x - n_x m_x \\ h_y - n_y m_y \\ H_{ext} - n_z M_z \end{pmatrix}. \tag{1.158}$$

This effective field has to fulfill the *Landau-Lifshitz-Gilbert equation* for the precessive motion of the magnetic moments

$$\frac{\partial \mathbf{M}}{\partial t} = -\gamma \mathbf{M} \times \mathbf{H_{tot}} + \frac{\alpha}{M_z}\left(\mathbf{M} \times \frac{\partial \mathbf{M}}{\partial t}\right). \tag{1.159}$$

Here,

$$\gamma \approx 2.21276 \cdot 10^5 \frac{\mathrm{A}}{\mathrm{m} \cdot \mathrm{s}} \tag{1.160}$$

denotes the gyromagnetic ratio and α is an empirically introduced damping coefficient. Inserting equation 1.158 in 1.159 and using the time-harmonic dependencies, we calculate for the three vector components

$$\frac{\mathrm{d}m_x}{dt} = -\gamma\Big(m_y(H_{ext} - n_z M_z) - M_z(h_y - n_y m_y)\Big) - \frac{\alpha}{M_z} M_z \frac{\mathrm{d}m_y}{dt} \tag{1.161}$$

$$\frac{\mathrm{d}m_y}{dt} = -\gamma\Big(M_z(h_x - n_x m_x) - m_x(H_{ext} - n_z M_z)\Big) + \frac{\alpha}{M_z} M_z \frac{\mathrm{d}m_x}{dt} \tag{1.162}$$

$$0 = -\gamma\Big(m_x(h_y - n_y m_y) - m_y(h_x - n_x m_x)\Big) + \frac{\alpha}{M_z}\left(m_x \frac{\mathrm{d}m_y}{dt} - m_y \frac{\mathrm{d}m_x}{dt}\right). \tag{1.163}$$

Because of the assumption $H_{ext} \gg h_x, h_y$ and, consequently, $M_z \gg m_x, m_y$, we can restrict to linear terms of h_x, h_y, m_x and m_y. Performing the derivatives, we get after marginal rearrangements two relevant equations

$$-h_y \omega_m = (i\alpha\omega - \omega_m n_y - \omega_0 + n_z \omega_m) m_y + i\omega m_x \tag{1.164}$$

$$h_x \omega_m = i\omega m_y - (-n_x \omega_m - \omega_0 + n_z \omega_m + i\alpha\omega) m_x \tag{1.165}$$

in which we introduced the frequencies

$$\omega_m = \gamma M_z \tag{1.166}$$

and

$$\omega_0 = \gamma H_{ext}. \tag{1.167}$$

Comparing these relations with the known linkage

$$\mathbf{M} = \boldsymbol{\chi}\mathbf{H} \tag{1.168}$$

we can derive the susceptibility tensor by writing the above relations as one vectorial equation and inverting the emerging matrix. Because α takes small values for most materials, we ignore higher-order terms and obtain the *Polder tensor*

$$\boldsymbol{\chi} = \begin{pmatrix} \chi & -\kappa \\ \kappa & \chi \end{pmatrix} \tag{1.169}$$

with

$$\chi = \frac{\omega_m\Big(\omega_0 + i\alpha\omega + \omega_m(n_y - n_z)\Big)}{\omega_{res}^2 - \omega^2 + 2i\alpha\omega\Big(\omega_0 + \frac{\omega_m}{2}(n_x + n_y - 2n_z)\Big)} \tag{1.170}$$

$$\kappa = \frac{i\omega\omega_m}{\omega_{res}^2 - \omega^2 + 2i\alpha\omega\Big(\omega_0 + \frac{\omega_m}{2}(n_x + n_y - 2n_z)\Big)} \tag{1.171}$$

as it can be also found in textbooks like [19], for example. In this derivation, we introduced the resonance angular frequency ω_{res} which is determined by *Kittel's equation*

$$\omega_{res}^2 = \Big(\omega_0 + (n_x - n_z)\omega_m\Big)\Big(\omega_0 + (n_y - n_z)\omega_m\Big). \tag{1.172}$$

Typical curves of the real and imaginary parts of μ_r and κ are shown in figure 1.16.

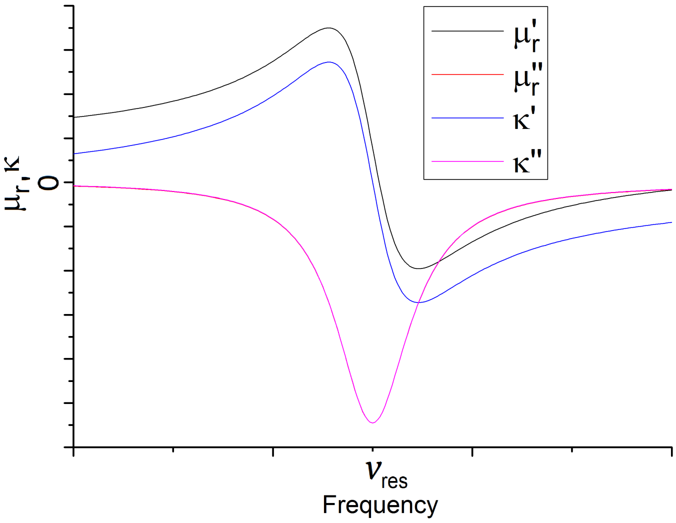

FIGURE 1.16 – *Typical graphs for the entries of the Polder tensor. Demagnetization factors are omitted, as it is the case for bulk material or for a sphere, where* $n_x = n_y = n_z = \frac{1}{3}$ *and, consequently, eliminate each other. Note that imaginary parts* μ_r'' *and* κ'' *coincide.*

1.3 Effective Medium Theory

The main target of the present work is to gain knowledge on the permeability of composites material, consisting of a surrounding matrix and inclusions which are small enough in order to describe the whole composite as an effective medium. Accordingly, we want to focus on existing effective medium theories concerning the permittivity and permeability of composite materials in order to understand and compare the results of this work. Although these theories are commonly derived for the effective permittivity, we can simply apply the same methodes for the permeability because of the equivalence of electric and magnetic equations in the absence of charges and currents. For that purpose, we rely in the following on the works [20–22].

1.3.1 Introduction of the Effective Permeability

One way to introduce the effective permeability μ_{eff} is the usage of the general relation between the flux density and the magnetic field

$$\mathbf{B} = \mu_0 \mu_r \mathbf{H} \tag{1.173}$$

and apply it on heterogeneous material, where neither **B** nor **H** are spatial constant. There, we use the volume average for an arbitrary vector quantity **X** in volume V

$$\langle \mathbf{X} \rangle = \frac{1}{V} \int_V \mathbf{X} \mathrm{d}V \tag{1.174}$$

and define the effective permeability of an inhomogeneous material via

$$\langle \mathbf{B} \rangle = \mu_0 \mu_{eff} \langle \mathbf{H} \rangle . \tag{1.175}$$

Regarding a composite with only one species of a number of N_{inc} inclusions with volume V_{inc} in a matrix, forming a two-phase-composite, we can derive

$$\langle \mathbf{H} \rangle = f \langle \mathbf{H} \rangle_{inc} + (1-f) \langle \mathbf{H} \rangle_m \tag{1.176}$$

$$\langle \mathbf{B} \rangle = \mu_0 \mu_{inc} f \langle \mathbf{H} \rangle_{inc} + \mu_0 \mu_m (1-f) \langle \mathbf{H} \rangle_m = \mu_0 \mu_{eff} \langle \mathbf{H} \rangle \tag{1.177}$$

where index m denotes matrix phase, while inc describes the inclusions which occupy a fraction $f = \frac{N_{inc} V_{inc}}{V_{tot}}$ of the total volume V_{tot}. Inserting equation 1.176 into 1.177, we obtain

$$\mu_{eff} = \frac{\mu_{inc} f \langle \mathbf{H} \rangle_{inc} + \mu_m (1-f) \langle \mathbf{H} \rangle_m}{f \langle \mathbf{H} \rangle_{inc} + (1-f) \langle \mathbf{H} \rangle_m} . \tag{1.178}$$

At this point, a substantially problem occurs when analytically examining this equation: Beneath the determined quantities μ_{inc}, μ_m and f, the averaged fields in the matrix and inclusion phases appear. These values strongly depend on the system's microstructure and can only be analytically calculated in special cases. Two examples for such arrangements are used in the derivations of *Maxwell-Garnett* and *Bruggemann equations*, which will be introduced in the following sections as examples for effective medium mixing formulas. Actually, a high number of such formulas have been developed, which are suitable for different microstructures and parameter ranges. In order to introduce the Maxwell-Garnett equation, we firstly derive the *Clausius-Mosotti relation*, which is fundamental to this mixing formula.

1.3.2 Clausius-Mosotti

As already mentioned, the Clausius-Mosotti relation was originally derived for the permittivity, but an analog derivation of an equivalent formula concerning the permeability is possible. An exemplaric derivation for diamagnetic materials can be found in [23], for example. Here, we choose the consideration of a magnetic moment $\mathbf{p_m}$ of a molecule, experiencing the local field $\mathbf{B_{loc}}$, as starting point, yielding the relation

$$\mathbf{p_m} = \alpha_m \mathbf{B_{loc}} . \tag{1.179}$$

Within this, α_m denotes the magnetic polarisability (as an analog to electric polarizability in the relation $\mathbf{p} = \alpha \mathbf{E}$) and $\mathbf{B_{loc}}$ is defined as the flux density which results from an external applied field and from further dipole moments on a fictional hollow sphere around the regarded dipole (as a magnetic analog to Lorentz field). Accordingly, the resulting macroscopic magnetization in a system of such molecules can be calculated via

$$\mathbf{M} = \frac{1}{V}\sum_{j=1}^{N} \mathbf{p_{m,j}} \tag{1.180}$$

$$= n\alpha_m \mathbf{B_{loc}} \tag{1.181}$$

where $n = \frac{N}{V}$ denotes particle density. Once more, we use the already known relation between magnetization and applied magnetic field $\mathbf{M} = \chi\mathbf{H} = (\mu_r - I)\mathbf{H}$ and $\mathbf{B_{loc}} = \mu_0\mathbf{H_{loc}}$, receiving

$$n\alpha_m\mu_0\mathbf{H_{loc}} = (\mu_r - 1)\mathbf{H}. \tag{1.182}$$

Therein, one has to obey that the local field is enforced by surrounding magnetization compared to the applied field, according to

$$\mathbf{H_{loc}} = \mathbf{H} + \frac{1}{3}\mathbf{M} = \left(1 + \frac{\mu_r - 1}{3}\right)\mathbf{H}, \tag{1.183}$$

leading to the desired Clausius-Mossotti relation

$$n\alpha_m\mu_0\left(1 + \frac{\mu_r - 1}{3}\right)\mathbf{H} = (\mu_r - 1)\mathbf{H} \tag{1.184}$$

$$\Leftrightarrow \frac{\mu_r - 1}{\mu_r + 2} = \frac{n\alpha_m\mu_0}{3}, \tag{1.185}$$

which connects the microscopic polarisability to the macroscopic permeability and therefore serves as a starting point for several fundamental mixing formulas.

1.3.3 Maxwell-Garnett

Now, we want to regard spherical inclusions with permeability μ_{inc} dilutely distributed in a non-magnetic host matrix. Formula 1.185 yields for the polarisability of such an inclusion

$$\alpha_{m,inc} = \frac{3}{n\mu_0}\frac{\mu_{inc} - 1}{\mu_{inc} + 2}. \tag{1.186}$$

Additionally, we can replace the dipole density n by

$$n = \frac{N_{inc}}{V} = \frac{1}{\frac{4}{3}\pi r_{inc}^3} \tag{1.187}$$

with the inclusions' radius r_{inc} when each particle is assumed to carry one dipole moment $p_{m,inc}$. It follows

$$\alpha_{m,inc} = \frac{4\pi r_{inc}^3}{\mu_0}\frac{\mu_{inc} - 1}{\mu_{inc} + 2}, \tag{1.188}$$

which can be inserted in equation 1.185 again. When μ_r is replaced by the effective permeability of the composite μ_{eff}, we obtain

$$\frac{\mu_{eff}-1}{\mu_{eff}+2}=f\frac{\mu_{inc}-1}{\mu_{inc}+2}, \tag{1.189}$$

where $f=\frac{N_{inc}}{V_{tot}}\cdot\frac{4}{3}\pi r_{inc}^3$ denotes the volume fraction occupied by N_{inc} inclusions in the total volume V_{tot}, as before. Deriving equation 1.189 for a composite with a magnetic matrix with permeability μ_m, one finds

$$\frac{\mu_{eff}-\mu_m}{\mu_{eff}+2\mu_m}=f\frac{\mu_{inc}-\mu_m}{\mu_{inc}+2\mu_m}, \tag{1.190}$$

which is known as Maxwell-Garnett equation [24, 25]. Rearranging delivers

$$\mu_{eff}=\frac{\mu_{inc}+2\mu_m+2f(\mu_{inc}-\mu_m)}{\mu_{inc}+2\mu_m-f(\mu_{inc}-\mu_m)}\mu_m. \tag{1.191}$$

Contrary, changing the roles of host and inclusion medium by switching $\mu_{inc}\leftrightarrow\mu_m$ and $f\leftrightarrow(1-f)$ yields

$$\mu_{eff}^{*}=\frac{\mu_m+2\mu_{inc}+2(1-f)(\mu_m-\mu_{inc})}{\mu_m+2\mu_{inc}-(1-f)(\mu_m-\mu_{inc})}\mu_{inc}, \tag{1.192}$$

which does not deliver the same results as equation 1.191. This point highlights that the effective permeability of a composite does not only depend on the parameters μ_m, μ_{inc} and f, but also the regarded microstructure and the topology have a strong influence. A drawback of the Maxwell-Garnett approach becomes clear, when trying to expand the formula to composites with several types of inclusions, as done in [26], leading to

$$\frac{\mu_{eff}-\mu_m}{\mu_{eff}+2\mu_m}=\sum_i f_i\frac{\mu_i-\mu_m}{\mu_i+2\mu_m}. \tag{1.193}$$

Using this equation and regarding the case in which the host material is completely replaced by the inclusions, meaning $\sum_i f_i=1$, μ_{eff} still depends on μ_m. This irrational fact shows that this expansion is not meaningful within the Maxwell-Garnett formalism.

1.3.4 Bruggeman

Contrary to the model of Maxwell-Garnett, in which spherical inclusions are dispersed in a host matrix, a slightly changed arrangement is chosen by Bruggeman [27]. Here, a model is described in which all involved materials are taken into account in the same manner, leading to a mixing formula for a multiple phase composite

$$\sum_i f_i\left(\frac{\mu_i-\mu_{eff}}{\mu_i+2\mu_{eff}}\right)=0, \tag{1.194}$$

where index i denotes different materials. Such a microstructure, in which all involved materials are symmetrically treated, is called aggregate topology. The counterpart, in which inclusions are surrounded by a host matrix, meaning an asymmetric structure, is referred to as cermet topology (see schematic sketches in figure 1.17).

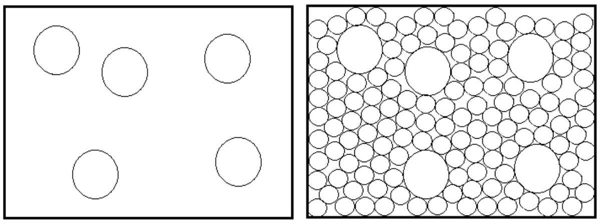

Figure 1.17 – *A cermet topology of spherical inclusions, which is assumed in the model of Maxwell-Garnett, is exemplarily illustrated in the left picture, while an aggregate structure of spheres is shown right. In case of an aggregate structure consisting out of spherical components, a complete filling of the available space is only possible for polydisperse systems.*

Regarding a composite of two materials, equation 1.194 approaches to 1.189 in the limit of small volume fractions of inclusions, $f \to 0$, but also gives meaningful results for multicomponent systems. Unfortunately, this theory has also its insufficiencies. For example, in [28] it was shown by numerical calculations, that there are critical values for the material parameters in which the theory extremely fails.

1.3.5 Bounds of the Effective Medium

In addition to the previously described mixing formulas, one can also look for upper and lower bounds of the effective properties of a composite material which will be discussed in the following. For simplicity, we restrict to scalar- and real-valued permeabilities, as it is the case when regarding isotropic and lossless materials, and to two-phase composites with permeabilities μ_1 and μ_2 with $\mu_1 < \mu_2$ and the volume fraction f for material 1 and $(1-f)$ for material 2.

The most naive approach for the determination of boundaries is that the resulting effective permeability should not fall below the lower value but also should not exceed the higher one according to

$$\mu_1 \leq \mu_{eff} \leq \mu_2. \tag{1.195}$$

These bounds should hold independently of the geometric arrangements or parameter values. Beyond these obvious limits, it is possible to define sharper bounds when considering different microstructures. For that purpose, one should think of patterns of the composite material which maximize or minimize the effective permeability. Such arrangements can be found in the structures shown in figure 1.18: When slices of different materials are parallely aligned to the magnetic field, the magnetic field is constant in the whole device due to the continuity of the tangential component of the **H**-field (see equation 1.84). Consequently, the flux **B** takes the values $\mathbf{B_{1,2}} = \mu_{1,2}\mu_0\mathbf{H}$ in the different phases. Then, the resulting effective permeability can be computed according to equation 1.178 as the arithmetic mean value

$$\mu_{eff,max} = f\mu_1 + (1-f)\mu_2. \tag{1.196}$$

Regarding a parallel alignment of the materials perpendicular to the magnetic field, the magnetic flux $\mathbf{B}$ remains constant in the complete sample due to the continuity of its normal component (see equation 1.150). Accordingly, $\mathbf{H_{1,2}} = \frac{1}{\mu_{1,2}\mu_0}\mathbf{B}$ is valid in the two phases, leading to an effective permeability of

$$\mu_{eff,min} = \left(\frac{f}{\mu_1} + \frac{(1-f)}{\mu_2}\right)^{-1}, \tag{1.197}$$

calculated as the harmonic mean value of the two material permeabilities, which minimizes effective permeability. These derived limitations are called *Wiener bounds.* Actually, it is even possible to derive sharper bounds under the assumption that the system is macroscopically isotropic, what is not the case for the two structures in the calculation above. For that purpose, Hashin and Shtrikman [29] defined a functional for the magnetostatic energy of a multiphase mixture and used variational methods in order to derive upper and lower bounds of the effective permeability. For a two-phase composite, these bounds can be written in the form

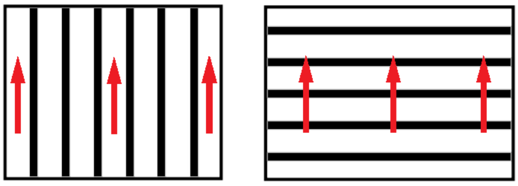

Figure 1.18 – *The maximizing (left) and minimizing (right) microstructures for the permeability. The magnetic field is indicated by red arrows and points parallely or perpendicularly to material layers. The continuity conditions for the* $\mathbf{H}-$ *and* $\mathbf{B}-$*field allow an exact calculation of the effective permeabilities.*

$$\mu_{eff,1} = \mu_1 + 3f\mu_1 \frac{\mu_2 - \mu_1}{\mu_2 + 2\mu_1 - f(\mu_2 - \mu_1)} \tag{1.198}$$

$$\mu_{eff,2} = \mu_2 + 3(1-f)\mu_2 \frac{\mu_1 - \mu_2}{\mu_1 + 2\mu_2 - (1-f)(\mu_1 - \mu_2)} \tag{1.199}$$

which are equivalent to the Maxwell-Garnett formula when spherical inclusions with a permeability of μ_2 are distributed in a matrix medium with μ_1 ($\mu_{eff,1}$) or the other way around ($\mu_{eff,2}$). These results, obtained by different approaches, highlight the consistence of the basic theories. The different bounds are visualized in picture 1.19.

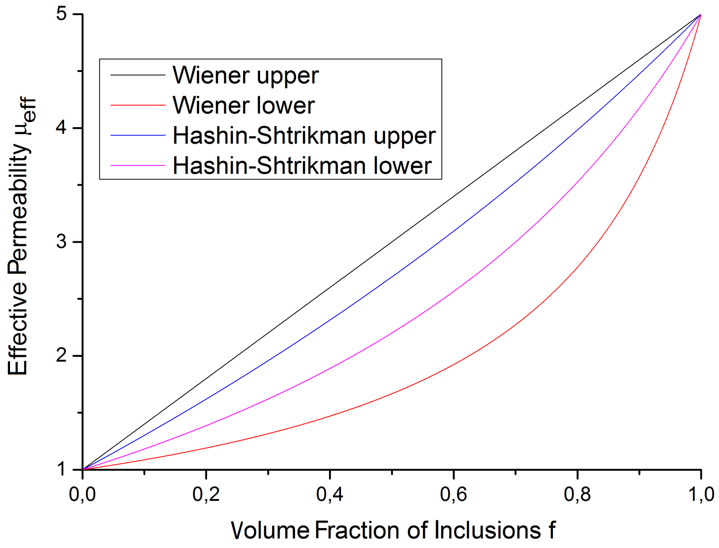

FIGURE 1.19 – *The Wiener and Hashin-Shtrikman bounds for the effective permeability of a composite consisting out of spherical, isotropic inclusions with* $\mu_{inc} = 5$ *and a host medium with* $\mu_m = 1$.

In case of complex valued permeabilities, i. e. lossy materials, the determination of the discussed bounds is more complicated and was treated in the works of [30–34]. In this context, the accessible region for the effective permeability in the complex plane is limited by arcs, as exemplarily shown for Wiener bounds in figure 1.20.

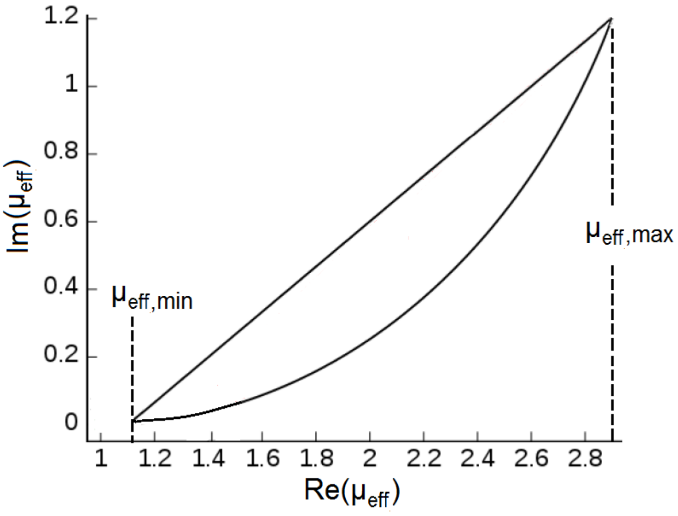

FIGURE 1.20 – *The complex Wiener bounds for the effective permeability with a host medium with* $\mu_m = 1$ *and inclusions with* $\mu_{inc} = 20 - 12i$, *which occupy* $f = 10$ % *of the composite's volume. Picture adapted from [35].*

Chapter 2

State of the Art

After the introduction of the fundamentals in the previous chapter, the latest published results which are relevant for this work will be focused in the following. The aspect of highest interest, the ferromagnetic resonance of composite systems, was handled by V. B. Bregar and M. Pavlin in 2004 [36] and again by Bregar in 2005 [37]. Therefore, these two publications will be especially treated in this chapter.

2.1 Fully Magnetized Noninteracting Inclusions in a Non-magnetic Matrix

In the work of [36], the authors regard a dilute composite consisting of spherical ferromagnetic inclusions in a non-magnetic host medium. Within this, the distances between inclusions are assumed to be large enough in order to neglect interparticle interactions. Moreover, it is presumed that the externally applied magnetic field is strong enough to fully magnetize the ferromagnetic material. Consequently, the Polder tensor is used for calculations of the resulting permeability.
Considering this case, the authors argue that, due to the missing interactions between inclusions, every ferromagnetic particle in the composite is exposed to the same field determining the resonance frequency. Accordingly, the resonance of the whole composite should arise at the same frequency as for a single, isolated sphere. In this regard, one can consider Kittel's equation for the ferromagnetic resonance angular frequency (compare with 1.172)

$$\omega_{res}^2 = \Big(\omega_0 + (n_x - n_z)\omega_m\Big)\Big(\omega_0 + (n_y - n_z)\omega_m\Big) \tag{2.1}$$

which delivers the same value for bulk material (volume fraction $f = 1$, accordingly zero demagnetization factors n_x, n_y, n_z) as for an isolated sphere in a large non-magnetic matrix ($f \to 0$, $n_x = n_y = n_z = 1/3$). Following this, resonance frequencies should be equal in both cases.
Regarding the Maxwell-Garnett equation (1.190) for the effective susceptibility of such a composite (with $\chi = \mu_r - 1$ and $\chi_m = 0$), one obtains for the diagonal component of the Polder tensor

$$\chi_{eff} = f\left(\frac{3\chi_{inc}}{3 + \chi_{inc}(1 - f)}\right) \tag{2.2}$$

where indices m and inc again denote the matrix material or the inclusions, respectively. Now, one can insert the inclusions' susceptibility χ_{inc} as determined by Polder tensor (see equation 1.169). Considering that spherical shape was already taken into account in the corresponding derivation (see chapter 1.3), we use the expression for an infinitely extended sample, meaning with demagnetization factors $n_x = n_y = n_z = 0$. By this, we can calculate the effective susceptibilities of such composites under a constant externally applied field for different values of f, as shown in figure 2.1.

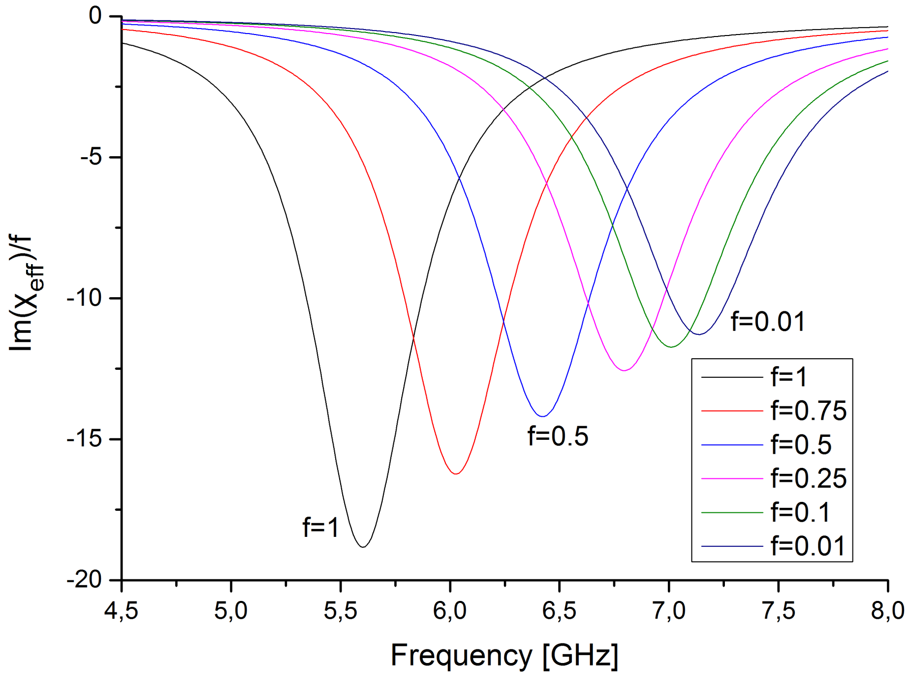

FIGURE 2.1 – *Maxwell-Garnett, equation 2.2, and Polder tensor, equation 1.169, deliver the effective susceptibility which is normalized with respect to to the inclusions' volume fraction and plotted over a given frequency range. Obviously, a shift of the resonance frequency occurs in this formalism when the externally applied field* $H_{ext,z}$ *remains constant.*
Parameters were chosen as in [36]: $\omega_0 = \gamma H_{ext,z} = 35.2$ *GHz* ($\nu_0 = 5.6$ *GHz*), $\alpha = 0.05$, $\omega_m = \gamma M_s = 66.3$ *GHz.*

Contrary to the previous train of thought, resonance angular frequency shifts as a function of inclusions' volume fraction towards the limit

$$\omega_{res}^2 \xrightarrow{f\to 0} \omega_0 \left(\omega_0 + \frac{\omega_m}{3}\right) \tag{2.3}$$

and does not reproduce the equivalence of the cases $f \to 0$ and $f \to 1$ which is crucial due to the missing dipolar interaction in both cases. Accordingly, this shifting behavior can not be meaningfully interpreted and has to be seen as an artifact of this formalism which appears despite the considered interactions in the corresponding derivation (see sections 1.3.2 and 1.3.3). Motivated by this, two different solutions for this discrepancy have been analyzed:
Firstly, one can use theory of ferromagnetism, i.e. *Landau-Lifshitz-equation* (which is

the general form of 1.159)

$$\frac{\partial \mathbf{M}}{\partial t} = \gamma(\mathbf{M} \times \mathbf{H_{int}}) - \frac{\alpha\gamma}{M}\left(\mathbf{M} \times (\mathbf{M} \times \mathbf{H_{int}})\right) \tag{2.4}$$

with the internal magnetic field $\mathbf{H_{int}}$. The static external field $H_{ext,z}$ is assumed to point parallely to the magnetization $\mathbf{M}$ and the system's $z-$axis while the high-frequent magnetic field $\mathbf{h_{ext}}$ oscillates in the $x-y-$plane and raises a high-frequent magnetization $\mathbf{m}$. Accordingly, due to demagnetization effects of finite samples (see equation 1.153), fields can be put into context via

$$H_{int,z} = H_{ext,z} - n_z M_s \tag{2.5}$$

$$\mathbf{h_{int}} = \mathbf{h_{ext}} - \mathbf{N}\mathbf{m}. \tag{2.6}$$

As usual, one assumes the high-frequent magnetic field and magnetization as time harmonic, delivering

$$\mathbf{M} = M_s\mathbf{e_z} + (m_x\mathbf{e_x} + m_y\mathbf{e_y})\exp(-i\omega t) \tag{2.7}$$

$$\mathbf{H_{ext}} = H_{ext,z}\mathbf{e_z} + (h_x\mathbf{e_x} + h_y\mathbf{e_y})\exp(-i\omega t). \tag{2.8}$$

Moreover, magnetization and external field can be linked via the particle susceptibility $\boldsymbol{\chi}$

$$\mathbf{m} = \boldsymbol{\chi}\mathbf{h_{ext}} \tag{2.9}$$

which is given by the Polder tensor with the right choice of demagnetization factors. In addition to these considerations, which are quite similar to the derivation of the Polder tensor, we regard the inclusions' magnetic dipole moment $\mathbf{p_{inc}}$ which is linked with magnetization and the inclusions' volume V_{inc}

$$\mathbf{p_{inc}} = V_{inc}\mathbf{m} \tag{2.10}$$

$$= V_{inc}\boldsymbol{\chi}\mathbf{h_{ext}}. \tag{2.11}$$

For the purpose of drawing conclusions on the composite, the effective dipole moment of the whole sample is considered. In the case of dilute composites, in which interactions between the N_{inc} particles can be neglected, and at sufficiently large distance of the observer, the relation

$$\mathbf{p_{eff}} = \sum_{i=1}^{N_{inc}} \mathbf{p_{inc}} = N_{inc}\mathbf{p_{inc}} \tag{2.12}$$

is valid. In an analog manner to equation 2.11, one can define

$$\mathbf{p_{eff}} = V_{tot}\boldsymbol{\chi_{eff}}\mathbf{h_{ext}}. \tag{2.13}$$

with the total volume of the composite V_{tot}. Combining equations 2.11, 2.12 and 2.13, one finds

$$\boldsymbol{\chi_{eff}} = \frac{N_{inc}V_{inc}}{V_{tot}}\boldsymbol{\chi} = f\boldsymbol{\chi}. \tag{2.14}$$

This result shows that resonance frequency should remain constant and the normalized permeability of a composite should not vary with filling factor f when the external field is the same for every filling factor. This finding contradicts the outcomes illustrated in picture 2.1, which result from Maxwell-Garnett.
The second approach in order to find this result is very similiar to a possible way of deriving the Maxwell-Garnett formula, but includes further characteristics of this magnetostatic problem:
First of all, the tensor form of the permeability, which strongly depends on the static magnetic field, has to be taken into account instead of assuming scalar values. Furthermore, one has to strictly distinguish between the internal magnetic field inside the inclusions and the externally applied magnetic field, which are only equal in non-magnetic or infinite samples. Accordingly, internal flux-density $\mathbf{b_{int}}$ and internal magnetic field $\mathbf{h_{int}}$ can be connected via

$$\begin{aligned} \mathbf{b_{int}} &= \mu_0(\mathbf{h_{int}} + \mathbf{m}) \qquad (2.15)\\ &= \mu_0(1 + \boldsymbol{\chi_{int}})\mathbf{h_{int}}. \qquad (2.16) \end{aligned}$$

In the above relation, $\boldsymbol{\chi_{int}}$ denotes the local susceptibility and differs from $\boldsymbol{\chi}$ in equation 2.11, which refers on external fields. Nevertheless, it is reasonable to assume the same non-diagonal structure for both, according to the Polder tensor

$$\boldsymbol{\chi_{int}} = \begin{pmatrix} \chi_{int} & -\kappa_{int} \\ \kappa_{int} & \chi_{int} \end{pmatrix}. \tag{2.17}$$

This local susceptibility tensor can now be inserted into the magnetostatic problem, described by Laplace's equation

$$\boldsymbol{\nabla}^2\Phi = 0, \tag{2.18}$$

where Φ is the magnetic potential fulfilling $\mathbf{H} = -\boldsymbol{\nabla}\Phi$. By considering the boundary conditions for the potential and the magnetic field, an expression for the potential outside the particle is found [39]

$$\Phi = \left(-\mathbf{I} + \mathbf{G}\frac{R^3}{r^3}\right)\mathbf{h_{ext}} \cdot \mathbf{r} \tag{2.19}$$

where

$$\mathbf{G} = \frac{1}{(\chi_{int}+3)^2 + \kappa_{int}^2}\begin{pmatrix} (\chi_{int}+3)\chi_{int} + \kappa_{int}^2 & -3\kappa_{int} \\ 3\kappa_{int} & (\chi_{int}+3)\chi_{int} + \kappa_{int}^2 \end{pmatrix}, \tag{2.20}$$

r is the distance of the observer and R the radius of the inclusions. [1]
Now, this calculation should be done again for the whole sample of the effective medium, which is assumed to be shaped as a sphere with radius R_{eff} (for the sake of equal demagnetization factors $n_x = n_y = n_z = 1/3$ as for the spherical inclusions), analogically delivering

$$\Phi = \Big(-\mathbf{I} + \mathbf{G_{eff}} \frac{R_{eff}^3}{r^3}\Big)\mathbf{h_{ext}} \cdot \mathbf{r} \tag{2.21}$$

with

$$\mathbf{G_{eff}} = \frac{1}{(\chi_{eff}^{int}+3)^2 + (\kappa_{eff}^{int})^2} \begin{pmatrix} (\chi_{eff}^{int}+3)\chi_{eff}^{int} + (\kappa_{eff}^{int})^2 & -3\kappa_{eff}^{int} \\ 3\kappa_{eff}^{int} & (\chi_{eff}^{int}+3)\chi_{eff}^{int} + (\kappa_{eff}^{int})^2 \end{pmatrix}, \tag{2.22}$$

in which χ_{eff}^{int} and κ_{eff}^{int} denote the entries of the effective susceptibility tensor of the composite sphere, relying on the effective internal magnetic field $\mathbf{h_{eff}}$, according to

$$\mathbf{m_{eff}} = \boldsymbol{\chi_{eff}^{int}} \mathbf{h_{eff}}. \tag{2.23}$$

As in the ferromagnetic derivation, we assume an observer far enough from the effective sphere so that dipole contributions of the effective material appear as the sum of the N_{inc} inclusions' dipole moments. At this point, it should be again highlighted that composites are assumed to be so dilute that we can neglect interactions between the inclusions, but particles of course carry a dipolar moment, nevertheless. Accordingly, we can equate the dipole terms in equations 2.19 and 2.21 according to

$$\Big(\mathbf{G_{eff}} \frac{R_{eff}^3}{r^3}\Big)\mathbf{h_{ext}} \cdot \mathbf{r} = N_{inc}\Big(\mathbf{G} \frac{R^3}{r^3}\Big)\mathbf{h_{ext}} \cdot \mathbf{r}. \tag{2.24}$$

Using the relation for the filling factor $f = \frac{N_{inc}R^3}{R_{eff}^3}$, one can conclude

$$\mathbf{G_{eff}} = f\mathbf{G}. \tag{2.25}$$

In frequency ranges which are remotely located from resonance, meaning $\kappa_{int} \rightarrow 0$, equation 2.25 reduces to

$$\frac{\chi_{eff}^{int}}{\chi_{eff}^{int}+3} = f\frac{\chi_{int}}{\chi_{int}+3} \tag{2.26}$$

which is the common formula of Maxwell-Garnett for a non-magnetic host medium with $\chi = 0$. However, this formula applies only for the internal susceptibilities.
For gaining knowledge on the quantity of χ_{eff} instead, the next task is to determine the coefficients in this matrix equation. For this purpose, further information can be drawn from the relations for the dynamic magnetization and the usage of equations

---

[1] An analog, but more detailed calculation of this expression can be found in section 2.2.

2.6 and 2.9, according to

$$
\begin{aligned}
&\mathbf{m} = \boldsymbol{\chi}_{\boldsymbol{int}}\mathbf{h}_{\mathbf{int}} = \boldsymbol{\chi}\mathbf{h}_{\mathbf{ext}} \quad \textit{(by definition)} && (2.27)\\
\Leftrightarrow \quad &\boldsymbol{\chi}_{\boldsymbol{int}}(\mathbf{h}_{\mathbf{ext}} - \mathbf{N}\mathbf{m}) = \boldsymbol{\chi}\mathbf{h}_{\mathbf{ext}} && (2.28)\\
\Leftrightarrow \quad &\boldsymbol{\chi}_{\boldsymbol{int}}\mathbf{h}_{\mathbf{ext}} = \boldsymbol{\chi}\mathbf{h}_{\mathbf{ext}} + \boldsymbol{\chi}_{\boldsymbol{int}}\mathbf{N}\mathbf{m} = (\mathbf{I} + \boldsymbol{\chi}_{\boldsymbol{int}}\mathbf{N})\mathbf{m} && (2.29)\\
\Leftrightarrow \quad &\boldsymbol{\chi}_{\boldsymbol{int}}\mathbf{h}_{\mathbf{ext}} = (\mathbf{I} + \boldsymbol{\chi}_{\boldsymbol{int}}\mathbf{N})\boldsymbol{\chi}\mathbf{h}_{\mathbf{ext}}. && (2.30)
\end{aligned}
$$

By this, we have derived a relation linking $\boldsymbol{\chi}$, coupling magnetization and external magnetic field, and the internal tensor $\boldsymbol{\chi}_{\boldsymbol{int}}$, coupling magnetization and internal magnetic field. Applying the diagonal form of the demagnetization tensor $\mathbf{N}$ for a sphere and performing a matrix inversion, one calculates

$$
\begin{aligned}
\boldsymbol{\chi} &= (\mathbf{I} + \boldsymbol{\chi}_{\boldsymbol{int}}\mathbf{N})^{-1}\boldsymbol{\chi}_{\boldsymbol{int}} && (2.31)\\
&= \frac{3}{(\chi_{int}+3)^2 + \kappa_{int}^2}\begin{pmatrix} (\chi_{int}+3)\chi_{int} + \kappa_{int}^2 & -3\kappa_{int} \\ 3\kappa_{int} & (\chi_{int}+3)\chi_{int} + \kappa_{int}^2 \end{pmatrix} && (2.32)\\
&= 3\mathbf{G}. && (2.33)
\end{aligned}
$$

In a completely analog manner, one obtains for the effective parameters of the composite

$$
\begin{aligned}
\mathbf{m}_{\mathbf{eff}} &= \boldsymbol{\chi}_{\boldsymbol{eff}}^{\boldsymbol{int}}\mathbf{h}_{\mathbf{eff}} = \boldsymbol{\chi}_{\boldsymbol{eff}}\mathbf{h}_{\mathbf{ext}} && (2.34)\\
\Leftrightarrow \boldsymbol{\chi}_{\boldsymbol{eff}} &= 3\mathbf{G}_{\mathbf{eff}}. && (2.35)
\end{aligned}
$$

Furthermore, by the usage of equations 2.25 and 2.33, the same result as in the ferromagnetic approach is obtained

$$\boldsymbol{\chi}_{\boldsymbol{eff}} = 3\mathbf{G}_{\mathbf{eff}} = 3f\mathbf{G} = f\boldsymbol{\chi}. \tag{2.36}$$

In summary, V. B. Bregar and M. Pavlin modified the conventional effective medium theory for tensorial susceptibilites and showed that Maxwell-Garnett formula can be only meaningfully applied far away from resonance (see equations 2.25 and 2.26). This is caused by the susceptibility's tensorial form which must be observed in the vicinity of the ferromagnetic resonance.

Moreover, the not always carefully done, but important distinction between the local and external magnetic fields is highlighted by the authors which plays an important role due to demagnetization effects at the boundaries between media with different magnetizations. The unphysical frequency shift, arising under a constant externally applied magnetic field in a dilute composite with negligible interactions, shown in figure 2.1, has shown to be a consequence of this disregarded distinction.

Contrary, resulting from the here reproduced considerations, it was derived that effective susceptibility tensor of such a dilute composite, in which interactions between inclusions can be neglected, divided by the volume fraction f of ferromagnetic material should be independent of f when externally applied magnetic field remains constant.

The same assumptions as done in the work presented in this section were included in our simulations in section 4.2 in which dipolar interactions can be neglected due to the arrangement of the inclusions on a simple cubic lattice. This simulative approach delivers the same results as gained in the here reproduced analytic work.

2.2 Inclusion of Particle Interactions via an Effective Medium Approach

One year later, in his subsequent work [37], Bregar extended his former approach by also taking into account particle interactions, i.e. the static magnetization of neighbouring inclusions by an effective medium approach and distinguished three different situations: a fully magnetized composite, a composite with single-domain particles and a composite with demagnetized particles. The results for the first two of these different cases will be described in the following, while the composite consisting out of demagnetized inclusions is not of interest for the present work.

2.2.1 Fully Magnetized Composite

Firstly, a fully magnetized composite is regarded. As a starting point, the magnetostatic potential Φ with $\mathbf{H} = -\boldsymbol{\nabla}\Phi$ is considered which fulfills in ferromagnetic materials

$$\boldsymbol{\nabla}^2\Phi = \boldsymbol{\nabla}\mathbf{M}. \tag{2.37}$$

When only considering the fundamental mode of moment precession, meaning a coherent rotation, $\boldsymbol{\nabla}\mathbf{M} = 0$ applies. Consequently, equation 2.37 reduces again to Laplace's equation

$$\boldsymbol{\nabla}^2\Phi = 0. \tag{2.38}$$

As in the previous work, magnetization and external magnetic field are assumed as superpositions of static components $\mathbf{H_{ext,z}}$ and $\mathbf{M}$, defining the $z-$axis, and time harmonic components oscillating in $x - y-$direction (compare to equation 2.8). Furthermore, the Polder form of the susceptibility tensor (see equation 1.169), linking high-frequent magnetization $\mathbf{m}$ and magnetic field $\mathbf{h_{ext}}$ as in equation 2.9, is assumed for the inclusions.
As before, the solution of equation 2.37 should be found, for which the ansatz of

$$\Phi = \mathbf{a} \cdot \mathbf{b} + \mathbf{b} \cdot \frac{\mathbf{r}}{r^3} \tag{2.39}$$

is followed. Now, boundary conditions for magnetic fields and flux densities are considered (see section 1.2.1). Within this, a single inclusion embedded in an effective medium is considered in order to gain insight into the internal fields. Due to the continuity condition of the potential on the particles' surface, one can write

$$\Phi_{inc}|_{boundary} = \Phi_{eff}|_{boundary}. \tag{2.40}$$

Moreover, the normal component of the magnetic flux density is continous (see section 1.2.1), leading to

$$\mathbf{B_{inc}} \cdot \mathbf{n}|_{boundary} = \mathbf{B_{eff}} \cdot \mathbf{n}|_{boundary} \tag{2.41}$$
$$(\mu_0 \mathbf{H_{inc}} + \mu_0 \mathbf{M_{inc}}) \cdot \mathbf{n}|_{boundary} = (\mu_0 \mathbf{H_{eff}} + \mu_0 \mathbf{M_{eff}}) \cdot \mathbf{n}|_{boundary} \tag{2.42}$$

in which $\mathbf{n}$ denotes a normal surface vector on the particle boundary. In the next step, we can again split fields into their static and dynamic components and use the definition of the susceptibility tensor (equation 2.9). By this, we obtain

$$\begin{aligned}&\Big(\mu_0(\mathbf{H_{inc,z}} + \mathbf{h_{inc}}) + \mu_0(\mathbf{M_s^{inc}} + \mathbf{m_{inc}})\Big) \cdot \mathbf{n}|_{boundary}\\ =&\Big(\mu_0(\mathbf{H_{eff,z}} + \mathbf{h_{eff}}) + \mu_0(\mathbf{M_{eff}} + \mathbf{m_{eff}})\Big) \cdot \mathbf{n}|_{boundary}\end{aligned} \tag{2.43}$$

$$\begin{aligned}\Leftrightarrow \quad &\mu_0\Big(\mathbf{H_{inc,z}} + \mathbf{M_s^{inc}} + \mathbf{h_{inc}} + \boldsymbol{\chi_{inc}^{int}}\mathbf{h_{inc}}\Big) \cdot \mathbf{n}|_{boundary}\\ =&\mu_0\Big(\mathbf{H_{eff,z}} + \mathbf{M_{eff}} + \mathbf{h_{eff}} + \boldsymbol{\chi_{eff}^{int}}\mathbf{h_{eff}}\Big) \cdot \mathbf{n}|_{boundary}.\end{aligned} \tag{2.44}$$

Within this, it should be highlighted that the regarded fields are internal quantities. Consequently, the chosen susceptibility tensors connect these internal fields. In case that an infinitely extended host medium is regarded, externally applied magnetic field and the effective field in the medium are equal to each other.
By substituting $\mathbf{H_{inc}} = -\boldsymbol{\nabla}\Phi_{inc}$ and $\mathbf{H_{eff}} = -\boldsymbol{\nabla}\Phi_{eff}$ and solving the above equation system (consisting out of equation 2.39, 2.42 and 2.44), one finds

$$\Phi_{eff} = \left(-\mathbf{I} + \mathbf{G}\frac{R^3}{r^3}\right)\mathbf{H_{ext}} \cdot \mathbf{r} + \frac{(M_s^{inc} - M_{eff})R^3}{3r^3}\mathbf{z} \cdot \mathbf{r} \tag{2.45}$$

which can be seen as an adjusted form of equation 2.19. Within this equation, G is a tensor quantity, as before, and is given by

$$\mathbf{G} = \frac{1}{(\chi_{inc}^{int} + 2\chi_{eff} + 3)^2 + (\kappa_{inc}^{int} + 2\kappa_{eff})^2}\begin{pmatrix} G_{11} & G_{12} & 0\\ G_{21} & G_{22} & 0\\ 0 & 0 & 0\end{pmatrix} \tag{2.46}$$

with

$$G_{11} = G_{22} = (\chi_{inc}^{int} - \chi_{eff})(\chi_{inc}^{int} + 2\chi_{eff} + 3) + (\kappa_{inc}^{int} - \kappa_{eff})(\kappa_{inc}^{int} + 2\kappa_{eff} + 3) \tag{2.47}$$
$$G_{12} = -G_{21} = -3(\kappa_{inc}^{int} - \kappa_{eff} + \chi_{eff}\kappa_{inc}^{int} + \chi_{inc}^{int}\kappa_{eff}). \tag{2.48}$$

Remembering demagnetization effects (see section 1.2.1 and especially equation 1.153), we can link the magnitudes of the two static magnetic fields in the particles and the surrounding medium via

$$H_{inc,z} = H_{eff,z} - \frac{M_s^{inc} - M_{eff}}{3}. \tag{2.49}$$

This relation should be used for the determination of the particles' intrinsic susceptibility $\boldsymbol{\chi_{inc}^{int}}$, leaving the effective quantities χ_{eff}, κ_{eff} and M_{eff} as unknown in equation 2.45.

At this point, it has to be highlighted that a self-consistent effective-medium approximation should be followed, meaning that the sum of the dipole contributions of the system has to vanish when the effective field should remain constant for different filling factors. Expressed in formulas, we can write for the total effective field H_{eff} and the effective field without dipolar interactions H_{eff}^{wd}

$$H_{eff} = H_{eff}^{wd} + \sum_i N_i H_{dip,i} \overset{H_{eff}=const.}{\rightarrow} \sum_i N_i H_{dip,i} = 0 \tag{2.50}$$

Regarding equation 2.45, dipole contributions are given by the second and third term, thus leading to the condition

$$\sum_i \left(\mathbf{G_i H_{ext}} N_i R_i^3 + \frac{(M_s^{inc,i} - M_{eff}) N_i R_i^3}{3} \mathbf{z} \right) = 0 \tag{2.51}$$

for a system consisting of several types of spherical particles indexed with i and a respective number of N_i. It should be emphasized that this analytic step means the introduction of an aggregate microstructure consisting exclusively of spherical inclusions (compare to section 1.3.4) which form the effective medium.

Actually, condition 2.51 consists out of three equations, from which the one for the $z-$component reduces to

$$M_{eff} = \frac{\sum_i M_s^{inc,i} N_i R_i^3}{\sum_i N_i R_i^3} = \sum_i f_i M_s^{inc,i} \tag{2.52}$$

with the inclusions' volume fractions f_i. This result is coherent with the definition of the magnetization (see equation 2.11).

Moreover, the equations for the $x-$ and $y-$components can be transformed into

$$\sum_i f_i G_i = 0 \tag{2.53}$$

which can be used for numerical calculations of χ_{eff} and κ_{eff}. Regarding frequencies far from resonance, $\kappa_{inc}^{int}, \kappa_{eff} \rightarrow 0$ is valid, and equation 2.53 reduces to one single equation

$$\sum_i f_i \frac{\chi_{inc}^{int} - \chi_{eff}}{\chi_{inc}^{int} + 2\chi_{eff} + 3} = 0 \tag{2.54}$$

which was already introduced as Bruggeman's mixing formula (equation 1.194). Actually, the obtainment of the Bruggeman formula far from resonance frequency is a consequence of the analog approaches in the here presented derivation including the

the solution of the Laplace's equation for one magnetized sphere in a homogeneous environment (see equation 2.45) and applying the results on a system consisting out of different types of spheres under self-consistency condition (included via equation 2.51). Restricting to a system with only one single type of inclusions embedded in a non-magnetic matrix medium (labeled with index m), the derived equations simplify to

$$M_{eff} = f M_s^{inc} \tag{2.55}$$

$$f\mathbf{G_{inc}} + (1-f)\mathbf{G_m} = 0 \tag{2.56}$$

in which $\mathbf{G_{inc}}$ and $\mathbf{G_m}$ are calculated according to equation 2.46 with $\boldsymbol{\chi_{inc}^{int}}$ according to the Polder model or $\boldsymbol{\chi_m^{int}} = \mathbf{0}$. With these results, the entries of the effective susceptibility tensor can be calculated and subsequently, the frequency of the resonance can be determined for different volume fractions with a constant externally applied field. Exemplary results are shown in figures 2.2-2.5.

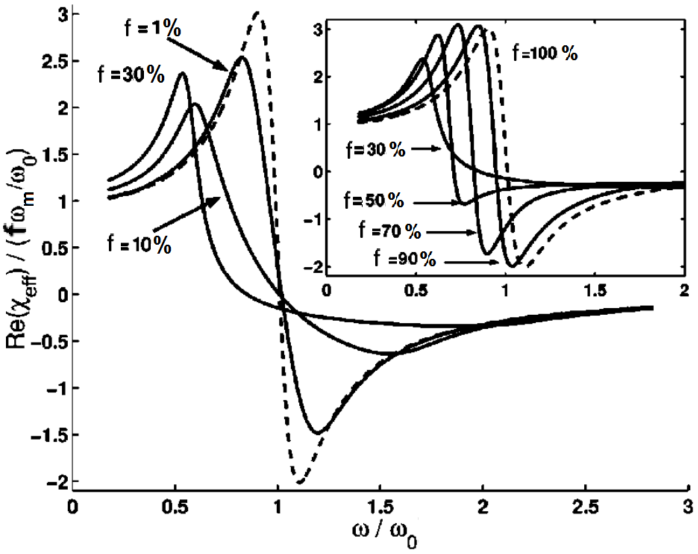

Figure 2.2 – *The real part of the diagonal component χ_{eff} of the effective susceptibility tensor, which is normalized with regard to volume fraction f and frequency ratio $\frac{\omega_m}{\omega_0} = \frac{M_s^{inc}}{H_{ext,z}}$ in dependence of angular frequency ratio $\frac{\omega}{\omega_0}$ and for different values of f. The non-interacting case is shown by dashed lines. Values of the inclusions' parameter are chosen according to $M_s^{inc} = 3 \cdot 10^5 \frac{A}{m}$ and $\alpha = 0.1$, which are quite realistic for ferromagnetic materials. Moreover, an external magnetic field of $H_{ext,z} = 1.6 \cdot 10^5 \frac{A}{m}$ remaining constant for different volume fractions is regarded. Since an infinitely extended effective medium is regarded, $H_{ext,z}$ and $H_{eff,z}$ correspond to each other. Accordingly, equation 2.49 is used for calculating the internal magnetic field inside the inclusions, determining the entries of the Polder tensor. Picture taken from [37].*

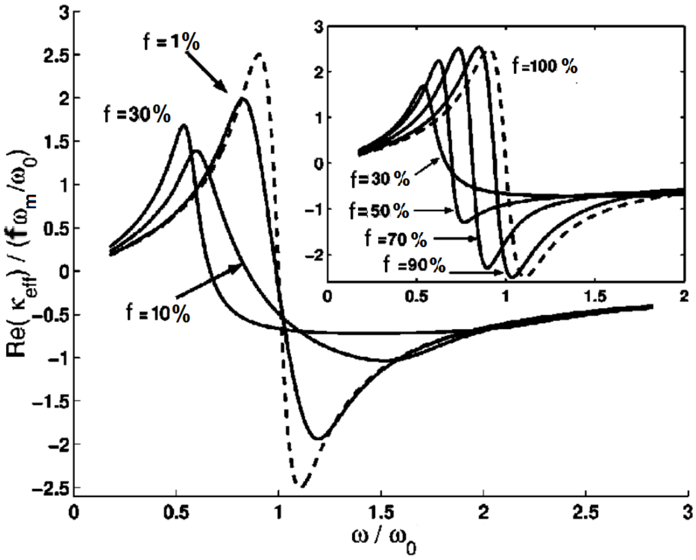

FIGURE 2.3 – *The real part of the off-diagonal component* κ_{eff} *of the effective susceptibility tensor for different volume fractions. Normalization and parameters are the same as in figure 2.2. Picture taken from [37].*

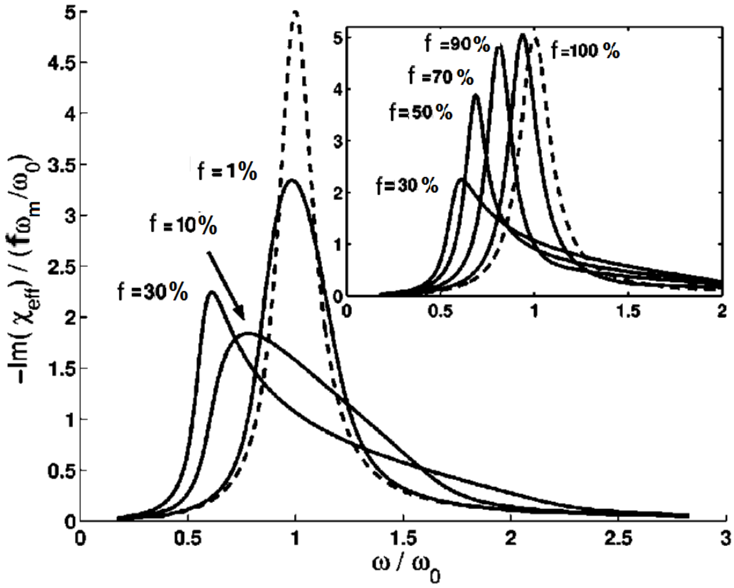

FIGURE 2.4 – *The imaginary part of the components of the effective susceptibility tensor for different volume fractions. Normalization and parameters are the same as in figures 2.2 and 2.3. Please note imaginary parts of* χ_{eff} *and* κ_{eff} *take the same values in this calculation. Picture taken from [37].*

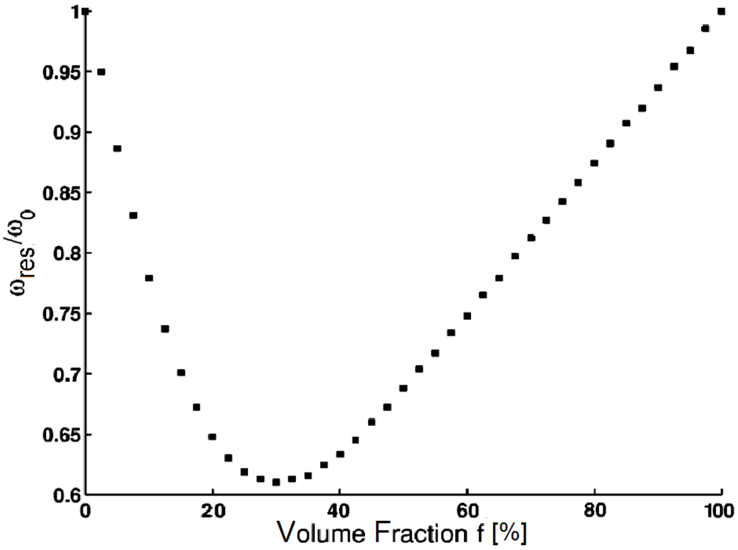

FIGURE 2.5 – *From the previously calculated entries of the permeability tensor (see figures 2.2-2.4), resonance angular frequency can be determined for different volume fractions when externally applied field remains constant. Picture taken from [37].*

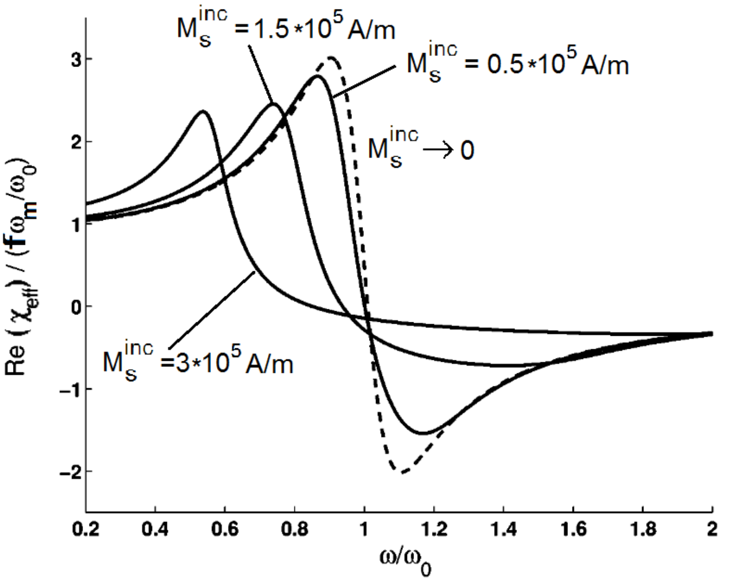

FIGURE 2.6 – *The real part of* χ_{eff} *for a volume fraction of* $f = 30$ %*, which marks the strongest variation from the non-interacting case, is plotted for different values of* M_s^{inc}*. All other parameters are the same as in figures 2.2-2.5. Picture taken from [37].*

Within these diagrams, it can be seen that even for low volume fractions of ferromagnetic material as $f = 1$ %, there is a clear discrepancy between the non-interacting and interacting case. This difference, which also changes the resonance frequency, increases until $f = 30$ % is reached before curves approach again the values of the bulk material. This turning back for $f \rightarrow 100$ % can be explained by the the identical behavior of bulk and spherical ferromagnetic samples. As expected, the strength of the variation from the non-interacting case can be tuned by the inclusions' saturation magnetization, as shown in figure 2.6.

Looking at these results, especially the shift of the resonance frequency is of high interest. In the model of Polder and for small values of the damping coefficient α, the frequency of the resonance only depends on the internal magnetic field. Accordingly, a shift of the resonance frequency must be a consequence of a change of the magnetic fields inside the sample by the effect of neighbouring inclusions, which can be either tuned by different volume fractions or different magnetization of inclusions, which is in coherence with the presented results.

2.2.2 Composite with Isotropically Orientated Single-Domain Inclusions

The second case examined in the work of [37] is a composite consisting of single-domain particles which are also magnetized in the absence of an external magnetic field. Consequently, the orientations of the single magnetic moments are not necessarily in alignment to a given bias, but can be arbitrarily chosen. Despite of this freedom of orientation, one can also consider a perfect alignment of single-domain inclusions, which again leads to the same results as in the previous section with the anisotropy field H_a, generated by the crystal structure, instead of an external field. Therefore, the consideration of an isotropical distribution of the magnetic moments is more interesting and yields further results, which will be reproduced in the following.

Just like in the previously considered case of an external magnetization source, we regard an incident high-frequent magnetic wave oscillating in $x-y-$direction, defining the laboratory coordinate system. Contrary to the previously examined case, all magnetization vectors do not point in $z-$ direction in this laboratory system. Thus, we have to introduce an internal coordinate system for every inclusion, where the $z'-$axis is defined by its magnetic moment's orientation. As shown in many textbooks as [41], a transformation between two of such coordinate systems can be done with the help of a transformation matrix A which can be written with the three Euler angles ϕ, θ, ψ in the form

$$\mathbf{A} = \begin{pmatrix} \cos\psi\,\cos\phi - \cos\theta\,\sin\phi\,\sin\psi & -\sin\psi\,\cos\phi - \cos\theta\,\sin\phi\,\cos\psi & \sin\theta\,\sin\phi \\ \cos\psi\,\sin\phi - \cos\theta\,\cos\phi\,\sin\psi & -\sin\psi\,\sin\phi + \cos\theta\,\cos\phi\,\cos\psi & -\sin\theta\,\sin\phi \\ \sin\theta\,\sin\psi & \sin\theta\,\cos\psi & \cos\theta \end{pmatrix}. \tag{2.57}$$

Following this, we can relate the magnetizations in different systems $\mathbf{M}$ and $\mathbf{M}'$ via

$$\mathbf{M} = A\mathbf{M}' = A(\chi'\mathbf{h}' + M_s\mathbf{z}') = \underbrace{A\chi' A^{-1}}_{\boldsymbol{\chi}}\mathbf{h} + M_s A\mathbf{z}' = \chi\mathbf{h} + M_s\mathbf{z}. \tag{2.58}$$

Within this, we found an expression for the individual susceptibility tensors $\boldsymbol{\chi}$ in the laboratory system which can be used in order to solve Laplace's equation again. Contrary to the corresponding previous calculation, we can use the susceptibility of the effective medium χ_{eff} as a scalar value because of the isotropic distribution of the dipoles' orientation. Apart from this, the same steps as in the derivation of equation 2.45 are repeated for an arbitrary direction of magnetization, delivering

$$\Phi_m = -\left(\mathbf{I} + \mathbf{B^{-1}D}\frac{R^3}{r^3}\right)\mathbf{h_{ext}} \cdot \mathbf{r} + M_s^{inc}\frac{R^3}{3r^3}(\mathbf{B^{-1}Az}) \cdot \mathbf{r} \tag{2.59}$$

for the magnetostatic potential outside the inclusions. Within this expression B and D denote tensorial terms given by

$$\mathbf{B} = \chi_{\mathbf{inc}}^{\mathbf{int}} + (3 + 2\chi_{eff})\mathbf{I} \tag{2.60}$$

$$\mathbf{D} = \chi_{eff}\mathbf{I} - \chi_{\mathbf{inc}}^{\mathbf{int}} \tag{2.61}$$

containing the inclusions' susceptibility tensor in the laboratory system, determined by material properties, the magnetic orientation and the internal magnetic field. The latter is the superposition of the anisotropy field and demagnetization effects which are given from the inclusions' inner magnetostatic potential according to

$$H_d = -\frac{M_s^{inc}}{3 + 2\chi_{eff}}. \tag{2.62}$$

For a non-magnetic material, **B** and **D** become scalar values and the above equations reduce to

$$B = (3 + 2\chi_{eff}) \tag{2.63}$$

$$D = \chi_{eff} \tag{2.64}$$

$$\Rightarrow \Phi_m = -\left(1 + \frac{\chi_{eff}}{3 + 2\chi_{eff}}\frac{R^3}{r^3}\right)\mathbf{h_{ext}} \cdot \mathbf{r}. \tag{2.65}$$

Again, self-consistency requires the sum of the dipole parts of the system to vanish. Before summarizing, we average the dipole contributions (second and third term in equation 2.59) over all possible orientations. Thereby, we notice that averaging of the third term yields

$$< M_s^{inc}\frac{R^3}{3r^3}(\mathbf{B^{-1}Az}) \cdot \mathbf{r} > \tag{2.66}$$

$$= M_s^{inc}\frac{R^3}{3r^3}\underbrace{< (\mathbf{B^{-1}Az}) \cdot \mathbf{r} >}_{0} \tag{2.67}$$

$$= 0$$

due to the isotropic distribution of the dipole orientations. Summing up over all i types of inclusions and the non-magnetic matrix delivers

$$\underbrace{\sum_i f_i < \mathbf{B_i^{-1}D_i} >}_{inclusions} + \underbrace{(1 - \sum_i f_i)\frac{\chi_{eff}}{2\chi_{eff} + 3}\mathbf{I}}_{matrix} = 0. \tag{2.68}$$

Within this, the term $< \mathbf{B_i^{-1}D_i} >$ also becomes scalar through averaging, leading to a completely scalar valued equation which can be solved in order to determine the complexed valued quantity χ_{eff}. For the purpose of calculating the inclusions' intrinsic susceptibility, the Polder model is used with an anisotropy field H_a instead of an external magnetic bias, which is given by $H_a = \frac{2K}{\mu_0 M_s^{inc}}$ with the anisotropy constant K and points along the direction of magnetization. For simplicity's sake, we assume a crystal with an uniaxial anisotropy, meaning that there is only one prefered direction of magnetization. Choosing an exemplary set of parameters and a composite consisting of only one type of inclusions in the non-magnetic matrix medium, the scalar valued effective susceptibility is calculated and plotted in figure 2.7.

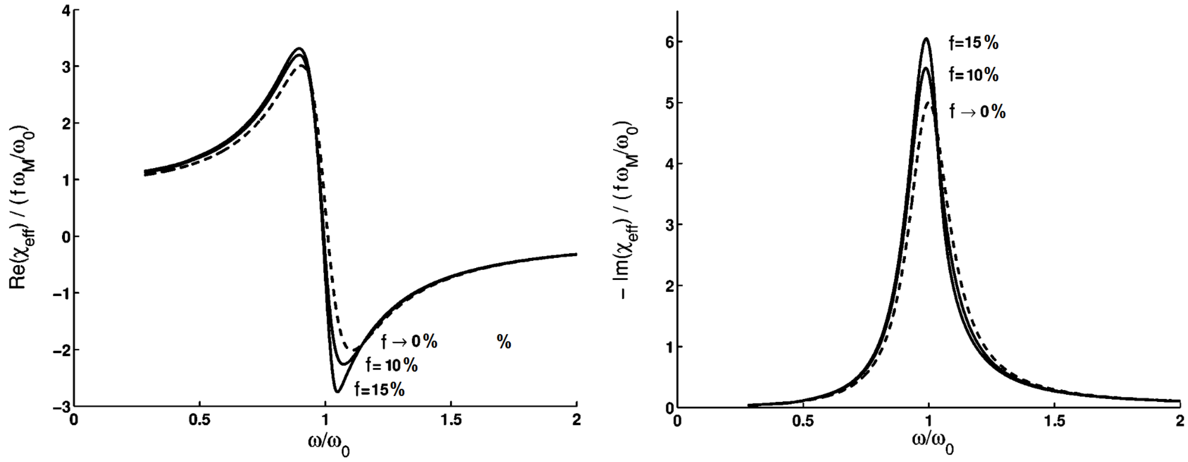

FIGURE 2.7 – *The real (left) and imaginary part (right) of the normalized effective susceptibility for a composite of single-domain ferromagnetic inclusions whose magnetic orientations are isotropically distributed in a non-magnetix matrix. The inclusions' parameters are chosen as anisotropy constant* $K = 3 \cdot 10^4 \frac{J}{m^3}$*, saturation magnetization* $M_s^{inc} = 3 \cdot 10^5 \frac{A}{m}$ *and damping coefficient* $\alpha = 0.1$*. The later two are the same as before, while the anisotropy constant is also chosen in the range of values of real ferrites and leads to an anistropy field* $H_a = \frac{2K}{\mu_0 M_s^{inc}} \approx 1.6 \cdot 10^5 \frac{A}{m}$*, comparable to the external field in the previous section. For the purpose of normalizing the results,* $\omega_0 = \gamma \frac{2K}{\mu_0 M_s^{inc}}$ *and* $\omega_m = \gamma M_s^{inc}$ *are defined. Picture taken from [37].*

Obviously, the filling factor's influence on the susceptibility is much smaller than before and almost no shift of the resonance frequency can be observed. Thus, the results for isotropically orientated single domain particles strongly differ from the previously examined case of a fully magnetized composite, in which all dipole moments are perfectly aligned.

2.3 Discussion and Motivation for this Work

In the paper of [36], the authors highlighted that the tensor form of the susceptibility and a clear distinction between the internal and external fields have to be taken into account when using effective medium theory for ferromagnetic materials. Not disregarding these facts, the unphysical result of a shifting resonance frequency for non-interacting inclusions in a non-magnetic host matrix is adjusted. Moreover, it is shown that the normalized susceptibility tensor's entries do not vary with the filling factor when interactions are negligible, as in a very dilute composite.

Expanding this approach in the work of [37] by including static magnetization of surrounding particles in a mean field approximation, results are refined and show a strong variation of the non-diagonal susceptibility tensor with inlusions' volume fraction in a fully magnetized composite, connected with a significant shift of the resonance frequency. This shift increases until filling factor reaches a value of approximately 30 %, before curves turn back for higher volume fractions and approach the ones of a bulk material, again. Contrary, in a composite of single-domain inclusions with isotropic orientation, these effects are much smaller and effective susceptibility becomes scalar valued.

Although these results are substantial and allow much insight into the topic of composites with ferromagnetic inclusions in the vicinity of the ferromagnetic resonance, the underlying equations are derived with the help of mean field approximations, meaning that one single inclusion is treated as embedded in a homogeneous medium with calculated properties, and later applied on composites with an aggregate topology. Actually, this approach disregards local inhomogeneities in the field distributions which may have a significant influence on the composite's behavior. Accordingly, the local influence of static magnetization of surrounding particles and the interplay between the externally applied field and the magnetic fields generated by the inclusions' dipole moments should be regarded in order to further refine the results. Naturally, this exceeds the possibilities of the accessible analytic methods. Consequently, one has to restrict to numerical methods in order to gain further insight into this topic, which should be done in this work. For that purpose, different simulation and evaluation methods are chosen which will be described in the following chapter.

Chapter 3

Methods

In this chapter, the different computational approaches which are chosen in order to generate the later presented results should be introduced. At first, the experimental transmission- and reflection method in waveguides in which the $S-$parameters can be determined are discussed. As it will be highlighted, these experimental set-ups must be adjusted according to the device under test: An isotropic sample with scalar valued permittivity and permeability requires a less complicated arrangement and evaluation procedure than an anisotropic device with tensorial properties. In each context, the used computation algorithm for the determination of the permittivity and permeability is presented, as the Nicholson-Ross-Weir (NRW) method for isotropic [41–44] and the elaborate procedure by Queffelec et al. for anisotropic materials [45, 46].
Afterwards, the commercial *High Frequency Structure Simulator* (HFSS), a finite element method solver by Ansys Incorporation, is presented, in which the experimental set-ups are reconstructed, finite element meshes are generated and $S-$parameters can be calculated. Due to run time optimization, theses meshes are exported to the systems of *Lehrstuhl für theoretische Elektrotechnik* (LTE) at Saarland University by Romanus Dyczij-Edlinger in order to calculate the $S-$parameters with model order reduction (MOR) methods, which will also be introduced in this chapter.
In addition to these tools, a numerical computing method of the local magnetic fields due to the inclusions' moments is needed in order to respect dipolar interactions in the composite. This procedure is described in the end of the present chapter.

3.1 Transmission and Reflection Methods

In the paper of [42], the former works of [43] and [44] are extended and a method for the determination of the permittivity ε and permeability μ of a sample in one single experiment is described. This Nicholson-Ross-Weir method, which will be discussed at first, was worked out for isotropic materials. Afterwards, the more complex method by Queffelec et al. [45, 46], which also applies for anisotropic samples and must be used for the examination of the ferromagnetic composites of interest in this work, will be introduced.

3.1.1 Isotropic Samples

In order to determine the electric and magnetic properties of a sample at microwave frequencies, ε and μ, the device under test is brought into a waveguide (or into a transmission line, which is not regarded in this work), in such a way that the total cross section is filled (see set-up shown in figure 3.1).

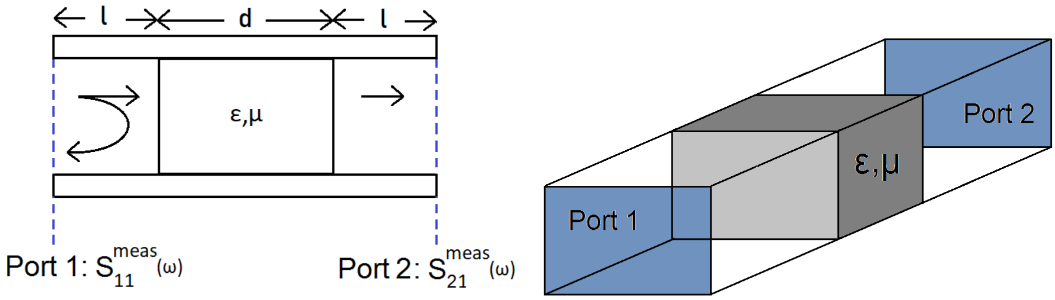

FIGURE 3.1 – *The experimental set-up for determining ε and μ within the transmission-reflection method. Left picture shows structures from the side while waves travel from left to right. Right picture highlights that the whole cross section is filled by the sample.*

The inner waveguide dimensions are chosen in such a way that only one mode can propagate in the frequency range of interest, while the others are damped in the air or vacuum filled segment of length l (see section 1.1.2). This experiment can be done either with a rectangular waveguide, for example supporting frequencies of the so called X-band (waveguide cross section of 2.286 cm × 1.016 cm with a frequency range of around 7 to 12 GHz), or in a parallel plate waveguide. For both types, the NRW method, which will be introduced in the following, can be applied.
First of all, the $S-$parameters $S_{11}^{meas}(\omega)$ and $S_{21}^{meas}(\omega)$ have to be measured for each frequency point of interest. Because of the finite distance of l between the device under test and the places of measurement, a phase correction of these parameters has to be done according to

$$S_{11} = S_{11}^{meas} \cdot \exp\left(-2i\beta_0 l\right) \tag{3.1}$$

$$S_{21} = S_{21}^{meas} \cdot \exp\left(-2i\beta_0 l\right) \tag{3.2}$$

with the propagation constant in the vacuum filled waveguide β_0, which depends on the chosen type of waveguide and its geometry (see equations 1.49 and 1.59). Here, the factor of 2 appears due to the wave passing the distance of length l twice: once from port 1 to the first sample boundary and a second time through reflection in case of S_{11} or through travelling from the second sample boundary to port 2 in case of S_{21}. By this calibration, we obtain the $S-$parameters which are given by equations 1.108 and 1.113

$$S_{11} = \frac{(1-a^2)r}{1-r^2a^2} \tag{3.3}$$

$$S_{21} = \frac{(1-r^2)a}{1-r^2a^2} \tag{3.4}$$

with the material propagation constant (see sections 1.1.2.3 and 1.1.2.4)

$$\beta_m = \begin{cases} \beta_0\sqrt{\varepsilon_r\mu_r} & \text{TEM mode in parallel plate waveguides} \\ \sqrt{\beta_0^2\varepsilon_r\mu_r - k_c^2} & \text{TE mode in rectangular waveguides} \end{cases}, \tag{3.5}$$

the phase factor

$$a = \exp\left(i\beta_m d\right) \tag{3.6}$$

and the reflection coefficient

$$r = \frac{1-\sqrt{\frac{\varepsilon_r}{\mu_r}}}{1+\sqrt{\frac{\varepsilon_r}{\mu_r}}} \tag{3.7}$$

as described in section 1.1.3. Afterwards, the following calculations are performed as intermediate steps in order to isolate ε_r and μ_r. First of all, a magnitude K is defined as

$$K = \frac{S_{11}^2(\omega) - S_{21}^2(\omega) + 1}{2S_{11}(\omega)} \tag{3.8}$$

which is useful in order to determine the reflection coefficient r via

$$r = K \pm \sqrt{K^2-1}. \tag{3.9}$$

Within this calculation, the plus or minus sign is chosen in such a way that the condition $|r| \leq 1$, which is set by energy conservation, is fulfilled. Afterwards, the propagation factor can be calculated according to

$$a = \frac{S_{11}^2(\omega) + S_{21}^2(\omega) - r}{1 - \left[S_{11}(\omega) + S_{21}(\omega)\right] r}. \tag{3.10}$$

Then, μ_r and ε_r are given by

$$\mu_r = \frac{1+r}{\Lambda(1-r)\sqrt{\frac{1}{\lambda_0^2} - \frac{1}{\lambda_c^2}}} \tag{3.11}$$

$$\varepsilon_r = \frac{(\frac{1}{\Lambda^2} + \frac{1}{\lambda_c^2})\lambda_0^2}{\mu_r} \tag{3.12}$$

with

$$\frac{1}{\Lambda^2} = -\left[\frac{1}{2\pi d}\ln\left(\frac{1}{a}\right)\right]^2, \tag{3.13}$$

$\lambda_0 = \frac{c}{f}$ and the cut-off wavelength λ_c (see section 1.1.2).
In this procedure, two problems occur: In equation 3.13, the logarithm of the complex valued magnitude $\frac{1}{a}$ is calculated. Due to the logarithmic identity for a complex number

$z = |z| \exp\Big(i\mathrm{Arg}(z)\Big)$,

$$\log(z) = \log(|z|) + i\mathrm{Arg}(z) \tag{3.14}$$

$$\tag{3.15}$$

and the periodicity of the complex exponential function, according to

$$\begin{aligned} z &= z\exp(i2\pi k) && (3.16)\\ &= |z|\exp\Big(i\mathrm{Arg}(z)\Big)\exp(i2\pi k) && (3.17)\\ &= |z|\exp\Big(i(\mathrm{Arg}(z) + 2\pi k)\Big) && (3.18)\end{aligned}$$

with an integer number k, the computation in equation 3.13 is not unambiguous. Consequently, a resolution of this ambiguity is needed which is found in

$$\ln\left(\frac{1}{a}\right) = \ln\left(\left|\frac{1}{a}\right|\right) + i(\mathrm{Arg}\left(\frac{1}{a}\right) + 2\pi k), \tag{3.19}$$

$$\tag{3.20}$$

where k equals the highest integer number smaller than $\frac{d}{\lambda_m}$ and corresponds to the number of full wavelengths performed by the dominant mode inside the sample. Within this, the wavelength in the material filled guide is given by

$$\lambda_m = \mathrm{Re}\left(\left(\frac{\varepsilon_r\mu_r}{\lambda_0^2} - \frac{1}{\lambda_c^2}\right)^{-1/2}\right) \tag{3.21}$$

and must be estimated by predictions of ε_r and μ_r. Otherwise, k can also be found by trying different integer values.

The second occuring problem within the NRW method becomes obvious regarding equation 3.8: When S_{11} approaches zero, then S_{21} approaches one, because energy conservation requires $|S_{11}|^2 + |S_{21}|^2 = 1$. Consequently, equation 3.8 becomes a fraction in the form of $\frac{0}{0}$. From the mathematical point of view, this represents a removable singularity, but becomes unstable under experimental conditions (or in simulations) which are always linked with noisy measurements or calculations. The described situation appears for low loss materials at frequency points fulfilling the condition $d = n\frac{\lambda_m}{2}$. Exemplary experimental results appearing as a consequence of this issue are shown in figure 3.2. Contrary to the problem of the ambiguous complex logarithm, this drawback can not be resolved in the NRW evaluation method, but bypassed by the usage of short devices, which avoid satisfying $d = n\frac{\lambda_m}{2}$ in the frequency range of interest. Unfortunately, the shortening of the sample reduces accuracy in experiments, which marks the great disadvantage of the analytic NRW method.

Alternatively, it is possible to solve equations 1.108 and 1.113 by numerical computations, as Newton's method, in which the problem of removable singularities does not appear. Within this, one can use the results from NRW method as an estimation for ε_r and μ_r in the first frequency point. Naturally, this is much more akward then analytic calculations. The results for the different methods with $S-$parameter drawn from HFSS simulations will be analyzed in section 3.2.2.

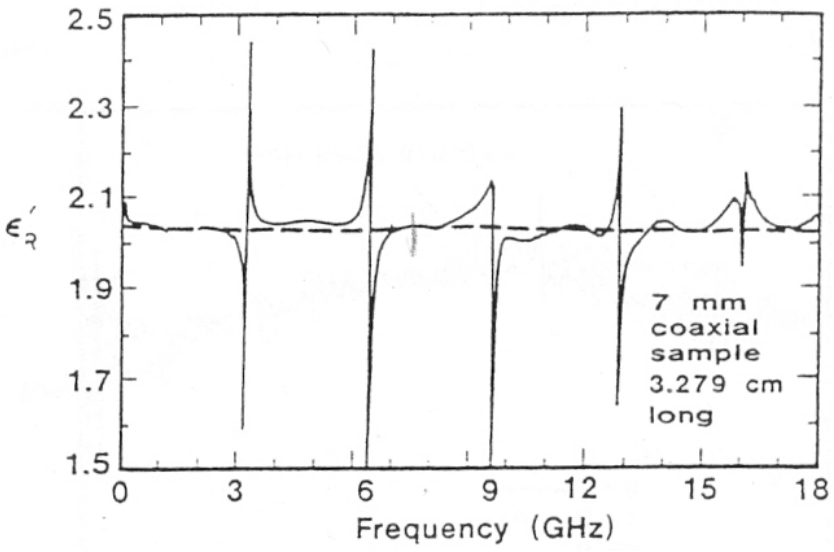

FIGURE 3.2 – *A* 3.279 *cm long teflon sample in a transmission line is analyzed by the NRW method. In the determination of* ε_r *and* μ_r *of this low loss material, singularities appear at special frequencies which are determined by the sample length. Picture taken from [47].*

3.1.2 Anisotropic Samples

In the previous described methods, two complex valued magnitudes, $S_{11} = S_{22}$ and $S_{21} = S_{12}$, are used in order to determine two different complex valued parameters ε and μ. Regarding anisotropic samples, with a non-diagonal permeability tensor in the form of

$$\mu = \begin{pmatrix} \mu & -\kappa \\ \kappa & \mu \end{pmatrix}, \tag{3.22}$$

an additional unknown and complex valued magnitude κ appears. Consequently, a further complex magnitude must be measured in order to obtain a determinable problem. In this context, P. Quéffélec et al. developed a method in which the sample's anisotropy is used in order to create a non-reciprocal experimental set-up (leading to $S_{21} \neq S_{12}$), whereby a third measured magnitude is gained. In order to determine ε, μ and κ, the following strategy is chosen: Firstly, one examines the so called direct problem, which means the calculation of $S-$parameters out of previously defined permittivity and permeability values of the sample. Afterwards, a sequential quadratic programming method is used in order to bring the calculated $S-$parameters into accord with the results of the experiment or simulation, whereby solutions for the material parameters ε, μ and κ are found.

3.1.3 Direct Problem: Determination of Scattering Parameters

The realization of a non-reciprocal cell and the solution of the direct problem are treated in [45]. In this work, the following configuration of the measurement cell is chosen (see figure 3.3): An uniform static magnetic field is applied along the small side of a rectangular waveguide (defined as $y-$direction) with a cross section of dimensions a and b. This cross section is only partially filled with an auxiliary dielectric slab from $x = 0$ to $x = h$, which increases the cell's sensitivity, and the ferritic material of interest from $x = h$ to $x = l$ with $0 < h < l < a$.

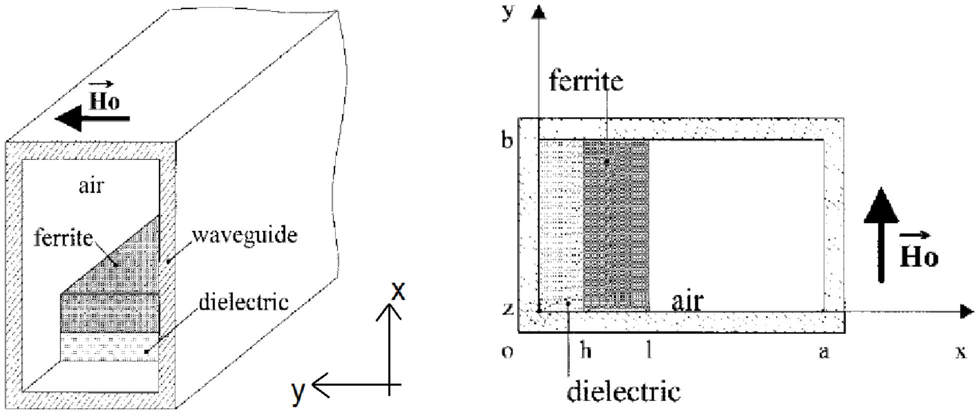

FIGURE 3.3 – *The proposed non-reciprocal measurement cell. Contrary to the previous described experimental set-ups for isotropic samples, the waveguide's cross section is not completely filled by the sample. Pictures taken from [45] and adapted.*

In order to reduce numerical effort in the FEM simulations used in the present work, the dispensable dielectric slab is omitted here. Consequently, there is only one material slab of the ferrite material from $x = 0$ to $x = l$. Nevertheless, both configurations produce three different $S-$parameters in transmission-reflection experiments, as we will see in following calculations, which can be also found in textbooks like [11]. Starting point is Helmholtz equation for the magnetic field in a medium with permittivity ε and permeability μ in the form [1]

$$\boldsymbol{\nabla}^2 \mathbf{H} - \boldsymbol{\nabla}(\boldsymbol{\nabla}\mathbf{H}) + \omega^2 \varepsilon_0 \varepsilon \mu_0 \mu \mathbf{H} = \mathbf{0}. \tag{3.23}$$

As already mentioned, direction of the static magnetic field is defined as $y-$direction, leading to a Polder permeability tensor in the form

$$\mu = \begin{pmatrix} \mu & 0 & -\kappa \\ 0 & \mu_y & 0 \\ \kappa & 0 & \mu \end{pmatrix} \tag{3.24}$$

---

[1] Contrary to Helmholtz equation for the electric field, an additional term $\boldsymbol{\nabla}(\boldsymbol{\nabla}\mathbf{H})$ appears, because $\boldsymbol{\nabla}\mathbf{H} \neq 0$, while $\boldsymbol{\nabla}\mathbf{E} = 0$.

in which μ_y does not influence further results, as will become clear later. As usual, the ansatz of

$$\begin{pmatrix} H_x \\ H_y \\ H_z \end{pmatrix} = \begin{pmatrix} H_{r_x} \\ H_{r_y} \\ H_{r_z} \end{pmatrix} \exp\Big(-i(\beta_x x + \beta_y y + \beta_z z)\Big) \tag{3.25}$$

is chosen in order to solve equation 3.23. Within this, β_i, $i = x, y, z$ represent propagation constants in different directions and H_{r_i} (or E_{r_i}) denote the different magnitudes of the magnetic (or electric) field. Accordingly, the electric field can also be written in the form

$$\begin{pmatrix} E_x \\ E_y \\ E_z \end{pmatrix} = \begin{pmatrix} E_{r_x} \\ E_{r_y} \\ E_{r_z} \end{pmatrix} \exp\Big(-i(\beta_x x + \beta_y y + \beta_z z)\Big). \tag{3.26}$$

In the next step, we use the conditions for the electric field at the waveguide walls at $y = 0$ and $y = b$: Here, the parallel components E_x and E_z of the electric field have to disappear (compare to equation 1.77). Consequently, we can conclude

$$\begin{pmatrix} E_x \\ E_z \end{pmatrix} = \begin{pmatrix} E_{r_x} \\ E_{r_z} \end{pmatrix} \sin(\beta_y y) \exp\Big(-i(\beta_x x + \beta_z z)\Big) \tag{3.27}$$

with $\beta_y = \frac{n\pi}{b}$ and $n = 0, 1, 2...$. By applying equation 1.1 in the form of $\boldsymbol{\nabla}\mathbf{E} = 0$ one finds

$$E_y = E_{r_y} \cos(\beta_y y) \exp\Big(-i(\beta_x x + \beta_z z)\Big). \tag{3.28}$$

Furthermore using equation 1.4 in the form of $\boldsymbol{\nabla} \times \mathbf{E} = -\mu_0 \boldsymbol{\mu} \frac{\mathrm{d}}{\mathrm{d}t}\mathbf{H}$ and inserting the found expressions for $\mathbf{E}$, one finds

$$\begin{pmatrix} H_x \\ H_y \\ H_z \end{pmatrix} = \begin{pmatrix} H_{r_x} \cos(\beta_y y) \\ H_{r_y} \sin(\beta_y y) \\ H_{r_z} \cos(\beta_y y) \end{pmatrix} \exp\Big(-i(\beta_x x + \beta_z z)\Big). \tag{3.29}$$

As shown in works like [48], the fields in a rectangular waveguide, excited by a $\mathrm{TE}_{1,0}$ mode, can be interpreted as superposition of TE eigenmodes, which do not depend on the $y-$coordinate. Since the discontinuities in the regarded measurement cell also only appear in $x-$ and $z-$direction, we can set $\beta_y = 0$ and conclude

$$E_x = E_z = H_y = 0, \tag{3.30}$$

$$E_y = E_{r_y} \exp\Big(-i(\beta_x x + \beta_z z)\Big) \tag{3.31}$$

and

$$\begin{pmatrix} H_x \\ H_z \end{pmatrix} = \begin{pmatrix} H_{r_x} \\ H_{r_z} \end{pmatrix} \exp\Big(-i(\beta_x x + \beta_z z)\Big). \tag{3.32}$$

These derived expressions for **H** can be inserted again in equation 3.23. Using the tensor form of permeability, this leads to a system of equations for the fields in the ferrite material

$$\begin{pmatrix} \mu k_r^2 - \beta_z^2 & \beta_x\beta_z - k_r^2\kappa \\ \beta_x\beta_z + k_r^2\kappa & \mu k_r^2 - \beta_x^2 \end{pmatrix} \begin{pmatrix} H_{r_x} \\ H_{r_z} \end{pmatrix} = \mathbf{0} \tag{3.33}$$

with $k_r^2 = \omega\varepsilon_0\mu_0\varepsilon$. Non-trivial solutions of equation 3.33 only exist, if the system's determinant equals zero. Accordingly, one finds the condition

$$\pm\beta_x = \sqrt{k_r^2\frac{\mu^2+\kappa^2}{\mu} - \beta_z^2}. \tag{3.34}$$

Regarding both solutions $\pm\beta_x$ separately, field amplitudes H_{r_x} and H_{r_z} can be determined by solving the system of 3.33. Naturally, this system allows an infinite number of solutions in which only the ratio between the amplitudes is fixed. For the purpose of simplicity, the following solution is chosen for $+\beta_x$:

$$H_{r_x}^+ = -\beta_x\beta_z + k_r^2\kappa \tag{3.35}$$

$$H_{r_z}^+ = \mu k_r^2 - \beta_z^2. \tag{3.36}$$

Subsequently, relation 1.2 in the form of $\boldsymbol{\nabla} \times \mathbf{H} = \varepsilon_0\varepsilon\frac{\partial\mathbf{E}}{\partial t}$ can be used in order to calculate the amplitude of the electric field, delivering

$$E_{r_y}^+ = \omega\mu_0(\mu\beta_x - \kappa\beta_z). \tag{3.37}$$

Repeating the same procedure for $-\beta_x$, one finds:

$$H_{r_x}^- = \beta_x\beta_z + k_r^2\kappa \tag{3.38}$$

$$H_{r_z}^- = \mu k_r^2 - \beta_z^2 \tag{3.39}$$

$$E_{r_y}^- = \omega\mu_0(-\mu\beta_x - \kappa\beta_z). \tag{3.40}$$

Accordingly, we write the total expressions for the fields in the ferrite as superposition of both solutions with amplitude factors A and B as:

$$H_x = \Big(AH_{r_x}^+\exp(-i\beta_x x) + BH_{r_x}^-\exp(i\beta_x x)\Big)\exp(-i\beta_z z) \tag{3.41}$$

$$H_z = \Big(AH_{r_z}^+\exp(-i\beta_x x) + BH_{r_z}^-\exp(i\beta_x x)\Big)\exp(-i\beta_z z) \tag{3.42}$$

$$E_y = \Big(AE_{r_y}^+\exp(-i\beta_x x) + BE_{r_y}^-\exp(i\beta_x x)\Big)\exp(-i\beta_z z) \tag{3.43}$$

For the purpose of eliminating one of the amplitude factors, we use the boundary condition for the electric field, which imposes for the tangential component at the waveguide wall

$$
\begin{aligned}
E_y(x=0) &= 0 && (3.44)\\
\Leftrightarrow \quad 0 &= AE_{r_y}^{+} + BE_{r_y}^{-} && (3.45)\\
\Leftrightarrow \quad B &= -A\frac{E_{r_y}^{+}}{E_{r_y}^{-}} && (3.46)\\
&= A\frac{\mu\beta_x - \kappa\beta_z}{\mu\beta_x + \kappa\beta_z}. && (3.47)
\end{aligned}
$$

Analogically, one can derive field expressions for the vacuum or air-filled region in the waveguide by changing the tensor permeability to unity and setting $\varepsilon = 1$. In conclusion, we find the following field expressions for the tangential field components in the different waveguide regions:
From $x = 0$ to $x = l$ (ferrite material)

$$
\begin{aligned}
H_x &= A\left(H_{r_z}^{+}\exp\left(-i\beta_x x\right) - \frac{E_{r_y}^{+}}{E_{r_y}^{-}}H_{r_z}^{-}\exp\left(i\beta_x x\right)\right)\exp(-i\beta_z z) && (3.48)\\
H_z &= AH_{r_z}^{+}\left(\exp(-i\beta_x x) - \frac{E_{r_y}^{+}}{E_{r_y}^{-}}\exp(-i\beta_x x)\right)\exp(-i\beta_z z) && (3.49)\\
E_y &= -2iAE_{r_y}^{+}\sin\left(\beta_x x\right)\,\exp(-i\beta_z z) && (3.50)
\end{aligned}
$$

and from $x = l$ to $x = a$ (air or vacuum)

$$
\begin{aligned}
H_{x,0} &= C\frac{k_{r,0}^2 - \beta_{x,0}^2}{\beta_{x,0}\beta_z}\cos\Big(\beta_{x,0}(x-a)\Big)\exp(-i\beta_z z) && (3.51)\\
H_{z,0} &= -C\cos\Big(\beta_{x,0}(x-a)\Big)\exp(-i\beta_z z) && (3.52)\\
E_{y,0} &= C\frac{i\omega\mu_0}{\beta_{x,0}}\sin\Big(\beta_{x,0}(x-a)\Big)\exp(-i\beta_z z). && (3.53)
\end{aligned}
$$

Within the derivation of the fields in the air or vacuum region, the boundary condition $E_{y,0}(x = a) = 0$ was used again in order to get rid of one amplitude constant. Therein, $\beta_{x,0}$ denotes the propagation constant in $x-$direction in this region and $k_{r,0}^2 = \omega\varepsilon_0\mu_0$. The two remaining constants, A and C are subjected to the following equation system, which can be concluded from the continuity condition of the tangential field components at $x = l$,

$$
\begin{pmatrix}
2H_{r_z}^{+}\left(\mu\beta_x\cos\left(\beta_x l\right) - i\kappa\beta_z\sin\left(\beta_x l\right)\right) & \left(\mu\beta_x + \kappa\beta_z\right)\cos\left(\beta_{x,0}(l-a)\right)\\
-2iE_{r_y}^{+}\sin\left(\beta_x l\right) & \frac{i\omega\mu_0}{\beta_{x,0}}\sin\left(\beta_x(l-a)\right)
\end{pmatrix}
\begin{pmatrix} A\\ C \end{pmatrix} = \mathbf{0}. \tag{3.54}
$$

Within the entries of this matrix, the propagation constant in $z-$direction, β_z, is included in the prefactors $E_{r_y}^{+}$ and $H_{r_z}^{+}$ and can be, analogically to the derivation of expression 3.34, determined by setting the corresponding determinant $F(\beta_z) = 0$. Because β_z is generally complex-valued, the occuring problem is non-trivial and an adequate solution technique has to be chosen. As tested by Quéffélec et al., different existing methods (as described in [49] and [50]) mainly showed ineffectiveness in solving this special problem. Accordingly, a more suitable technique was developed which will be described in the following.

At first, a square with defined edge length c and vertices z_i^1 with $i = 1, 2, 3, 4$ is defined with its midpoint in the origin of the complex plane. Then, $Re\,(F(z_i^1))$ and $Im\,(F(z_i^1))$ are calculated at these vertices while the signs of the results are compared to each other. If there are changes in the sign of F between two vertices in the real as in the imaginary part, the root search is continued with a smaller square with edge length $c/2$, firstly placed in the upper right corner of the larger square. If no doubled change of sign of F is detected between the vertices of a square, it is shifted according to the form of a helix in the complex plane and new vertices z_i^2 are defined (see figure 3.4). The search for a single root is continued until a given treshold of square edge length c_{min} is undershot while the possible number of roots to search is unlimited, in principle, and has to be chosen by the user. For the purpose of decreasing calculation time, the described method is only used for the determination of roots at the lowest frequency points. Afterwards, Taylor series expansions are used in order to estimate solutions at higher frequency points and initialize the root search at these values. By this performance, the dispersion relations of forward travelling modes are found. Accordingly, dispersion relations of backwards travelling modes can be calculated by an analog procedure in which the material regions in $x-$direction are switched, i.e. ferrite from $x = a - l$ to

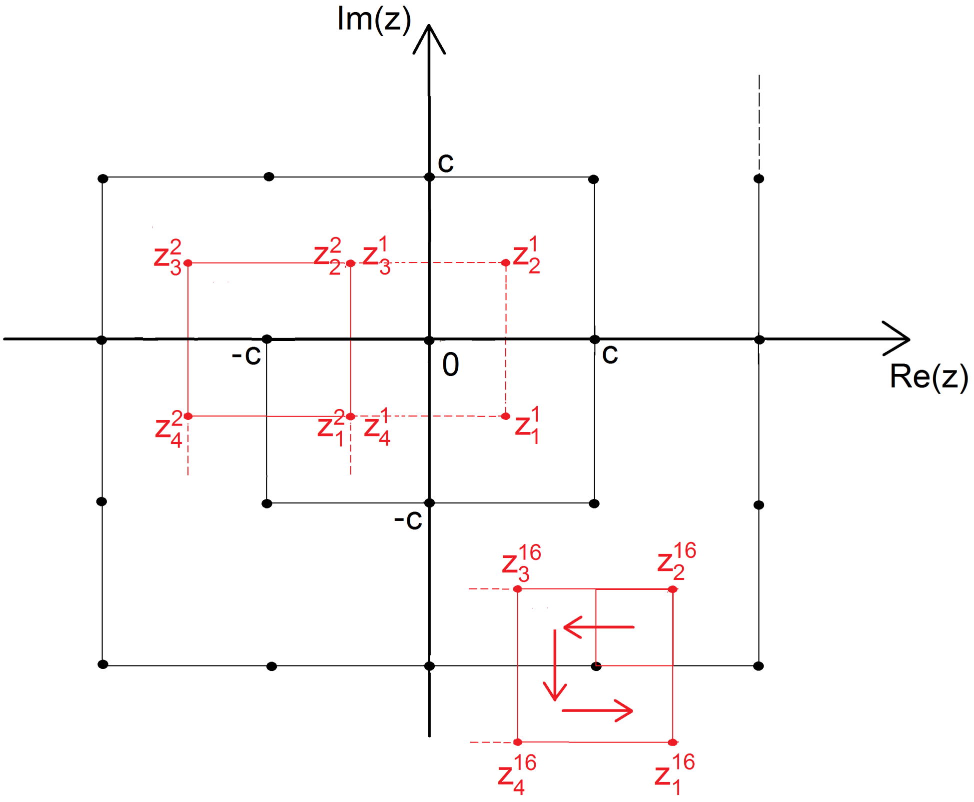

FIGURE 3.4 – *The procedure how the complex plane is scanned. When a doubled change of sign of F is detected, a smaller square with halved edge length is defined and scans the area of the previously defined square with more precision, as indicated for the square which is defined by z_i^{16}.*

$x = a$ and vacuum or air from $x = 0$ to $x = l$. After this calculation of the propagation constants β_{zi}, the field distributions of each mode can be determined by solving system 3.54, delivering values for constants A and C.
The next step is the calculation of the $S-$parameters out of the previously gained results. For that purpose, modal matching techniques are applied which take advantage of the continuity conditions for the tangential components of the field at the boundaries between the different waveguide regions in direction of wave propagation (see figure 3.5).

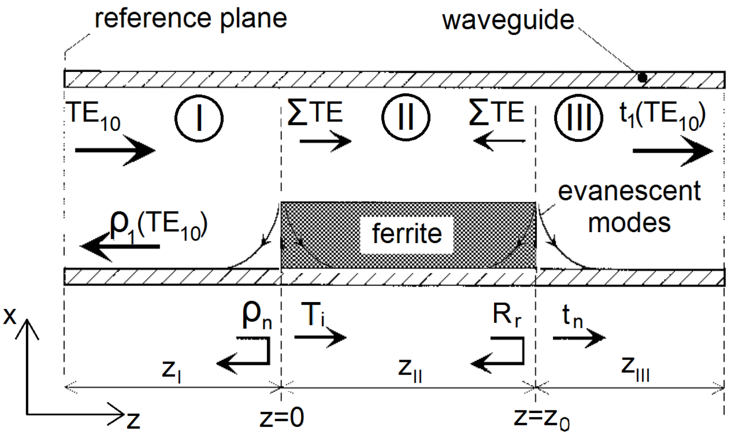

FIGURE 3.5 – *The waveguide regarded from $y-$direction. The electromagnetic wave incides from left in the empty region I and propagates through the partially filled region II and empty region III. Picture adapted from [45].*

At the boundary between region I and II, defined by $z = 0$, the dominant $\mathrm{TE}_{1,0}$ mode is partially reflected and transmitted, whereby higher order modes are additionally excited. Accordingly, in region I, the incident and reflected part of the $\mathrm{TE}_{1,0}$ mode and backwards travelling excited modes must be regarded. On the other side of the boundary, transmitted parts of the incoming signal are splitted into different modes which partly reach the next boundary at $z = z_0$, where they again excite reflected modes which also reach the boundary at $z = 0$ after travelling over a length of z_0. In summary, the boundary conditions at this plane can be written in the form

$$(1+\rho_1)E^I_{y1} + \sum_{i=2}^{N} \rho_i E^I_{yi} = \sum_{i=1}^{N} T_i E^{II}_{yi} + \sum_{i=1}^{N} R_i E^{II}_{yi} \exp\left(\beta^{II}_{zi} z_0\right) \tag{3.55}$$

$$(1-\rho_1)H^I_{x1} - \sum_{i=2}^{N} \rho_i H^I_{xi} = \sum_{i=1}^{N} T_i H^{II}_{xi} - \sum_{i=1}^{N} R_i H^{II}_{xi} \exp\left(\beta^{II}_{zi} z_0\right). \tag{3.56}$$

Within these equations, ρ_i and T_i denote the reflection and transmission coefficients of mode i at the regarded boundary. Analogically, reflection at $z = z_0$ plane is described by R_i and transmission by t_i. Roman numbers label the waveguide region, in which fields or propagation constants are regarded. Accordingly, the previously determined roots of system 3.54 are denoted with β^{II}_{zi} while number of considered modes is given by N. The negative signs in the equations for the magnetic field result from the phase shift of the $H-$component when being reflected. By the same considerations, equations for the second boundary between region II and III can be found

$$\sum_{i=1}^{N} T_i E_{yi}^{II} \exp\left(-\beta_{zi}^{II} z_0\right) + \sum_{i=1}^{N} R_i E_{yi}^{II} = \sum_{i=1}^{N} t_i E_{yi}^{III} \tag{3.57}$$

$$\sum_{i=1}^{N} T_i H_{xi}^{II} \exp\left(-\beta_{zi}^{II} z_0\right) - \sum_{i=1}^{N} R_i H_{xi}^{II} = \sum_{i=1}^{N} t_i H_{yi}^{III}. \tag{3.58}$$

Of course, these relations are only true in the case of $N \to \infty$. Nevertheless, under certain conditions (as shown in [51]), convergence can already reached with a finite number of modes, which will be also analyzed for the situation in this work in section 4.2.

Obviously, we find four equations with $4N$ unknowns (ρ_i, T_i, R_i and t_i with $i = 1, 2, 3...N$). Consequently, we require further information for determining an unique solution, which can be found in the orthogonality condition for TE modes [48]

$$\iint_S E_{yi} H_{xj} \, dS = 0, \text{ if } i \neq j \tag{3.59}$$

where S denotes the waveguide's aperture. Fortunately, this relation is still maintained in waveguides partially filled with ferrite material [52, 53] and, therefore, can be used in the context of the problem at hand. By using the orthogonality relation, we can generate N equations out of every of the four derived conditions, which will be exemplary demonstrated for equation 3.55. At first, we multiply with H_{x1}^{I} and perform integration $\iint_S \ldots dS$, delivering

$$\begin{aligned}
&(1+\rho_1) \iint_S E_{y1}^{I} H_{x1}^{I} \, dS + \sum_{i=2}^{N} \underbrace{\iint_S \rho_i E_{yi}^{I} H_{x1}^{I} \, dS}_{=0, \text{ orthogonality!}} \\
&= \sum_{i=1}^{N} T_i \iint_S E_{yi}^{II} H_{x1}^{I} \, dS + \sum_{i=1}^{N} R_i \exp\left(\beta_{zi}^{II} z_0\right) \iint_S E_{yi}^{II} H_{x1}^{I} \, dS
\end{aligned} \tag{3.60}$$

$$\begin{aligned}
\Leftrightarrow\ &(1+\rho_1) \iint_S E_{y1}^{I} H_{x1}^{I} \, dS \\
&= \sum_{i=1}^{N} T_i \iint_S E_{yi}^{II} H_{x1}^{I} \, dS + \sum_{i=1}^{N} R_i \exp\left(\beta_{zi}^{II} z_0\right) \iint_S E_{yi}^{II} H_{x1}^{I} \, dS.
\end{aligned} \tag{3.61}$$

By evaluating

$$
\begin{aligned}
\iint_S E^I_{y1} H^I_{x1}\, dS &= -\exp(-i2\beta^I_{z1} z) \int_0^b \int_0^a \frac{i\omega\pi}{k_c^2 a}\frac{i\beta^I_{z1}\pi}{k_c^2 a}\sin^2\left(\frac{\pi}{a}x\right)\, dx\, dy && (3.62)\\
&= \frac{\omega\beta^I_{z1}\pi^2 b}{k_c^4 a^2}\exp(-i2\beta^I_{z1} z)\underbrace{\int_0^a \sin^2\left(\frac{\pi}{a}x\right)\, dx\, dy}_{=a/2} && (3.63)\\
&= \frac{\omega\beta^I_{z1}\pi^2 b}{2k_c^4 a}\exp(-i2\beta^I_{z1} z) && (3.64)\\
\iint_S E^{II}_{yi} H^I_{x1}\, dS &= \int_0^b dy\left[\underbrace{\int_0^l E_{yi}H^I_{x1}dx}_{\text{Ferrite}} + \underbrace{\int_l^a E_{yi,0}H^I_{x1}dx}_{\text{Air or Vacuum}}\right] && (3.65)\\
&= \exp(-i(\beta^I_{z1}+\beta^{II}_{zi})z)\int_0^b dy\Bigg[\int_0^l (-2)iA_iE^+_{r_{yi}}\sin\left(\beta_{xi}x\right)\\
&\quad \frac{i\beta^I_{z1}\pi}{k_c^2 a}\sin\left(\frac{\pi}{a}x\right) dx + \int_l^a C_i\frac{i\omega\mu_0}{\beta_{xi,0}}\sin\left(\beta_{xi,0}(x-a)\right)\frac{i\beta^I_{z1}\pi}{k_c^2 a}\sin\left(\frac{\pi}{a}x\right) dx\Bigg] && (3.66)\\
&= \exp(-i(\beta^I_{z1}+\beta^{II}_{zi})z)b\Bigg[\frac{2A_i\beta^I_{z1}\pi}{k_c^2 a}E^+_{r_{yi}}\int_0^l \sin\left(\beta_{xi}x\right)\ \sin\left(\frac{\pi}{a}x\right) dx\\
&\quad - C_i\frac{\omega\mu_0\beta^I_{z1}\pi^2}{\beta_{xi,0}k_c^2 a}\int_l^a \sin\left(\beta_{xi,0}(x-a)\right)\ \sin\left(\frac{\pi}{a}x\right) dx\Bigg] && (3.67)
\end{aligned}
$$

with

$$
\begin{aligned}
&\int_0^l \sin\left(\beta_{xi}x\right)\ \sin\left(\frac{\pi}{a}x\right) dx\\
&= \frac{a\left(-\pi\cos\left(\frac{l\pi}{a}\right)\ \sin\left(\beta_{xi}l\right) + a\beta_{xi}\cos\left(\beta_{xi}l\right)\ \sin\left(\frac{l\pi}{a}\right)\right)}{(-a\beta_{xi}+\pi)(a\beta_{xi}+\pi)} && (3.68)\\
&\int_l^a \sin\left(\beta_{xi,0}(x-a)\right)\ \sin\left(\frac{\pi}{a}x\right) dx\\
&= -\frac{a}{\pi^2 - a^2\beta_{xi}^2}\left(\pi\cos\left(\frac{\pi l}{a}\right)\ \sin\left(\beta_{xi}(a-l)\right) + a\beta_{xi}\sin\left(\frac{\pi l}{a}\right)\ \cos\left(\beta_{xi}(a-l)\right)\right) && (3.69)
\end{aligned}
$$

(terms for E^I_{y1} and H^I_{x1} derived in 1.1.2.3) we find the first equation in the system to derive. By multiplying equation 3.55 with H^I_{xi} with $i = 2, ..., N$ and repeating the same steps again, N equations can be derived in total. Applying the same strategy on equations 3.57 and on 3.56 and 3.58, but with multiplication by E^I_{yi} instead of H^I_{xi}, a system of $4N$ equations with $4N$ unknowns is obtained, which can be solved in order to determine ρ_i, T_i, R_i and t_i. Regarding the analog problem for the backwards travelling modes, one finds different values for the transmission and reflection parameters which will be denoted with ρ'_i, T'_i, R'_i and t'_i. Because of the damping of higher order modes in waveguide regions I and III, the entries of the scattering matrix are given by

$$S_{11} = \rho_1 \exp(-2\beta_{z1}^{I} z_I) \tag{3.70}$$

$$S_{21} = t_1 \exp(-\beta_{z1}^{I}(z_I + z_{III})) \tag{3.71}$$

$$S_{12} = t_1' \exp(-\beta_{z1}^{I}(z_I + z_{III})) \tag{3.72}$$

$$S_{22} = \rho_1' \exp(-2\beta_{z1}^{I} z_{III}). \tag{3.73}$$

Within this, z_I and z_{III} denote the lengths of waveguide regions I and III, respectively. Summarizing, a technique which enables to calculate the $S-$parameter out of given material characteristics μ and κ and geometric parameters was derived in this section, solving the direct problem. In the following, we will deal with the vice-versa problem, which is of great interest in this work.

3.1.4 Inverse Problem: Determination of Permittivity and Permeability

Due to the complexity of the present problem, it is not possible to analytically calculate ε, μ and κ from the $S-$parameters. Consequently, one has to use numerical methods in order to solve this inverse problem. In this context, the following procedure is chosen [46]: First of all, we measure the $S-$parameters from the described experimental or in-silico set-up to which we refer as S_{ij}^{meas} in the following. Then, we use initial guess values for ε, μ and κ and calculate the corresponding theoretical $S-$parameters, S_{ij}^{theo}, according to the previously described direct problem's solving method. Afterwards, we define an objective function as

$$E(\mathbf{x}) = \sum_{i=1}^{2}\sum_{j=1}^{2} |S_{ij}^{meas} - S_{ij}^{theo}(\mathbf{x})|^2 \tag{3.74}$$

with $\mathbf{x} = (\varepsilon', \varepsilon'', \mu', \mu'', \kappa', \kappa'')$ which has to be minimized in order to bring the theoretical $S-$parameters as close as possible to the measured data. In the present work, this minimization process is done via a sequential quadratic programming method (SQP) (firstly developed in [54], modern formulation can be found in many textbooks and essays as [55] and [56]). The corresponding mathematical recipe will be described in the following.

In the general form, we consider a non-linear optimization problem, in which an objective function $f(\mathbf{x})$ in dependence of a $n-$dimensional vector $\mathbf{x}$ has to be minimized. Furthermore, we can define m non-linear inequality constraints in the form of

$$g_i(\mathbf{x}) \geq 0, \text{with } i = 1...m. \tag{3.75}$$

In our case, we can use this inequalities in order to restrict to possible values for the permittivity and permeability according to bounds of effective media (see section 1.3.5). During the solution procedure, a constraint $g_i(\mathbf{x})$ is called active if $g_i(\mathbf{x}) = 0$ is fulfilled.

The corresponding Lagrangian function with its multipliers u_i is given by

$$L(\mathbf{x}, u_1...u_h) = f(\mathbf{x}) + \sum_{i=1}^{h} u_i g_i(\mathbf{x}) \tag{3.76}$$

in which g_i with $i = 1...h$ are the active constraints at $\mathbf{x}$.
In order to solve this problem, we use an initial guess value for the solution, $\mathbf{x_0}$, and formulate a quadratic subproblem in which we search the minimum of

$$f_0(\mathbf{d_0}) = \frac{1}{2}\mathbf{d_0}^T \mathbf{B_0} \mathbf{d_0} + (\boldsymbol{\nabla} f(\mathbf{x_0}))^T \mathbf{d_0} \tag{3.77}$$

under the conditions

$$g_{0,i}(\mathbf{d_0}) = (\boldsymbol{\nabla} g_i(\mathbf{x_0}))^T \mathbf{d_0} + g_i(\mathbf{x_0}) \geq 0 \text{ with } i = 1...h \tag{3.78}$$

which are given by the active constraints at $\mathbf{x_0}$. Within these formulas, $\mathbf{B_0}$ denotes the Hessian matrix of the Lagrangian

$$\mathbf{B_0} = \begin{pmatrix} \frac{\partial^2 L}{\partial x_1^2} & \frac{\partial^2 L}{\partial x_1 \partial x_2} & \cdots & \frac{\partial^2 L}{\partial x_1 \partial x_n} \\ \frac{\partial^2 L}{\partial x_2 \partial x_1} & \frac{\partial^2 L}{\partial x_2^2} & \cdots & \cdots \\ \cdots & \cdots & \cdots & \cdots \\ \frac{\partial^2 L}{\partial x_n \partial x_1} & \cdots & \cdots & \frac{\partial^2 L}{\partial x_n^2} \end{pmatrix} \tag{3.79}$$

and $\mathbf{d}$ the $n-$dimensional optimization parameter. In fact, this step is just a quadratic Taylor expansion of the Lagrangian and a linear Taylor expansion of the active constraints. In conclusion, we approximate the actual problem. Subsequently, the corresponding solution $\mathbf{d}_0$ can be found by applying Lagrange's method

$$L_0(\mathbf{d_0}) = f_0(\mathbf{d_0}) + \sum_{i=1}^{h} u_{0,i} g_{0,i}(\mathbf{d_0}) \tag{3.80}$$

$$\frac{\partial L_0}{\partial d_1} = 0 \tag{3.81}$$

$$\cdots$$

$$\frac{\partial L_0}{\partial d_n} = 0 \tag{3.82}$$

$$\frac{\partial L_0}{\partial u_{0,1}} = 0 \tag{3.83}$$

$$\cdots$$

$$\frac{\partial L_0}{\partial u_{0,h}} = 0 \tag{3.84}$$

which delivers $n + h$ linear equations with the same numbers of unknowns. By solving this problem, we obtain $\mathbf{d_0}$ and $u_{0,i}$ with $i = 1...h$, which we can use in order to update our approximation of the total solution via

$$\mathbf{x_1} = \mathbf{x_0} + \mathbf{d_0}. \tag{3.85}$$

Using this new $\mathbf{x_1}$, we define a new quadratic subproblem according to equation 3.77 and check which constraints are active at this point, leading to new conditions according to system 3.78. Then, the whole procedure is repeated until convergence is reached.
When implementing this algorithm, derivatives have to be approximated by using difference quotients in the form of $\frac{\partial f}{\partial x} = \frac{f(x+h)-f(x)}{h}$ with a problem adjusted parameter h. Furthermore, the initial guess value of $\mathbf{x_0}$ has to be chosen properly in order to reach convergence. In the present work, it was also noticed that a limiting step length d_{max} in the updating process (equation 3.85) can be useful. This means that we reduce $\mathbf{d_k}$ to the length d_{max} while maintaining its direction in case that $|\mathbf{d_k}| > d_{max}$. For solving the system of linear equations 3.80-3.84, Gaussian algorithm is used.
Combining the presented SQP method with the previously described calculations of the direct problem, one obtains a laborious, but effective and reliable method for the computation of the Polder susceptibility tensor which is used for gaining the later presented results.

3.2 Simulation Methods

In the following section, the simulation methods which are used in this work will be brought into focus. First of all, we want to introduce the finite element method (FEM) with respect to electromagnetic phenomena. Based on this method, the commercial software *High Frequency Structure Simulator* (HFSS) was developed by *Ansys Inc.* which will be used in order to generate our experimental set-up in silico and discretize our model on finite element meshes. Due to different reasons, these meshes are then exported to model order reduction (MOR) software, supplied by *Lehrstuhl für theoretische Elektrotechnik* (LTE) from Saarland University, in which $S-$parameters are calculated.
As a preparatory work before using high-frequency simulations, we also have to perform static simulations in which the local dipole fields inside the inclusions in our sample are computed. For this purpose, a simple numerical procedure was developed which is presented in the end of this section.

3.2.1 The Finite Element Method and Model Order Reduction

All calculations in HFSS and MOR are based on the FEM, which is a numerical technique for solving differential equations underlying given boundary conditions. Since these calculations are the crucial element of all results presented in this work, we want to introduce the mathematical basics of this technique with regard to electromagnetic field modeling. For that purpose, we refer to [57], but the same issues can be found in several textbooks dealing with numerical solution techniques of differential equations. Subsequently, the rudiments of MOR are presented which can be read in more detail in [58].

In general, a boundary value problem is given by one or several governing differential equations in a domain Ω according to

$$L\phi = f \tag{3.86}$$

in which L denotes a differential operator, ϕ is the physical or mathematical field of interest and f an excitation term. Moreover, Ω is surrounded by a boundary Γ, on which certain conditions are imposed. Due to lack of analytic solutions in most cases, various numerical solution techniques were developed. Among these, the FEM is best-suited when domain Ω, in our case a specified volume, becomes inhomogeneous with inseperable geometries. Consequently, with regard to our topic of interest, electromagnetic fields in composite materials, the approach with FEM is adequate.
For the purpose of calculating an approximative solution in FEM, Ω has to be discretized in smaller elements as line segments in one, triangles in two and tetrahedra in three dimensions, for example. This discretization has to cover the whole domain Ω, while the non-overlapping subdomains are connected to their neighbours, forming a mesh of finite elements. In order to solve equation 3.86 with FEM approximation, different techniques can be used while we restrict to the method by *Petrov-Galerkin* in the following. Within this, the unknown field is approximated as

$$\phi = \sum_{j=1}^{N} \omega_j c_j = \boldsymbol{\omega}^T \mathbf{c} \tag{3.87}$$

where w_j are polynomial functions with coefficients c_j and N denotes their maximal regarded order. Inserting the ansatz of 3.87 in equation 3.86, we are able to compute the resulting residual error r

$$r = L\boldsymbol{\omega}^T \mathbf{c} - f. \tag{3.88}$$

Now, the idea is to weight this residual with the testing functions ω_j and to seek a solution for which the weighted average residual in a domain Ω disappears. This approach leads to a linear system of requirements

$$\iiint_\Omega \boldsymbol{\omega} r dv = 0 \tag{3.89}$$

$$\Leftrightarrow \left(\iiint_\Omega \boldsymbol{\omega} L \boldsymbol{\omega}^T dv\right) \mathbf{c} = \iiint_\Omega \boldsymbol{\omega} f dv. \tag{3.90}$$

For the purpose of calculating the electric field with this method, one uses the already derived wave equation 1.18 as starting point which is a consequence of the governing Maxwell's equations 1.1-1.4. Under assumption of time-harmonic fields, we can write

$$\nabla \times \boldsymbol{\mu_r}^{-1} \nabla \times \mathbf{E} + i\omega\mu_0\sigma\mathbf{E} - \omega^2\mu_0\varepsilon_0\varepsilon_r\mathbf{E} = 0. \tag{3.91}$$

Additionally, we have to include different boundary conditions. First of all, the boundary conditions between different media surfaces inside the regarded volume Ω are given by the continuity conditions for the fields,

$$\mathbf{n} \times (\mathbf{E_1} - \mathbf{E_2}) = \mathbf{0} \tag{3.92}$$

$$\mathbf{n} \cdot (\mathbf{D_1} - \mathbf{D_2}) = \rho_s \tag{3.93}$$

$$\mathbf{n} \times (\mathbf{H_1} - \mathbf{H_2}) = \mathbf{J}_s \tag{3.94}$$

$$\mathbf{n} \cdot (\mathbf{B_1} - \mathbf{B_2}) = 0, \tag{3.95}$$

which can partly be found in different forms in equations 1.77, 1.84 and 1.150. Within this, $\mathbf{n}$ denotes the unit normal vector on the boundary, ρ_s the interface's charge density and $\mathbf{J}_s$ the electric current density on the surface. Furthermore, the conditions at the enclosing boundary Γ must be defined in order to obtain a problem with an unique solution. When the regarded domain is restricted to the volume inside a rectangular or parallel plate waveguides, as in this work, we have to distinguish between three different types of conditions on Γ (see also figure 3.6):

- Perfect electric conductor: At the waveguide walls, perfect electric conductance is assumed (compare 1.1.2.1), leading to the condition $\mathbf{n} \times \mathbf{E} = \mathbf{0}$ on these areas, which is in accordance with equation 3.92.
- Perfect magnetic conductor: Regarding parallel plate waveguides, two waveguide walls are virtually infinitely far away from each other. Due to finity of Ω, this can not be modeled directly, but the same behavior of the fields is reproduced by the choice of the condition of a perfect magnetic conductor $\mathbf{n} \times \mathbf{H} = \mathbf{0}$ at corresponding areas.
- Ports: At the waveguide ports i, $i = 1, 2$, the electromagnetic signal enters and leaves the system. Accordingly, the high-frequent excitation of the system takes place at the corresponding areas Γ_{P_i}. In this regard, tangential components of $\mathbf{E}$ and $\mathbf{H}$ can be written as

  $$\mathbf{E}_t^i = \sum_{k=1}^{\infty} a_k^i \mathbf{E}_{tk}^i \exp\left(-\beta_k^i x\right) + b_k^i \mathbf{E}_{tk}^i \exp\left(\beta_k^i x\right) \tag{3.96}$$

  $$\mathbf{H}_t^i = \sum_{k=1}^{\infty} a_k^i \mathbf{H}_{tk}^i \exp\left(-\beta_k^i x\right) - b_k^i \mathbf{E}_{tk}^i \exp\left(\beta_k^i x\right) \tag{3.97}$$

  in which a_k^i and b_k^i denote the complex amplitude of the mode k travelling forward and backward in $x-$direction.

The thereby defined boundary value problem can be discretized. By this procedure, we obtain a sparse equation system in the form of

$$\mathbf{A}\mathbf{z} = \mathbf{b}. \tag{3.98}$$

Within this, the entries of $\mathbf{A}$ and $\mathbf{b}$ are given by

$$\begin{aligned} A_{kl} = &\int_\Omega (\boldsymbol{\nabla} \times \boldsymbol{\omega}_k) \boldsymbol{\mu_r}^{-1} (\boldsymbol{\nabla} \times \boldsymbol{\omega}_l) d\Omega + i\omega\mu_0 \int_\Omega \boldsymbol{\omega}_k \sigma \boldsymbol{\omega}_l d\Omega - \omega^2 \varepsilon_0 \varepsilon_r \mu_0 \int_\Omega \boldsymbol{\omega}_k \boldsymbol{\omega}_l d\Omega \\ &- \sum_{j=1}^{2} \frac{i}{\mu_r} \beta_1^i \int_{\Gamma_{P_i}} (\mathbf{n} \times \boldsymbol{\omega}_k)(\mathbf{n} \times \boldsymbol{\omega}_l) d\Gamma \end{aligned} \tag{3.99}$$

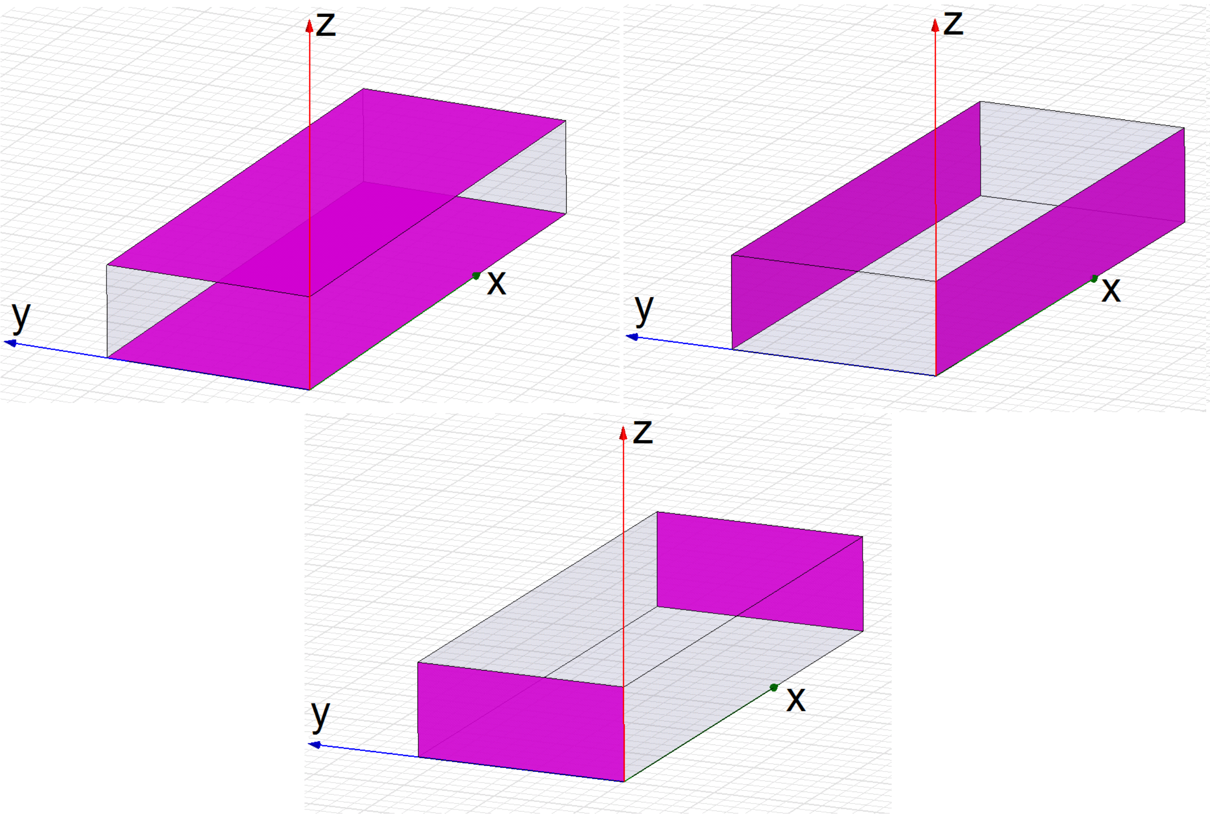

Figure 3.6 – *When simulating field distributions in a rectangular or parallel plate waveguide, the shown model geometry has to be used. The purple labeled areas in the top left picture have to be defined as perfect electric conductors in both cases, while the marked ones in the top right picture are defined as perfect electric conductors in case of a rectangular waveguide, but as perfect magnetic conductors for a parallel plate waveguide. In the lower picture, the ports' area are highlighted. Please note that there is no sample defined inside the waveguide.*

and

$$b_k = -2 \sum_{j=1}^{2} \frac{i}{\mu_r} \beta_1^i \int_{\Gamma_{P_i}} (\mathbf{n} \times \boldsymbol{\omega}_k)(\mathbf{n} \times \mathbf{E}^{\mathbf{i}}_{\mathbf{t1}}) d\Gamma \tag{3.100}$$

with the three dimensional ansatz functions $\boldsymbol{\omega}_i$ which are chosen in such a way that perfect electric boundary conditions are fulfilled in advance and integrals over perfect magnetic areas disappear. Solving system 3.98 delivers the components of $\mathbf{z}$, from which the fields can be calculated via

$$\mathbf{E}(\mathbf{r}) = \sum_{i=1}^{N} z_i \boldsymbol{\omega}_i(\mathbf{r}) \tag{3.101}$$

$$\mathbf{H}(\mathbf{r}) = \frac{i}{\omega \mu_0} \sum_{i=1}^{N} z_i \boldsymbol{\nabla} \times \boldsymbol{\omega_i}(\mathbf{r}) \tag{3.102}$$

with $\mathbf{r} \in \Omega$. For a more detailed discussion of finite element simulations and the comprehensive derivation of equation 3.98, we refer to [57].

Of course, the system of 3.98 depends on the regarded frequency. Accordingly, it is necessary to generate and solve such a system for every single frequency point in the range of interest, which can be very time-consuming. However, changes in the electromagnetic fields in dependence of frequency are observed to be very small. This fact induces the fundamental idea behind MOR: Instead of using a large FEM problem in every frequency point, this is only done at a few frequency sites ν_i with $i = 1, ..., n$ while solutions in between are interpolated as linear combinations of the fields at these evaluation points. From a mathematical point of view, this strategy reduces the order of the solution space and, as a consequence, the calculation times for the fields at the frequency points between the ν_i. Because this technique delivers only an approximation of the right FEM solution (which itself is also only an approximation of the real fields), one has to analyze the convergence and accuracy of the results. As for FEM, this can be also done via the computation of the residual error as in equation 3.88 [58]. The used MOR software which delivers the results presented in this work was implemented by Lehrstuhl für theoretische Elektrotechnik at Saarland University, chaired by Romanus Dyczij-Edlinger. A further insight into the explicit details of this programs can be found in [59].

3.2.2 Ansys High Frequency Structure Simulator

As already mentioned, the HFSS program by Ansys is used in order to model the experimental set-ups in silico and generate meshes for FEM simulations. Within this, a three-dimensional model and the already discussed boundary conditions must be defined before the mesh generator subdivides the volume into tetrahedral elements (see picture 3.7). For these and all further regarded simulations during the elaboration of this work, the following settings for the mesh generator are used:

- Initial mesh: lambda target of 0.6667 (default)
- Maximum refinement per pass: 25 %
- Solution order: second
- Solution frequency: 12 GHz (always the highest frequency of interest).

Consequently, the initial mesh is generated in such a way, that the edge lengths of the corresponding finite elements undershot 0.6667 of the material dependent wave length. Then, this mesh can be refined in subsequent passes or iteration steps, in which up to 25 % of the number of existing tetrahedra can be added in order to improve solutions. Via the parameter solution order, the number of unknowns for each tetrahedron can be adjusted, while second order is the maximum value and corresponds to the highest accuracy. Furthermore, the solution frequency determines the frequency point at which the mesh is generated. Because wavelengths decrease with increasing frequency, it is senseful to generate meshes at the highest frequency of interest before a sweap uses this mesh in order to calculate further results at lower frequency points. In this case, we examine the so called $X-$band between $8 - 12$ GHz. In later examinations, in which results depend on frequency, we will expand the region of interest to $7 - 12$ GHz which causes no problems concerning mode propagation in our simulations.

Moreover, the mesh generating process can be automatically stopped via the maximum

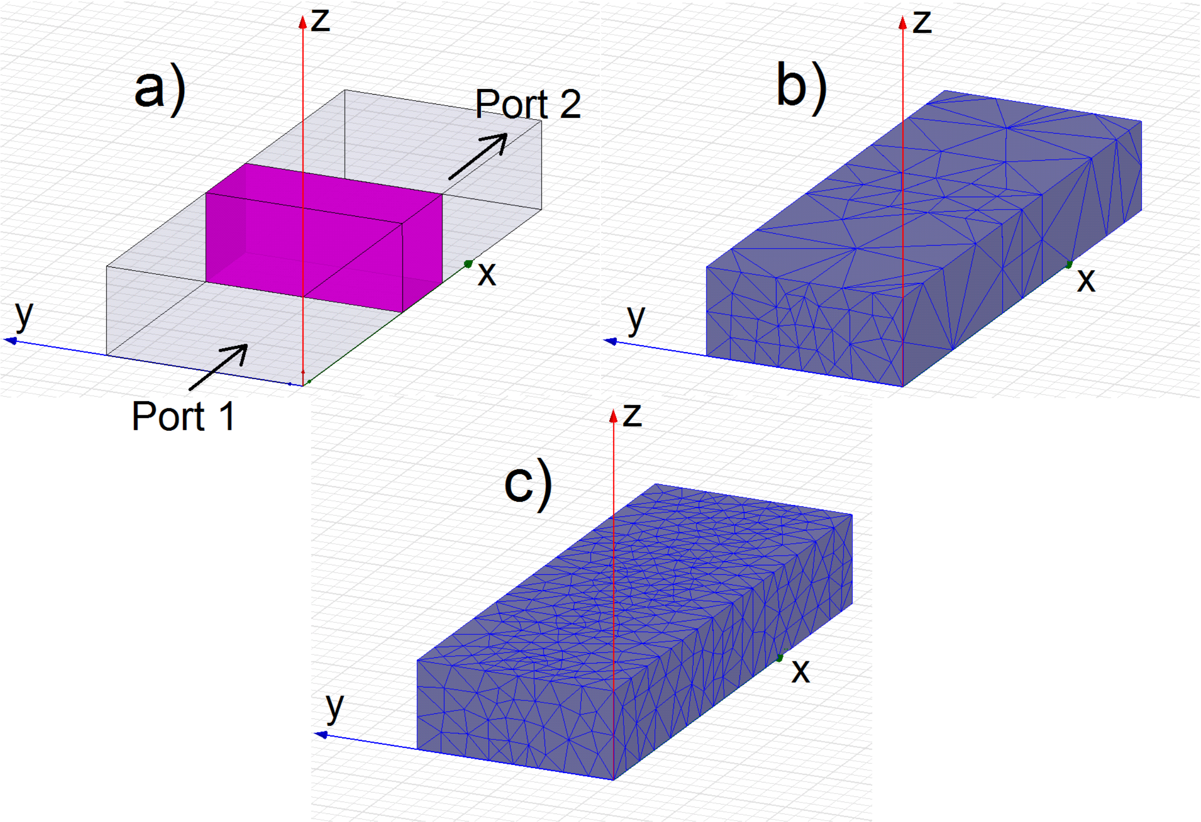

FIGURE 3.7 – *a) A waveguide filled with a homogeneous sample of* $\varepsilon = 5$ *and* $\mu = 1$ *(purple box) is modeled in HFSS. The waveguide's dimensions amount* $2.286\ cm \times 1\ cm \times 6\ cm$*. Accordingly, the usage with only one propagating mode is possible between* $6.56 - 13.11$ *GHz. The sample with a length of* $1\ cm$ *is placed in the waveguide's middle concerning direction of propagation. Accordingly, two* 2.5 *cm long vacuum filled regions between sample and the two ports are defined. All other boundaries of the geometry underly perfect electric or perfect magnetic conditions in dependence of the modeled type of waveguide (see section 3.2.1). Two corresponding meshes are shown in picture b) and c): The mesh in b) corresponds to the first iteration step with* 563 *tetrahedra, while the mesh in c) is much more accurate and consists out of* $10\ 813$ *tetrahedra (iteration step* 15*).*

Delta S criterion: This value is calculated between passes $l-1$ and l according to

$$\text{maximum Delta S}_l = \max_{i,j=1,2} |S_{ij}^{l-1} - S_{ij}^{l}|. \tag{3.103}$$

Accordingly, mesh refinement process stops if this value falls below the chosen treshold. Actually, in this work, this criterion is not used but results calculated out of the $S-$parameters are compared between different steps in order to guarantee convergence (see section 4.1). Further information on HFSS can be found in the corresponding user's guide [60].

After this short introduction, we want to analyze the accuracy of HFSS and the presented evaluation methods (see section 3.1.1) for a homogeneous material in a rectangular or parallel plate waveguide as shown in figure 3.7. For that purpose, we firstly compare $S-$parameters which can be analytically computed according to equations 3.3 and 3.4 with the ones generated by HFSS. Exemplaric results are shown in figure 3.8

and show very good agreement.

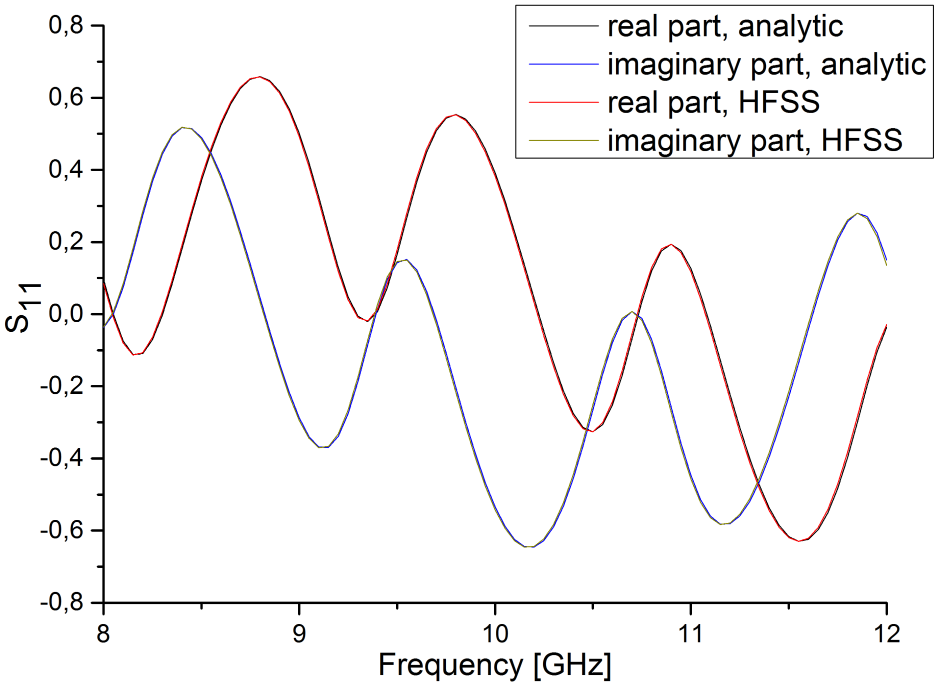

FIGURE 3.8 – *The real and imaginary part of the* S_{11}*−parameter of a parallel plate waveguide containing a* $d = 5.0$ *cm long device with* $\varepsilon = 5$ *and* $\mu = 1$ *(as shown in figure 3.7 a)) are calculated in the frequency region of* $8 - 12$ *GHz with the help of HFSS and via equation 3.3. Although simulation is performed with the initially generated mesh without further refinement passes, a very high accuracy is reached.*

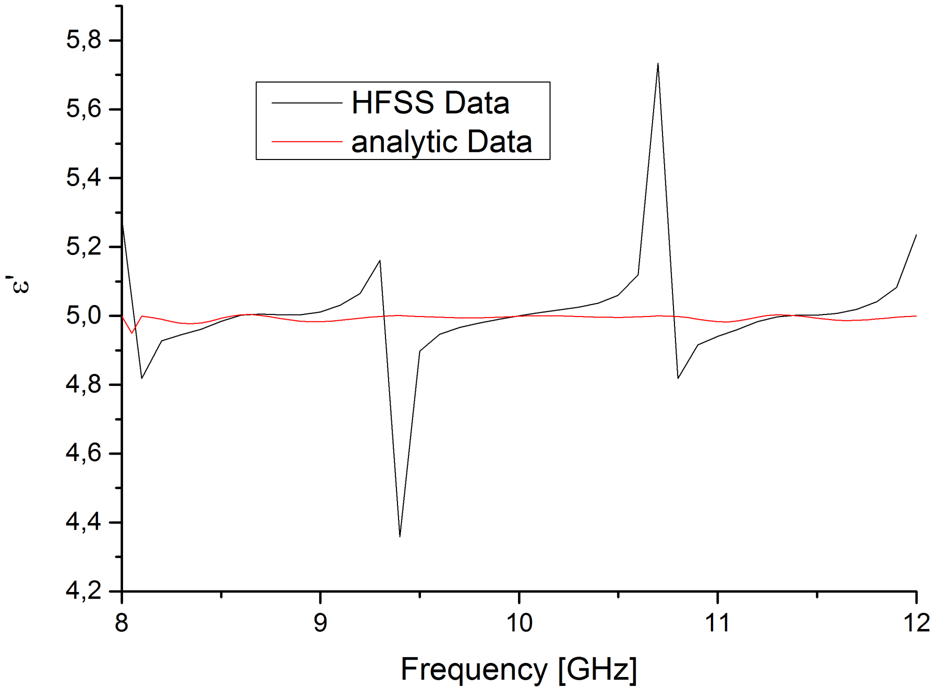

FIGURE 3.9 – *Data of figure 3.8 is evaluated with the method by NRW.*

Of course, we also want to use the produced $S-$parameters and calculate the permittivity ε of the corresponding samples. In this context, we firstly want to demonstrate the arising of divergencies when evaluating simulated (or experimentally) gained $S-$parameters of long devices with the NRW method, shown in figure 3.9 (compare to figure 3.2). Contrary, the evaluation with the analytically produced data leads to much smoother results, highlighting small simulation noise as origin of the divergencies (see section 3.1.1). As already mentioned, these divergencies occur at frequency points fulfilling $d = n\frac{\lambda_m}{2}$. Consequently, the choice of short samples, for which this condition is not valid at any frequency point in the regarded range, prevents the appearance of this phenomenon. This is shown for a device with a length of $d = 1$ cm in both types of waveguides in figure 3.10. Results for this shorter sample show deviations up to 5 % for the rectangular waveguide and only 1 % for the parallel plate waveguide.

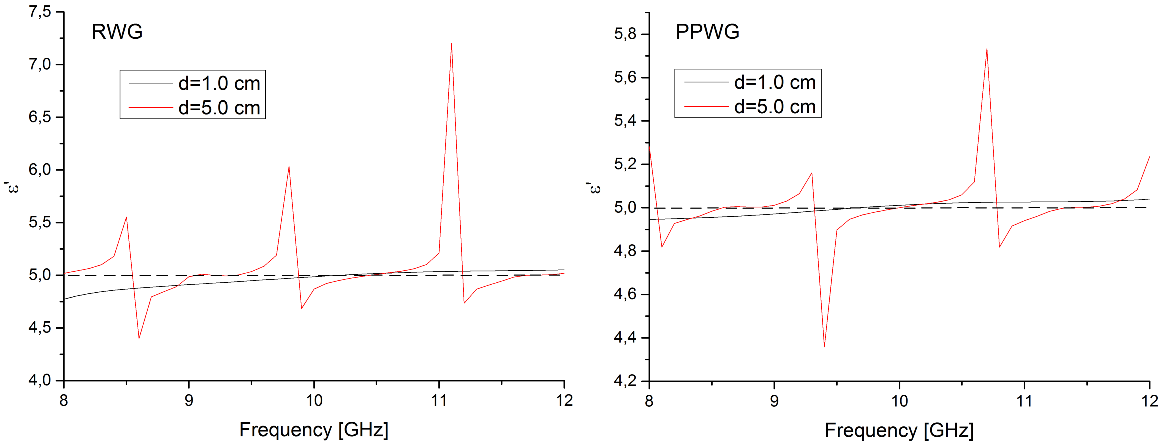

FIGURE 3.10 – *The $S-$parameters from HFSS simulations are evaluated with the help of the NRW method. Left picture shows results for a rectangular waveguide (RWG) while the outcomes for a parallel plate waveguide (PPWG) are shown on the right side. In both cases, sample lengths of $d = 1$ cm and $d = 5$ cm are regarded while $\varepsilon = 5$ is still valid.*

Additionally, the avoidance of these divergencies is also possible for arbitrary sample lengths by applying Newton's method for solving the corresponding equations (see section 3.1.1) which is performed for generating data shown in figure 3.11 for devices of $d = 1$ cm and $d = 5$ cm in a parallel plate and rectangular waveguide. Here, we obtain deviations in the range of 8 % ($d = 1.0$ cm) or 2 % ($d = 5.0$ cm) in the rectangular waveguide and 0.6 % ($d = 1.0$ cm) or 0.3 % ($d = 5.0$ cm) in the parallel plate waveguide.

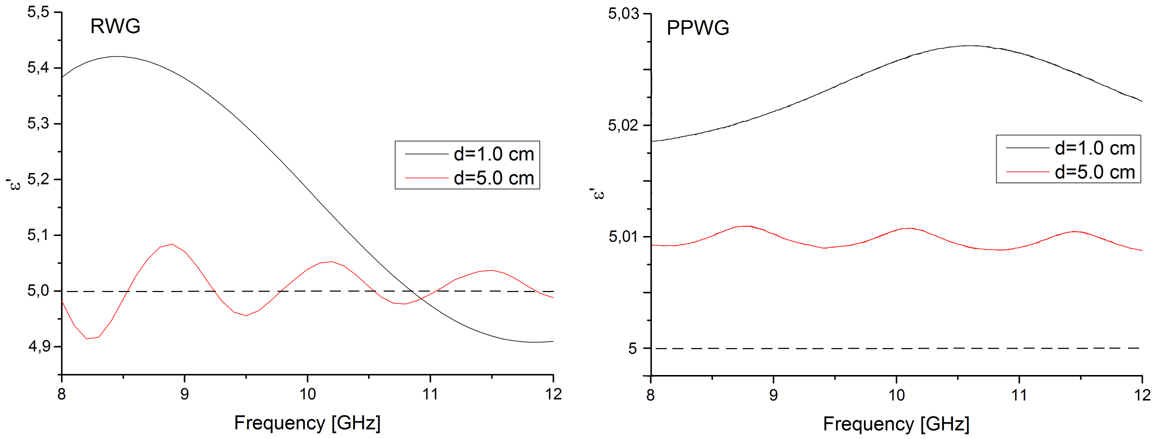

Figure 3.11 – *The same* $S-$*parameters as in figure 3.10 (sample with* $\varepsilon = 5$ *and a length of* $d = 1$ *cm or* $d = 5$ *cm, respectively) are evaluated with Newton's method. In this example, equation 3.4 for* S_{21} *is used in order to calculate permittivity. Left picture shows again results for the rectangular waveguide while a parallel plate waveguide is used in order to produce results on the right. Please note different scalings of the* $\varepsilon-$*axis.*

Within this, we observe results for longer devices to be more precise when using Newton's method (see figure 3.11). Moreover, accuracy shows up to be always higher for simulations in the parallel plate waveguide.

In summary, the usage of short samples is recommended when evaluation should be performed via NRW method, while longer samples improve results when Newton's method is applied. Considering all outcomes, the analysis of long devices in a parallel plated waveguide and subsequent evaluation with Newton's method shows highest accuracy concerning our methods. Although this first examination of a homogeneous and isotropic medium is problem-free and accurate to handle with the help of HFSS, simulation times can become huge when modeling composites with ferritic inclusions. These large simulation times are caused by strongly increased numbers of tetrahedra, especially at the inclusions's surfaces, which are necessary in order to produce precise results. Hence, HFSS will be only used in order to generate models and meshes before these data are imported into MOR software by LTE.

3.2.3 Numerical Computing of the Local Magnetic Dipole Fields

In general, the magnetic dipole-dipole interaction between the inclusions plays an important role and must be included in our model in order to achieve more realistic results. Unfortunately, the commercial software of HFSS is only capable to process pre-defined static magnetic biases, while their interaction and following changes in their orientation (relaxation) are not taken into account. Consequently, a method must be implemented in order to analyze the influence of the interaction between the several dipole moments. For that purpose, many existing models can be found in literature (see [61], for example), from which the following calculation method is chosen: At first, a given number N_{inc} of inclusions with a appropriate diameter is distributed randomly (or in a deterministic manner, see section 4.3) in a well-defined sample volume in such a way that desired volume fractions of inclusions are realized. Moreover, inclusions are supposed to be fully magnetized and the correlated magnetic moments $\mathbf{p}$ are calculated via

$$\mathbf{p} = \int_V \mathbf{M_s}\, \mathrm{d}V = \frac{4}{3}\pi r_{inc}^3 \mathbf{M_s^{inc}} \tag{3.104}$$

under the assumption of a homogeneous magnetization inside the inclusions with radius r_{inc} and saturation magnetization $\mathbf{M_s^{inc}}$. In the beginning, these magnetic moments are supposed to be perfectly aligned parallely to the static magnetic field, pointing in $z-$direction. The physical interpretation of these starting conditions is that the whole composite sample is exposed to an external field which is much stronger than the field caused by the inclusions. Consequently, it is able to fully magnetize it. Then the field in the sample is reduced to a lower value of H_{eff}, increasing the influence of the interactions between the inclusions' moments. For the purpose of including these effects into our simulations, one inclusion j inside the sample is randomly chosen and the local internal field at its center is computed according to

$$\mathbf{H_{inc,j}^{dip}} = \mathbf{H_{eff}} - \frac{1}{3}\mathbf{M_s^{inc}} + \sum_{i=1, i\neq j}^{N_{inc}} \left(\mathbf{H_{ij}} + \underbrace{\sum_{h=1}^{26} \mathbf{H_{i_h j}}}_{PBC!} \right) \tag{3.105}$$

with the interaction fields

$$\mathbf{H_{ij}} = \frac{1}{4\pi r_{ij}^2} \frac{3\mathbf{r_{ij}}(\mathbf{p}\ \cdot\ \mathbf{r_{ij}}) - \mathbf{p}\ \cdot\ \mathbf{r_{ij}}^2}{r_{ij}^3} \tag{3.106}$$

and the distance vector $\mathbf{r_{ij}}$ between the centers of inclusion i and j.

In case that infinitely extended material should be simulated, periodic boundary conditions are needed, which are included via the summation of the interaction fields resulting from the 26 periodic disposed copies of each inclusion. Then, the magnetic moment $\mathbf{p_j}$ of inclusion j is orientated parallely to the local field $\mathbf{H_{int,j}}$, meanwhile its magnitude remains constant $|\mathbf{p_j}| = \frac{4}{3}\pi r_{inc}^3 M_s$. This procedure is schematically illustrated in figure 3.12.

In the following, this calculation is done for every inclusion in a random sequence in one update step, while these steps are repeated until no moment's orientation is changed anymore by an angle greater than one degree. Accordingly, the simulation delivers the vector components of every inclusion's internal magnetic field in the equilibrium state of the static case.

The results of this numerical procedure become important in section 4.3, in which they are also presented. Furthermore, a discussion of the model assumptions and their physical influence is given there.

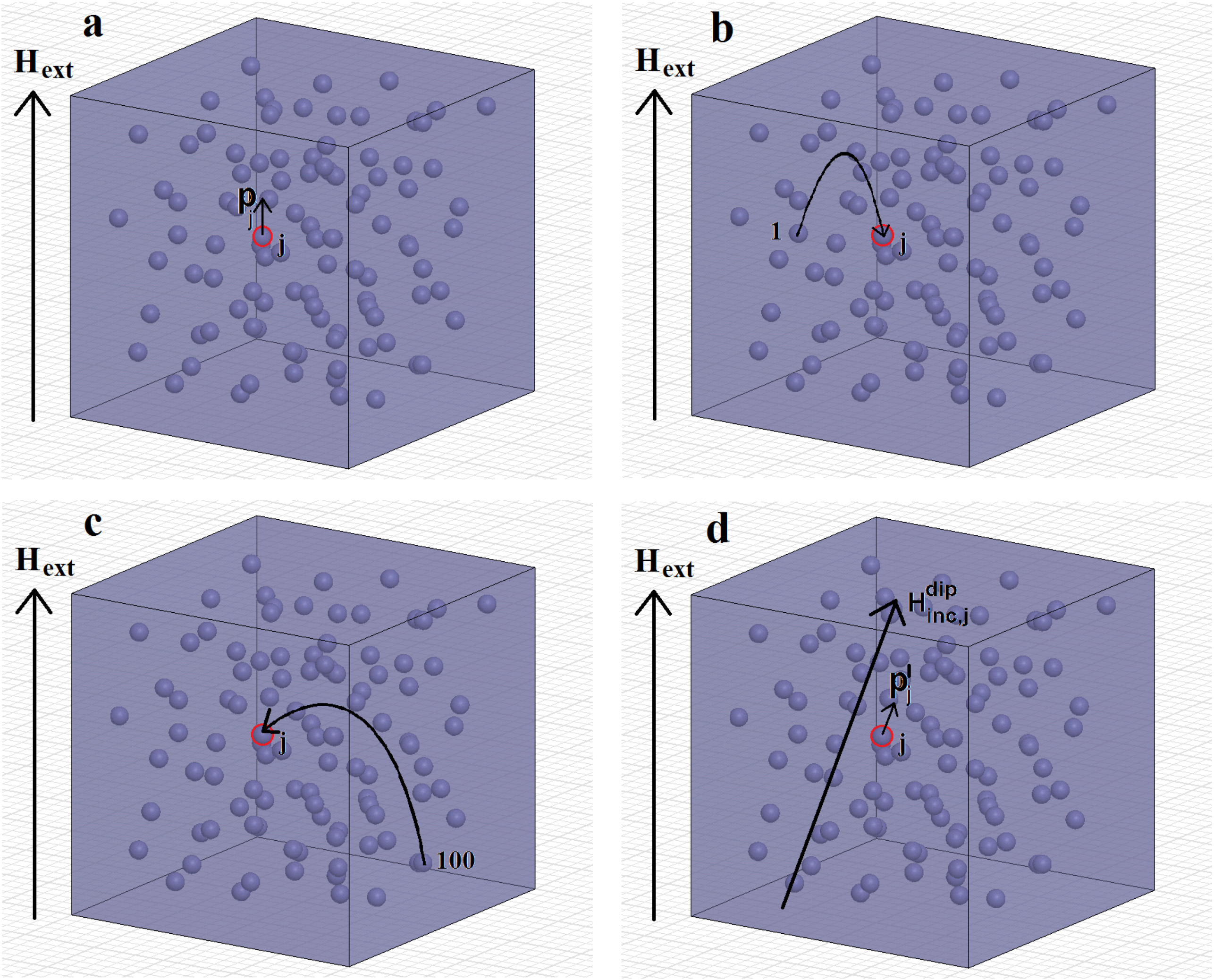

FIGURE 3.12 – *A schematic sketch of the calculation mechanism for an inclusion number of* $N_{inc} = 100$. *At first (a), one inclusion* j *with magnetic moment* $\mathbf{p_j}$ *is randomly chosen. In the beginning, this vector is aligned parallely to the field* $\mathbf{H_{eff}}$. *Afterwards, the contributions to the local internal field* $\mathbf{H^{dip}_{inc,j}}$ *from all other inclusions are computed (b and c). In picture (d), the new alignment of the updated magnetic moment* $\mathbf{p'_j}$ *is shown.*

Chapter 4

Examination of Composite Material with Infinite Extensions

In this chapter, the first results of the simulations done during this work are presented. We consider composites consisting of ferromagnetic inclusions in a non-magnetic host matrix (accordingly, a cermet topology is under test, see figure 1.17) with the target of studying the behavior of such heterogeneous devices and draw analogies to effective, homogeneous materials. In this context, we firstly concentrate on determining material parameters for infinitely extended samples, requiring certain conditions and procedures which will be illuminated.

As a simple as possible starting point, we analyze devices containing inclusions arranged on a simple cubic lattice before dealing with randomly generated microstructures in the following. Though, a detailed and exact examination of accuracy of the physical approximations, the simulation techniques and the evaluation methods is needed in order to justify our results. Contrary to the contents of this chapter, the analysis of finite samples will be done in chapter 5.

4.1 Previous Considerations

Before analyzing results, an extensive consideration of possibly sources of inaccuracy should be done, which will be given in this section. Concerning the topic and the methods of this work, one can differ between three types of challenges.

1. Physical issues: First of all, the effective medium approach requires the wavelength λ to be much larger than the inclusions' radius r_{inc}, which is no problem to fullfill in experiments, where inclusions on micro- and even nanometer scales (see [8], for example) are analyzed in the frequency range of microwaves (wavelengths in the order of centimeters). Contrary, in our simulation, a low inclusions' diameter leads to high inclusion numbers, requiring high memory allocation capacity. Therefore, the treat-off between small particles and limited computing resources has to be well-considered.

   Additionally, the composite's microstructure naturally influences the behavior of the effective medium via different interactions (demagnetizing effects, dipole-dipole interaction) between inclusions. Accordingly, different types of well-described arrangements and their effects concerning interactions are analyzed in simulations.

Last, but not least, one has always to be aware of the fact that our computations are done in finite samples which underly surface effects which are highly undesired in this chapter and have to be eliminated in order to study pure material properties.

2. Simulation accuracy: Of course, the accuracy of the used simulation techniques has to be verified by analyzing the convergence behavior of the computational methods. This includes the discretization of meshes in HFSS and the choice of the order of ansatz functions and the maximum residuum in ROM.
3. Evaluation accuracy: Another point is the choice of many different parameters in numerical evaluation methods as for the approximation of derivatives, for example. The most important issue in our case is a sufficiently high choice of the number of considered modes in the modal-matching technique.

First of all, we want to investigate the influence of the inclusions' radius in order to verify that $\lambda \gg r_{inc}$ is sufficiently reached in our simulations.
One approach for that purpose could be to analyze the two structures shown in figure 4.1. Both have a filling factor of 1 %.

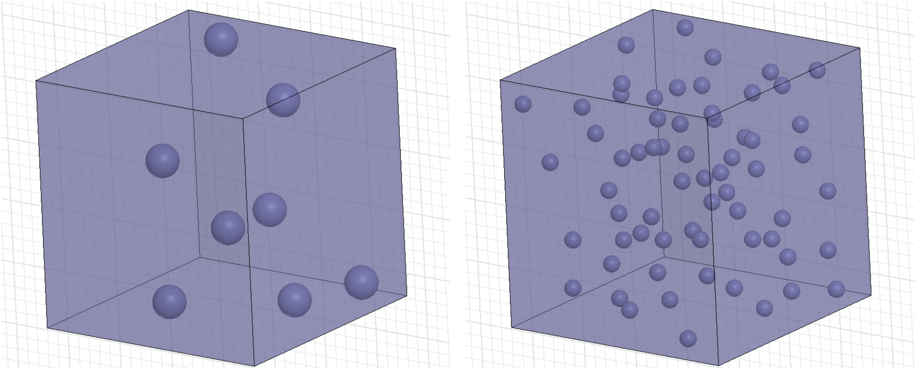

FIGURE 4.1 – *Two cubes with an edge length of* 1 *cm, containing* $N_{inc} = 8$ *inclusions with a radius of* $r_{inc} = 0.0668$ *cm (left) or* $N_{inc} = 64$ *inclusions with a radius of* $r_{inc} = 0.0334$ *cm (right), respectively. Consequently, the filling factor is* $f = 1$ % *in both cases, whereby microstructure is randomly generated. For the purpose of comparing both samples, inclusions' material parameters are the same in both cases.*

Simulating wave propagation in both systems and calculating the resulting effective permeability tensor then delivers different results. Now, the appearing problem is that one is not able to isolate the dependence on the inclusions' radius. The differences in the results may also occure due to the completely different microstructures. Accordingly, this must also be kept comparable in both cases in order to draw sensible conclusions.
At this point, several solutions for this task are possible. For example, one could use a given randomly microstructure and realize different inclusion sizes by shrinking the whole device (inclusions and host matrix) by a suitable factor. This maintains the filling factor, but changes the extensions of the device, which has a strong influence on the results, as we will see later in this chapter. Therefore, this examination is done with

no randomly microstructure, but an arrangement on a simple cubic lattice inside the matrix. Now, one changes the number of inclusions (in case of a cubic device restricted to cubic numbers, i.e. $N_{inc} = 1, 8, 27, 64, 125...$) and chooses the inclusions' radius in such a way that filling factor and device geometry are maintained. This is done for the three cases of $N_{inc} = 8, 27$ and 64, as illustrated in figure 4.2.

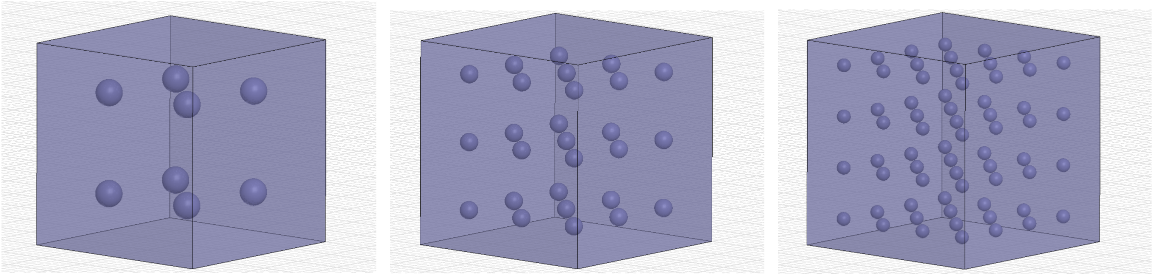

FIGURE 4.2 – *Three cubes with an edge length of* 1 *cm and filling factor* $f = 1$ %. *The influence of inclusions' radii should be analyzed. For that purpose,* N_{inc} *inclusions are placed on a simple cubic lattice with* $N_{inc} = 8$ *and* $r_{inc} = 0.0668$ *cm (left),* $N_{inc} = 27$ *and* $r_{inc} = 0.0445$ *cm (middle) or* $N_{inc} = 64$ *and* $r_{inc} = 0.0334$ *cm (right).*

Following measurements are done with material parameters $M_s^{inc} = 302\ 394.5\ \frac{\mathrm{A}}{\mathrm{m}}$ (= 3800 Gs) and $\alpha = 0.05$, which are actually in the range of these values for ferrite materials and also used in the works of V. Bregar (see [36] and [37]). For the reason of receiving a resonance frequency of $\nu_0 = 10$ GHz for an isolated sphere, the magnitudes of the internal magnetic biases of the inclusions are chosen according to

$$\begin{aligned} \omega_0 = 2\pi\nu_0 = \gamma H_{eff} \quad &\text{with} \quad H_{eff} = H_{inc} + \frac{M_s^{inc}}{3} \\ \Leftrightarrow H_{inc} &= \frac{2\pi\nu_0}{\gamma} - \frac{M_s^{inc}}{3} \\ &= 183\ 154\ \frac{\mathrm{A}}{\mathrm{m}}. \end{aligned}$$

These biases are orientated parallely to $z-$axis, while waves propagate in $x-$direction (see figure 4.3). Within this, γ denotes again the gyromagnetic ratio (as introduced in equation 1.160). For simplicity's sake, dipolar interactions between inclusions are neglected in these simulations. This will be further justified later in this section.

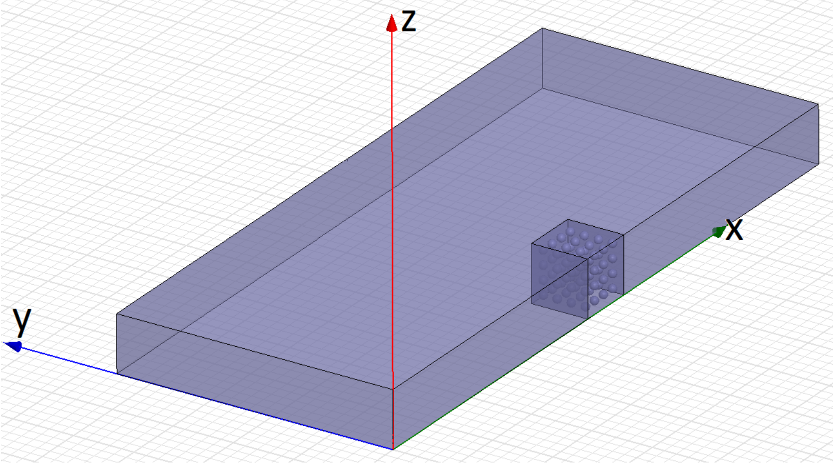

Figure 4.3 – *The whole waveguide model as produced in HFSS. Static magnetization of inclusions points along $z-$direction. Waves propagating along $x-$axis have to pass a 2.5 cm long empty part in the waveguide before reaching the device under test in order to damp higher ordered modes.*

The models of these microstructures are created with HFSS, in which different meshes are considered in order to determine the necessary discretization. The settings of HFSS mesh generator are the same which are described in section 3.2.2. Subsequently, meshes and models were exported to the MOR software of LTE and corresponding calculations are done with the following settings, unless otherwise stated:

- Solution order: fourth
- Maximum residuum: 10^{-3}
- 201 frequency points between 7 GHz and 12 GHz.

In the presented evaluation method (see section 3.1.2), 50 forwards and backwards travelling modes are considered. All these settings will be justified later. At this point, one minor technical problem occurs considering the software in use: When already defining anisotropic material in HFSS, the exportation of meshes into the MOR software of LTE fails. Accordingly, HFSS meshes are generated with isotropic materials whose permeabilities are chosen to have the maximum values of the Polder tensor's diagonal component of the anisotropic material of interest in the analyzed frequency range. This means that μ''_{iso} of the isotropic material is chosen to have the value of $\mu''_{max} = \mu''_{aniso}(\nu_{res})$ of the anisotropic material at resonance frequency, while μ'_{iso} of the isotropic material also amounts the highest value of μ'_{aniso} of the anisotropic material reached in the frequency range under test. Afterwards, the permeabilities of the magnetic materials are calculated according to Polder tensor (see equation 1.169) in the MOR software of LTE. By this, the results shown in figures 4.4, 4.5, 4.6 and 4.7 are produced, which highlight, that the second discretization pass is already convergent in case of an filling factor of $f = 1$ %. Nevertheless, we use the third pass for safety's sake.

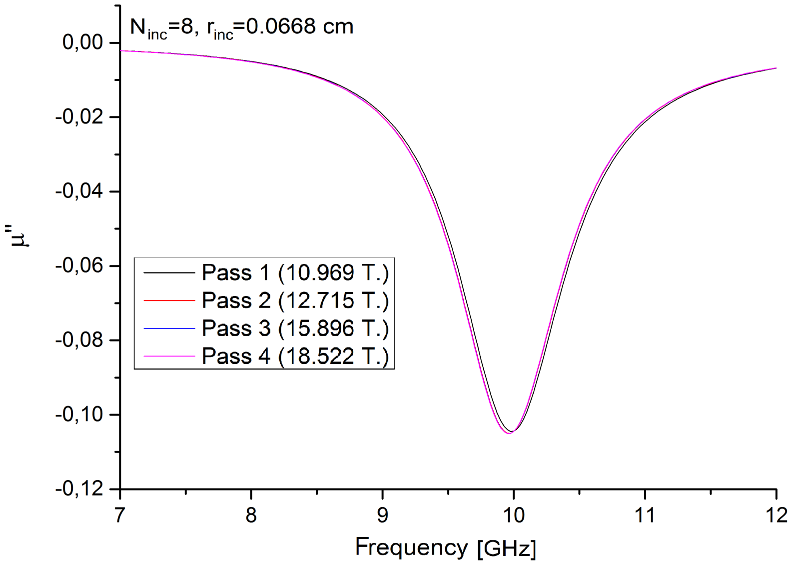

FIGURE 4.4 – *Imaginary part of* μ *for* $N_{inc} = 8$ *inclusions and* $r_{inc} = 0.0668$ *cm in dependence of frequency for different passes of mesh discretizations in HFSS. Regarded host matrix is a cube with an edge length of* 1 *cm, leading to a filling factor of* $f = 1$ %*. Numbers in brackets denote the number of tetrahedra of the different meshes. Results for the first four passes are given. There are only small variations between the first and second pass, but almost no changes when further increasing mesh discretization.*

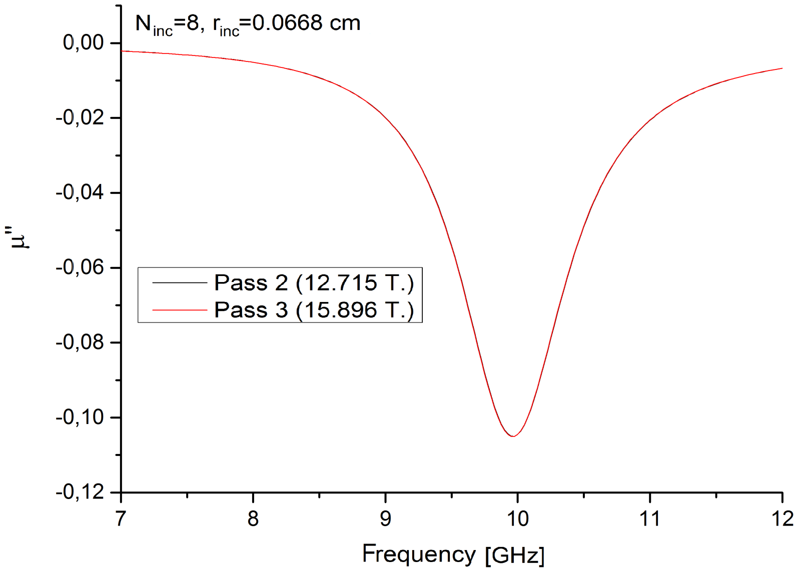

FIGURE 4.5 – *Results of discretization pass* 2 *and* 3 *as in figure 4.4 are shown again in order to highlight that there are almost no more differences between them.*

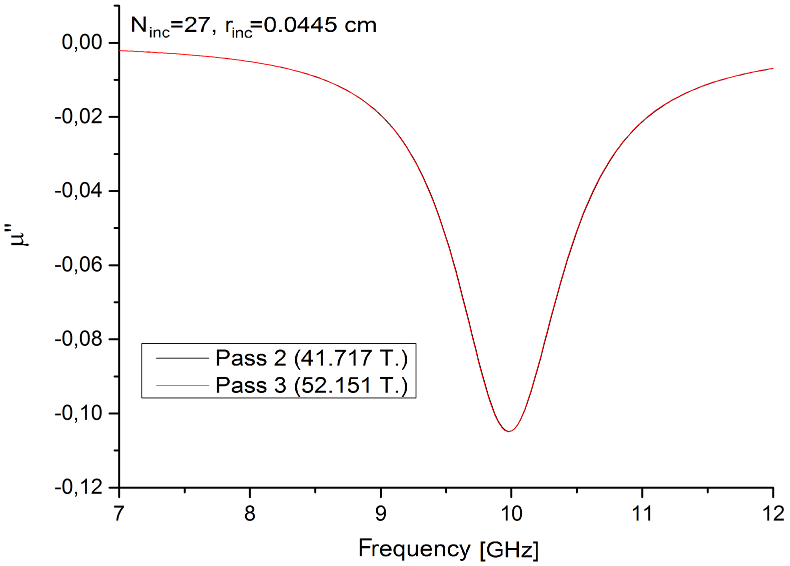

Figure 4.6 – *For* $N_{inc} = 27$*, one can draw the same conclusions as for* $N_{inc} = 8$*: the second pass of mesh refinement is already sufficient. Measurements are again done with a cube of an edge length of* 1 *cm and a filling factor of* $f = 1$ %.

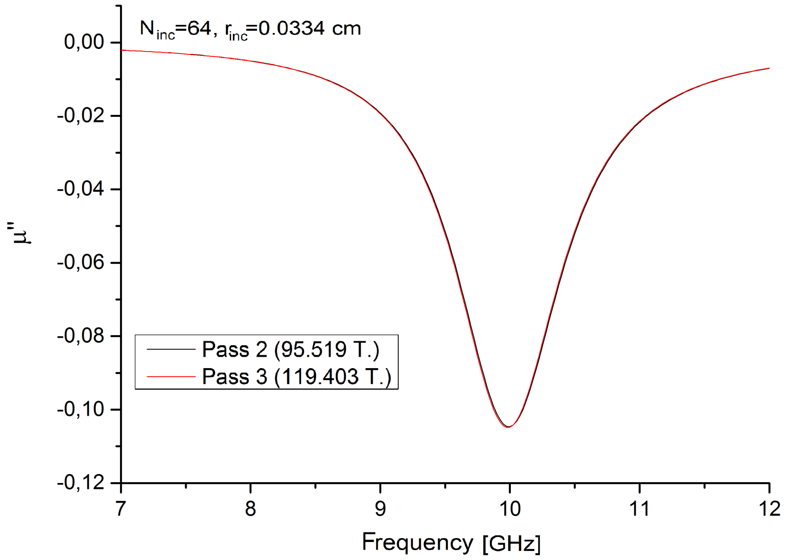

Figure 4.7 – *As shown in figure 4.6 for* $N_{inc} = 27$*, the second discretization pass is also sufficient for a further increased inclusion number of* $N_{inc} = 64$.

Within these simulations, one also notices the increased numbers of required tetrahedras when inclusion number grows (15 896 for $N_{inc} = 8$ in pass 3 and 119 403 for the same settings with $N_{inc} = 64$). This can be explained by the growing boundary surface between matrix and inclusions, at which more tetrahedras are necessary in order to guarantee accuracy.
After this first verification of simulation accuracy, one can compare the results for the different microstructures (figures 4.8 and 4.9). As we notice, only small differences

between samples with inclusions of different sizes and almost identical results between the arrangements with $N_{inc} = 27$ and $N_{inc} = 64$ inclusions are obtained.

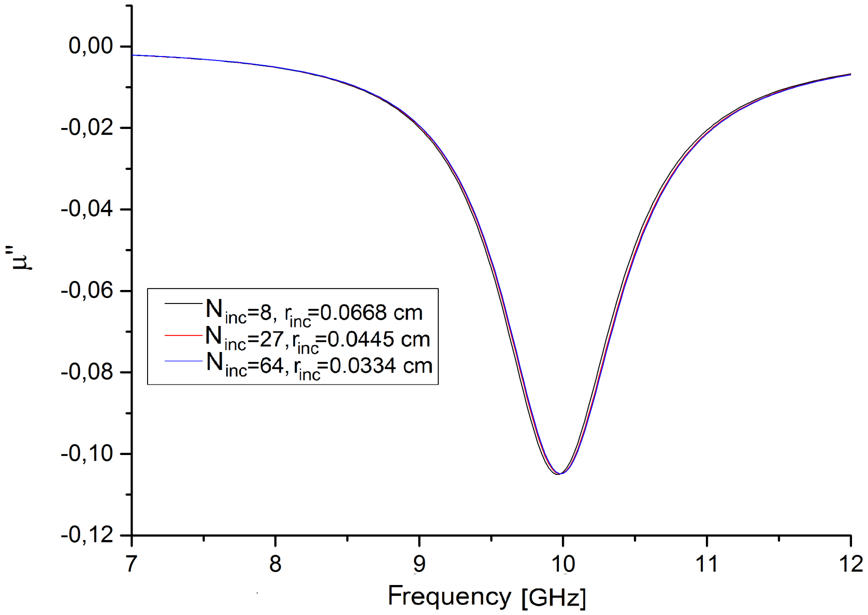

FIGURE 4.8 – *A comparison between the three described microstructures shows that there are only small changes in dependence of inclusions' radii in the regarded range.*

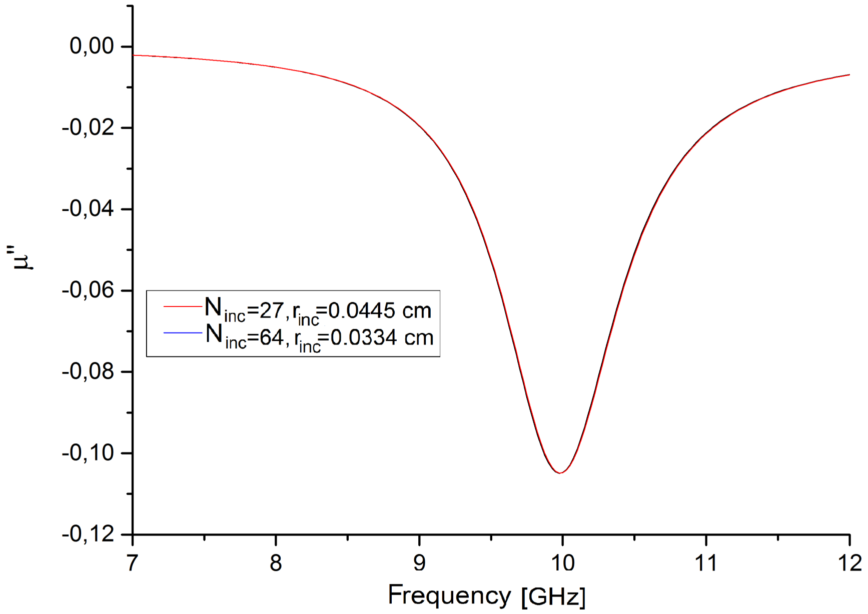

FIGURE 4.9 – *Only plotting the results for the structures with* $N_{inc} = 27$ *and* $N_{inc} = 64$ *highlights that the condition for the effective medium approach, namely* $\lambda \gg r_{inc}$, *is sufficiently satisfied.*

Because simulations are desired to be analyzed in the range of $f = 1\ \%\ldots 10\ \%$, the same examination is also done for the highest filling factor. In order to realize different volume fractions of inclusions while maintaining their radius, the host matrix is shrinked to smaller edge lengths, as $a = 0.464$ cm in case of $f = 10\ \%$. The corresponding result is shown in figure 4.10, which confirms $N_{inc} = 27$ inclusions with $r_{inc} = 0.0445$ cm to be sufficiently small, even for a volume fraction of $f = 10\ \%$. Consequently, $\lambda \gg r_{inc}$ is supposed to be fulfilled in the frequency range of interest when $r_{inc} \leq 0.0445$ cm is chosen.
At this point, one has to admit that it is not possible to decide if the deviation between the simulations with $N_{inc} = 8$ inclusions with a radius of $r_{inc} = 0.0668$ cm and the ones with higher numbers and smaller radii is a consequence of too few or too large inclusions. Nevertheless, due to convergence, one can be sure that all necessary criteria are fulfilled.

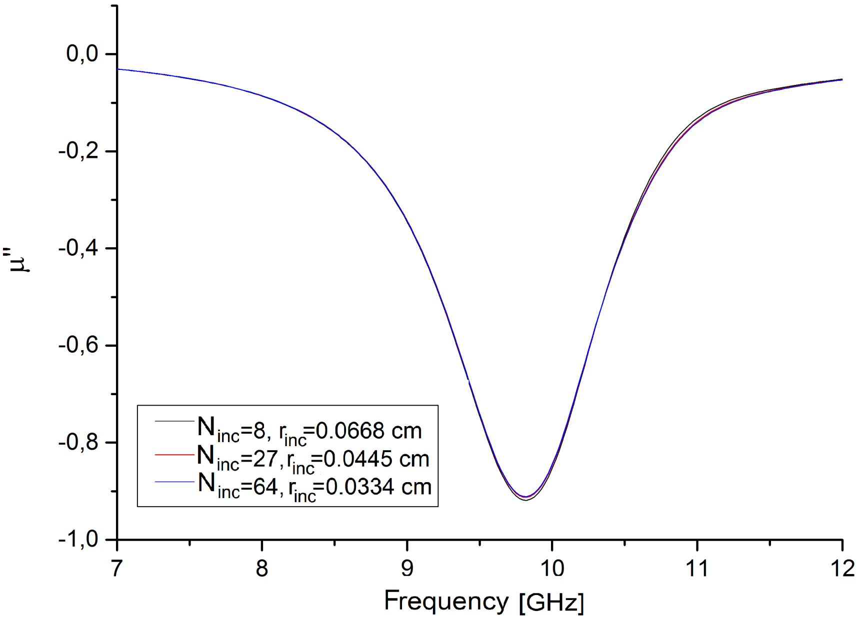

Figure 4.10 – *For* $f = 10\ \%$*, the cubic host matrix is shrinked to an edge length of* $a = 0.464$ *cm, while microstructures, inclusion numbers and radii are maintained. Again, the results for* $N_{inc} = 27$ *and* $N_{inc} = 64$ *are almost identical.*

Additionally, the sufficience of the used order of ansatz functions in the MOR software should be analyzed. For that purpose we consider a sample with $N_{inc} = 27$ inclusions on a simple cubic lattice and a volume fraction of $f = 1\ \%$ and $f = 10\ \%$. All other parameters (material parameters, static field, mesh discretization) are used as described before, but order of ansatz function is changed between two and four (see figures 4.11 and 4.12). These results highlight the influence of the order of ansatz functions, because the usage of an order of two strongly distinguishes from higher orders in both cases. Interestingly, differences between the results for an order of three and four decrease when volume fraction f rises. According to the shown results, we will use an order of four in order to obtain the highest level of accuracy. Moreover, the influence of the maximum residual error (see section 3.2.1), which is an input parameter in MOR software, should be examined in order to ensure that no significant inaccuracies arise.

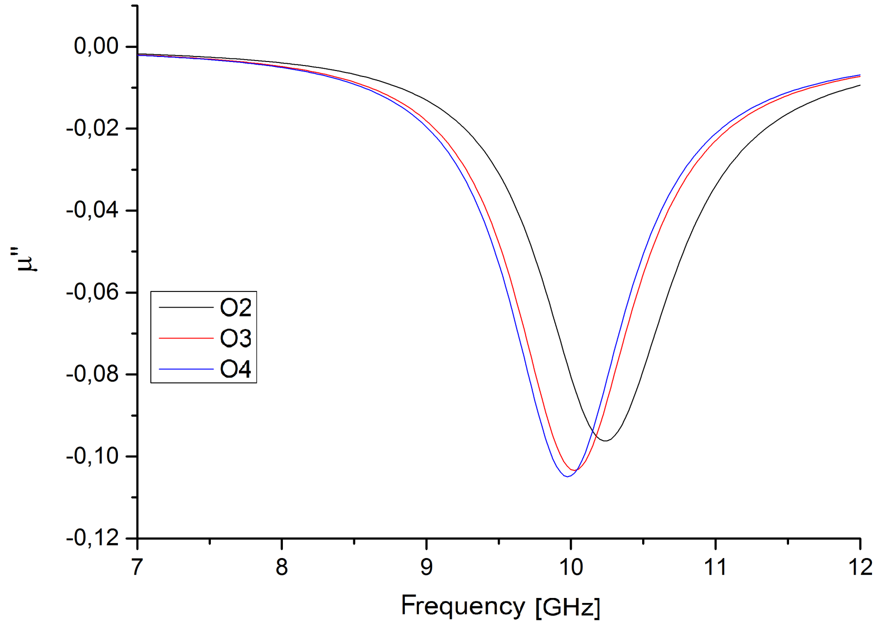

FIGURE 4.11 – *For $f = 1$ % and $N_{inc} = 27$ inclusions, different orders of ansatz function are tested. Obviously, an order of two differs much from higher orders, but also the results for orders of three and four can be clearly distinguished from each other.*

For this, we use again the same simulation parameters as before and samples with $f = 1$ % and $f = 10$ %, but vary the maximum residuum between $res_{max} = 10^n$ with $n = -1, -2, -3$. The corresponding results are shown in 4.13 and 4.14, proving that a value of 10^{-3} is sufficiently small in both cases.

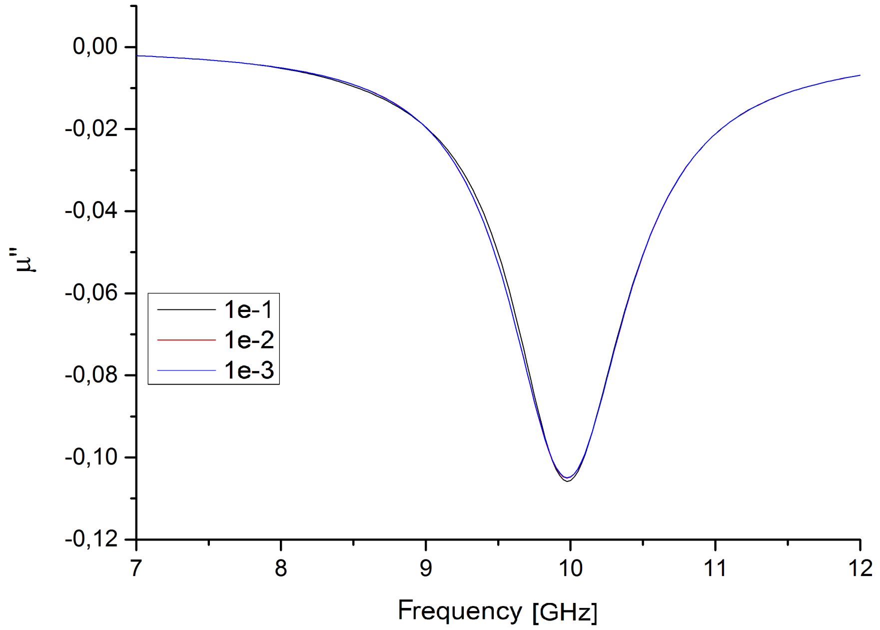

FIGURE 4.13 – *The influence of the maximum residuum on the results is analyzed. Small deviations between the results for $res_{max} = 10^{-1}$ and $res_{max} = 10^{-2}$ are detected, while the curves for $res_{max} = 10^{-2}$ and $res_{max} = 10^{-3}$ do not differ. Picture shows results for $f = 1$ %*

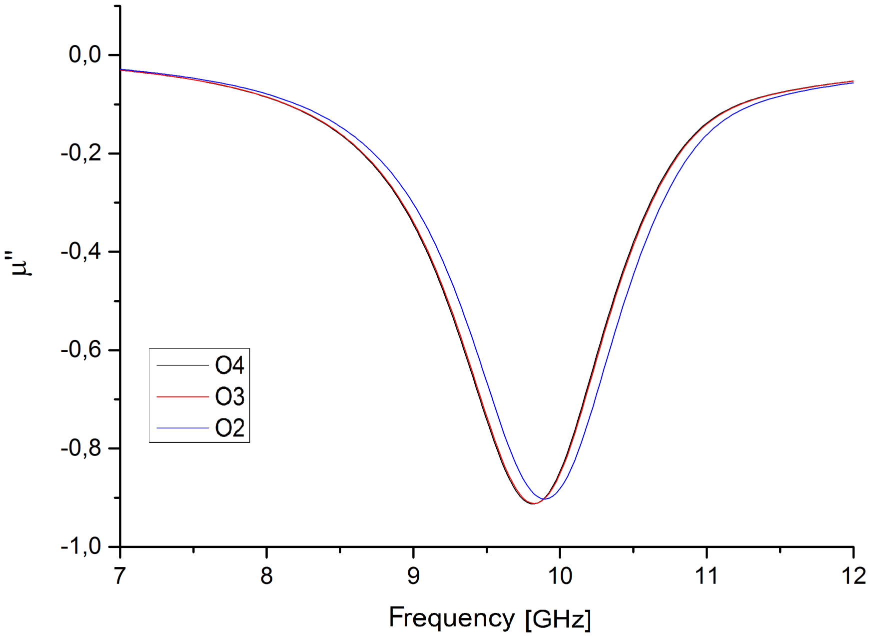

FIGURE 4.12 – *For $f = 10$ % and $N_{inc} = 27$, the differences between the results for an order of three and four are much smaller than for $f = 1$ %.*

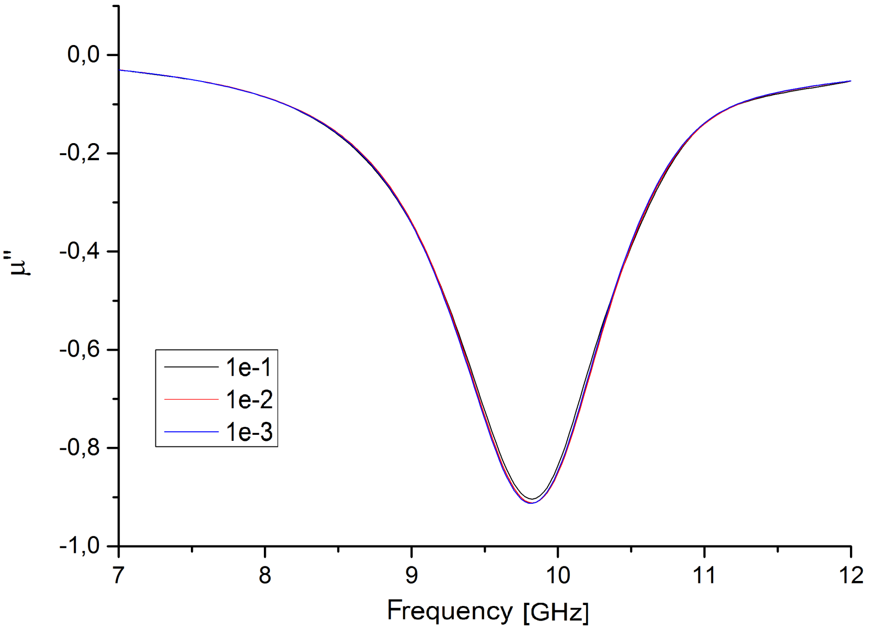

FIGURE 4.14 – *The same analysis as in figure 4.13 is done for a filling factor of $f = 10$ %. Again, a maximum residuum of 10^{-3} is proven to be more than sufficiently accurate.*

The last point of accuracy to analyze at this point is modal matching's convergence behavior. For that purpose, we again use the $S-$parameters from simulations with the outworked accuracy parameters. Contrary to the previous considerations, we can restrict to consideration of the case of $f = 10$ % because here, due to highest resulting effective permeability, more modes will be arised comparing to lower volume fractions. Evaluating the corresponding simulated data with different numbers of considered modes, we obtain the results shown in figure 4.15. Convergence becomes obviously for more than ten modes. Nevertheless, due to the minor numerical effort of evaluation compared with simulations, 50 modes are considered in the following sections.

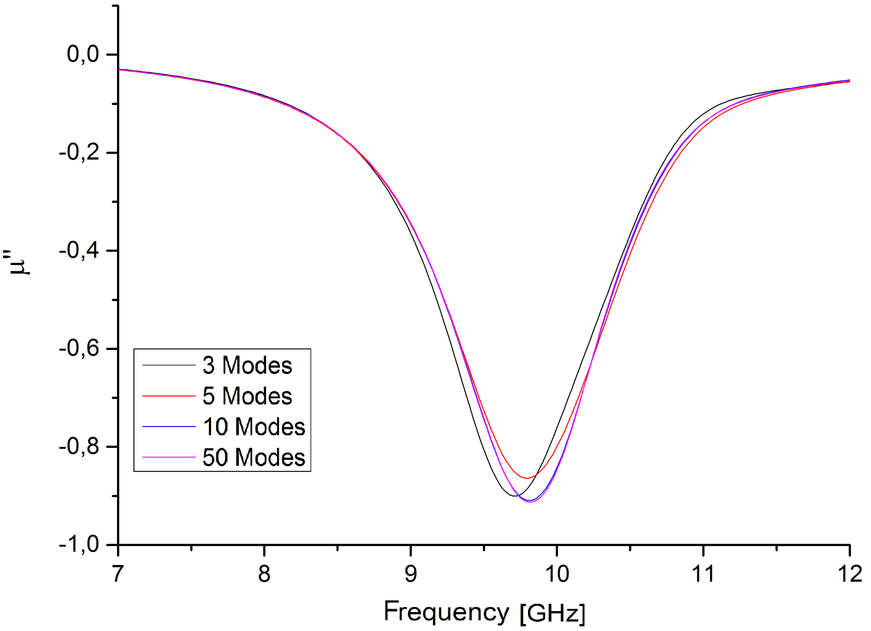

Figure 4.15 – *Influence of the number of modes is tested for a composite with* $N_{inc} = 27$ *inclusions, a filling factor of* $f = 10\ \%$ *and the justified accuracy parameters. When increasing from three to five or five to ten strong differences become clear concerning the strength of the peak and shifting of the resonance frequency. A consideration of more than 10 modes does not change the results anymore.*

Summarizing, we have justified a set of parameters with which we are able to meaningfully analyze the system's behavior.

4.2 Inclusions on a Simple Cubic Lattice

4.2.1 Simulation Investigation

In first simulation sequences, the structure with inclusions placed on a simple cubic lattice will be maintained for two reasons: Firstly, this delivers a very simple first case in order to analyze the influence of differently generated microstructures. The second motive becomes clear assuming a strong static magnetic field in $z-$direction which saturates magnetization of all inclusions. Consequently, dipole moments of all inclusions show parallely in $z-$direction and resulting magnetic field of one inclusion i evaluated at the place of another inclusion j is described through

$$\mathbf{H}_{ij} = \frac{1}{4\pi r_{ij}^2} \frac{3\mathbf{r}_{ij}(\mathbf{p}\cdot\mathbf{r}_{ij}) - \mathbf{p}\cdot\mathbf{r}_{ij}^2}{r_{ij}^3} \tag{4.1}$$

as introduced by equation 3.106. Regarding one pointlike inclusion j placed on and surrounded by an infinite simple cubic lattice of identical inclusions, we can determine the resulting dipolar field at center of inclusion j by

$$\begin{align} \mathbf{H}_{dip,j} &= \sum_{i=1,i\neq j}^{\infty} \mathbf{H}_{ij} \tag{4.2}\\ &= \sum_{i\in M_{ij}} \mathbf{H}_{ij} + \sum_{i\notin M_{ij}} \mathbf{H}_{ij}. \tag{4.3} \end{align}$$

wherein $M_{ij} = \{i|\text{inclusion } i \text{ is nearest neighbour of inclusion } j\}$ denotes the set of nearest neighbours of j at distance r_{nn}, which we numerate according to figure 4.16.

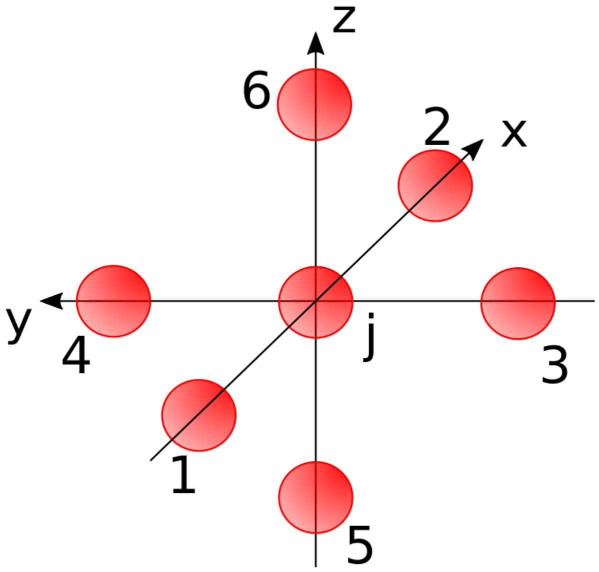

FIGURE 4.16 – *Inclusion j is surrounded by six neareast neigbours on a simple cubic lattice.*

Continuing evaluation, we find

$$\begin{aligned}
\sum_{i \in M_{ij}} \mathbf{H}_{ij} &= \mathbf{H}_{1j} + \mathbf{H}_{2j} + \mathbf{H}_{3j} + \mathbf{H}_{4j} + \mathbf{H}_{5j} + \mathbf{H}_{6j} && (4.4)\\
&= \frac{1}{4\pi r_{nn}^2} \frac{3 r_{nn} \mathbf{x} \left(p\mathbf{z} r_{nn} \mathbf{x} \right) - p\mathbf{z} r_{nn}^2}{r_{nn}^3} && (4.5)\\
&+ \frac{1}{4\pi r_{nn}^2} \frac{-3 r_{nn} \mathbf{x} \left(-p\mathbf{z} r_{nn} \mathbf{x} \right) - p\mathbf{z} r_{nn}^2}{r_{nn}^3} && (4.6)\\
&+ \frac{1}{4\pi r_{nn}^2} \frac{3 r_{nn} \mathbf{y} \left(p\mathbf{z} r_{nn} \mathbf{y} \right) - p\mathbf{z} r_{nn}^2}{r_{nn}^3} && (4.7)\\
&+ \frac{1}{4\pi r_{nn}^2} \frac{-3 r_{nn} \mathbf{y} \left(-p\mathbf{z} r_{nn} \mathbf{y} \right) - p\mathbf{z} r_{nn}^2}{r_{nn}^3} && (4.8)\\
&+ \frac{1}{4\pi r_{nn}^2} \frac{3 r_{nn} \mathbf{z} \left(p\mathbf{z} r_{nn} \mathbf{z} \right) - p\mathbf{z} r_{nn}^2}{r_{nn}^3} && (4.9)\\
&+ \frac{1}{4\pi r_{nn}^2} \frac{-3 r_{nn} \mathbf{z} \left(-p\mathbf{z} r_{nn} \mathbf{z} \right) - p\mathbf{z} r_{nn}^2}{r_{nn}^3} && (4.10)\\
&= \frac{1}{4\pi r_{nn}^3} \left(-6p\mathbf{z} + 3p\mathbf{z} + 3p\mathbf{z} \right) && (4.11)\\
&= 0. && (4.12)
\end{aligned}$$

Accordingly, the magnetic fields caused by the nearest neigbours equalize themselves at the center of inclusion j. The same phenomenon can be shown for the second, third and so on nearest neighbours (see textbooks like [38], for example) or simply calculated by our simulation software presented in section 3.2.3. Obviously, this holds for every inclusion in case of an infinite sample, wherefore dipole-dipole interactions do not have to be considered here. Regarding a finite sample, consisting of a limited number of inclusions as $N_{inc} = 64$, this is not true anymore. But, remembering our goal of drawing conclusions concerning infinitely extended material, disregarding dipole-dipole interactions in case of a simple cubic lattice is justified under the condition that other artifacts due to the finite device are also eliminated. Consequently, only static magnetic field (determining the permeability tensor according to Polder without crystal anisotropy) and demagnetization effects will influence the results given in this section.

Now, we want to analyze the composites' permeability with different volume fractions of inclusions with a constant internal magnetic bias $H_{inc} = 183\ 154\ \frac{\mathrm{A}}{\mathrm{m}}$. For these examinations, we use the derived accuracy parameters and the further material properties as described before. Although only μ'' was used in order to analyze the accuracy of the results, we also regard the corresponding results for all four entries of the Polder tensor, which are shown in figures 4.17-4.20. In order to intensively analyze the behavior of the resonance frequency, the components of μ'' are normalized with regard to the inclusions' volume fraction in figure 4.21.

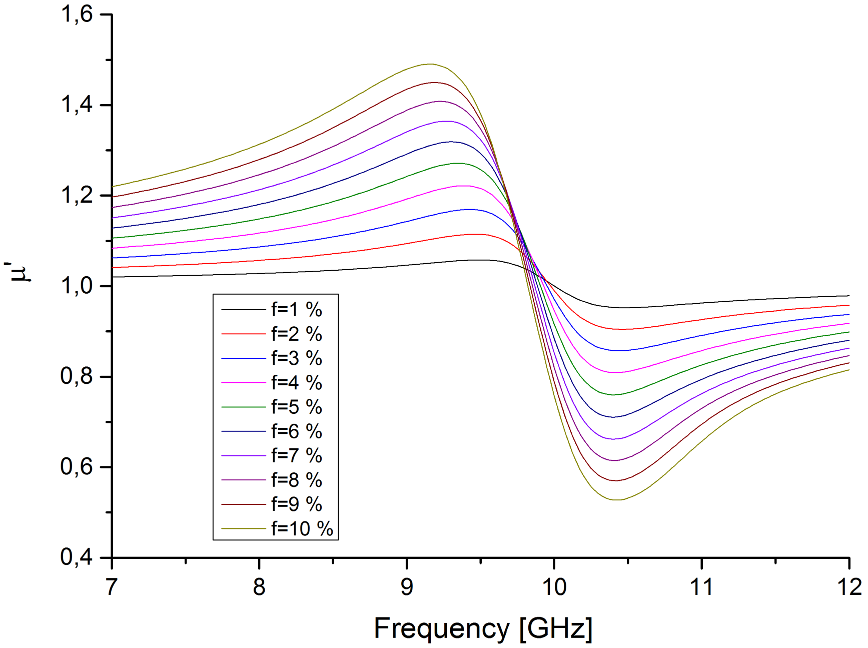

FIGURE 4.17 – *The described parameters are used in order to study the system's behavior with different volume fractions of inclusions f. This is realized by shrinking the host matrix for higher values of f. In this graph, we regard the behavior of μ' int the case of $H_{inc} = const.$.*

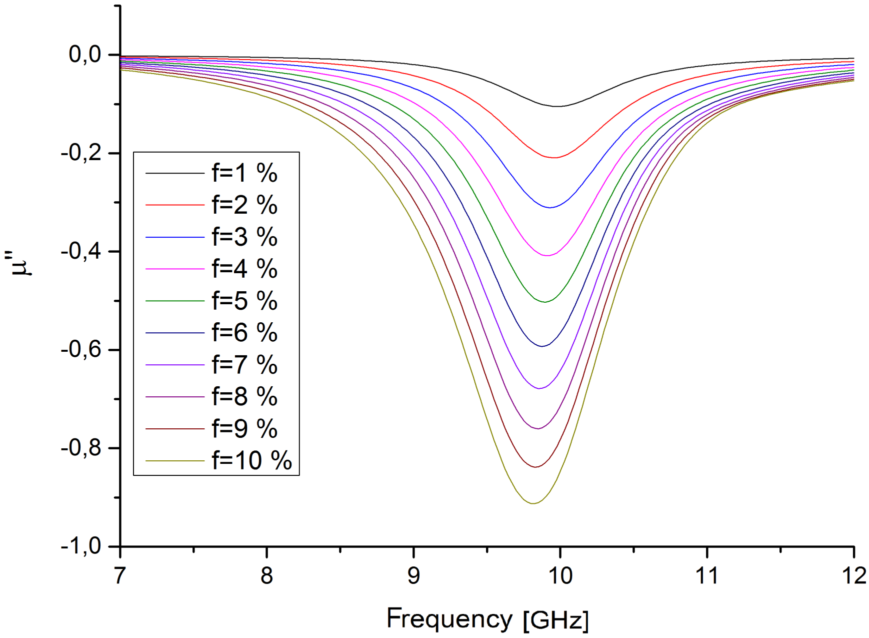

FIGURE 4.18 – *When regarding μ'', we notice the strength of the resonance peak to increase with higher filling factors, which is not surprising. Additionally, resonance shifts towards lower frequencies when $H_{inc} = const.$ is valid for every filling factor.*

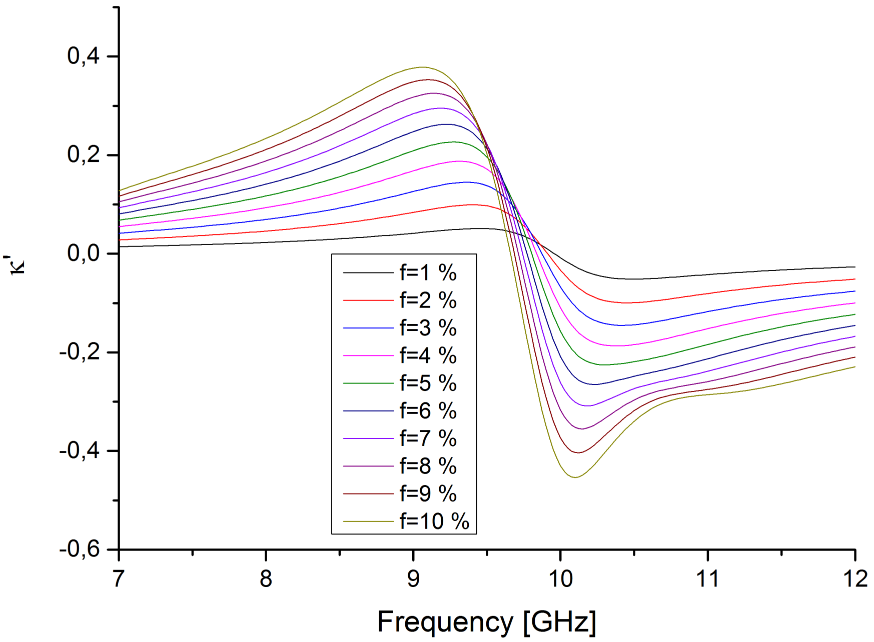

FIGURE 4.19 – *By the methods at hand, we also determine the non-diagonal entry* κ *of the Polder tensor. Here, the real part for different volume fractions with* $H_{inc} = const.$ *is shown.*

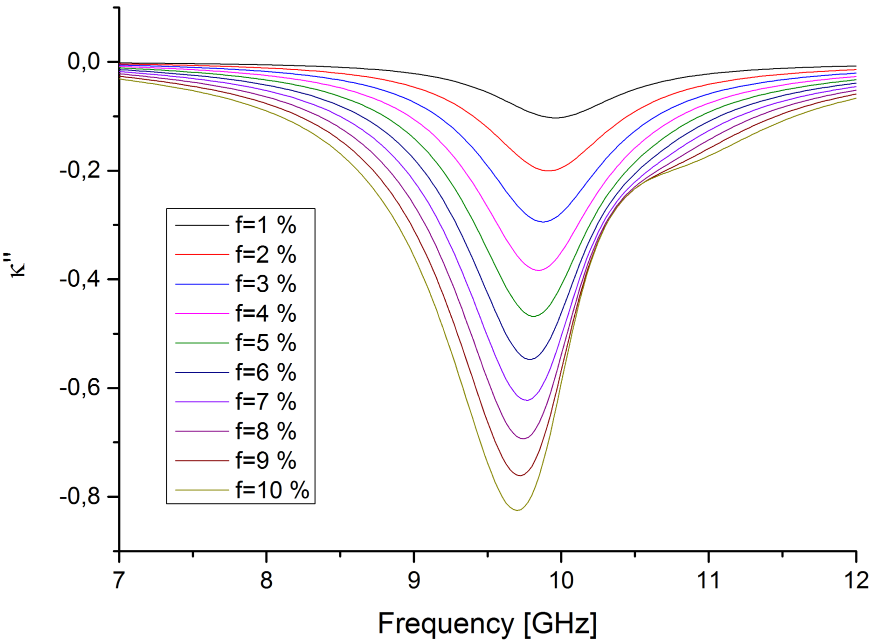

FIGURE 4.20 – *The imaginary part of* κ *for different filling factors with* $H_{inc} = const.$ *is shown in this graph.*

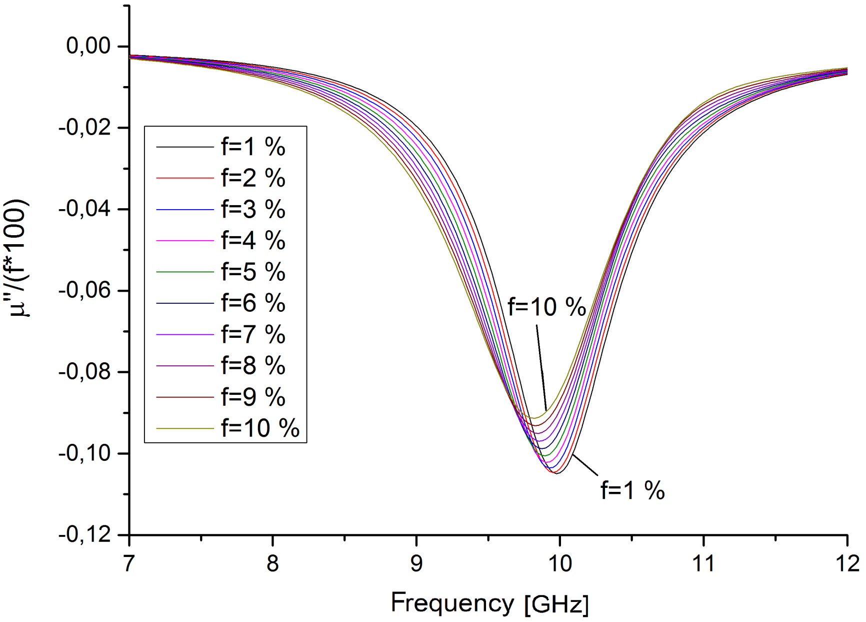

FIGURE 4.21 – *While in figure 4.18, absolute values for μ'' are shown, the above curves are normalized due to the inclusions' volume fractions. In this plot, normalized strength of the resonance peak decreases with increasing volume fraction.*

Before interpreting these outcomes, one has to be aware of the fact that different filling factors were analyzed by changing the device geometry, which is linked with a change of surface effects influencing our results. In order to highlight the effect of this disturbing phenomenom, even at the matrix's surface of composite materials, three different geometries (see figure 4.22) are analyzed, with the results shown in picture 4.23.

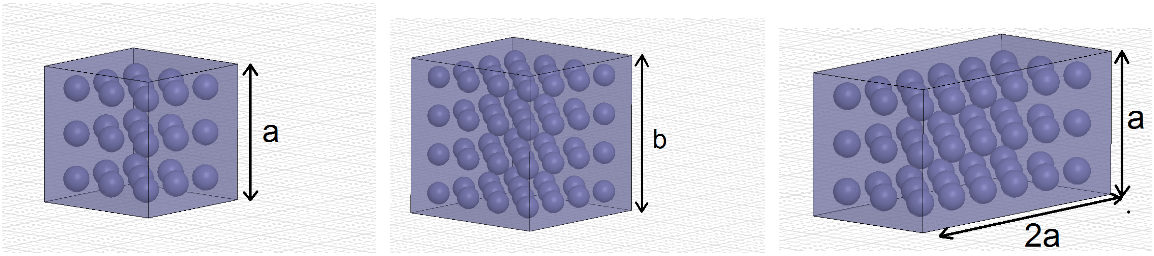

FIGURE 4.22 – *The different device geometries with the same inclusion size are considered. In the left picture, the previously considered cube with $N_{inc} = 27$ inclusions is shown. The second device, shown in the middle, is an increased cube, which contains $N_{inc} = 64$ inclusions. Thirdly, a non-cubic device with a doubled length in propagation direction and a square cross section is used, which is shown at the right side. This sample contains $N_{inc} = 54$ inclusions. The volume fraction is $f = 10$ % in every case, geometric dimensions are $a = 0.464$ cm and $b = 0.618$ cm.*

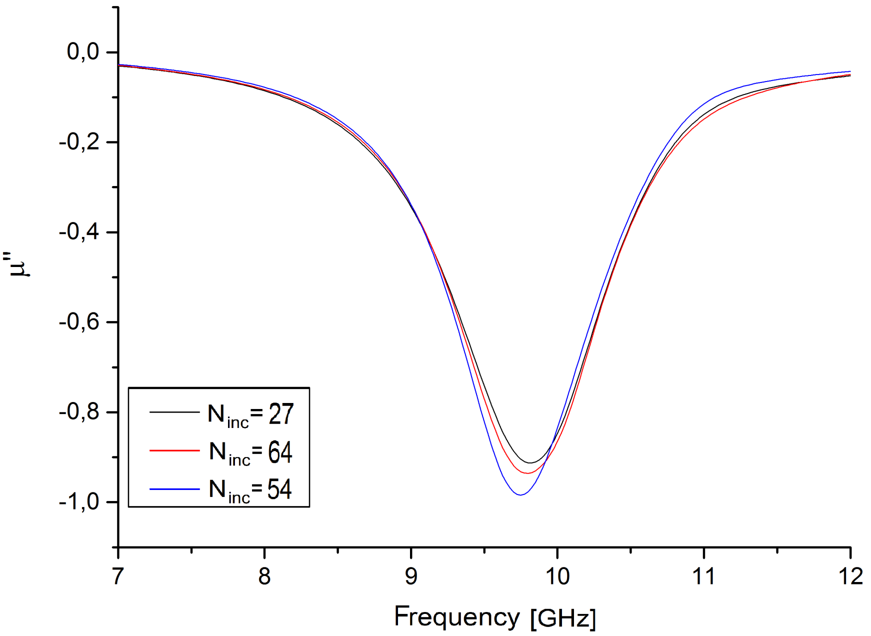

FIGURE 4.23 – *The three device geometries shown in figure 4.22 deliver different resonance peaks, although material parameters and inclusions' volume fractions are the same.*

This geometry-dependence is highly undesired and has to be eliminated in order to study the material characteristics. For that purpose, the following procedure is used: for every analyzed composite, a homogeneous sample with equal geometric dimensions is considered. Then, material properties H_{int} and M_s, labelling the internal magnetic field and saturation magnetization, for the homogeneous material, which are input parameters in simulations, are varied until the same results are produced as for the composite device. Afterwards, the accordance with this parameter set is tested for other geometries. If the found parameters of the homogeneous sample then actually reproduce the results of the heterogeneous composite for different geometries, then effective medium parameters for the composite materials are found in our input data. In the following, we refer to these values as H_{eff} and M_{eff}. In this consideration, material parameter α is always maintained because the origin of this damping term is on an atomic or molecular scale and should not vary with volume fraction. The analysis of the homogeneous samples is done with the same accuracy parameters as for the composites, but number of mesh discretazion passes in HFSS is increased to 20 in order to ensure exactness. This can be done without problems concerning computation resources because of the much lower number of required mesh elements for homogeneous samples. Fortunately, the described procedure is succesful and it is possible to find effective parameters which reproduce the composite's behavior very well, as shown for a volume fraction of $f = 10$ % in figures 4.24, 4.25 and 4.26. The requirements to find the effective parameters were defined in such a way that resonance frequencies of composite and homogeneous material differ not more than 0.025 GHz and the maximum deviation of μ'' is less than 2.5 % in every evaluated frequency point, whereby minimum deviations in single frequency points reach values in the order of 0.001 %. The trial of further reducing maximum deviation fails because a minimization of error in one frequency point increases deviation at other frequencies. Nevertheless, curves are in very good agreement.

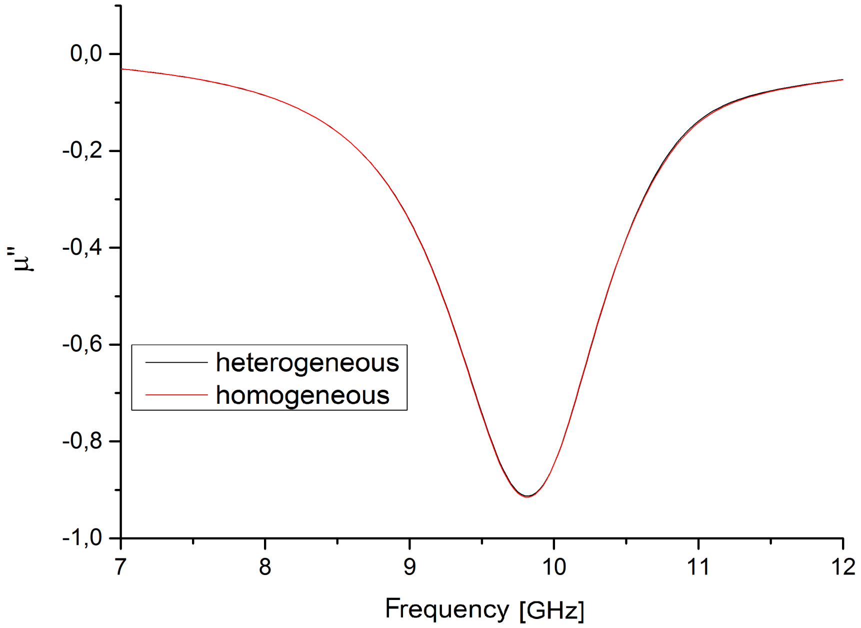

FIGURE 4.24 – *The cubic sample with* $N_{inc} = 27$ *shown in figure 4.22 is considered and input material parameters* H_{eff} *and* M_{eff} *for the homogeneous samples are varied until results agree with the heterogeneous composite's behavior for this geometry. Found values amount:* $H_{eff} = 274\,582\ \frac{A}{m}$ *and* $M_{eff} = 29\,444\ \frac{A}{m}$*. Note the very high accordance of the curves.*

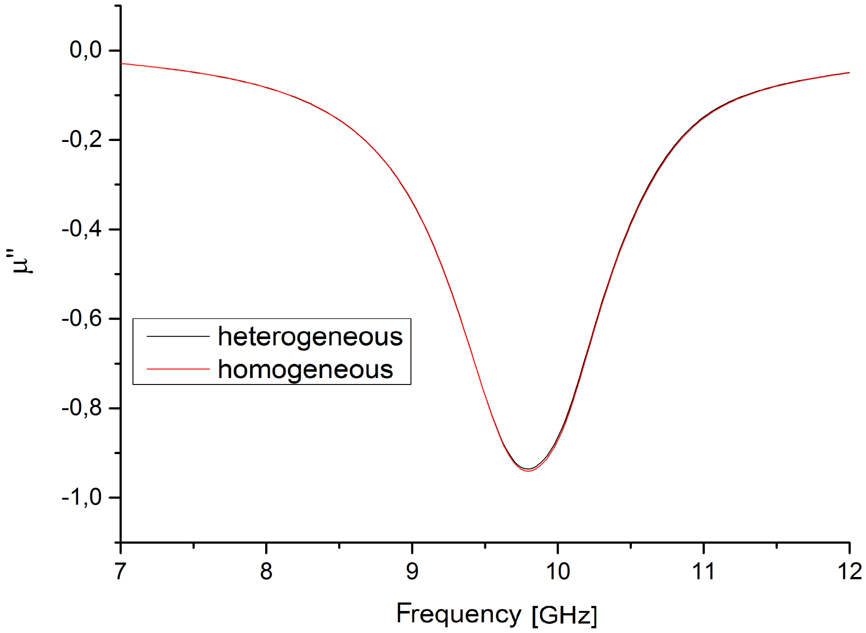

FIGURE 4.25 – *For producing these curves, the cubic sample with* $N_{inc} = 64$ *shown in figure 4.22 was analyzed. Concerning the homogeneous sample, we use* H_{eff} *and* M_{eff} *as found for the smaller cube (see figure 4.24), delivering again very good matching results.*

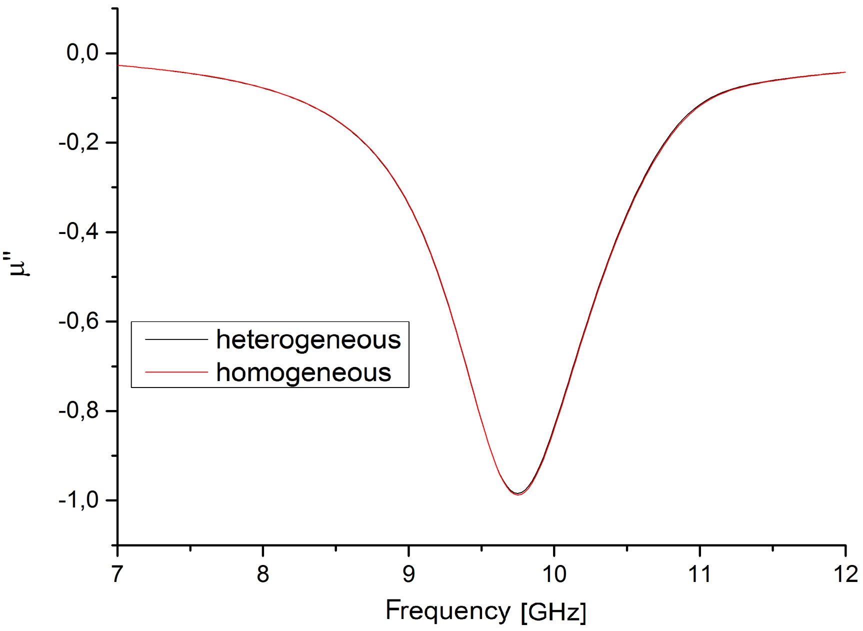

FIGURE 4.26 – *The sample with an increased length in propagation direction is examined and again the found values of H_{eff} and M_{eff} are used for the homogeneous device. Also in this case, we get results with high accordance.*

Repeating this procedure for every desired volume fraction of inclusions (actually done with the smaller cubic sample, accordingly the resonance curves shown in figure 4.18 are in use) under the condition $H_{inc} = const.$, one finds the correlations for H_{eff} and M_{eff} as functions of filling factor f as shown in figure 4.27.
Linear fitting processes with the help of OriginLab deliver

$$M_{eff}(f) = (2934.5 \pm 4.3)\ \frac{\mathrm{A}}{\mathrm{m}\ \%} \cdot f[\%] \tag{4.13}$$

$$H_{eff}(f) = 283\ 952\ \frac{\mathrm{A}}{\mathrm{m}} - (942.6 \pm 3.1)\ \frac{\mathrm{A}}{\mathrm{m}\ \%} \cdot f[\%]. \tag{4.14}$$

The fixed conditions for $y-$interceptions take into account that M_{eff} has to be zero if samples include no magnetic material and that internal magnetic field is chosen in such a way that resonance should occur at $\nu = 10$ GHz for an isolated sphere in a non-magnetic matrix.
Regarding the effective magnetization M_{eff}, the identified slope with respect to volume fraction of inclusions of $(2934.5 \pm 4.3)\ \frac{\mathrm{A}}{\mathrm{m}\ \%}$ is very close to the intuitively expected value of $\frac{M_s^{inc}}{100\ \%} = 3023.9\ \frac{\mathrm{A}}{\mathrm{m}\ \%}$, with a deviation of only 3.04 %.

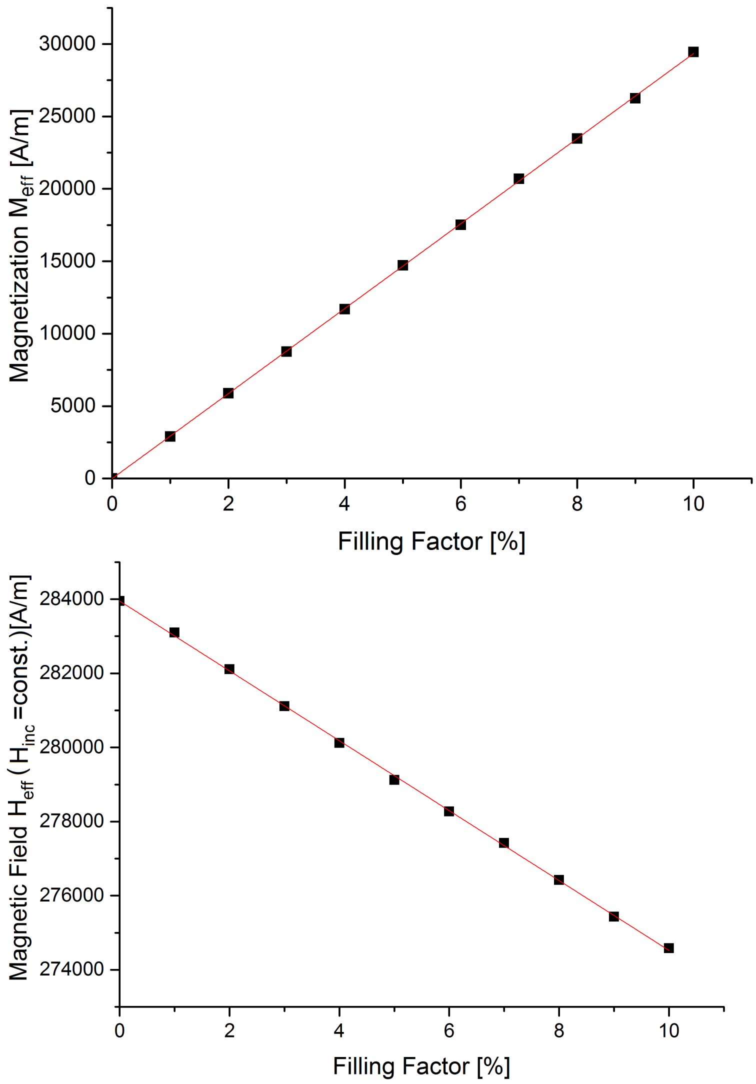

FIGURE 4.27 – *The found values for* M_{eff} *and* H_{eff} *are linear fitted with fixed conditions for* $f = 0$ %*:* $M_{eff}(f = 0\ \%) = 0\ \frac{A}{m}$ *(sample without magnetic material) and* $H_{eff}(f = 0\ \%) = 283\ 952\ \frac{A}{m}$ *(defined by the condition* $\nu_0 = \frac{\gamma}{2\pi} H_{ext} = 10$ *GHz). In the corresponding simulation sequence,* $H_{int} = 183\ 154\ \frac{A}{m}$ *was kept constant for every filling factor.*

Considering the effective magnetic field H_{eff}, one has to recall demagnetization theory in order to understand this result. Accordingly, the internal magnetic bias of the inclusions H_{inc} can be correlated with the effective field according to equation 1.153. In conclusion, we find the relation

$$H_{eff} = H_{inc} + \frac{1}{3}(M_s^{inc} - M_{env}) \tag{4.15}$$

which determines the resonance frequency. In this, H_{inc} and M_s^{inc} are defined input parameter and M_{env} describes magnetization of the environmental medium around one regarded sphere. Consequently, in our simulation sequence, $H_{inc} = 183\ 154\ \frac{\mathrm{A}}{\mathrm{m}}$ and $M_s^{inc} = 302\ 394.5\ \frac{\mathrm{A}}{\mathrm{m}}$ remained constant, while M_{env} corresponds to the effective magnetization of the composite M_{eff}.

So, in this case, above equation can be written as

$$H_{eff}(H_{inc} = const.) = H_{inc} + \frac{1}{3}M_s^{inc} - \frac{1}{3}M_{eff}(f) \tag{4.16}$$

Comparing the determined slope of $-942.6\ \frac{\text{A}}{\text{m}\ \%}$ with the theoretically determined value of $-\frac{1}{3}M_{eff}(f) = -\frac{1}{3}\frac{M_s^{inc}}{100\ \%} \cdot f[\%] = -1007.98\ \frac{\text{A}}{\text{m}\ \%} \cdot f[\%]$, one recognizes a deviation of 6.49 %. Additionally, one can also use the before determined value of $M_{eff}(f) = 2934.5\ \frac{\text{A}}{\text{m}\ \%} \cdot f[\%]$, obtaining $-\frac{1}{3}M_{eff}(f) = -978.2\ \frac{\text{A}}{\text{m}\ \%} \cdot f[\%]$, which means again a deviation of 3.04 %.

Taking into account that we regarded a composite of $N_{inc} = 27$ inclusions with a volume of V_{sphere} for each in a total volume V, we have to consider the following fact: In this composite, one arbitrary sphere is surrounded by $(N_{inc} - 1) = 26$ other inclusions which determine demagnetization effects for this sphere in focus. Accordingly, not disregarding this detail, theoretical expectation of M_{eff} for an arbitrary sphere in a composite of N_{inc} inclusions refines to

$$\begin{aligned} M_{eff} &= \frac{1}{V}\sum_{i=1}^{N_{inc}-1} p_{m,i} && (4.17) \\ &= \frac{(N_{inc} - 1) \cdot M_s^{inc} \cdot V_{sphere}}{V} && (4.18) \end{aligned}$$

with $V = N_{inc} \cdot V_{sphere} \cdot \frac{100\ \%}{f[\%]}$, we obtain

$$M_{eff} = M_s^{inc} \cdot \frac{(N_{inc} - 1)}{N_{inc}} \cdot \frac{f[\%]}{100\ \%}, \tag{4.19}$$

delivering for $N_{inc} = 27$

$$M_{eff}(f) = 2911.9\ \frac{\text{A}}{\text{m}\ \%} \cdot f[\%].$$

Comparing this with results drawn from simulations, we discover an error of only 0.77 %. For the purpose of coming closer to the limit of $N_{inc} \to \infty$, we repeat the procedure with $N_{inc} = 64$ inclusions, with the same accuracy parameters (three passes in HFSS, fourth order of ansatz functions in LTE software, maximum deviation of μ'' of 2.5 % in every frequency point of the adapation with homogeneous material). According to equation 4.19, we theoretically expect

$$M_{eff}(f) = 2976.7\ \frac{\text{A}}{\text{m}\ \%} \cdot f[\%]$$

while simulation sequence delivers no noteworthy difference to the case of $N_{inc} = 27$, as mentioned before when dealing with accuracy parameters. Two explanations for this are possible: Either the chosen parameters, namely for the mesh descretization or the order of ansatz functions, are not sufficient for smaller particles or the principly reachable accuracy limit for these methods is reached. Considering the first assumption, one has to admit that further refinement of the meshes or higher orders of ansatz function are not possible because the related memory comsumption exceeds the available RAM of 147 GB.

On the one hand, these results, which are in very good agreement with theory, proof the accuracy of the simulation, the chosen parameters and the used methods and so enforce the trustworthyness for more complicated cases. But, on the other hand, the presented simulation sequence can not be compared with experiments or analytic computations, in which the *external* field remains constant for different volume fractions of magnetized material and a possible shift of resonance is analyzed. In the above described simulation runs, external field was involuntarily decreased by maintaining the input parameter H_{inc} constant, while M_{eff} increased with volume fraction. Consequently, the question for a possible shift of the resonance frequency under experimental conditions is not answered so far. For that purpose, we remember that resonance frequency for spherical samples is determined by the effective static field acting on them, which corresponds to H_{eff} in this case. Moreover, in case of infinite samples, this value is identical with an externally applied field. Following, we have to include a correction $corr(f)$ of our parameter as function of filling factor according to

$$H_{ext} = H_{eff} = H_{inc} + \frac{1}{3}\left(M_s^{inc} - M_{eff}(f)\right) + corr(f) \overset{!}{=} const. \tag{4.20}$$

From this, we conclude

$$corr(f) = \frac{1}{3}M_{eff}(f) \tag{4.21}$$

in order to keep the externally applied or effective field constant for all volume fractions. We will refer to examinations of the influence of different filling factors under a constant external or effective field by $H_{eff} = const.$, in the following, while $H_{inc} = const.$ labels analysis with a constant internal magnetic bias in the inclusions. According to previous thoughts, this constant effective field amounts

$$H_{ext} = H_{eff} = H_{inc} + \frac{1}{3}M_s^{inc} = 283\ 952\ \frac{\mathrm{A}}{\mathrm{m}} \tag{4.22}$$

and causes the resonance frequency of an isolated sphere in a non-magnetic environment to occur at $\nu = 10$ GHz, as mentioned before. For drawing conclusions on the behavior of infinitely extended composite material, we use the same device geometries as in the previous simulation sequence, choose $corr(f)$ according to equation 4.21 and eliminate geometry dependence again by comparing with a homogeneous sample, in which we define an *internal* magnetic bias of $H = \frac{2\pi}{\gamma} 10\ \mathrm{GHz} = 283\ 952\ \frac{\mathrm{A}}{\mathrm{m}}$, which also causes the resonance to occur at 10 GHz in an infinite sample. Accordingly, detected deviations of the resonance frequency of the homogeneous material from 10 GHz only appear due to the finite sample size. Within this, effective magnetization of the homogeneous device is chosen according to the determined values in the first simulation sequence (data in figure 4.27). In case that resonance frequency of the composite shifts as a function of filling factor f, the results of composite material and so-defined homogeneous media should differ. The obtained results are shown in figures 4.28, 4.29 and 4.30, showing again very good agreement of the corresponding graphs. Summarizing, resonance frequency is not shifted in the physical scenario presented in this chapter.

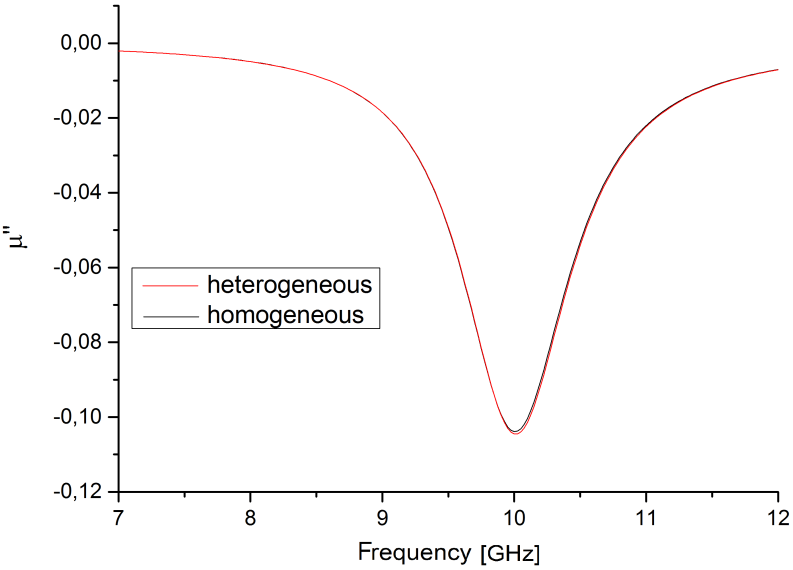

Figure 4.28 – *The comparison of the results for a composite and a homogeneous sample for the volume fraction of* $f = 1\ \%$ *shows good accordance for the chosen parameter, indicating the resonance frequency to be independent on the filling factor in this case. The case of* $H_{eff} = const.$ *is examined.*

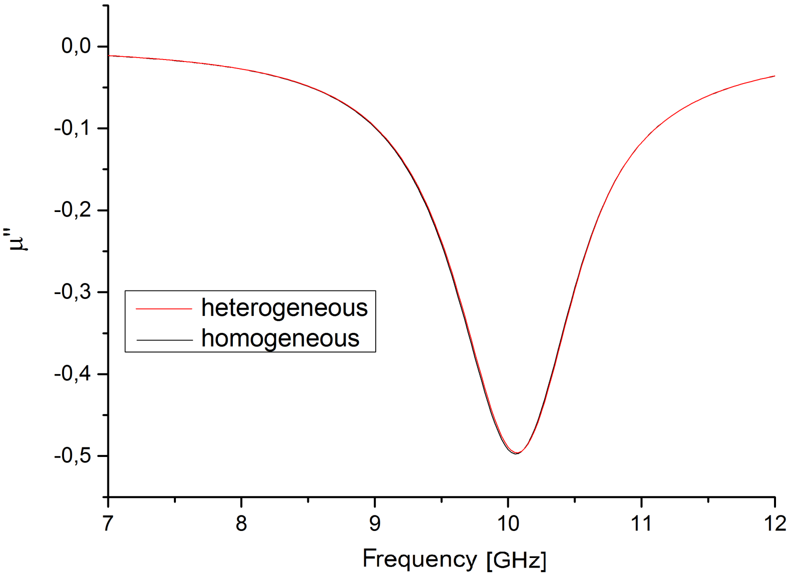

Figure 4.29 – *The same comparison with* $H_{eff} = const.$ *as in figure 4.28 is done for a filling factor of* $f = 5\ \%$*, which also shows very good agreement.*

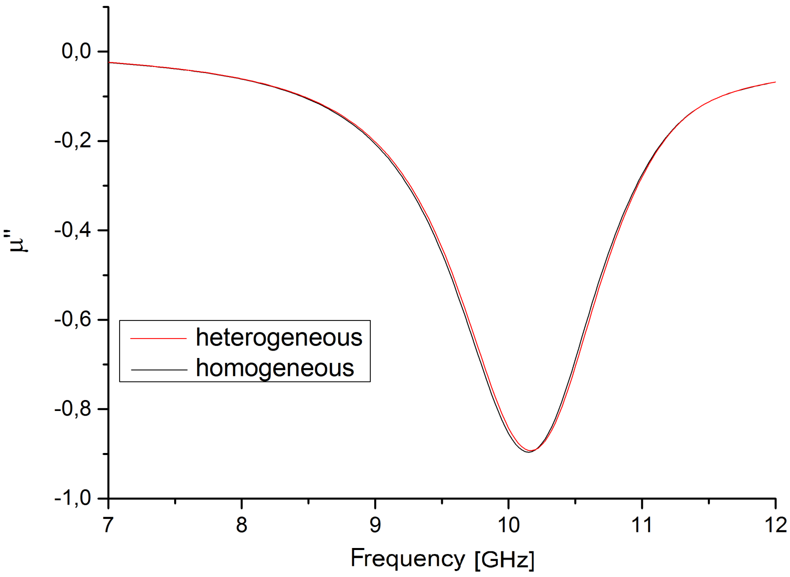

FIGURE 4.30 – *Even for an inclusion volume fraction of* $f = 10\ \%$*, no remarkable shift between the resonance frequencies of the heterogeneous and the homogeneous device occurs when* $H_{eff} = const.$ *is valid. Deviation from* 10 *GHz is a result of the finite sample size in the waveguide and according demagnetization effects.*

Additionally, we also want to analyze the behavior of the strength of the resonance peak $|\mu''_{max}|$ in dependence of the volume fraction for infinitely extended materials. In this case, we have shown that our composites would behave according to the Polder model, when we insert the previously gained values $H_{eff} = \frac{2\pi}{\gamma} 10\ \text{GHz} = 283952\ \frac{\text{A}}{\text{m}} = const.$ and $M_{eff}(f)$ for every filling factor. Accordingly, we can calculate the values of $|\mu''_{max}(f)|$ with the help of equation 1.170 and obtain the data plotted in figure 4.31.

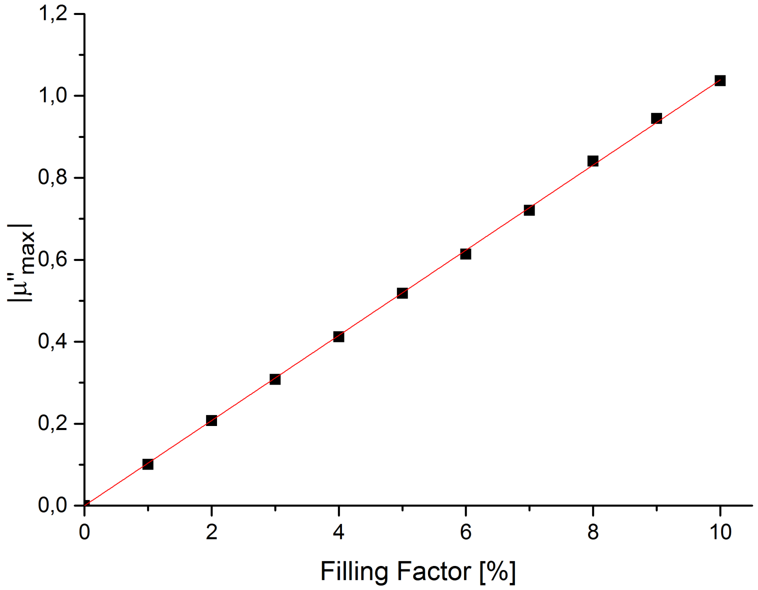

FIGURE 4.31 – *The calculated values for* $|\mu''_{max}|$ *are plotted for every filling factor* f *and linear fitted. Here, the case of* $H_{eff} = const.$ *for every filling factor is analyzed.*

Linear fitting with the help of OriginLab delivers

$$|\mu''_{max}| = \frac{(0.1039 \pm 3 \cdot 10^{-4})}{\%} \cdot f[\%]. \tag{4.23}$$

In order to explain this result, we analyze equation 1.170 for an infinitely extended material (i.e. $n_x = n_y = n_z = 0$), insert $\omega = \omega_0$ and separate into real and imaginary parts for the purpose of finding an expression for μ''_{max}. Accordingly, we find

$$|\mu''_{max}| = \frac{\omega_m}{2\alpha\omega_0} \tag{4.24}$$

$$= \frac{M_{eff}}{2\alpha H_{eff}}. \tag{4.25}$$

Using the determined linear relation 4.13 for $M_{eff}(f)$ and the constant values of H_{eff} and α, we calculate

$$|\mu''_{max}| = \frac{(0.1033 \pm 3 \cdot 10^{-4})}{\%} \cdot f[\%] \tag{4.26}$$

in good agreement with the result in equation 4.23, which is not surprising due to the calculation of all results with the same equation (1.170).
Moreover, we are also interested in the low frequency permeability $\mu'_{stat} = \lim_{\omega \to 0} \mu'$ for different volume fractions. Firstly, we want to check if our parameters from the adaptions of the resonance peak in the case of $H_{inc} = const.$ (see figures 4.24-4.26) also reproduce the values of μ' for all frequency points, which is shown in figures 4.32 and 4.33.

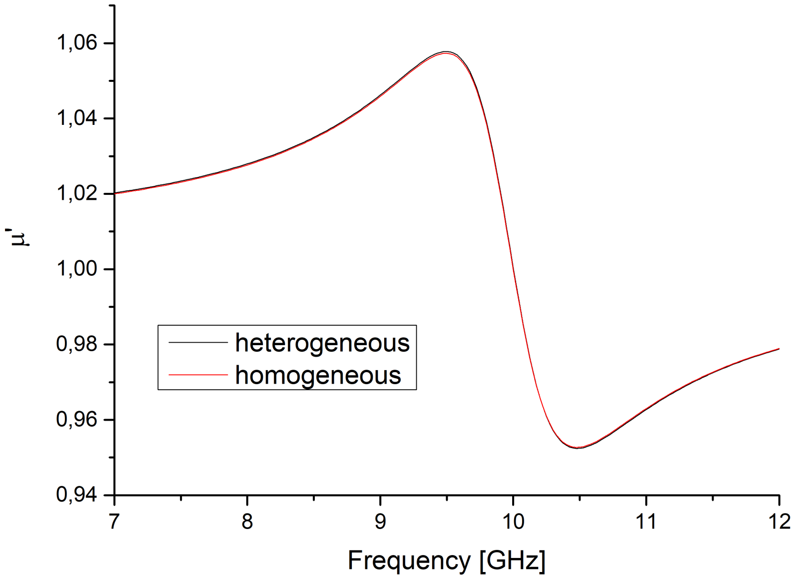

FIGURE 4.32 – *The behavior of μ' for the composite with the same input parameters as before and a volume fraction of $f = 1$ % is well reproduced by the homogeneous sample. Here, the case of $H_{inc} = const.$ is analyzed. Properties of the homogeneous sample correspond to data plotted in figure 4.27.*

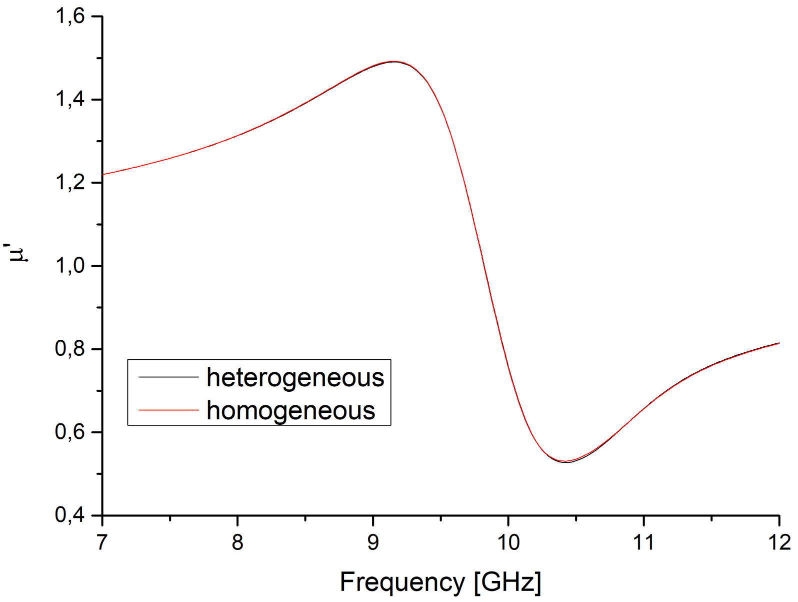

FIGURE 4.33 – *In an analogical manner to figure 4.32, a composite with* $f = 10$ % *is examined.*

Obviously, this is fulfilled with high accordance. In order to analyze μ'_{stat} in the case of $H_{eff} = const.$, we use again the found parameters of H_{eff} and $M_{eff}(f)$ and calculate the desired magnitudes with equation 1.170. Corresponding results are shown in figure 4.34.

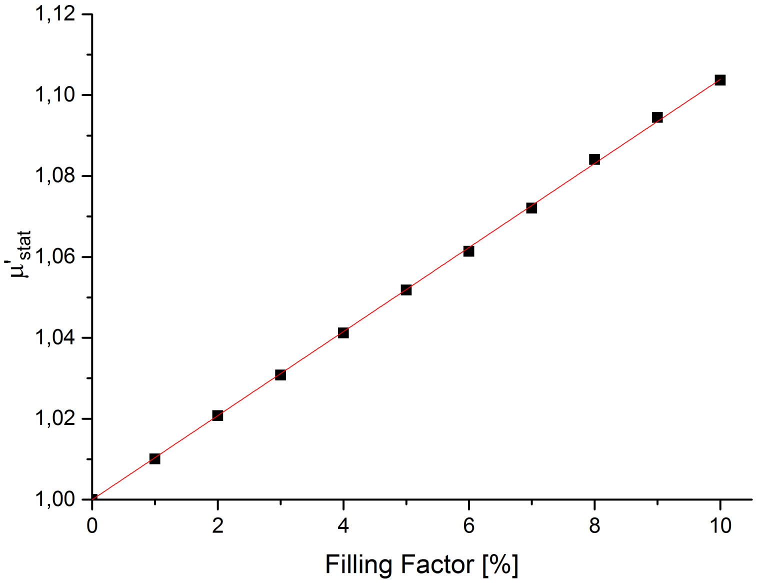

FIGURE 4.34 – *The low frequency values of* μ'_{stat} *are calculated and linear fitted. Here, the case of* $H_{eff} = const.$ *for every filling factor is analyzed.*

Again, we linear fit these data and obtain

$$\mu'_{stat} = 1 + \frac{(0.01039 \pm 3 \cdot 10^{-5})}{\%} \cdot f[\%] \tag{4.27}$$

As before, we take a deeper look at equation 1.170 and regard the limit for an infinitely extended material

$$
\begin{aligned}
\mu'_{stat} &= \lim_{\omega\to 0} \mu' && (4.28)\\
&= 1 + \frac{\omega_m}{\omega_0} && (4.29)\\
&= 1 + \frac{M_{eff}}{H_{eff}}. && (4.30)
\end{aligned}
$$

Inserting relation 4.13 and the constant value of H_{eff}, we find

$$\mu'_{stat} = 1 + \frac{(0.01033 \pm 2\,\cdot\,10^{-5})}{\%}\,\cdot\, f[\%] \qquad (4.31)$$

which is again in very good accordance with equation 4.27 due to the same reason as it was the case for the values of $|\mu''_{max}|$.

4.2.2 Conclusions

Although the presented results are mainly conventional theoretical issues, as demagnetizing effects of spheric samples, we can draw important and interesting conclusions out of this chapter:

First of all, the good agreement with analytic theory and consistence of the results enforce reliance on them and deliver a powerful tool in order to examine more complicated cases by generating microstructures randomly and switch on more interactions, as dipole-dipole coupling between inclusions.

Secondly, it has been shown that an almost perfect equivalence between composite and homogeneous material with regard to their resonance curves is valid in these finite-element-simulations (see figures 4.24-4.26, 4.28-4.30 and 4.32-4.33). It has to be highlighted that the given equation,

$$H_{eff} = H_{inc} + \frac{1}{3}(M_s^{inc} - M_{eff}), \qquad (4.32)$$

is only used as a mean field approach concerning composite materials in analytic calculations. By this, you treat the regarded sphere as embedded in a homogeneous medium with magnetization M_{eff}, ignoring the heterogeneous structure consisting out of further inclusions in the host matrix (see figure 4.35). Here, by obtaining almost identical permeabilities for composites and equivalent homogeneous material in simulations, which do not disregard local material distribution, and the found linear fitted data in figure 4.27, we showed that equation 4.32 is actually accurate in the considered case of inclusions on a simple cubic lattice.

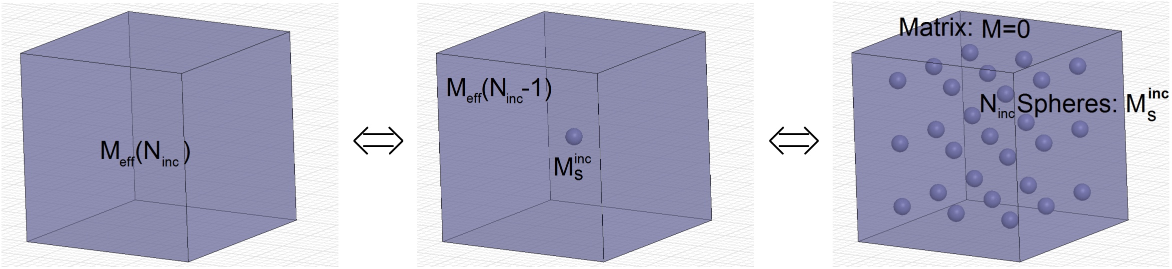

FIGURE 4.35 – *As shown by simulations, the three cases do not differ significantly: Despite spatial resolution in our simulations, it does not matter if we regard a homogeneous medium with an effective magnetization according to N_{inc} distributed spheres (left), an isolated sphere embedded in an effective medium whose magnetization, regarded as homogeneously distributed, is arised by $N_{inc} - 1$ spheres (middle) or a composite with N_{inc} inclusions located on a simple cubic lattice (right).*

Thirdly, we gain insight into the behavior of the effective field in the sample, determining resonance frequency, under different conditions. In the case of a constant internal magnetic bias inside the inclusions ($H_{int} = const.$), H_{eff} decreases with rising filling factor (as shown in figure 4.27). This phenomenon can be easily understood by taking into account that internal fields inside magnetic materials, in this case H_{int}, are always weakened compared to the fields in a surrounding non-magnetic medium. Accordingly, the effective field in the whole sample of Volume V, defined as the spatial mean value of the local fields

$$H_{eff} = \langle H(\mathbf{x}) \rangle = \frac{1}{V} \int_V H(\mathbf{x}) \mathrm{d}V, \tag{4.33}$$

shrinks when increasing volume fractions are occupied by the defined value of H_{int}. But actually, in the work of V. Bregar in 2004 [36] (see chapter 2.1) and in real experiments, the externally applied magnetic field is maintained for different volume fractions. For the purpose of comparing the corresponding outcomes to the ones of this work, we have to convert our results with regard to demagnetization effects by equation 4.20. Thereby, we achieve data which can be assigned to measurements performed with a constant externally applied field, which equals the effective field in infinitely extended samples. For this case, resonance frequency of the composite does not shift compared to homogeneous material (see accordance of both curves in figures 4.28-4.30 and note deviations of resonance from 10 GHz to be a consequence of the device geometry) and $|\mu''_{max}|$ and μ'_{stat} are analyzed (see figures 4.31 and 4.34).

Summarizing, in the considered case of irrelevant dipolar interactions between inclusions in an infinitely extended sample ($n_x = n_y = n_z = 0$), we can calculate the effective permeability tensor out of the inclusion material parameters (M_s^{inc} and α), the effective field H_{eff}, which corresponds to the externally applied field, and the filling factor f by inserting

$$\omega_m = \gamma M_{eff}(f) = \gamma M_s^{inc} \cdot \frac{f[\%]}{100} \tag{4.34}$$

$$\omega_0 = \gamma H_{eff} \tag{4.35}$$

into Polder's formula (see equations 1.169-1.171), while for damping parameter α, the inclusion material value is used.

4.3 Randomly Distributed Inclusions

4.3.1 Static Field Calculations

4.3.1.1 Previous Considerations

The next step in order to increase complexity is to distribute inclusions in a randomly manner in the host matrix and thereby switching on the dipole-dipole interaction between them. As already mentioned, the orientation of the numerous inclusions' magnetic moments in the equilibrium state has to be computed in a static magnetic simulation, which is done before the mesh generation in HFSS and the simulation run in MOR. The corresponding model is described in section 3.2.3. According to the prior examinations, we again use a saturation magnetization of $M_s^{inc} = 302\ 394.5\ \frac{\mathrm{A}}{\mathrm{m}}$ and an internal magnetic bias, which initially points along $z-$ direction and causes the resonance of a spherical, isolated inclusion to occur at $\nu_{res} = 10$ GHz ($H_{inc} = 183\ 154\ \frac{\mathrm{A}}{\mathrm{m}}$ for every filling factor). The simulation then calculates the equilibrium orientation of the magnetic moments, which are exposed to the dipolar fields of the surrounding inclusions.

Before presenting further results, we want to highlight the fundamental assumptions which form the basis of this procedure and analyze their influence. First of all, the model described in section 3.2.3 assumes the internal magnetic field at the midpoint of an inclusion as the magnitude of a homogeneous field in the whole sphere volume, which is actually an approximation in order to reduce numerical effort. In the limit of high inclusion numbers and corresponding small diameters, the influence of this simplification disappears, but in the case of low numbers of inclusions, it should be analyzed in order to guarantee the validity of our results. For this purpose, we generate samples with $N_{inc} = 27$ or $N_{inc} = 64$ inclusions, whose positions are stochastically varied until the distribution of the spheres' midpoints field reproduces the unambiguous large system limit of $N_{inc} \to \infty$ with a given accuracy. The technical details of this procedure are described later (in section 4.3.1.2). Afterwards, the calculation of the magnetic moments' static orientation is performed in these composites as described before. Then, the $z-$component of the internal local field is evaluated at 1 000 randomly distributed points inside every single sphere and the resulting distribution, especially the mean value of the internal fields and its standard deviation are compared to the internal field at the midpoint of the inclusion. This is done for a filling factor of $f = 1\ \%$ and $f = 10\ \%$ with a constant value of H_{inc} and inclusion numbers of $N_{inc} = 27$ and $N_{inc} = 64$ (see figures 4.36-4.47) in the case of $H_{inc} = const.$ for every filling factor.

Moreover, we also compare the gained data to the results when the same number of inclusions is distributed in the host matrix in a purely random manner, instead of using the arranging scheme decribed in section 4.3.1.2.

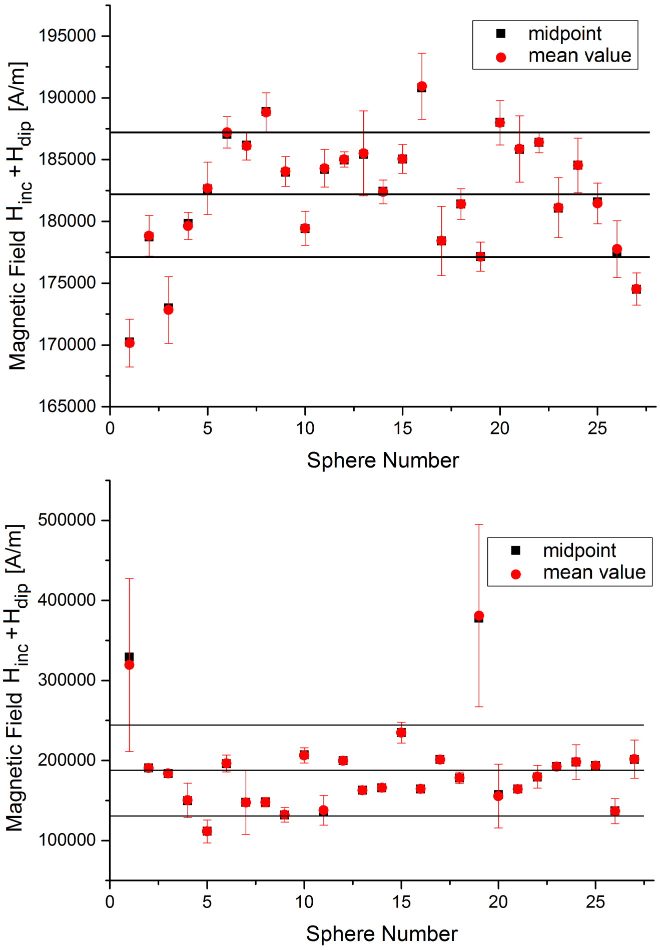

FIGURE 4.36 – *The averaged $z-$component of the magnetic field inside the different inclusions (red circles), the corresponding standard deviation of the field distribution (indicated by red error bars) and the internal magnetic field's $z-$components at the midpoints (black squares) are plotted for each of the $N_{inc} = 27$ inclusions. The middle black line marks the average $z-$component of the magnetic field at the inclusions' midpoints and the both outer inclose the area within one standard deviation of all inclusions' midpoint fields' $z-$component. Material parameters are the same as before. Here, the case of an filling factor of $f = 1$ % is examined. While the top picture shows results for the arranging strategy of section 4.3.1.2, the picture in the bottom shows the same outcomes for a purely random distribution. Note the different scaling of the magnetic field axis.*

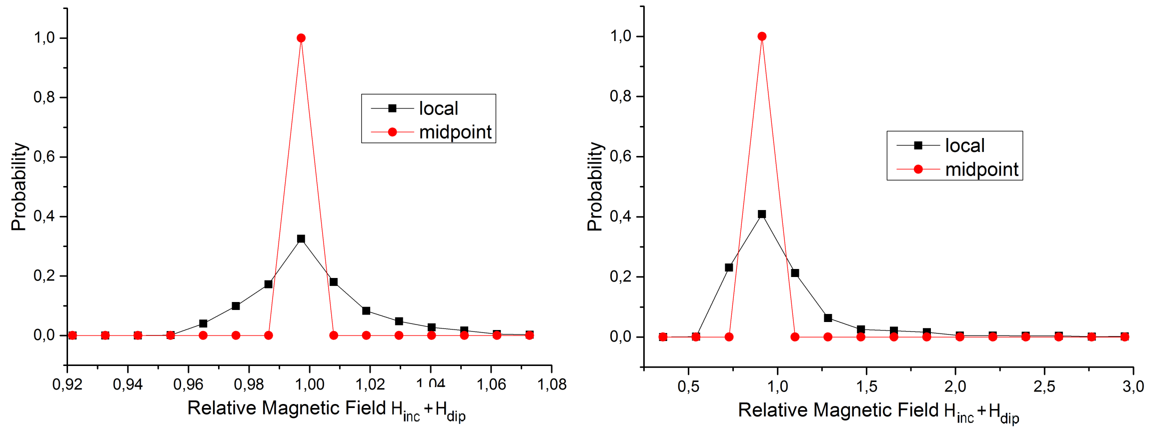

FIGURE 4.37 – *The probability distribution of the different internal magnetic field $z-$component values for one single sphere of the composite of $N_{inc} = 27$ inclusions is plotted against the relative magnetic field (field values divided by their mean value). In this figure, we regard the inclusions with the highest standard deviation of the magnetic field at the $1\ 000$ internal points which is sphere number 13 in the case of the proposed arranging strategy (left) and sphere number 19 for the random insertion (right, see also red error bars in figure 4.36). Black squares denote the distribution of the $1\ 000$ evaluated values inside the sphere while the red circles show the peaked distribution when assuming the magnetic field as homogeneous with the value at the center for the whole inclusion. Here, a composite with a volume fraction of $f = 1\ \%$ is regarded. Material parameters are the same as before. Note the different scaling of the relative magnetic field axis.*

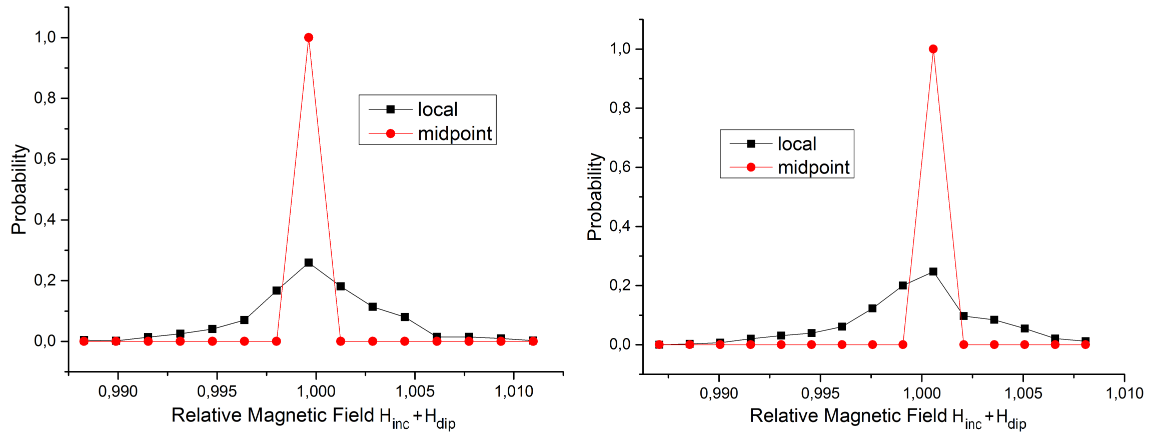

FIGURE 4.38 – *The same analysis as in figure 4.37 is done, but for the inclusions with the lowest standard deviation of the magnetic field at the $1\ 000$ internal points. In both cases (proposed arranging strategy left, random insertion right), sphere number 12 is regarded (see also red error bars in figure 4.36).*

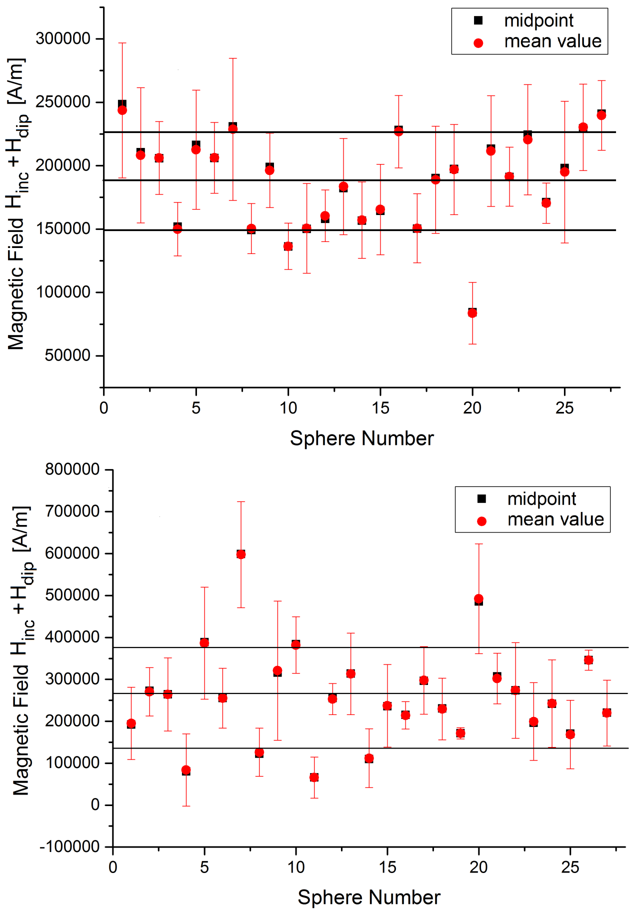

FIGURE 4.39 – *The same analysis as in figure 4.36 is done for a volume fraction of* $f = 10$ %. *Again, the picture at the top shows the results for the proposed arranging procedure while the picture at the bottom shows data for the purely random inclusion insertion. The magnetic field axes are differently scaled, as before.*

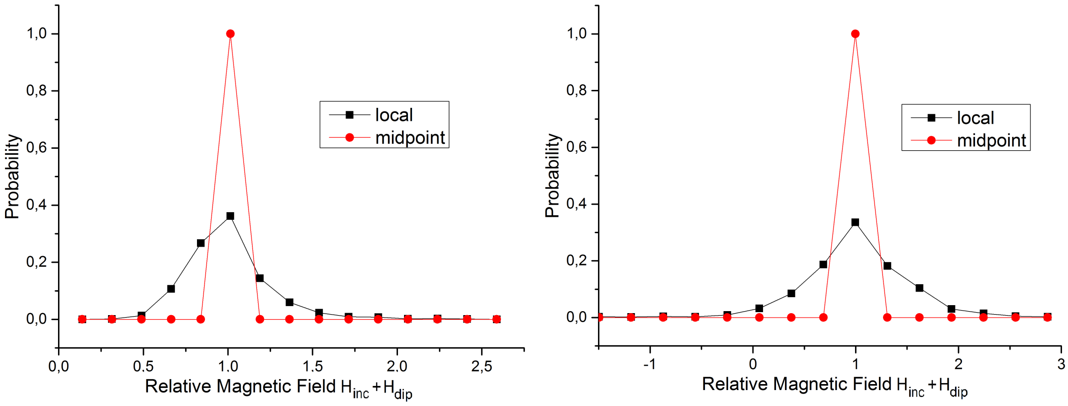

FIGURE 4.40 – *Again, we regard the spheres with the highest standard deviation concerning the internal field distribution as in figure 4.37, but for a filling factor of* $f = 10$ %. *Left side shows sphere number* 7 *for the proposed arranging method, right side sphere number* 9 *for the randomly inserted inclusions (see also red error bars in 4.39).*

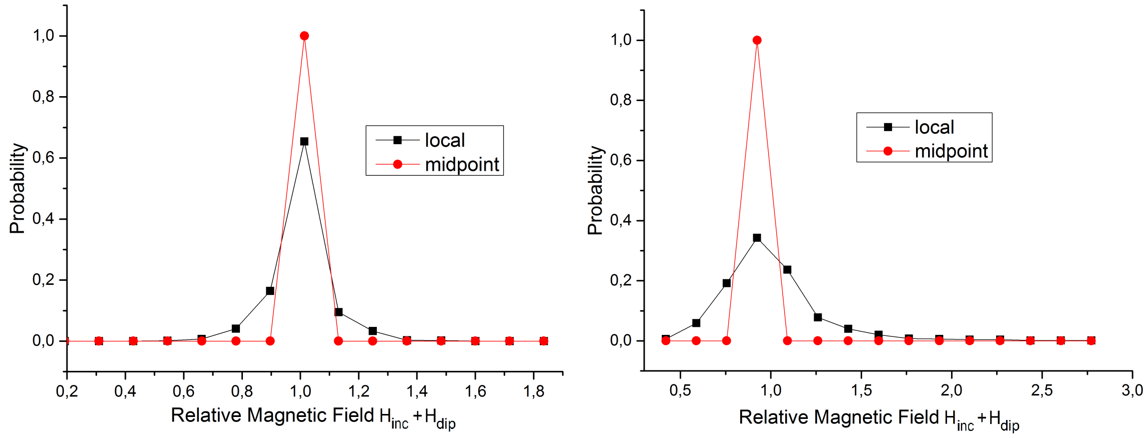

FIGURE 4.41 – *In this figure, we regard the spheres with the lowest standard deviation concerning the internal field distribution as in figure 4.38, but for a filling factor of* $f = 10\ \%$. *Left side shows sphere number* 24 *for the proposed arranging method, right side sphere number* 19 *for the randomly inserted inclusions (see also red error bars in 4.39).*

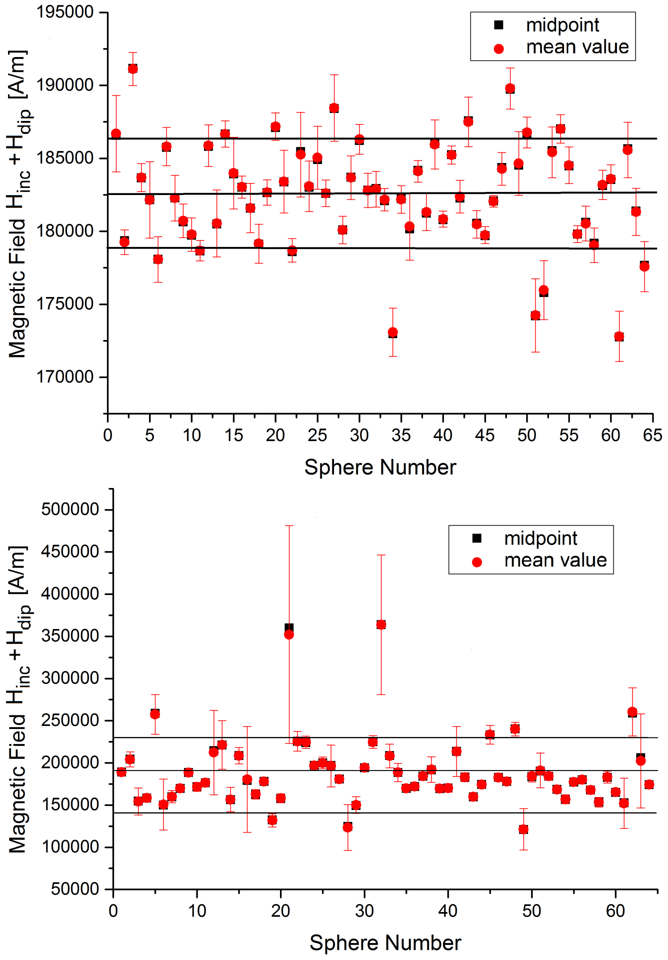

FIGURE 4.42 – *The same data as plotted in picture 4.36, but for* $N_{inc} = 64$ *inclusions. Filling factor amounts* $f = 1\ \%$. *Again, top picture shows results for the proposed arranging method, down picture shows data for the random insertion of spheres. Note the different scaling of the the magnetic field axes.*

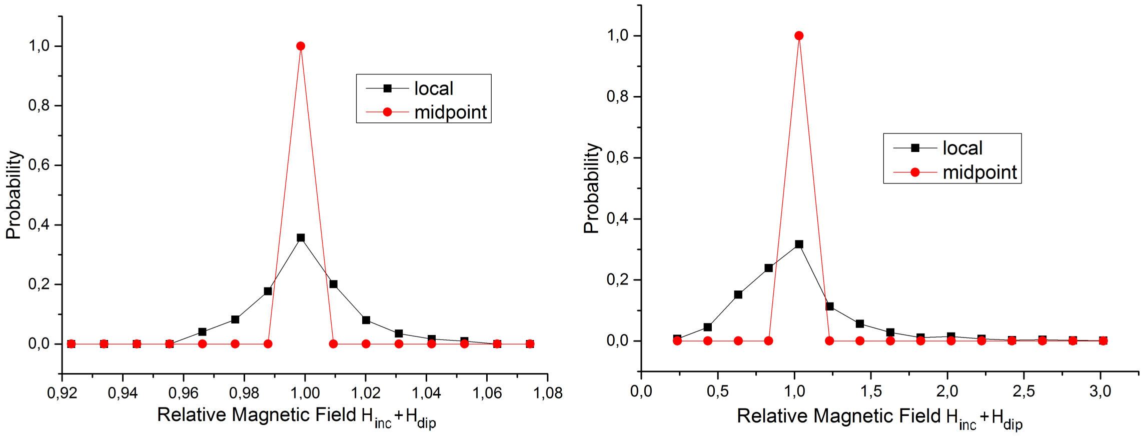

FIGURE 4.43 – *The same distribution as in figure 4.37 is shown for single spheres in a composite with* $N_{inc} = 64$ *inclusions and an inclusion volume fraction of* $f = 1$ %. *Again, we regard the inclusions with the highest standard deviation of the magnetic field at the* 1 000 *internal points. This is sphere number* 23 *in the case of the proposed arranging strategy (left) and sphere number* 21 *for the random insertion (right, see also red error bars in figure 4.42)*

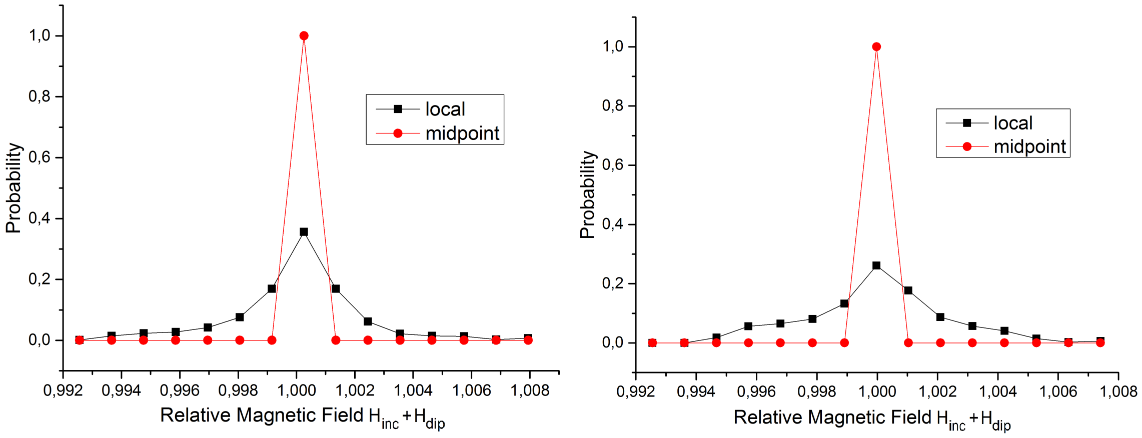

FIGURE 4.44 – *The same distribution as in figure 4.38 is shown for single spheres in a composite with* $N_{inc} = 64$ *inclusions and an inclusion volume fraction of* $f = 1$ %. *Again, we regard the inclusions with the lowest standard deviation of the magnetic field at the* 1 000 *internal points. This is sphere number* 46 *in the case of the proposed arranging strategy (left) and sphere number* 9 *for the random insertion (right, see also red error bars in figure 4.42)*

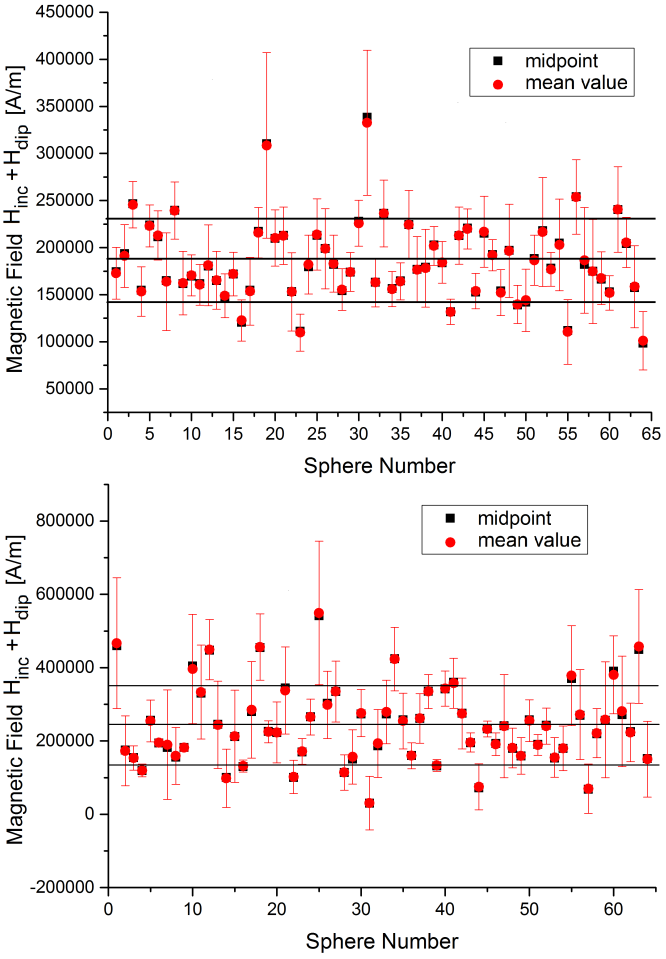

FIGURE 4.45 – *The same data as plotted in figure 4.39, but for* $N_{inc} = 64$ *inclusions. Filling factor amounts* $f = 10$ %. *Again, top picture shows results for the proposed arranging method, down picture shows data for the random insertion of spheres.*

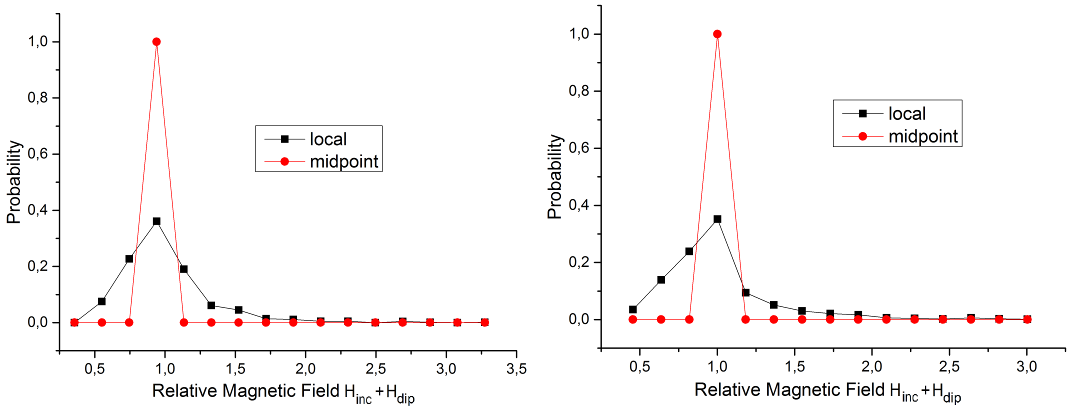

FIGURE 4.46 – *The same distribution as in figure 4.40 is shown for single spheres in a composite with* $N_{inc} = 64$ *inclusions and an inclusion volume fraction of* $f = 10$ %. *Again, we regard the inclusions with the highest standard deviation of the magnetic field at the* 1 000 *internal points. This is sphere number* 19 *in the case of the proposed arranging strategy (left) and sphere number* 25 *for the random insertion (right, see also red error bars in figure 4.45).*

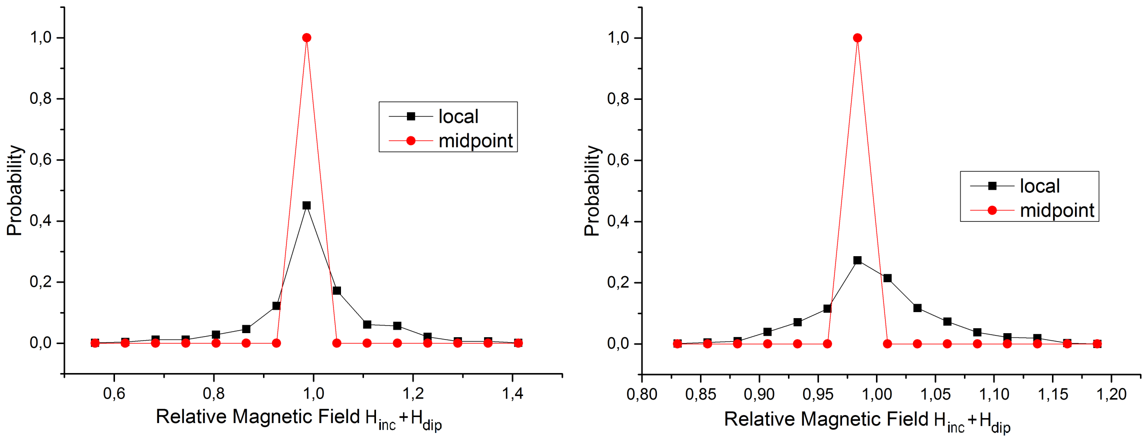

Figure 4.47 – *The same distribution as in figure 4.41 is shown for single spheres in a composite with* $N_{inc} = 64$ *inclusions and an inclusion volume fraction of* $f = 10\ \%$. *Again, we regard the inclusions with the lowest standard deviation of the magnetic field at the* 1 000 *internal points. This is sphere number* 41 *in the case of the proposed arranging strategy (left) and sphere number* 6 *for the random insertion (right, see also red error bars in figure 4.45)*

Through this analysis, several things become clear concerning the results for the proposed arranging strategy. First of all, the value of the magnetic field at the center of the spheres is always very close to the mean value of the fields at the 1 000 points distributed inside the sphere (compare positions of the red circles and black squares in figures 4.36, 4.39, 4.42 and 4.45). Secondly, the inner-sphere field distributions are quite symmetric (see distributions in the left sides of 4.37, 4.38, 4.40, 4.41, 4.43, 4.44, 4.46 and 4.47) and sharp compared to the field fluctuations between different inclusions (compare length of the red error bars to distance between black lines in 4.36, 4.39, 4.42 and 4.45) in all cases. Furthermore, it is obvious that the averaged standard deviations of the inner field distributions increase from $f = 1\ \%$ to $f = 10\ \%$ (see table 4.1), which is a result of the reduced distance and the thereby enforced interaction between single inclusions. Naturally, this effect will increase for higher package densities of inclusions. Accordingly, the assumption of a homogeneous magnetic field inside the sphere is only justified in the case of low volume fractions of well distributed inclusions. When comparing these results with the purely randomly generated microstructures, we notice the following aspects: Firstly, the midpoint field values are still very close to the mean values of the fields in the sphere, but the symmetry of their distribution is a little bit disturbed (compare left and right side of figure 4.46, for example). Most importantly, the field fluctuations inside single spheres and between the midpoints of different spheres (values of $\langle\sigma\rangle_{inc}$ and σ_{mid} in table 4.1) strongly increase compared to the values connected with the proposed arranging method. In contrast, these values decrease for higher inclusion numbers. Consequently, the inserting strategy described in section 4.3.1.2 is confirmed as a powerful tool in order to come closer to the behavior in the large system limit of $N_{inc} \to \infty$ without increasing the number of included spheres.

	$f = 1$ %				$f = 10$ %			
	$N_{inc} = 27$		$N_{inc} = 64$		$N_{inc} = 27$		$N_{inc} = 64$	
	arr.	rand.	arr.	rand.	arr.	rand.	arr.	rand.
$\langle \sigma \rangle_{inc}$ in $\frac{\text{A}}{\text{m}}$	1 737	18 905	1 383	14 533	33 925	35 156	32 511	78 853
σ_{mid} in $\frac{\text{A}}{\text{m}}$	4 955	56 001	3 680	42 168	38 077	116 997	42 508	107 646

TABLE 4.1 – *The standard deviation of the field distribution in a single inclusion, averaged over all spheres, $\langle \sigma \rangle_{inc}$ is always smaller than the standard deviation σ_{mid}, which describes the distributions of the middle point fields in all inclusions. Columns "arr." denote results for the proposed arranging strategy while columns "rand." denote data for the randomly generated microstructures. All values increase for denser systems.*

A further aspect of the model which should be highlighted is that the inclusion-induced magnetic fields are assumed as purely dipolar fields from pointlike sources. Exact calculations would require the additional consideration of higher moments which are homogeneously distributed in the spherical volume of the inclusions. Concerning higher moments, it was shown in [40] that they can be neglected for volume fractions up to $f = 10$ %, as it is the case in this work. The aspect of a spatial distribution of the magnetic sources will be analyzed in the following by comparing the resulting fields when considering only one pointlike source with an arrangement of $n_{sub} = 7$, $n_{sub} = 33$ or $n_{sub} = 87$ pointlike and parallely aligned dipolar moments for one single sphere, schematically shown in figure 4.48. For the purpose of analyzing the resulting fields of this single, but maybe subdivided, sphere, moments are aligned along $z-$direction and the $z-$component of the resulting field is calculated on a perpendicular axis through the center of the initial (red) sphere. The orientation of this axis in the $x-y$-plane does not influence the results due to the rotational symmetry of the dipolar fields and the considered arrangements of the magnetic moments. Corresponding results are shown in figures 4.49-4.52.

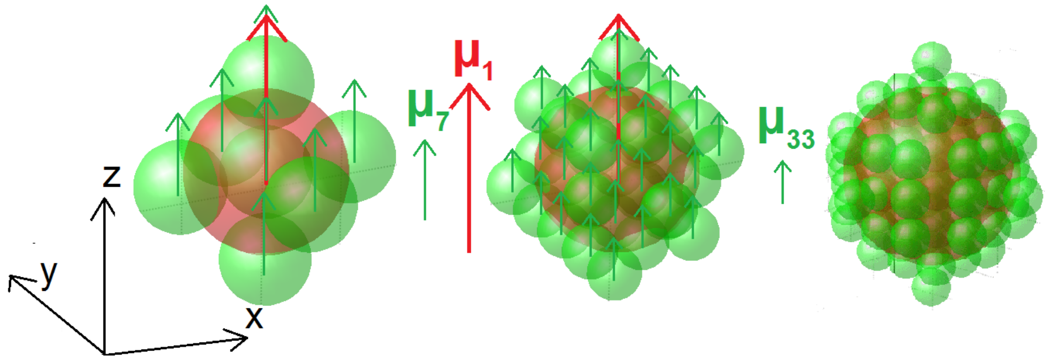

FIGURE 4.48 – *The magnetic dipolar field of one inclusion (red sphere with magnetic moment μ_1) is assumed as caused by seven (left), 33 (middle) or 87 magnetic dipoles (right), indicated by the green spheres. The corresponding results are compared to the case when magnetic moment is assumed to be caused by a pointlike source at the red sphere's midpoint. In the case of $n_{sub} = 87$, arrows are omitted in order to improve clarity. The sum of the magnetic moments of the four different formations are kept constant as indicated by the maintained total volume.*

Although only one single sphere, no complete composite, is examined, positions at which fields are evaluated are given in the units of the mean value of the distances between inclusions in the corresponding composite which can be calculated via

$$\overline{d}_{inc} = \left(\frac{V}{N_{inc}}\right)^{\frac{1}{3}} \tag{4.36}$$

with

$$f = \frac{N_{inc} V_{sphere}}{V} \tag{4.37}$$

$$\Leftrightarrow \; V = \frac{N_{inc} V_{sphere}}{f}. \tag{4.38}$$

In summary, we find

$$\overline{d}_{inc} = \left(\frac{V_{sphere}}{f}\right)^{\frac{1}{3}}. \tag{4.39}$$

Obviously, this value depends on V_{sphere} and, accordingly, on the regarded radius of the inclusions ($r_{inc} = 0.0445$ cm for $N_{inc} = 27$ and $r_{inc} = 0.0334$ cm for $N_{inc} = 64$). But actually, the shown results do not depend on this parameter due to the form of the magnetic dipolar fields. In order to prove this, we regard equation 3.106 and exemplarily insert $\mathbf{r}_{ij} = \overline{d}_{inc}\mathbf{x}$ and $\boldsymbol{\mu} = V_{sphere} M_s^{inc}\mathbf{z}$:

$$\begin{aligned}
\mathbf{H}_{\mathbf{dip}}(\overline{d}_{inc}) =& \frac{1}{4\pi \overline{d}_{inc}^2} \\
& \frac{3\overline{d}_{inc}\mathbf{x}(V_{sphere}M_s^{inc}\mathbf{z} \cdot \overline{d}_{inc}\mathbf{x}) - V_{sphere}M_s^{inc}\mathbf{z} \cdot (\overline{d}_{inc}\mathbf{x})^2}{\overline{d}_{inc}^3} && (4.40) \\
=& \frac{3}{4\pi \underbrace{\overline{d}_{inc}^3}_{V_{Sphere}/f}} \quad V_{sphere}\left(\mathbf{x}(M_s^{inc}\underbrace{\mathbf{z} \cdot \mathbf{x}}_{=0}) - \frac{M_s^{inc}}{3}\mathbf{z} \cdot \underbrace{\mathbf{x}^2}_{=1}\right) && (4.41) \\
=& -\frac{fM_s^{inc}}{4\pi}\mathbf{z} && (4.42)
\end{aligned}$$

Thereby, we found an expression which does not depend on the regarded inclusion sizes. Consequently, we do not have to distinguish according to this parameter.

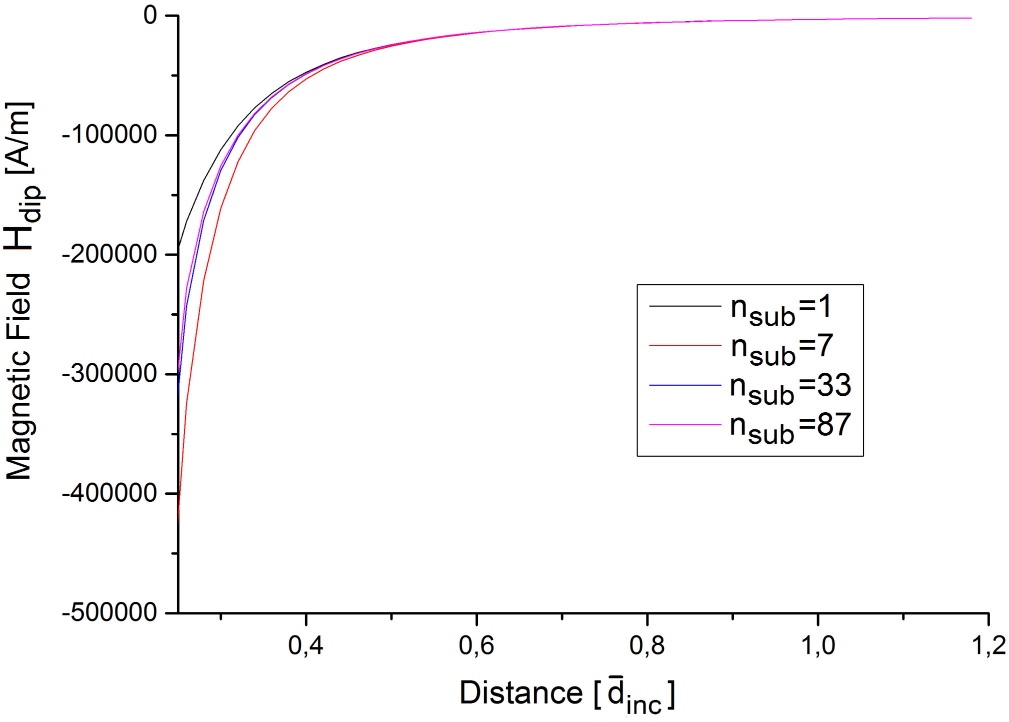

FIGURE 4.49 – *The* $z-$*component of the magnetic dipolar fields on a perpendicular axis caused by* $n_{sub} = 1,\ 7,\ 33$ *or* 87 *dipole moments, which are aligned in* $z-$*direction, are plotted in units of the mean distance between inclusions for a filling factor of* $f = 1\ \%$.

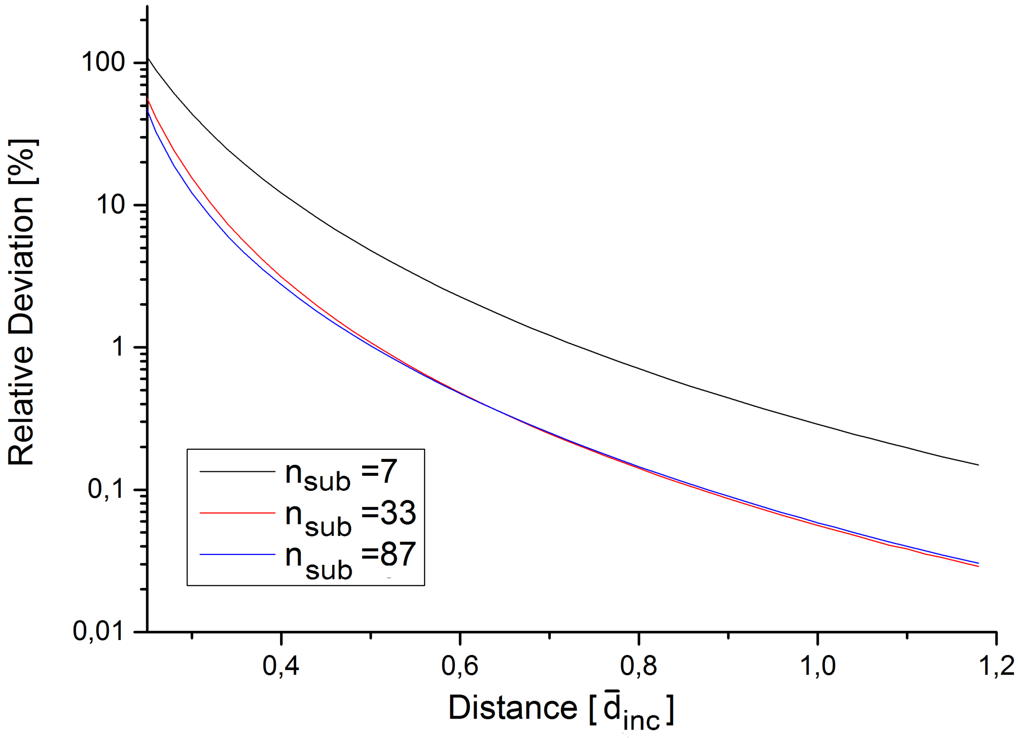

FIGURE 4.50 – *The relative deviations of the* $z-$*component of the magnetic dipolar fields with* $n_{sub} = 7,\ 33,\ 87$ *from the case with only one dipole moment are plotted for a volume fraction of* $f = 1\ \%$.

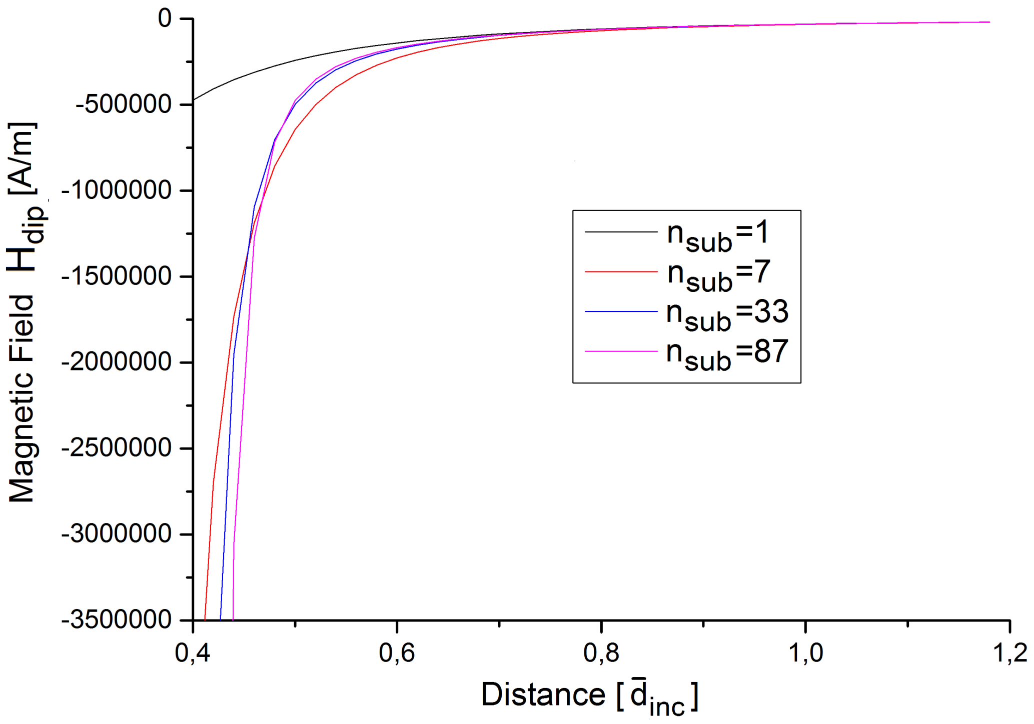

FIGURE 4.51 – *The same situation as in figure 4.49 is calculated for a volume fraction of* $f = 10$ %, *leading to a smaller mean value of the distance between the inclusions.*

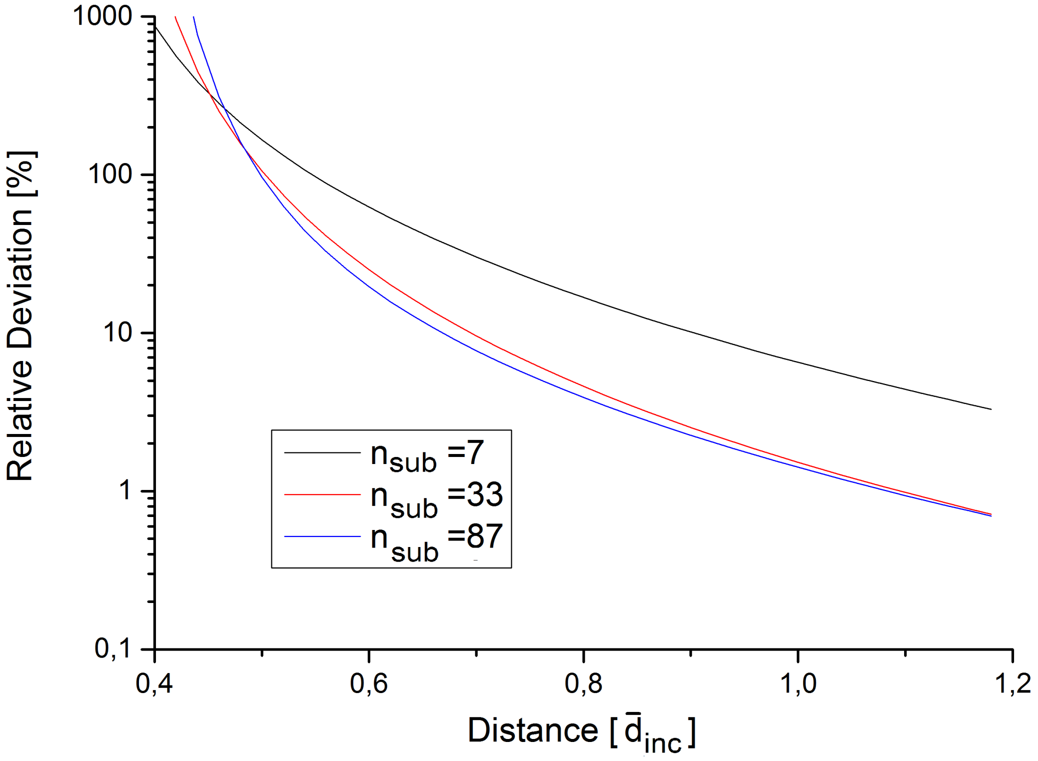

FIGURE 4.52 – *The relative deviations of* $n_{sub} = 7,\ 33,\ 87$ *from the case with only one dipole moment are plotted for a volume fraction of* $f = 10$ %.

Obviously, the cases of $n_{sub} = 33$ and $n_{sub} = 87$ do not significantly differ from each other, indicating that further subdividing of the magnetic moments is not necessary. Furthermore, deviations from the case of $n_{sub} = 1$ are smaller comparing to the results for $n_{sub} = 7$ due to the better approximation of the spherical volume. In summary, we can draw the same conclusions as before: the proposed model with a pointlike magnetic moment for every sphere is very accurate if inclusions are separated by a certain distance, but becomes more imprecise if this length is decreased. As can be seen in figures 4.50 and 4.52, relative deviations between the fields caused by one or 87 dipoles at the mean value of the distance between inclusions are in the range of 1 % or lower. Following this, the usage of the model is adequate in the case of quite homogeneous composites with low volume fractions in the range of $f = 1 \ldots 10$ %. If an extension to higher volume fractions is desired, a more accurate model, which takes into account higher ordered magnetic moments and higher resolved spatial definitions concerning field and magnetic source distribution should be used, which is unavoidably linked with higher computational effort.

Moreover, it is again important to analyze the model's convergence behavior concerning inclusion numbers and radii. For that purpose, we start with the highest volume fraction of $f = 10$ %, define a cubic sample with the same geometric extensions as used in section 4.2 and insert inclusions in a completely random manner, but with no overlapp between the spheres. For lower filling factors, we stretch the cubic matrix and the positions of the inclusions in all directions of space with the center of the sample as fixed point while the spheres' volumes are maintained. By this, a more homogeneous distribution of inclusions is produced for lower values of f comparing to a simple random insertion. With regard to the previous discussion of the error due to the pointlike magnetic moments in dependence of the distance, we firstly analyze the distribution of the spatial separation between the inclusions. For that purpose, we calculate the distance of each of the N_{inc} inclusions to every of the surrounding $N_{inc} - 1$ spheres. Then, we determine the minimum distance and the average over the distances to the six nearest neighbours (motivated by the six nearest neighbours in a simple cubic lattice). The distributions of both quantities is shown in figure 4.53.

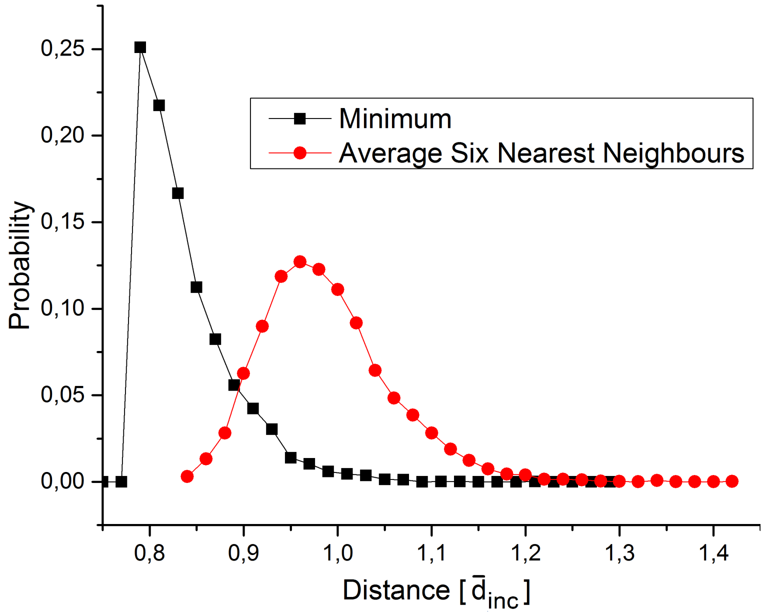

FIGURE 4.53 – *The distributions of the shortest distance between two inclusions and the average distance of the six nearest neigbours of one inclusion are plotted.*

Thereby, we obtain the peak of the minimum distance distribution at $d = 0.79 \cdot \overline{d}_{inc}$, corresponding to a relative deviation of the dipolar fields (comparing $n_{sub} = 1$ and $n_{sub} = 87$) of 0.15 % for $f = 1$ % and 3.92 % in the case of $f = 10$ % while the peak of the six nearest neighbour average is located at $d = 0.96 \cdot \overline{d}_{inc}$, meaning an error of 0.07 % for $f = 1$ % and 1.79 % for the higher packaging of $f = 10$ % (compare with relative deviations in figures 4.50 and 4.52). Accordingly, the reduction of the spatial distribution of the magnetic moments to a pointlike source will not have a great influence on our results.

In the following, we observe the trend of the internal magnetic field at the inclusions' centers, averaged over all inclusions, and its distribution in dependence of the number of inclusions. This is done for volume fractions of 1 % to 10 % and inclusion numbers (respectively radii r_{inc}) $N_{inc} = 50$ ($r_{inc} = 0.0363$ cm), $N_{inc} = 100$ ($r_{inc} = 0.0288$ cm), $N_{inc} = 500$ ($r_{inc} = 0.0168$ cm), $N_{inc} = 1\ 000$ ($r_{inc} = 0.0134$ cm), $N_{inc} = 5\ 000$ ($r_{inc} = 0.00782$ cm) and $N_{inc} = 10\ 000$ ($r_{inc} = 0.0062$ cm). Regarding the average midpoint fields, two facts are recognizable in figures 4.54 and 4.55: Firstly, the mean values of the components of the magnetic field at the inclusions' centers are almost constant and can be seen as free from artifacts due to the limited system size. Secondly, due to the strong external field in $z-$direction, the $\overline{H}_z$ component is much larger then the perpendicular components $\overline{H}_x$ and $\overline{H}_y$. Therefore, we neglect these components in the following and treat the internal fields as aligned along $z-$direction. Analyzing the values of $\overline{H}_z$ for different volume fractions and a high inclusion number of $N_{inc} = 5\ 000$, we obtain the graph shown in picture 4.56.

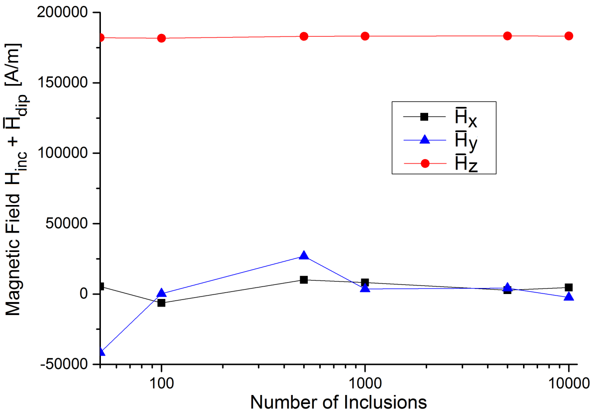

FIGURE 4.54 – *The average values of the internal magnetic field components are plotted for different numbers of inclusions and a filling factor of* $f = 1$ %.

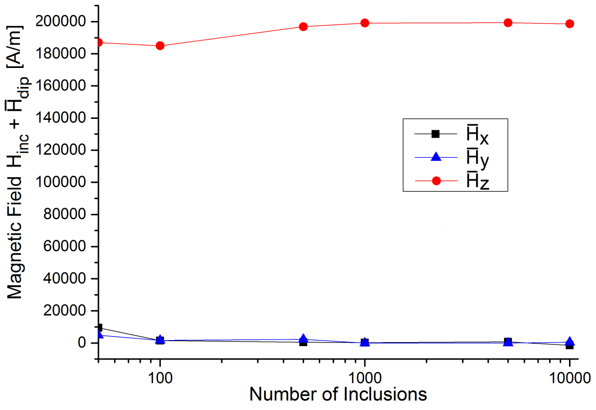

FIGURE 4.55 – *The same analysis as in figure 4.54 is done for a volume fraction of* $f = 10$ %.

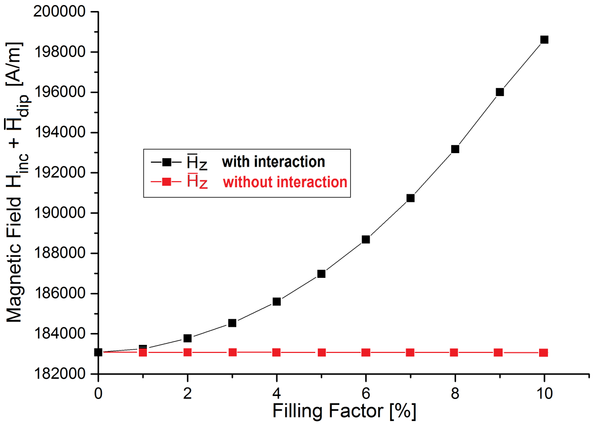

FIGURE 4.56 – *The mean value of the internal magnetic field in* $z-$*direction is plotted in dependence of inclusions' volume fraction in the sample, when dipolar interaction between randomly inserted spheres is taken into account (black squares). As it can be seen, a denser packaging of inclusions enforces the local effective field in the spheres. For the purpose of highlighting the influence of the dipolar interaction, red squares mark the corresponding field when inclusions are located on a simple cubic lattice, causing the dipolar effects to disappear (see section 4.2.1) and the field to remain constant.*

At first glance, the rising of the mean value of the fields at the positions of the inclusions seems to conflict with the requirement of self-consistency of the dipolar fields which is of vital importance in the analytic calculations in the work of [37] (see section 2.2). According to self-consistency, the average dipolar contribution to the effective field should be zero and, accordingly, a rising of the effective field in total would be an unphysical artifact of the simulation. For resolving this contradiction, we use the equilibrium configuration of systems with $N_{inc} = 10\ 000$ inclusions, calculate fields at 50 000 randomly chosen points in the devices and determine the mean values. Corresponding data is plotted in figure 4.57.

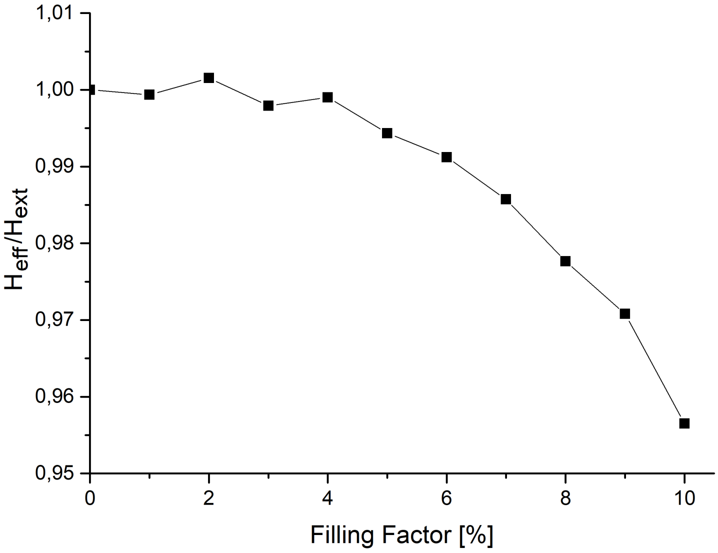

Figure 4.57 – *The effective field is calculated by averaging field values at* 50 000 *randomly chosen points for every filling factor. Afterwards, the result is divided by the value of the externally applied field. Self-consistency requires a constant value of one in this calculation.*

As it becomes obvious, the condition of self-consistency is satisfied with perturbations which are smaller than 1 % until a filling factor of $f = 7$ % is reached. For higher volume fractions, deviations grow which is caused by the discussed approximations of the simulation model, which become more inacurate for increasing values of f. Nevertheless, no unphysical artifact is included into the model.

Accordingly, the rising of the local effective field at the positions of the inclusions, shown in figure 4.56, is a consequence of the relaxation of the orientation of the magnetic moments in these simulations. During this process, magnetic moments prefer an orientation which enforce fields at the positions of the surrounding inclusions, at least in average. Consequently, the mean field at locations without inclusions decreases. In order to prove this explanation, the mean value of the magnetic field at the positions of the inclusions was also calculated without a relaxation process, meaning a strict alignment of all moments in $z-$direction. Of course, no growing of the average field was detected in this reduced model. For clarity's sake, we will refer to the local effective field at the positions of the inclusions (data in figure 4.56) in the following as H_{eff}^{loc}.

Besides the mean value of the internal field, we are also interested in its distribution, which is also examined in the range of 1 % to 10 % in dependence of the number of inclusions. The results are shown in the histogramms 4.58 and 4.59 and show convergence for $N_{inc} \geq 5\ 000$.

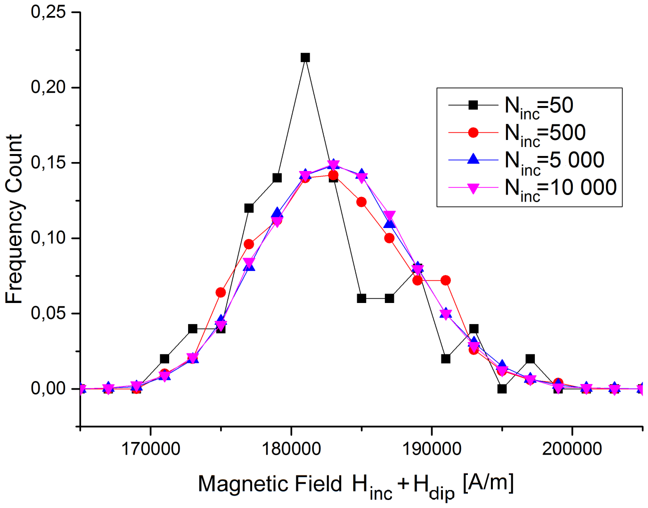

FIGURE 4.58 – *The whole distribution of the internal fields is analyzed. Comparing to the mean value, the distribution is stronger influenced by the inclusion number, but shows convergence for* $N_{inc} \geq 5\ 000$. *Dividing the different values into classes was done with the default settings of OriginLab's automatic frequency count for the highest inclusion number of* $N_{inc} = 10\ 000$. *Afterwards, these classes are used for smaller inclusion numbers. Picture shows results for a volume fraction of* $f = 1\ \%$.

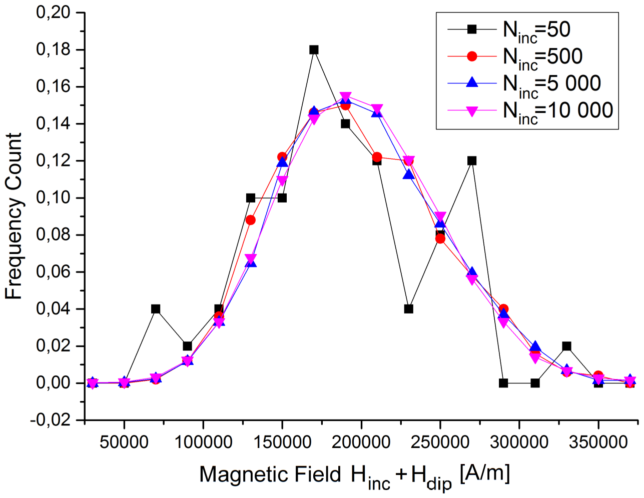

FIGURE 4.59 – *The same examination of the distribution of the magnetic fields at the inclusions' midpoints as in figure 4.58 is done for a filling factor of* $f = 10\ \%$.

In conclusion, we know the mean values and the distribution functions of the magnetic field inside the inclusion phase in the limit of an infinite system size. By the application of periodic boundary conditions in the described simulations, we found the values corresponding to an infinitely extended system.

4.3.1.2 Local Distribution of Inclusions

With this data, we now want to return to the HFSS simulations runs, in which we are again confronted with the limited memory allocation resources, allowing only inclusion numbers in the range of $N_{inc} \approx 10^1 - 10^2$. Unfortunately, convergence of the field distribution does not occur until inclusion number reached values in the range of $N_{inc} \approx 10^3 - 10^4$. Accordingly, the challenge is to find a scheme to reproduce the behavior of the large system with an inclusion number which is two orders of magnitude below. In other words: We want to find a representative system containing only few inclusions with the static characteristics occuring in the large system limit.

In order to achieve this goal, we again start with a sample with $N_{inc} = 27$ inclusions which are arranged on a simple cubic lattice, as before. Then, the positions of the inclusions are stochastically displaced until the field distributions in the limit of $N \to \infty$ (shown for $f = 1$ % and $f = 10$ % in figures 4.58 and 4.59, respectively) are reached with sufficient accuracy.

The shifting of the inclusions is done by adding a three dimensional vector to the positions of the spheres. For every inclusion, an individual vector is determined with components computed according to a random gaussian distribution with a mean value of zero and a standard deviation of $\overline{d}_{inc}/10$, where $\overline{d}_{inc}$ denotes the mean value of the distance between inclusions, which is defined in equation 4.36. Afterwards, the orientation of the magnetic moments is determined as described in section 4.3.1 and corresponding field distribution is calculated and compared to the large system limit, which was computed with $N_{inc} = 10\ 000$ inclusions. Subsequently, an error quantity Δ is defined according to

$$\Delta = \sum_{i=1}^{k} \Delta_i = \sum_{i=1}^{k} \left[\Phi_1(H_i) - \Phi_2(H_i)\right]^2 \tag{4.43}$$

where $\Phi_1(H_i)$ and $\Phi_2(H_i)$ denote the frequency count values of both distributions at the field value class of H_i (the same classes of the magnetic fields as in figures 4.58 and 4.59 are in use), meanwhile k denotes the number of classes in which the field distribution is divided. The deviations between the two distributions in the single points are squared in order to give high deviations a stronger weighting.

This procedure is repeated several times until a treshold of $\Delta_{min} = 0.005$ between the two distributions is undershot, while the mean fields, averaged over all inclusions' midpoints, do not differ more than 1 % in both cases, leading to the results for $f = 1$ % and $f = 10$ % exemplarily shown in figures 4.60 and 4.61. In these and following diagrams, the field distributions achieved according to the here presented strategy, which is based upon adding gaussianly distributed vectors to the positions of a simple cubic lattice, are labeled with “gaussian” while the distribution of composites with a purely random insertion of inclusion is denoted with “random”.

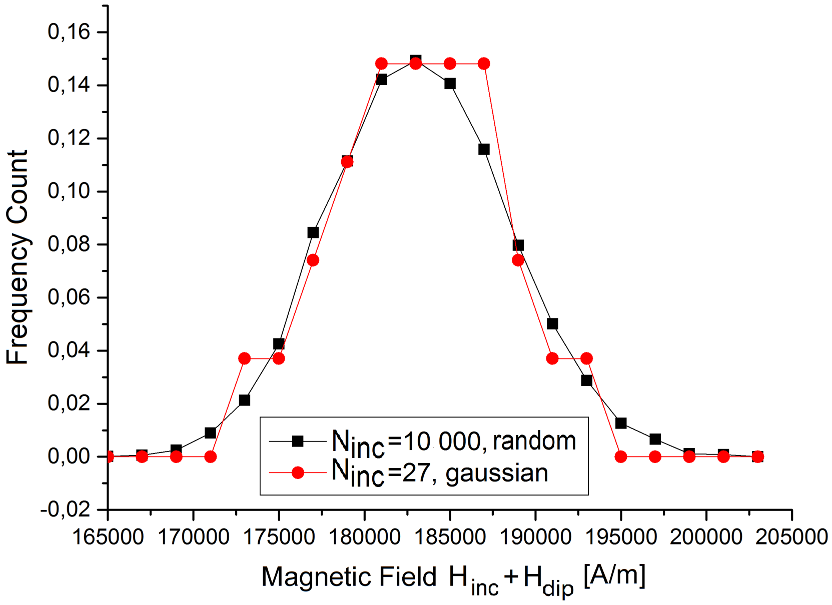

FIGURE 4.60 – *The described proceeding delivers good agreement between the both field distributions. In this histogram, a filling factor of* $f = 1$ % *is regarded, where* $\Delta = 0.0021$ *is reached.*

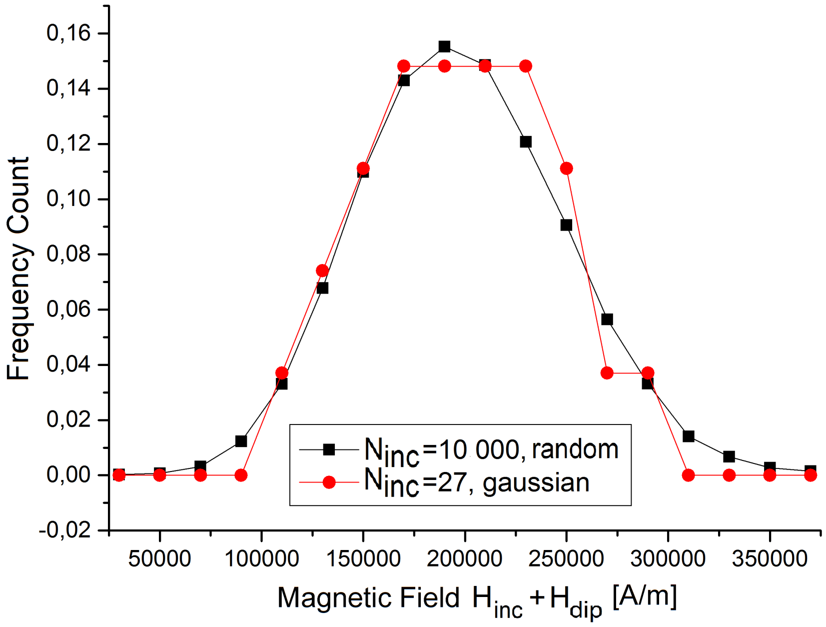

FIGURE 4.61 – *Analog to figure 4.60, we regard a volume fraction of* $f = 10$ %. *Again, a minimal deviation quantity of* $\Delta = 0.0021$ *is reached*

The corresponding arrangements of the inclusions in the samples are shown in figure 4.62. Obviously, this procedure generates microstructures which are quite similar to the previously regarded simple cubic lattice arrangements.

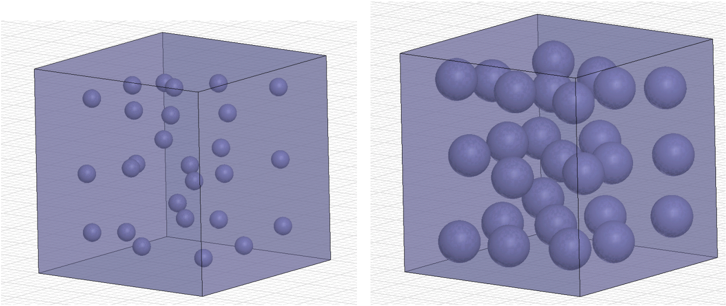

FIGURE 4.62 – *The corresponding microstructures to the distributions in figures 4.60 (left) and 4.61 (right) are shown. The arrangements are still very similar to a simple cubic lattice, but small local differences have great influences on the interactions. Average dislocation from the initial simple cubic lattice amounts* $\overline{\Delta x} = 1.33 r_{inc}$ *for* $f = 1\ \%$ *and* $\overline{\Delta x} = 0.57 r_{inc}$ *for* $f = 10\ \%$ *(*$r_{inc} = 0.0445$ *cm in both cases).*

Within this context, the question arises if there are also other well-suited methods in order to create such representatives systems with only few inclusions which reproduce the desired static $H-$field distribution. Therefore, we also analyzed the magnetic field distribution with completely random generated microstructures (with the only restriction that inclusions do not overlap), which was not very successful even after a large number of trials. Moreover, in further simulation sequences, we again randomly choose particle positions, but refuse the insertion if the distance between two inclusions undershots a minimum distance d_{min}. This procedure again delivers results which are comparable to the ones which were created with gaussianly distributed displacements. We refer to this insertion strategy in the following diagrams by the label "min. dist.". A comparison of typical field distributions for different insertion mechanisms are shown in figures 4.63 and 4.64.

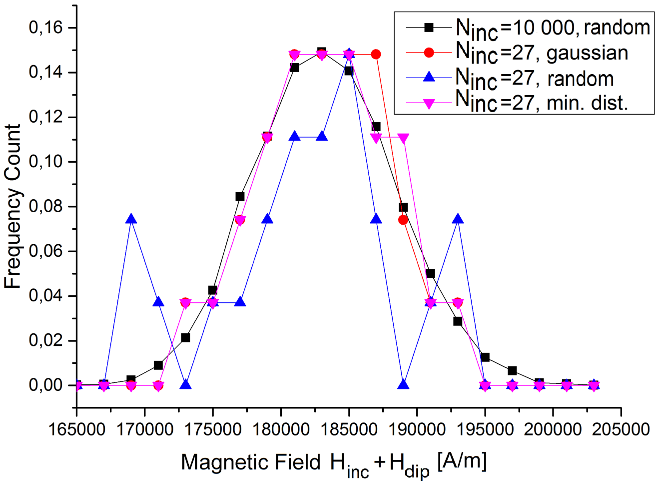

FIGURE 4.63 – *The* $H-$*field distribution of composites with* $N_{inc} = 10\ 000$ *inclusions is tried to reproduce in two additional manners: While the purely random insertion of spheres into the matrix does not show good agreement (blue triangles), keeping a minimum distance between single inclusions improves results again (pink triangles). Results for a filling factor of* $f = 1\ \%$ *are shown and the corresponding error quantities amount:* $\Delta_{gauss} = 0.0021$, $\Delta_{random} = 0.0231$, $\Delta_{min.dist.} = 0.002$, *while the minimum distance between inclusions is chosen to be* $d_{min} = 6 r_{inc}$.

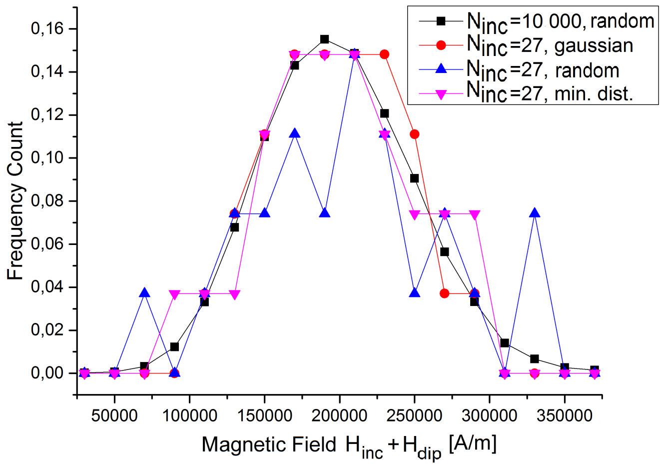

FIGURE 4.64 – *For* $f = 10$ %, *adaption trials yield error quantities of* $\Delta_{gauss} = 0.0021$, $\Delta_{random} = 0.0183$, $\Delta_{min.dist.} = 0.0042$, *with a reduced mimimum distance of* $d_{min} = 3r$ *due to higher packaging of inclusions compared to the case of* $f = 1$ %, *treated in figure 4.63.*

The assigned microstructures to the H−field distributions of the purely random insertion and the insertion with a minimum distance in the case of $f = 1$ % are shown in figure 4.65.

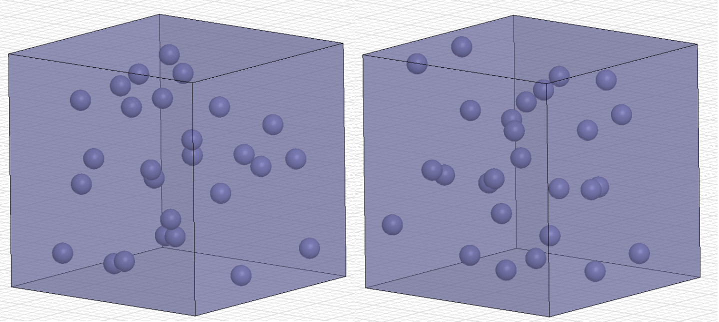

FIGURE 4.65 – *Left side shows the microstructure which is purely randomly generated and the microstructure with a minimum distance of* $d_{min} = 6r_{inc}$ *is shown on the right side. Filling factor amounts* $f = 1$ %.

Even if these outcomes show that good accordance with regard to the internal H−field distribution can not be achieved with an arbitrary stochastic insertion method, we also want to analyze the influence of the differently generated microstructures on the results of the high-frequent simulations. The corresponding results are shown in section 4.3.2.4 and highlight that agglomerations in composites with low inclusion numbers must be avoided in order to reproduce large systems. In the following dynamic field calculations (section 4.3.2), we use the microstructures generated by the gaussian displacements. Before, we want to analyze another situation in static simulations in the next section.

4.3.1.3 Polydisperse Inclusions

While the inclusions in one composite are always identical in the rest of the present work, we want to analyze the influence of different radii of the spheres in this section. For that purpose, we generate samples as before, but choose the radius of every inclusion according to a gaussian distribution with the mean value of r_{mean} which is chosen in dependence of the regarded inclusion number and the filling factor, as in the previous section, and a standard deviation of $\sigma = 0.1r_{mean}$ or $\sigma = 0.2r_{mean}$, respectively. One example of a device generated in this manner is shown in figure 4.66.

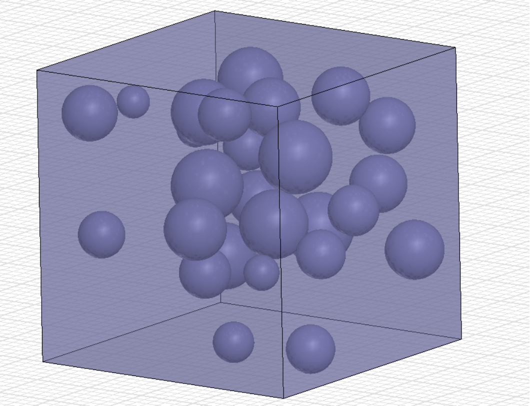

FIGURE 4.66 – *A sample with* $N_{inc} = 27$ *inclusions with* $r_{mean} = 0.0445$ *cm and radius standard deviation of* $\sigma = 0.2r_{mean}$ *filling the matrix with a volume fraction of* $f = 10$ %.

As before, we want to eliminate the influence of the finite inclusion numbers and therefore, increase N_{inc} until convergence with regard to the average internal magnetic field at the places of the inclusions is observed. Corresponding analyses are shown in figures 4.67-4.70.

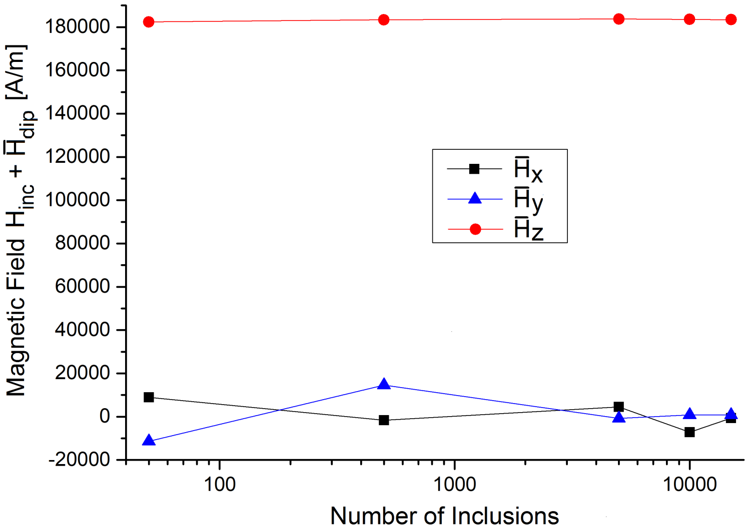

FIGURE 4.67 – *The components of the average magnetic field at the places of the spheres in the matrix in dependence of the inclusion numbers. Here, the sample with* $f = 1$ % *and an inclusion radius standard deviation of* $\sigma = 0.1r_{mean}$ *is under test.*

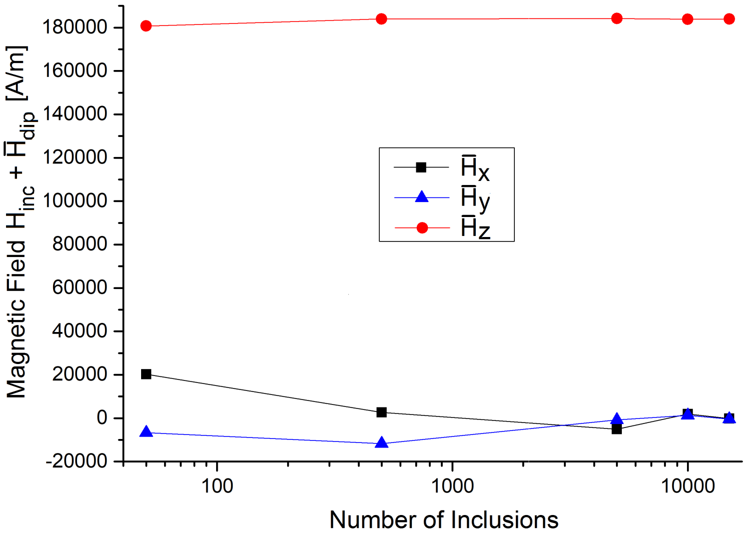

FIGURE 4.68 – *The same analysis as in figure 4.67 is done for a sample with* $f = 1$ % *and an inclusion radius standard deviation of* $\sigma = 0.2r_{mean}$.

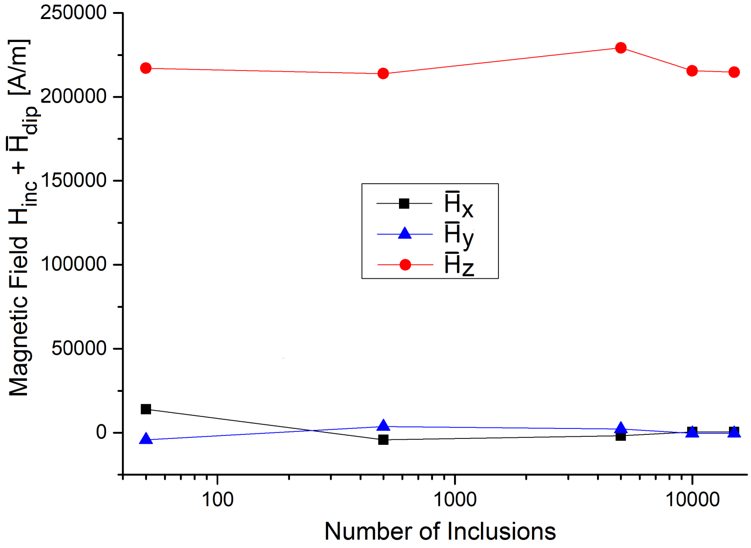

FIGURE 4.69 – *The same analysis as in figure 4.67 is done for a sample with* $f = 10$ % *and an inclusion radius standard deviation of* $\sigma = 0.1r_{mean}$.

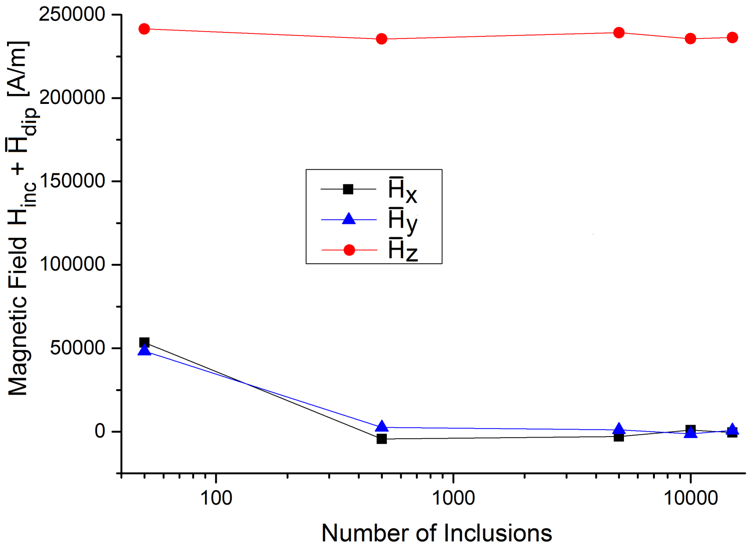

FIGURE 4.70 – *The same analysis as in figure 4.67 is done for a sample with $f = 10$ % and an inclusion radius standard deviation of $\sigma = 0.2 r_{mean}$.*

From these plots, we can drawback that convergence of the value of the mean field in the static simulations is reached without problems. Moreover, we learn that field components of H_x and H_y can be neglected, as before. In addition to the mean value of the magnetic field, we also want to examine the convergence of its distribution in dependence of the included spheres which is done in figures 4.71-4.74.

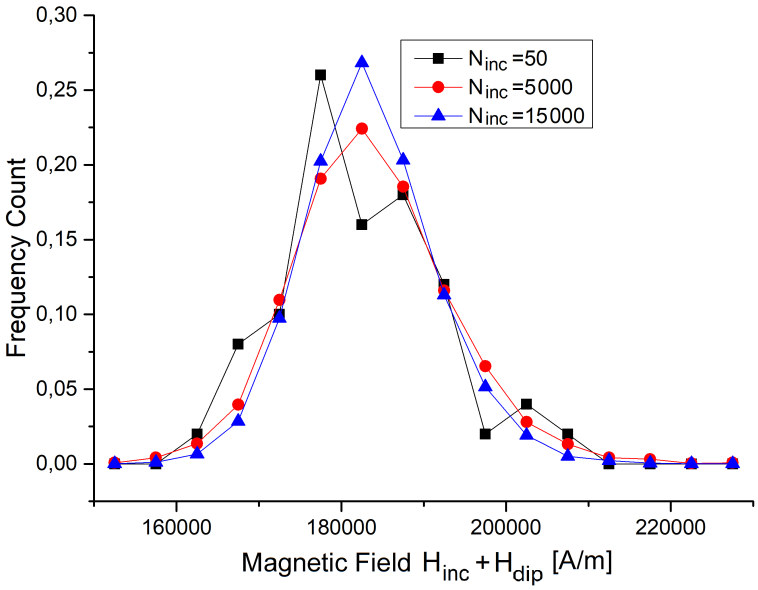

FIGURE 4.71 – *The distribution of the magnetic field in the sample with a filling factor of $f = 1$ % and $\sigma = 0.1 r_{mean}$ for different inclusion numbers.*

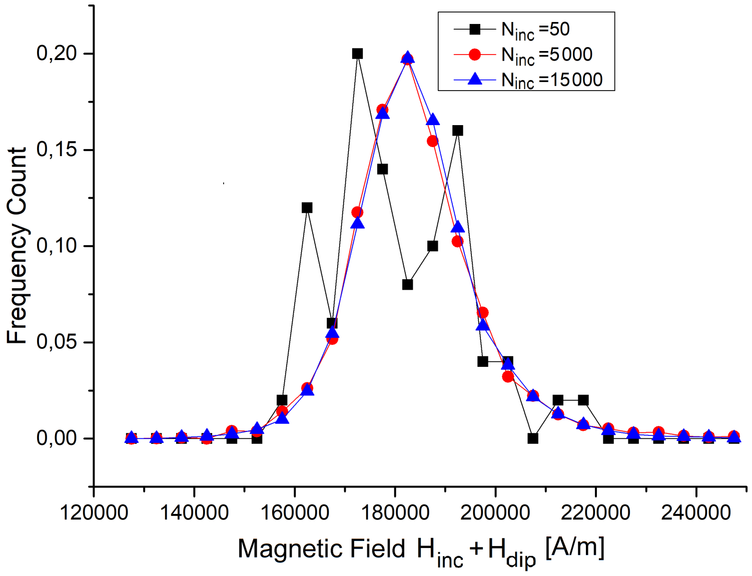

FIGURE 4.72 – *The distribution of the magnetic field in the sample with a filling factor of* $f = 1$ % *and* $\sigma = 0.2r_{mean}$ *for different inclusion numbers.*

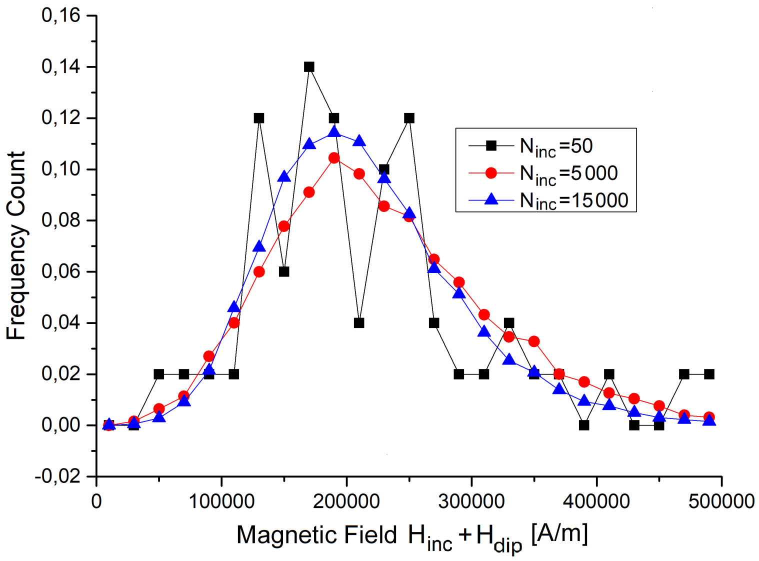

FIGURE 4.73 – *The distribution of the magnetic field in the sample with a filling factor of* $f = 10$ % *and* $\sigma = 0.1r_{mean}$ *for different inclusion numbers.*

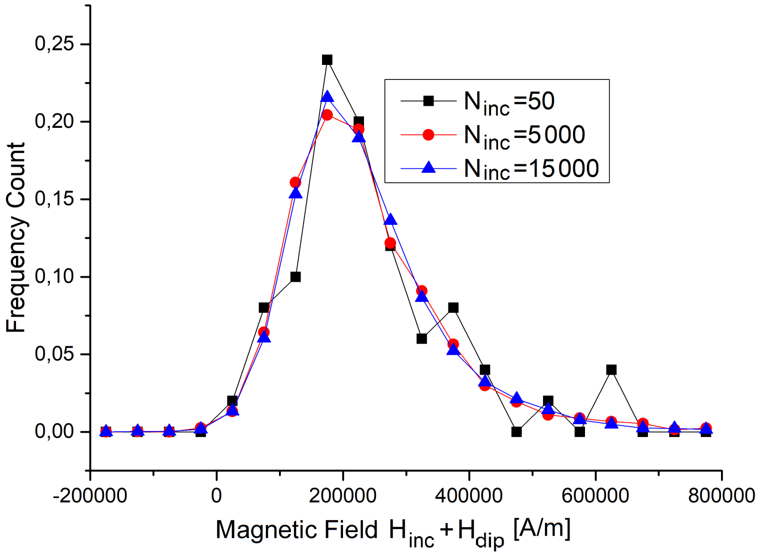

FIGURE 4.74 – *The distribution of the magnetic field in the sample with a filling factor of* $f = 10$ % *and* $\sigma = 0.2r_{mean}$ *for different inclusion numbers.*

In contrast to the mean values of the magnetic field, we need higher inclusion numbers to ensure convergence of the field distributions. Nevertheless, we see that values of $N_{inc} \geq 5\ 000$ are sufficiently large.

After this analysis of the convergence behavior, we are able to make justified statements about the influence of the regarded polydispersity. While the average magnetic field in direction of the external magnetic bias $\overline{H}_z$ increases with the standard deviation of the radius distribution (see figure 4.75), the distribution of the field values broadens (see figures 4.76 and 4.77).

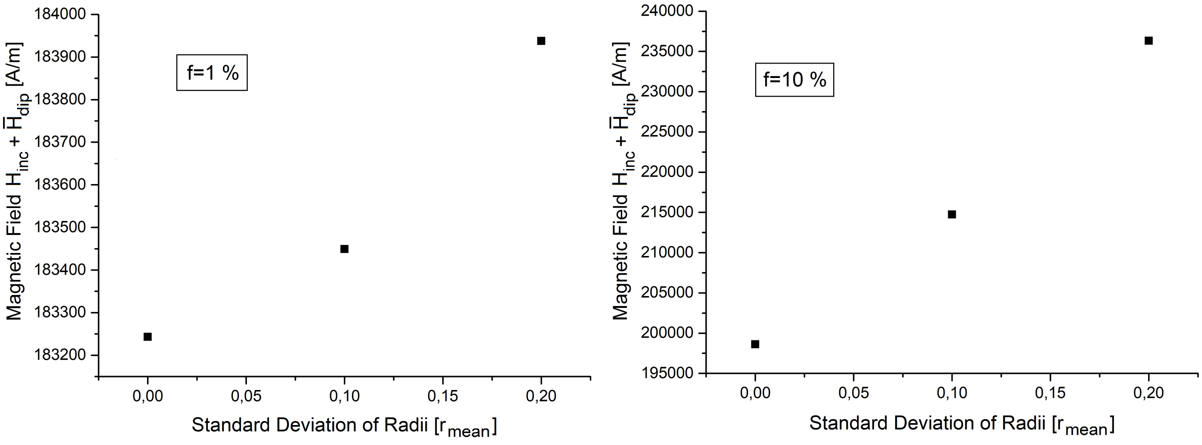

FIGURE 4.75 – *The mean values of the magnetic field component* $\overline{H}_z$ *for the three regarded cases of radius distributions. Left side belongs to the case of a filling factor of* $f = 1$ %, *right side to* $f = 10$ %.

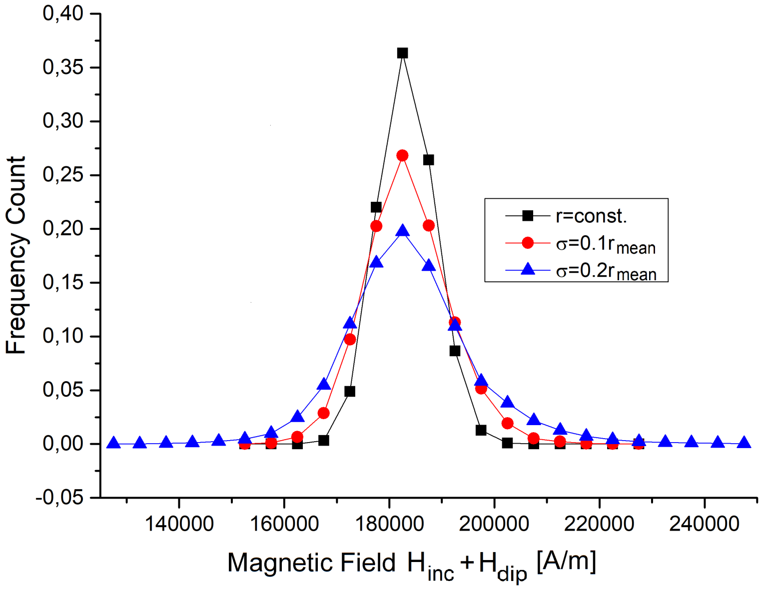

FIGURE 4.76 – *The distribution of the field values for the three regarded cases of radius distributions in the composites with a volume fraction of* $f = 1$ %.

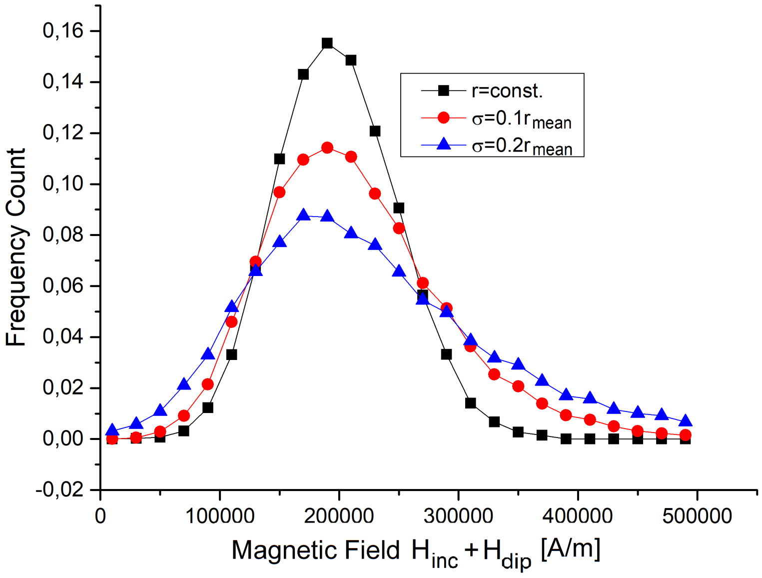

FIGURE 4.77 – *The distribution of the field values for the three regarded cases of radius distributions in the composites with a volume fraction of* $f = 10$ %.

Due to the linkage of the resonance frequency and the magnetic field via $\omega_0 = \gamma H_{eff}^{dip}$, we can assume that the regarded polydiversity will lead to resonances at higher values. In the next sections dealing with the following dynamic field calculations, we will also learn that the broadening of the magnetic field distribution also influences the resonance shifting, but strongly impedes a senseful analysis with low particle numbers in high-frequency simulations. For that purpose, we will not further examine the case of polydisperse inclusions in this work.

4.3.2 Dynamic Field Calculations

After these preparatory static calculations, we can come back to the high-frequency simulations with HFSS.

4.3.2.1 Neglection of Dipole-Dipole-Interaction

In order to isolate the influence of different characteristics of the system, we use the obtained configurations with the adapted positions of the inclusions, gained by the strategy described in the previous section with gaussianly distributed vectors, but again regard constant values of $H_{inc} = 183\ 154\ \frac{\mathrm{A}}{\mathrm{m}}$ and $H_{dip} = 0\ \frac{\mathrm{A}}{\mathrm{m}}$ for every inclusion. By this, we again switch off static dipole-dipole interaction between magnetic moments, at first. Afterwards, we repeat the simulation series leading to the results with inclusions on a simple cubic lattice shown in figure 4.27 with these new microstructures in order to analyze the effect of the inclusions' arrangement on the effective magnetization M_{eff} and effective magnetic field H_{eff}. Again, this includes the following steps: keeping inclusions' input parameter M_s^{inc} and H_{inc} constant, realizing different volume fractions by shrinking the sample volume and comparing with homogeneous devices with the same extensions (see section 4.2). Thereby, no significant difference to the simple cubic arrangements are noticed (see figures 4.78-4.80) and linear fitting processes (see figure 4.81) deliver quite similar values (compare to results in equations 4.13 and 4.14):

$$M_{eff}(f) = (2934 \pm 4.8)\ \frac{\mathrm{A}}{\mathrm{m}\ \%} \cdot f[\%] \tag{4.44}$$

$$H_{eff}(H_{inc} = const., f) = 283\ 952\ \frac{\mathrm{A}}{\mathrm{m}} - (925.5 \pm 8.8)\ \frac{\mathrm{A}}{\mathrm{m}\ \%} \cdot f[\%]. \tag{4.45}$$

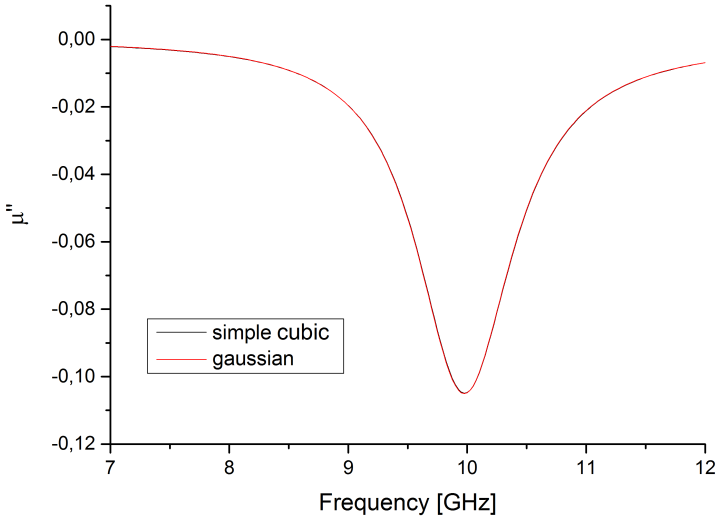

FIGURE 4.78 – *Comparison between μ'' of the devices with inclusions on a simple cubic lattice and with gaussianly distributed displacements. For a low volume fraction of $f = 1\ \%$, there is almost no difference between the both curves.*

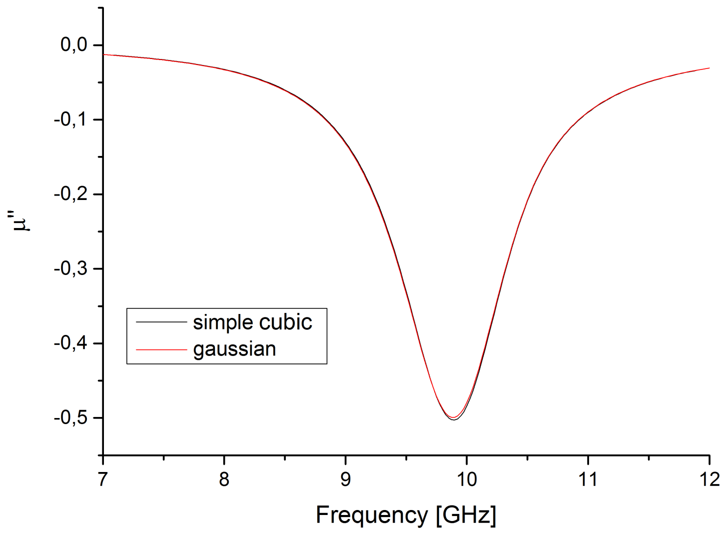

Figure 4.79 – *Regarding a filling factor of $f = 5$ %, there is also no significant deviation between the resonance peaks of the composites with inclusions on a simple cubic lattice and gaussianly displaced arrangements.*

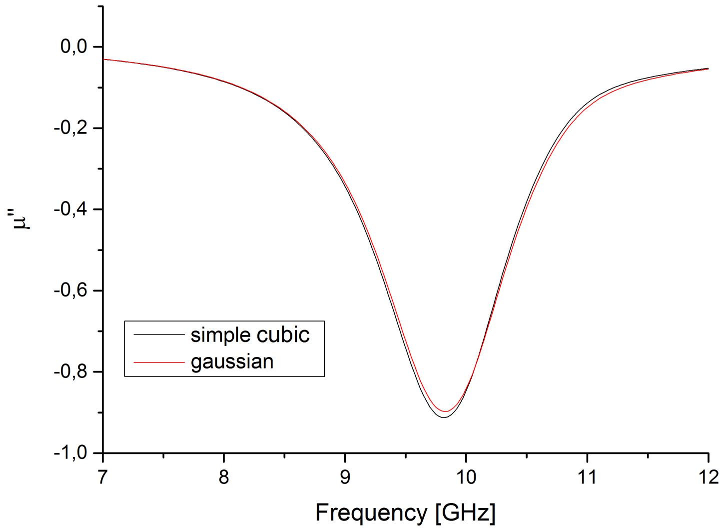

Figure 4.80 – *For the highest considered filling factor of $f = 10$ %, small differences at the resonance can be observed in contrast to the results shown in figures 4.78 and 4.79.*

These outcomes highlight that the regarded effective parameters are nearly independent of such small changes in the microstructure for a volume fraction range of 1 % to 10 % in these simulations. As a result of this numeric analysis, we can conclude that even in the structures with gaussian displacements of the inclusions, demagnetization fields are nearly the same for every inclusion as it is the case for the arrangement on a simple cubic lattice. Otherwise, a stronger deviation of the values in equations 4.44 and 4.45 comparing to 4.13 and 4.14 would be observed. Accordingly, a mean field approach for demagnetization effects is justified in this case.

4.3.2.2 Mean Field Approach for Dipole-Dipole-Interaction

Afterwards, we include the results from the calculation of the magnetic moments, but instead of taking into account the local field values at the places of the inclusions, we firstly restrict to the average internal magnetic field $\overline{H}_{inc}^{dip} = H_{inc} + \overline{H}_{dip}$ for every sphere while $H_{inc} = 183\ 155\ \frac{\mathrm{A}}{\mathrm{m}}$ is kept constant for different filling factor (data plotted in figure 4.56). Within this, $\overline{H}_{dip}$ denotes the mean value of the dipolar fields at the inclusions' center, averaged over all inclusions in the composite. Accordingly, a mean field approach for the dipolar fields is chosen in this intermediate stage and we will isolate the influence of the local field inhomogeneities when they are included in our simulations, afterwards.

Beyond this changed internal magnetic field ($H_{inc} \to H_{inc}^{dip}$) as input parameter, all further analyzes are again quite the same as for the simple cubic lattice. These deliver the results shown and compared to previous examinations in the graphs in figure 4.81. While effective magnetization M_{eff} is still not influenced, the effective magnetic field strongly deviates. The first of these two results can be easily understood, because of the definition of M_{eff} as the number of magnetic moments per volume, which is not affected by the switched-on dipolar interaction.

Contrary, the effective magnetic field of an equivalent homogeneous sample is enforced when higher densities of moments are placed in the composite regarding this model. This phenomenon is founded by the relaxation process of the magnetic moments, as discussed in connection with figure 4.56. Here, we worked out, that average fields increase at places of the inclusions, while average fields in total remain constant and correspond to the effective field in the composite. Accordingly, it would be misleading to refer to the so determined values of the magnetic fields in the homogeneous sample as H_{eff}. In order to overcome this problem, we emphasize the local enforcement of the fields at places of inclusions by choosing the label H_{eff}^{loc} for this case.

Remembering the results for the simple cubic lattice, we recognize that we again have to convert the obtained data, produced under the condition $H_{inc} = const.$ for every filling factor, in order to perform analog examinations as in experimental works, in which the externally applied field is the tunable parameter. Including demagnetization effects by again using relation 4.20 with the values of $H_{eff}^{loc}(H_{inc} = const.)$ shown by red circles in picture 4.81, we can analyze the composite samples' behavior under constant external field, which is exemplary done for $f = 1\ \%$, $f = 5\ \%$ and $f = 10\ \%$, with the results shown in figure 4.82. Furthermore, we compare these outcomes to the results for the effective sample without dipolar interaction, for which we put the values of $H_{eff}(H_{inc} = const.)$ (black squares in figure 4.81) in equation 4.20 in order to simulate a constant externally applied field. In this context, we remember that this data set without the influence of dipolar interaction corresponds to an unshifted resonance frequency.

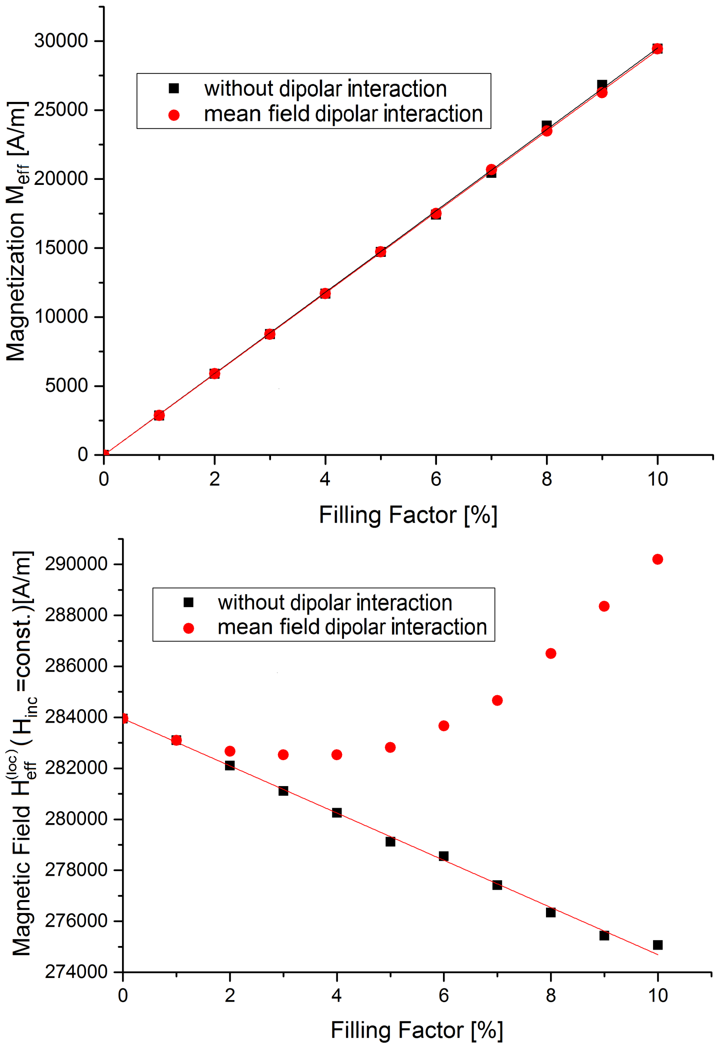

FIGURE 4.81 – *In the upper picture, the effective magnetization* M_{eff} *for different volume fractions is shown. This linear correlation is not influenced by the different analyzed models. Contrary, the effective magnetic field* $H_{eff}^{loc}(H_{inc} = const.)$ *is strongly increased for higher filling factors compared to the previously examined system. Black squares correspond to values of* $H_{eff}(H_{inc} = const.)$ *without dipolar interaction (according to equation 4.16, fitting process delivers relation 4.45) while red circles mark data for the composites in which the average magnetic field with switched-on dipolar interaction between inclusions is regarded. These values for* $H_{eff}^{loc}(H_{inc} = const.)$ *can be understood by considering equation 4.46. As before, values of* M_{eff} *and* $H_{eff}^{(loc)}(H_{inc} = const.)$ *are found by the comparison between the resonance curves of the homogeneous and heterogeneous materials and the variation of the input parameter for the magnetization and the internal magnetic field of the homogeneous device.*

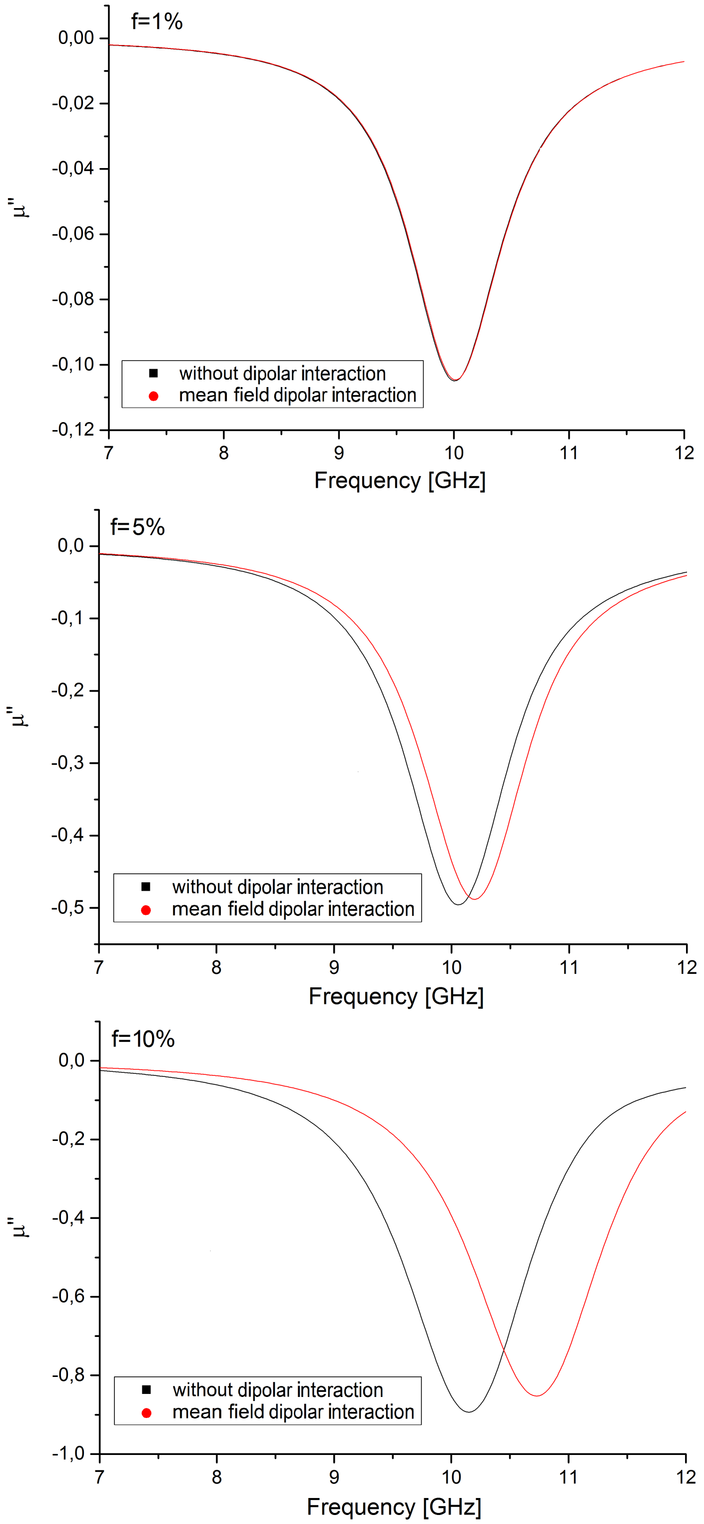

FIGURE 4.82 – *Contrary to the effective, homogeneous samples in which dipolar interaction is disregarded (black lines), a significant frequency shift to higher values for increasing volume fractions can be recognized when including the interaction of the magnetic moments in a mean field approach (red lines) for the effective samples. For producing these graphs, samples were exposed to a constant external field for different filling factors, as experimentally relevant. Compare to figures 4.28-4.30 for composites with inclusions arranged on a simple cubic lattice.*

Obviously, the resonance frequency is not constant anymore, but increases with inclusions' filling factor. In order to illuminate the background of this frequency shift, we recapitulate: Because the slope of $H_{eff}(H_{inc} = const.)$ from the interaction-free model

$$\frac{\mathrm{d}H_{eff}(H_{inc} = const.)}{\mathrm{d}f} = -(925.5 \pm 8.8)\ \frac{\mathrm{A}}{\mathrm{m}\ \%}$$

is very close to the magnitude of demagnetization effects on a spherical inclusion

$$\frac{1}{3}M_{eff} = \frac{1}{3}(2934 \pm 4.8)\ \frac{\mathrm{A}}{\mathrm{m}\ \%} = (978 \pm 1.6)\ \frac{\mathrm{A}}{\mathrm{m}\ \%}$$

and due to their different sign, both phenomena compensate when keeping the external magnetic field constant (see equation 4.20), whereby resonance frequency is maintained. Contrary, in the case with static dipolar interaction, effective magnetic field $H_{eff}^{loc}(H_{inc} = const.)$, whose values are taken from figure 4.81, can be interpreted as the sum

$$H_{eff}^{loc}(H_{inc} = const., f) = \underbrace{H_{inc} + \frac{1}{3}M_s^{inc} - \frac{1}{3}M_{eff}(f)}_{H_{eff}(H_{inc}=const.,f)} + \overline{H}_{dip}(f) \tag{4.46}$$

with the additional term $\overline{H}_{dip}$ comparing to equation 4.16 arising from the interaction of the magnetic moments which was calculated in the static simulation. For the purpose of determining the resonance frequency of such a material with infinite extensions, we cannot use the graphs in figure 4.82, because they are influenced by the finite sample geometries, as in the previous section. Nevertheless, we can gain insight into the frequency shift behavior under a constant external field by using the magnetic fields $H_{eff}^{loc}(H_{inc} = const.)$ and magnetizations M_{eff} for different volume fractions, drawn from the adaption of homogeneous and composite materials in the dynamic simulation (data from plots in 4.81). The fundamental assumption for this calculation of the resonance frequency of the system is that it is determined by the average static field around the particles, i.e. $\nu = \nu(H_{eff}^{loc})$, which is only a first trial. The consideration of the local field values around different particles will be treated in the next section.
As a first approach in this context, we calculate resonance frequencies which are determined by the local effective field $H_{eff}^{loc}(H_{eff} = const., f)$ according to

$$\nu_{res}^{dyn}(f) = \frac{\gamma}{2\pi}H_{eff}^{loc}(H_{eff} = const., f) \tag{4.47}$$

$$= \frac{\gamma}{2\pi}\Big(H_{eff}^{loc}(H_{inc} = const., f) + \frac{1}{3}M_{eff}(f)\Big). \tag{4.48}$$

The additional term $\frac{1}{3}M_{eff}$ is again chosen in order to keep the external magnetic field constant.
Alternatively, we can skip the dynamic simulation runs and use only the dipole contributions calculated in the static simulations and the input parameter H_{inc}, instead. By

this approach, we calculate resonance frequencies according to

$$\nu_{res}^{stat}(f) = \underbrace{\frac{\gamma}{2\pi}\left(H_{inc} + \frac{1}{3}M_s^{inc}\right)}_{\nu_0} + \underbrace{\frac{\gamma}{2\pi}\overline{H}_{dip}(f)}_{\nu_{shift}} \tag{4.49}$$

in which the first term ν_0 remains constant at 10 GHz for the used parameter set, as already discussed. The both resulting resonance behaviors are shown in figure 4.83 and are very similar to each other.

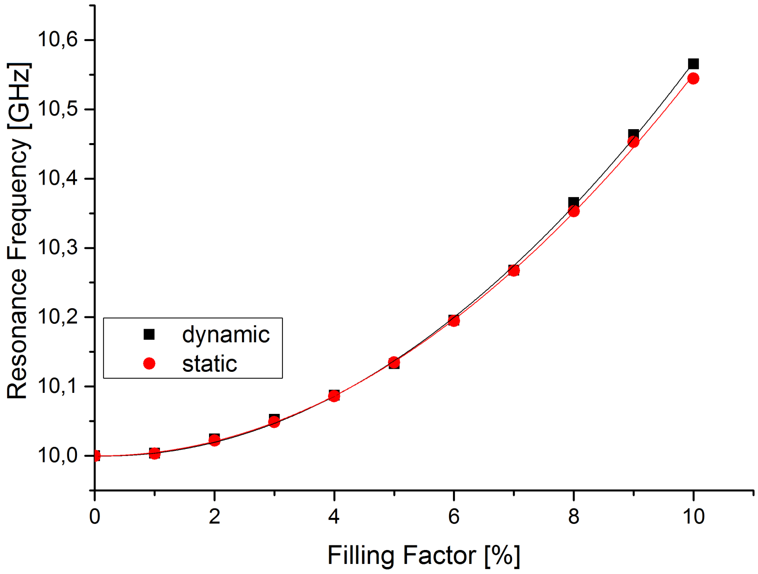

FIGURE 4.83 – *The progress of the resonance frequency in dependence of the filling factor when dipolar interaction is included in a mean field approach into the model. Model parameters are the same as before. Black squares show results from dynamic simulations (HFSS and MOR, see equation 4.48), while measure points marked by red circles completely rely on results from static simulations (see equation 4.49). A parabolic fitting of both data sets yields good agreements.*

Fitting of the data with a parabolic function delivers for our set of parameters

$$\nu_{res}^{dyn}(f) = (0.00588 \pm 1.2 \cdot 10^{-4}) f^2 \,\frac{\text{GHz}}{(\%)^2} - (0.00196 \pm 9.4 \cdot 10^{-4})\frac{\text{GHz}}{\%} f + 10 \text{ GHz} \tag{4.50}$$

for the dynamic results and

$$\nu_{res}^{stat}(f) = (0.00557 \pm 0.8 \cdot 10^{-4}) f^2 \,\frac{\text{GHz}}{(\%)^2} - (6.3 \cdot 10^{-4} \pm 8.8 \cdot 10^{-4})\frac{\text{GHz}}{\%} f + 10 \text{ GHz} \tag{4.51}$$

when restricting to static simulations. Naturally, this relations can only be true in the range of small volume fractions. Obviously, in the limit of $f \to 100$ %, we approach a homogeneous sample again, where resonance frequency cannot be shifted anymore. Accordingly, a maximum of the shift must be reached at some value of f before resonance frequency again approaches the initial value for $f \to 0$ of 10 GHz. Unfortunately, this cannot be examined with the help of the model in use because it is restricted to small volume fractions of inclusions, as already discussed. Nevertheless, the influence of the inclusions' saturation magnetization M_s^{inc} can be analyzed for what we restrict to static simulations. The corresponding results are shown in figure 4.84.

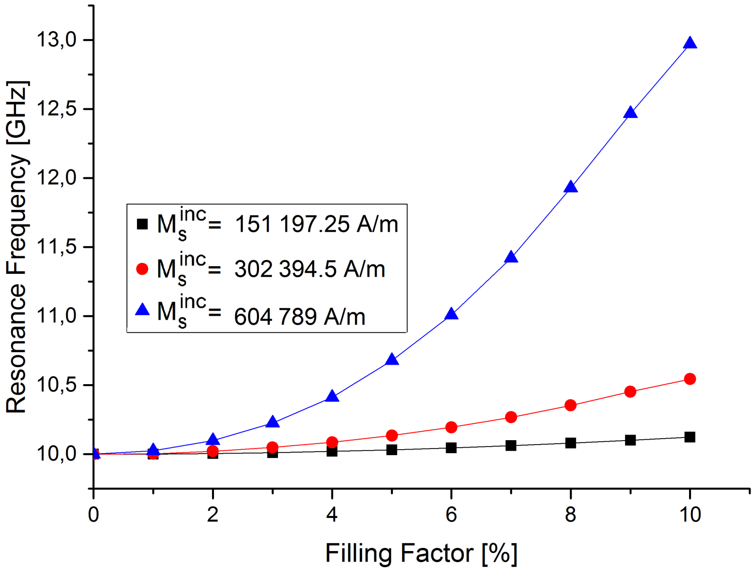

FIGURE 4.84 – *Static simulations are performed for different saturation magnetizations of inclusion material. According to expectations, higher saturation magnetizations enforce the resonance shift by stronger dipolar interactions.*

Parabolic fitting processes now deliver

$$M_s^{inc} = 151\ 197.25\ \frac{\text{A}}{\text{m}} : \tag{4.52}$$

$$\nu_{res}^{stat}(f) = (0.00122 \pm 4 \cdot 10^{-6}) f^2\ \frac{\text{GHz}}{(\%)^2} - (2.03 \cdot 10^{-4} \pm 3.4 \cdot 10^{-5}) \frac{\text{GHz}}{\%} f + 10\ \text{GHz} \tag{4.53}$$

$$M_s^{inc} = 604\ 789\ \frac{\text{A}}{\text{m}} : \tag{4.54}$$

$$\nu_{res}^{stat}(f) = (0.03247 \pm 6.9 \cdot 10^{-4}) f^2\ \frac{\text{GHz}}{(\%)^2} - (-0.0231 \pm 0.006) \frac{\text{GHz}}{\%} f + 10\ \text{GHz}. \tag{4.55}$$

As in the section dealing with inclusions on a simple cubic lattice inside the matrix, we also want to analyze the magnitudes of μ''_{max} and μ'_{stat}. For that purpose, we firstly have to check if the composites' permeabilities are again in such a good agreement with corresponding homogeneous materials, as before. If this is the case, then we can again use equations 4.25 and 4.30 along with the determined values of $M_{eff}(f)$ and $H_{eff}^{loc}(H_{eff} = const., f)$ in order to calculate the desired values. An exemplaric comparison between the real and imaginary parts of μ of the composite with a volume fraction $f = 10\ \%$ and the assigned homogeneous material is shown in figure 4.85, yielding that a very high accordance is reached, again.

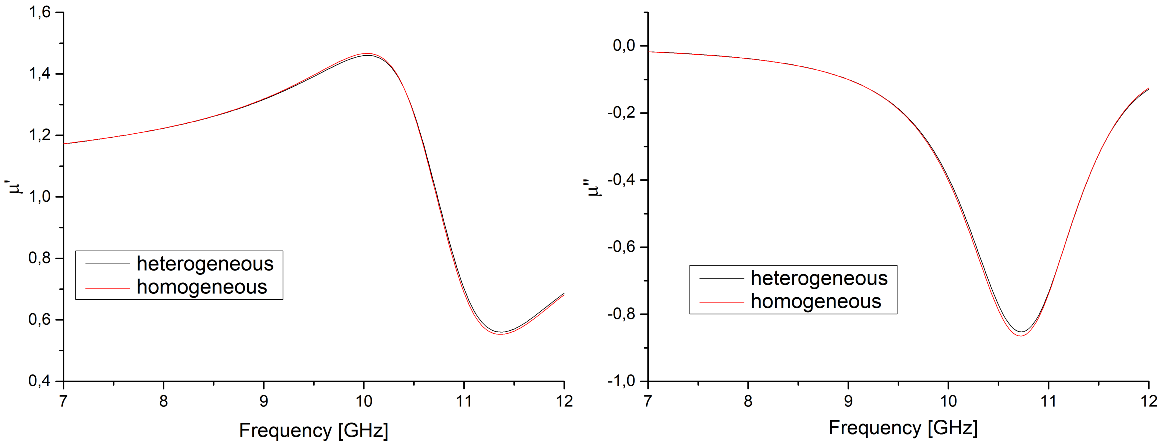

FIGURE 4.85 – *The real (left picture) and imaginary (right picture) part of* μ *of the composite with* $f = 10$ % *and the homogeneous device of the same extensions with* $M_{eff} = 29\ 443\ \frac{A}{m}$ *and* $H_{eff}^{loc}(H_{eff} = const.) = 300\ 012\ \frac{A}{m}$ *are plotted. In contrast to the effective magnetic fields of the homogeneous samples regarded in figure 4.82, the part of* $\overline{H}_{dip}(f)$ *is included.*

Accordingly, we are able to calculate the desired magnitudes of μ''_{max} and μ'_{stat} and compare them to the previously found values when there was no dipolar interaction between inclusions (see figures 4.86 and 4.87).

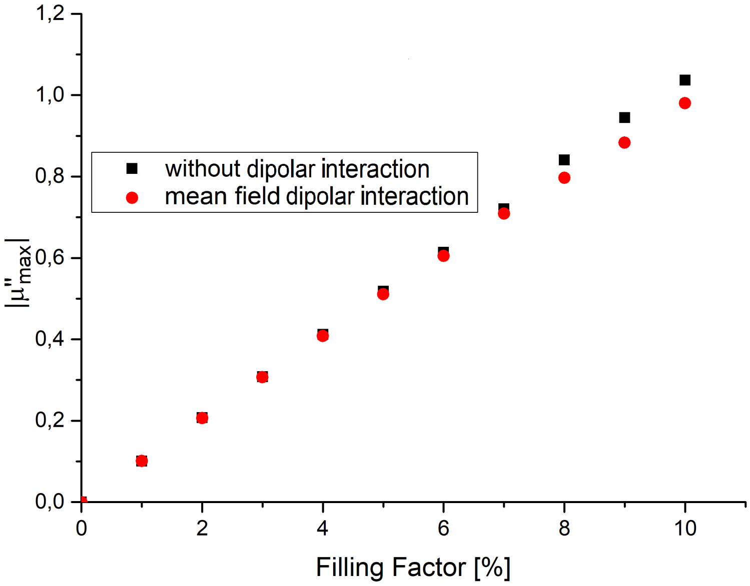

FIGURE 4.86 – *Equation 4.25 and the determined values of* $M_{eff}(f)$ *and* $H_{eff}^{loc}(H_{eff} = const., f)$ *are used in order to calculate* μ''_{max} *for every regarded volume fraction in case of a mean-field dipolar interaction (red circles). Found values are compared to the case of inclusions on a simple cubic lattice, in which no dipolar interaction takes place (black squares).*

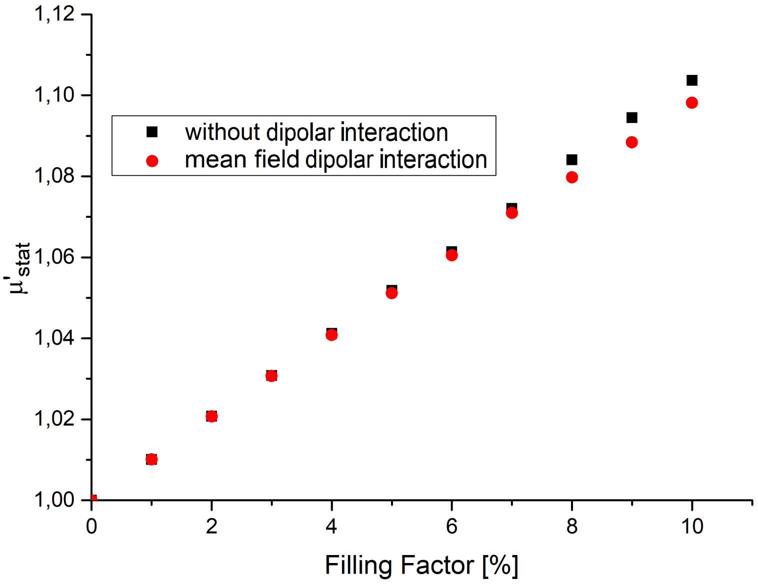

FIGURE 4.87 – *Equation 4.30 and the determined values of* $M_{eff}(f)$ *and* $H^{loc}_{eff}(H_{eff} = const., f)$ *are used in order to calculate* μ'_{stat} *for every regarded volume fraction in case of a mean-field dipolar interaction (red circles). Found values are compared to the case of inclusions on a simple cubic lattice, in which no dipolar interaction takes place (black squares).*

As we can see, both magnitudes decrease compared to the case of an inclusion arrangement on a simple cubic lattice while the differences increase with filling factor f. The reason for this can be found in the dipolar fields which raise the values of $H^{loc}_{eff}(H_{eff} = const., f)$ while the values of M_{eff} remain the same apart from this interaction. For the purpose of calculating the effective permeability tensor of an infinitely extended medium out of the input parameters $M^{inc}_s, \alpha, H_{inc}$ and f under a constant effective field , we recapitulate: Effective magnetization is not influenced by the switched-on dipolar interaction, meaning

$$\omega_m = \gamma M_{eff}(f) = \gamma M^{inc}_s \cdot \frac{f[\%]}{100} \tag{4.56}$$

still remains true, as in the case without this interaction (see section 4.2 and equation 4.34). Contrary, we observed that the local effective field at the places of the inclusions is enforced by the dipolar interaction, leading to an analog form of equation 4.49 for the circular resonance frequency

$$\omega_0 = \gamma \left(H_{inc} + \frac{1}{3} M^{inc}_s + \overline{H}_{dip} \right). \tag{4.57}$$

Now, the arising question is, if we are able to calculate the term of $\overline{H}_{dip}$ as a function of the filling factor f and the inclusions' magnetization M^{inc}_s. In order to analyze this, we plot $\overline{H}_{dip}$ in dependence of the inclusion volume fraction for the three different regarded values of M^{inc}_s in figure 4.88.

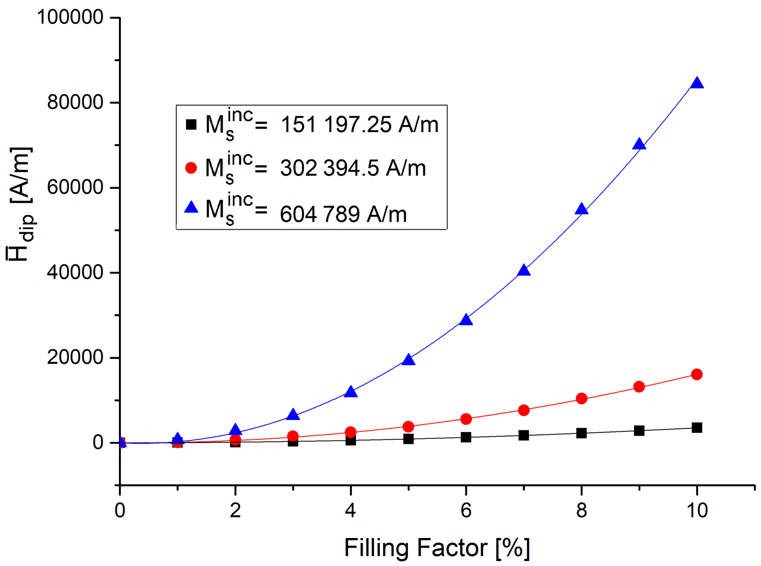

FIGURE 4.88 – *We regard three different values of* M_s^{inc} *and calculate the arising dipolar fields* H_{dip} *with the help of our static simulation. Compare to figure 4.84.*

Then, we apply a polynomial fit of second order with the help of OriginLab in the form of

$$\overline{H}_{dip}(f) = B_2 f^2 + B_1 f, \tag{4.58}$$

in which we respect that for $f = 0$, no dipolar fields arise, and determine the values of B_2 and B_1. The corresponding fitting curves are also shown in figure 4.88 and approximate the data set very well. We get

$$M_s^{inc} = 151\ 197.25\ \frac{\mathrm{A}}{\mathrm{m}} : \tag{4.59}$$

$$\overline{H}_{dip}(f) = (34.6 \pm 0.1) f^2\ \frac{\mathrm{A}}{\mathrm{m}(\%)^2} + (5.8 \pm 0.9) \frac{\mathrm{A}}{\mathrm{m}\%} f \tag{4.60}$$

$$M_s^{inc} = 302\ 394.5\ \frac{\mathrm{A}}{\mathrm{m}} : \tag{4.61}$$

$$\overline{H}_{dip}(f) = (166 \pm 3) f^2\ \frac{\mathrm{A}}{\mathrm{m}(\%)^2} - (56 \pm 27) \frac{\mathrm{A}}{\mathrm{m}\%} f \tag{4.62}$$

$$M_s^{inc} = 604\ 789\ \frac{\mathrm{A}}{\mathrm{m}} : \tag{4.63}$$

$$\overline{H}_{dip}(f) = (921 \pm 20) f^2\ \frac{\mathrm{A}}{\mathrm{m}(\%)^2} - (657 \pm 159) \frac{\mathrm{A}}{\mathrm{m}\%} f. \tag{4.64}$$

Afterwards, we analyze the obtained values in dependence of the inclusions' magnetization M_s^{inc} (see figure 4.89 and 4.90).

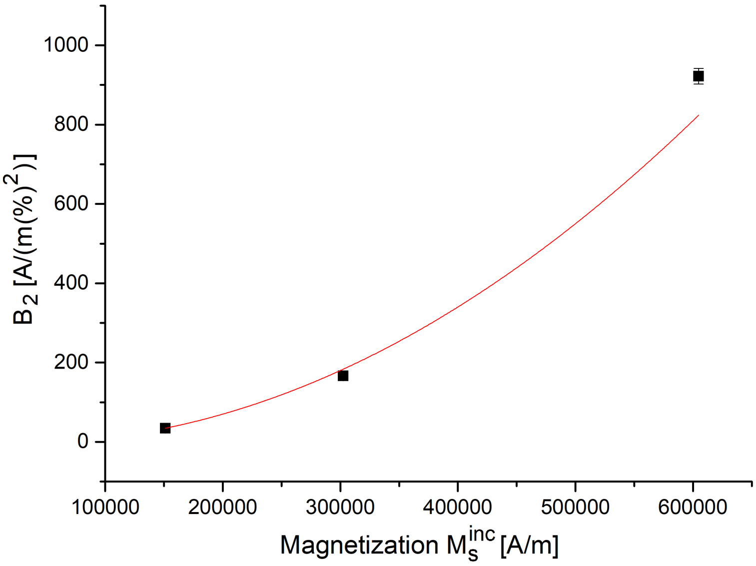

FIGURE 4.89 – *The fitting parameter B_2 is plotted and parabolic fitted in dependence of M_s^{inc}.*

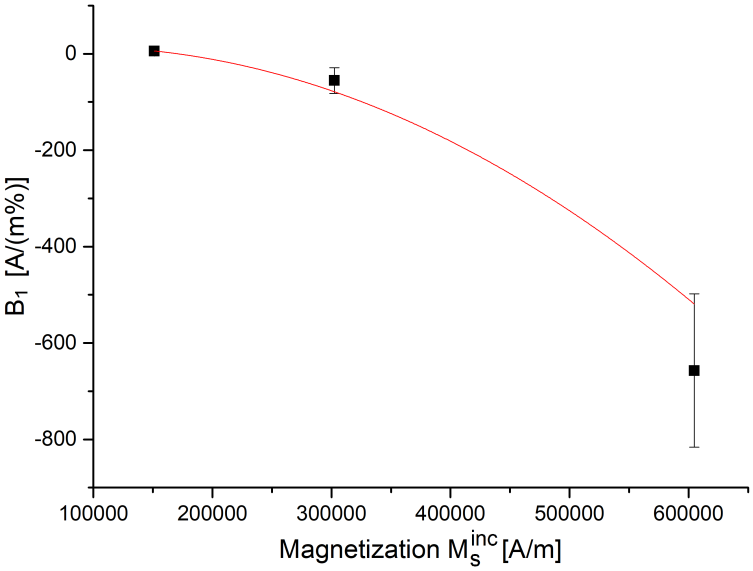

FIGURE 4.90 – *The fitting parameter B_1 is plotted and parabolic fitted in dependence of M_s^{inc}.*

Again, we use a parabolic fit and obtain

$$B_2(M_s^{inc}) = (2.5 \cdot 10^{-9} \pm 3 \cdot 10^{-10}) \left(M_s^{inc}\right)^2 - (1.5 \cdot 10^{-4} \pm 5 \cdot 10^{-5}) M_s^{inc} \tag{4.65}$$

$$B_1(M_s^{inc}) = (-1.9 \cdot 10^{-9} \pm 5 \cdot 10^{-10}) \left(M_s^{inc}\right)^2 - (3.4 \cdot 10^{-4} \pm 8 \cdot 10^{-5}) M_s^{inc} \tag{4.66}$$

In summary, we are able to calculate an approximation of the effective permeability tensor for this mean field approach for the dipolar interaction out of the given parameter set M_s^{inc}, H_{inc} and f, when we insert equation 4.56 and 4.57 in combination with 4.58 and the values in 4.65 and 4.66 into Polder's formula 1.169 while for damping parameter α, the inclusion material value is used, as before.

4.3.2.3 Inhomogeneous Fields

After this mean field approximation in which the resonance frequency $\nu_{res}(H_{eff}^{loc})$ was calculated as a function of the average local field, we want to further increase complexity and respect the local field distributions in connection with the generated microstructures gained from the procedure described in section 4.3.1. De facto, these field inhomogeneities imply different local effective magnetic fields for every inclusion and, consequently, different permeability tensors, according to Polder's model. Consequently, the internal magnetic biases of the inclusions are chosen as $H_{inc,j}^{dip} = H_{inc} + H_{dip,j}$ with different values of $H_{dip,j}$ for every sphere and $j = 1 \ldots N_{inc}$ instead of setting $\overline{H}_{inc}^{dip} = H_{inc} + \overline{H}_{dip}$ for all inclusions, which was done in the previous section. Due to this diversity, an inclusion number as high as possible in order to reduce statistical errors is desirable, wherefore numerical effort, meaning discretization passes in HFSS and solution order in MOR, is analyzed again in order to ensure convergence of the results for these systems with an inclusion number of $N_{inc} = 64$ (see figures 4.91 and 4.92). Within this analysis, it appears that the second discretization pass in HFSS and an order of four in MOR are sufficient while all other parameters remain the same as before.

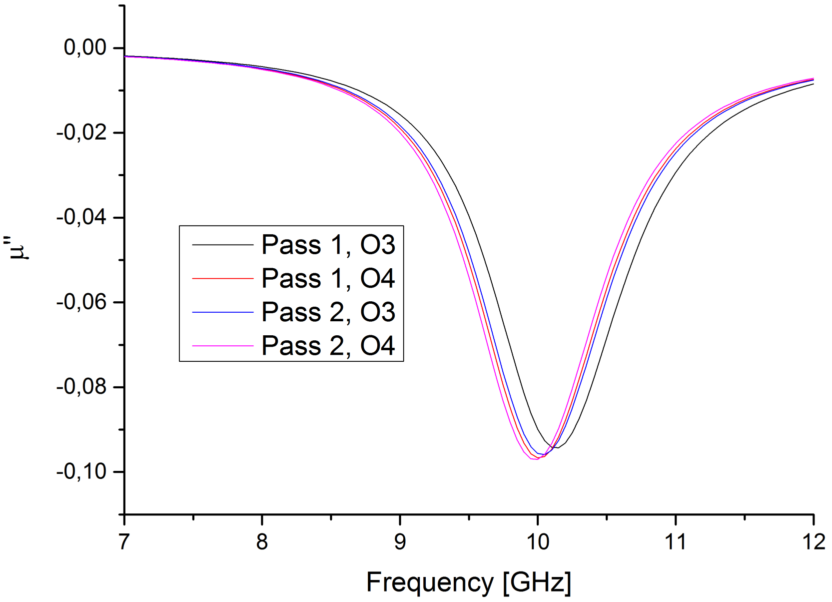

FIGURE 4.91 – *The influences of the number of passes in HFSS and the order of solution in MOR are analyzed for a composite with an inhomogeneous field distribution, a volume fraction of* $1~\%$ *and an inclusion number of* $N_{inc} = 64$. *Obviously, results for the first mesh from HFSS and a solution order of three in MOR strongly deviate from results calculated with more effort. Unfortunately, it is not possible to perform simulation runs with the third mesh discretization pass and a solution order of four, due to limited memory capacity.*

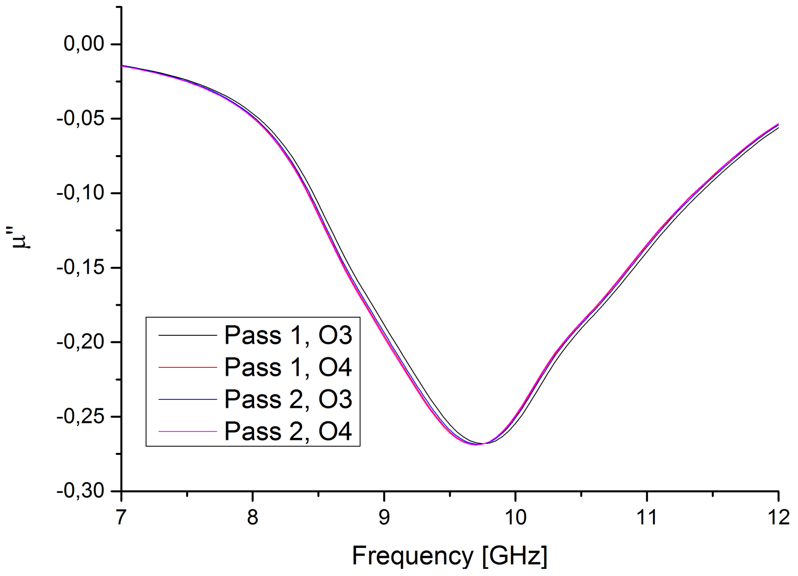

FIGURE 4.92 – *The same analysis as in figure 4.91 is performed for a volume fraction of* 5 %. *Here, convergence appears with less effort.*

As already indicated, higher inclusion numbers may be necessary compared to the previously analyzed mean field approaches. In order to gain insight into this, we compare results between systems with $N_{inc} = 27$ (third mesh discretization pass, fourth solution order) and $N_{inc} = 64$ inclusions and different volume fractions (see figures 4.93-4.95).

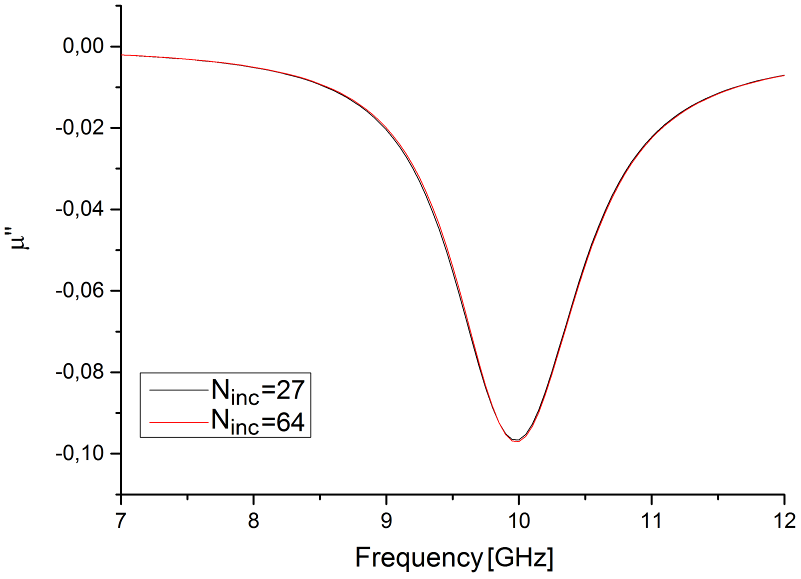

FIGURE 4.93 – *A comparison between the results for inclusion numbers of* $N_{inc} = 27$ *and* $N_{inc} = 64$ *for a volume fraction of* $f = 1$ %. *Although the composites' microstructures differ from each other, results are in good agreement and underline convergence with respect to inclusion number.*

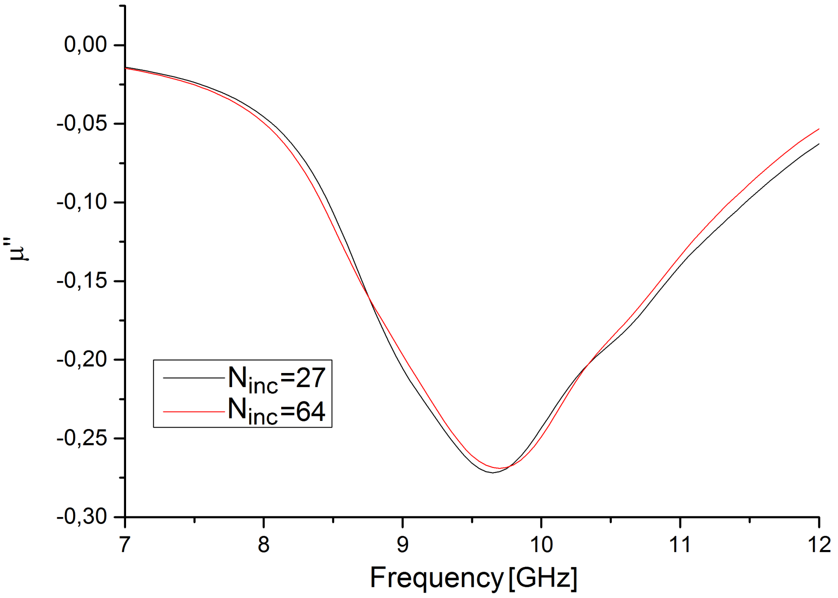

FIGURE 4.94 – *For a filling factor of* $f = 5$ %*, small differences in the resonance curves for* $N_{inc} = 27$ *and* $N_{inc} = 64$ *occur.*

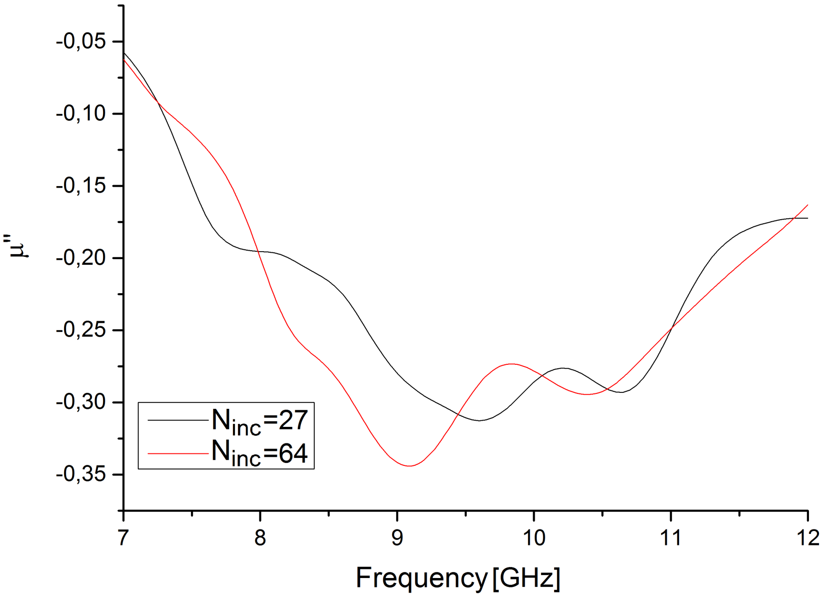

FIGURE 4.95 – *Further increasing inclusions' volume fraction to* $f = 10$ %*, strong deviations can be observed, indicating that artifacts due to the limited system size appear.*

Obviously, the deviation between $N_{inc} = 27$ and $N_{inc} = 64$ is quite small for volume fractions up to $f = 5$ %, indicating convergence with regard to inclusion numbers. Further increasing the filling factor, strong differences become obvious and highlight artifacts due to the low number of inclusions. As already mentioned, limited computation resources do not allow simulations with higher numbers of inclusions, wherefore we restrict to the range of $f = 1$ % to $f = 5$ % and use $N_{inc} = 64$ in the following. For that reason, accuracy analysis with regard to mesh discretization and order of ansatz function is also performed with $f = 1$ % and $f = 5$ % (see figures 4.91 and 4.92).

At first, we use the justified numerical parameters, the found microstructures and local field distributions in order to determine the effective permeability for different volume fractions in analog simulation sequences as in the previous sections. Then, we compare the new outcomes, for which every inclusion is supposed to different local effective fields, to the former results, in which a homogeneous effective field for all inclusions was assumed as a mean field approach. At this point, we regard the case of $H_{inc} = const.$ (see figures 4.96-4.98).

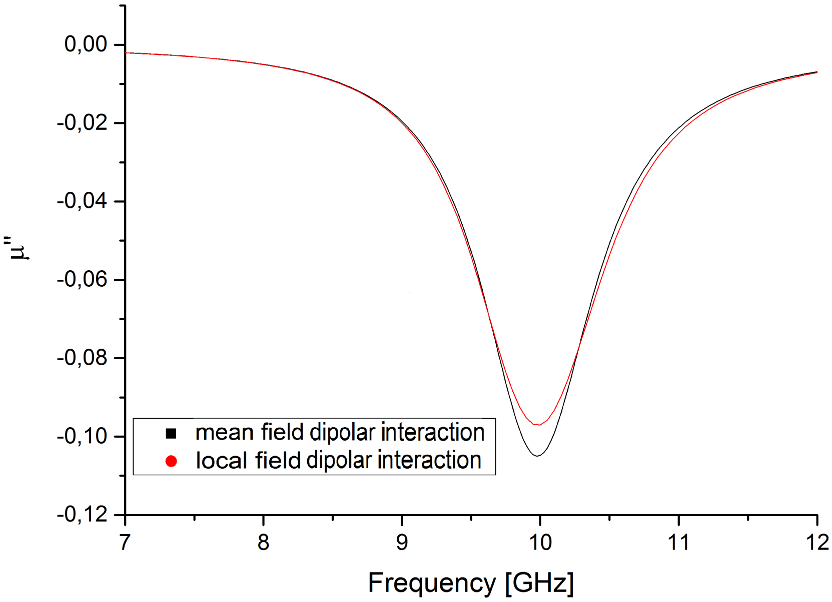

FIGURE 4.96 – *The results for the mean field approach, in which equal dipolar interactions are assumed for every inclusion,* $\overline{H}_{inc}^{dip} = H_{inc} + \overline{H}_{dip}$ *with* $H_{inc} = const.$*, are compared to the now performed simulation runs with regarding of the local field inhomogeneities, i.e. different values of* H_{dip} *for every inclusion instead of its mean value. Picture shows resonance curves for* $f = 1\ \%$.

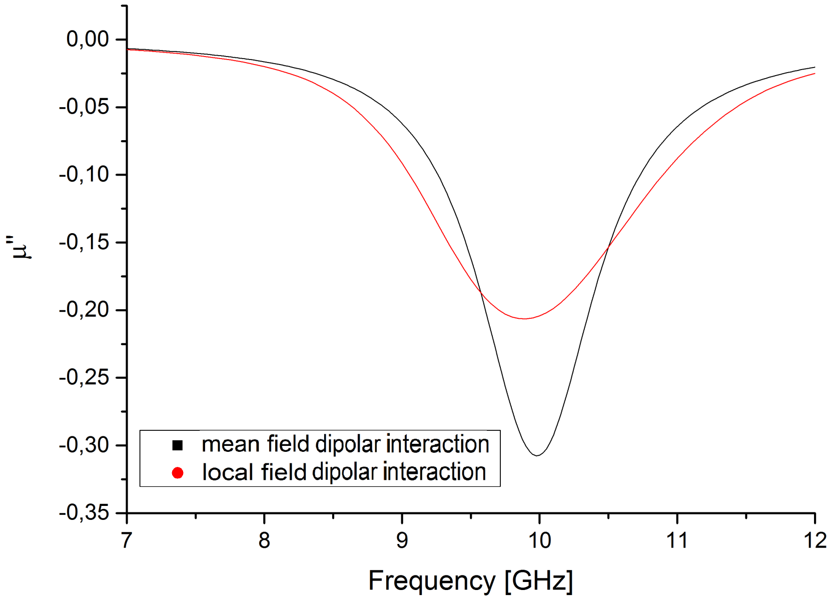

FIGURE 4.97 – *The same comparison as in figure 4.96 is regarded for a filling factor of* $f = 3\ \%$.

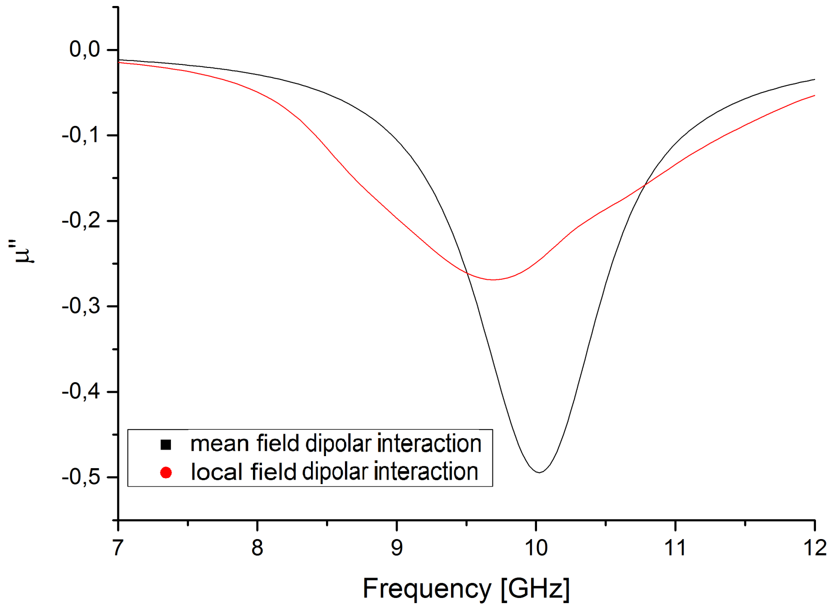

FIGURE 4.98 – *In this picture, a volume fraction of* $f = 5$ % *is regarded.*

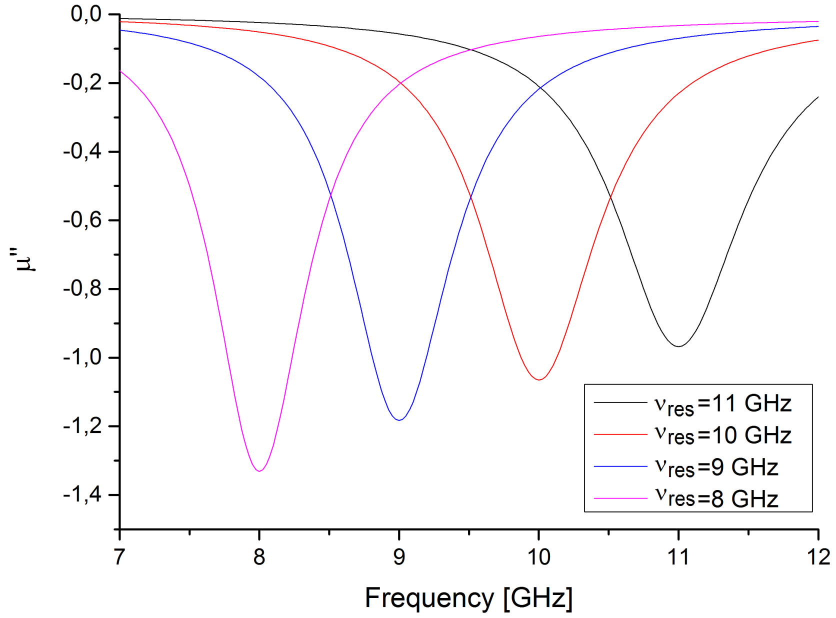

FIGURE 4.99 – *The imaginary part of* μ *according to Polder's model for infinitely extended material* ($n_x = n_y = n_z = 0$)*. Damping coefficient* $\alpha = 0.05$ *and saturation magnetization* $M_s = 30\,239.45\ \frac{A}{m}$ *are the same for every curve while static magnetic field* H *is varied in order to generate resonances in the range of* 8 *to* 11 *GHz, according to* $\nu_{res} = \frac{\gamma}{2\pi}H$.

Within this, three different tendencies can be observed: Firstly, the strength of the resonance peaks decreases while, secondly, its width grows with rising filling factor. The reason for these effects can be found in the local distribution of the effective magnetic fields in the sample: While in the mean field approach, every inclusion was exposed to the same effective field, determining and concentrating resonances at one frequency for all particles, inhomogeneous local field distributions disperse resonances

over a frequency range which grows with the filling factor. The third outcome is that resonances tend to lower frequencies when including local field distributions. In order to understand this phenomenon, one has to recall the characteristics of the implemented Polder model: When maintaining input parameters α, n_i with $i = x, y, z$ and M_s while decreasing resonance frequency by reducing H, the strength of the resonance peak is enforced (see figure 4.99). When superposing resonance curves of individual inclusions with different surrounding static magnetic fields, as it is more or less the case in the regarded composite samples, then peaks at lower frequencies are heavier weighted than at higher frequencies, wherefore resonance of the whole sample tends to lower values. Simultaneously, asymmetry of the resonance peaks increase due to the same reason.
In order to quantify these outcomes, we again try to assign material parameters for a homogeneous sample with the same dimensions, which reproduces the composites' behavior. Contrary to the previous considerations, α and $H^{loc}_{eff}(H_{inc} = const.)$ are varyed while M_{eff} is taken from former results. This strategy is founded by the already remarked widening of the resonance peak, which can be tuned via damping coefficient α, and the magnetization's independence on dipolar interactions. Within this procedure, it becomes clear that such an good agreement between homogeneous and heterogeneous samples as before is not possible in this case. Consequently, it was tried to reach a maximum of congruence at resonance peaks while disagreements in remoter frequency ranges must be accepted. The corresponding curves are shown in figure 4.100-4.102.

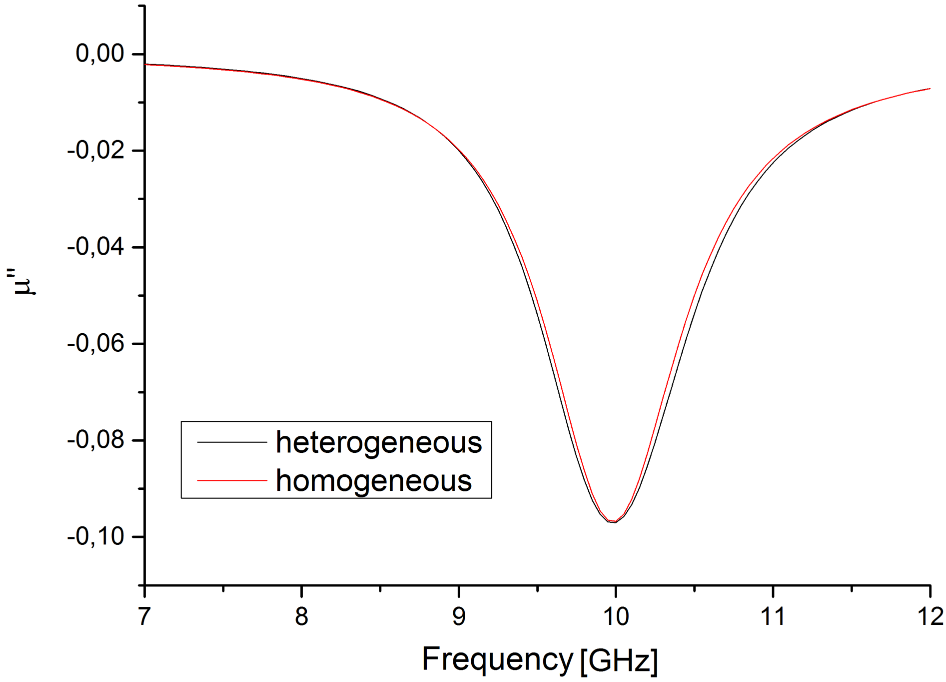

FIGURE 4.100 – *As before, we try to reproduce the behavior of the composites with homogeneous samples with the same geometry in order to eliminate boundary effects and assign effective material parameters. Picture shows results for a volume fraction of* $f = 1$ % *for which adaption can be performed with good agreement. Used input parameters for the homogeneous sample are:* $H^{loc}_{eff}(H_{inc} = const.) = 283\ 099\ \frac{A}{m}$, $M_{eff} = 2\ 865\ \frac{A}{m}$ *and* $\alpha_{eff} = 0.053$.

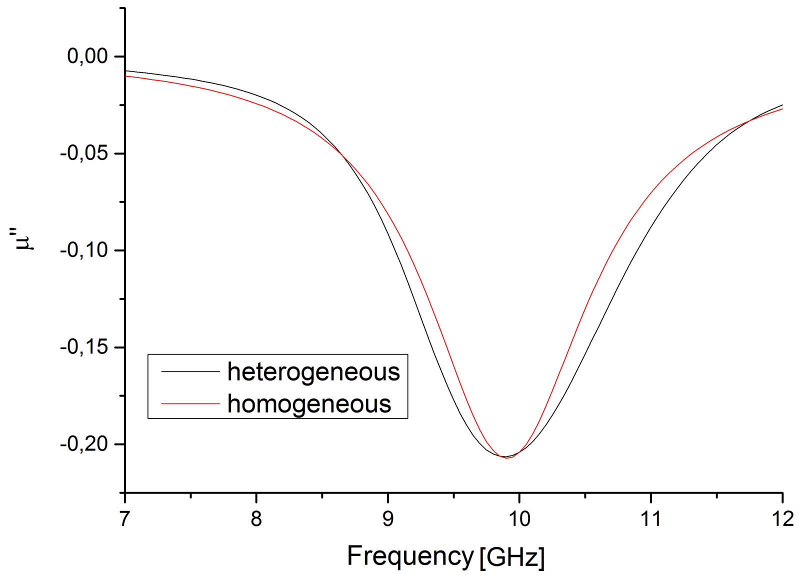

FIGURE 4.101 – *Regarding a filling factor of $f = 3$ %, differences between the homogeneous and the heterogeneous sample increase compared to lower volume fractions. Input parameters for the homogeneous sample are:* $H_{eff}^{loc}(H_{inc} = const.) = 281\ 111\ \frac{A}{m}$, $M_{eff} = 8\ 753\ \frac{A}{m}$ *and* $\alpha_{eff} = 0.075$.

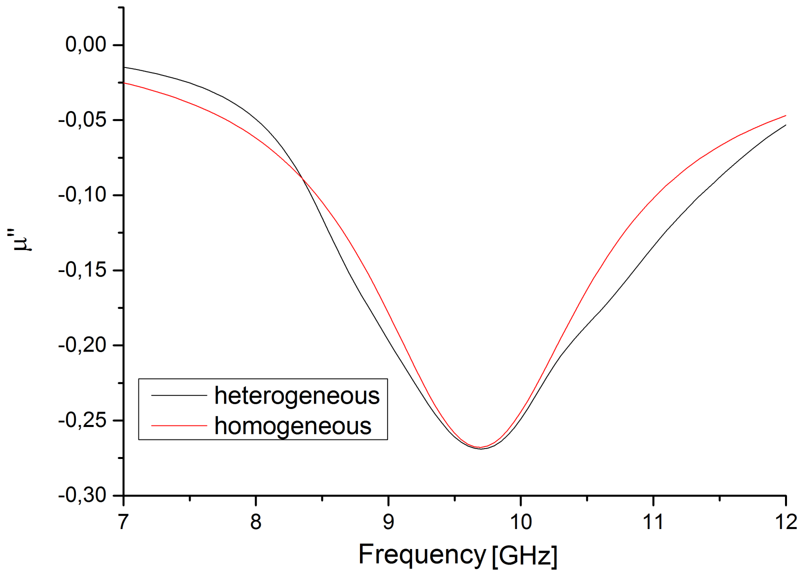

FIGURE 4.102 – *In the case of $f = 5$ %, we notice further growing variations between the resonance curves of the composite and the homogeneous device. Used input parameters for the homogeneous sample are:* $H_{eff}^{loc}(H_{inc} = const.) = 279\ 123\ \frac{A}{m}$, $M_{eff} = 14\ 722\ \frac{A}{m}$ *and* $\alpha_{eff} = 0.098$.

From these adaptions, we once again draw the local effective magnetic fields $H_{eff}^{loc}(H_{inc} = const.)$ and the effective damping parameters α_{eff} which are plotted in figures 4.103 and 4.104.

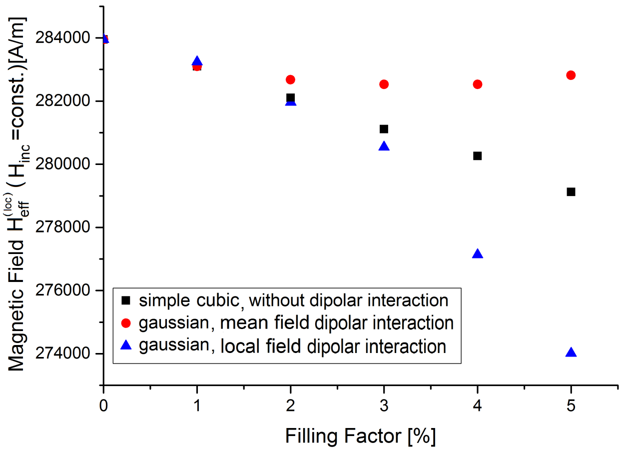

FIGURE 4.103 – *The assigned effective magnetic fields in the samples of the three regarded cases (inclusions on a simple cubic lattice, gaussianly displaced inclusions surrounded by a mean field and with inhomogeneous local field distribution), when* $H_{inc} = const.$ *is valid, are plotted in dependence on the filling factor.*

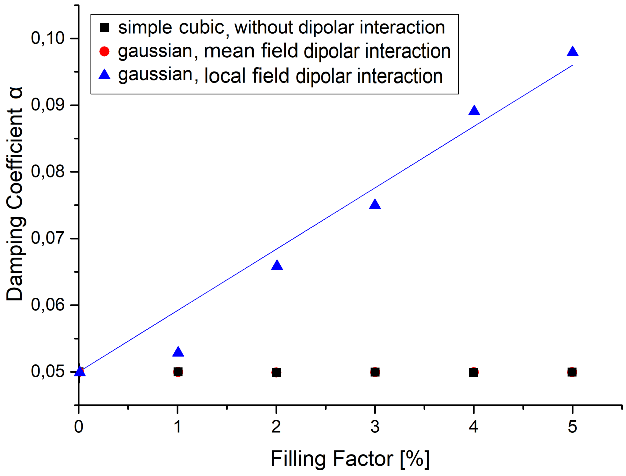

FIGURE 4.104 – *While damping coefficient previously remained constant at* $\alpha = 0.05$, *it is varyed in this case due to the broadening of the resonance peak by the field distribution. The assignment for different volume fractions is plotted and linear fitted here.*

Before we want to discuss these outcomes, we have to take into account that a conversion of the results is necessary in order to keep the effective field in the composite (corresponds to the externally applied field) constant instead of the internal magnetic biases in the inclusions (changing from $H_{inc} = const.$ to $H_{eff} = const.$), as in former considerations. As already shown in figure 4.81, dipolar interaction does not influence the present demagnetization fields in the composites. Accordingly, equation 4.20 remains valid for the purpose of receiving a constant external field. At this point, it should be again emphasized that this conversion is indeed also a mean field approach because demagnetization effects at the surfaces of the inclusions are assumed as the same at every place in the matrix. But, as already illustrated in figure 4.35, we discovered the almost perfect equivalence between this mean field approach and the local resolution of the fields in our simulations. Accordingly, this proceeding does not contain significant erros. Executing this correction, we obtain the resonance peaks shown in figure 4.105.

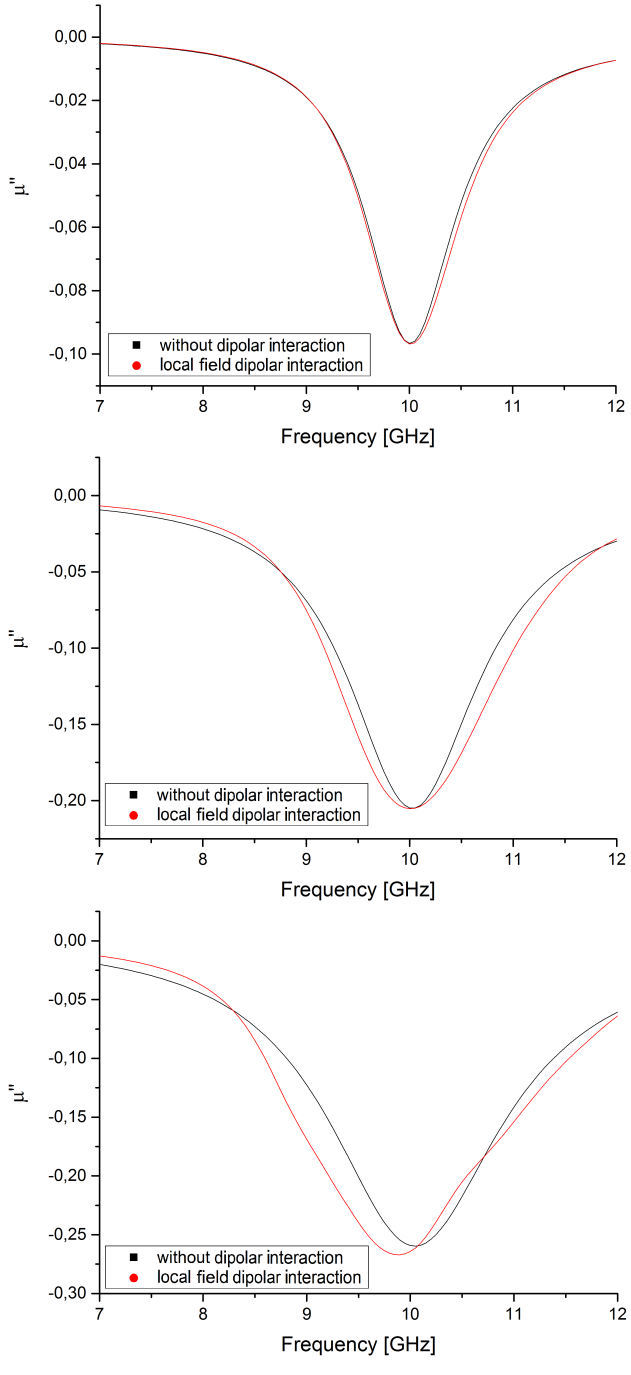

FIGURE 4.105 – *The homogeneous samples with the found effective magnetization* M_{eff} *and damping coefficient* α_{eff}*, but without dipolar interactions with regard to the magnetic field (accordingly,* H_{eff} *is given by the data set labelled with black squares in figure 4.103, inserted into equation 4.20) are compared to the corresponding composites with spatial resoluted inhomogeneous dipolar fields for the case of* $H_{eff} = const.$*. A slight tendency of the resonance peak to shift to lower values can be observed which is founded by the spatial resoluted dipolar interactions only occuring in the composites. Top picture shows the comparison for a filling factor of* $1\ \%$*, the middle one for* $3\ \%$ *and the one at the bottom for* $5\ \%$*.*

Within these plots, it can be observed that resonance frequency shifts qualitatively towards lower values. But, as in section 4.3.2.2 (see figure 4.82), the resonance curves in pictures 4.105 are influenced by the finite sample size and, therefore, can not be used in order to exactly determine resonance frequency of the composite material without boundary effects. For this purpose, we again use equation 4.48 with the values $H_{eff}^{(loc)}(H_{inc} = const.)$ from figure 4.103 and compare to the previously obtained results for the resonance behavior (see figure 4.106).

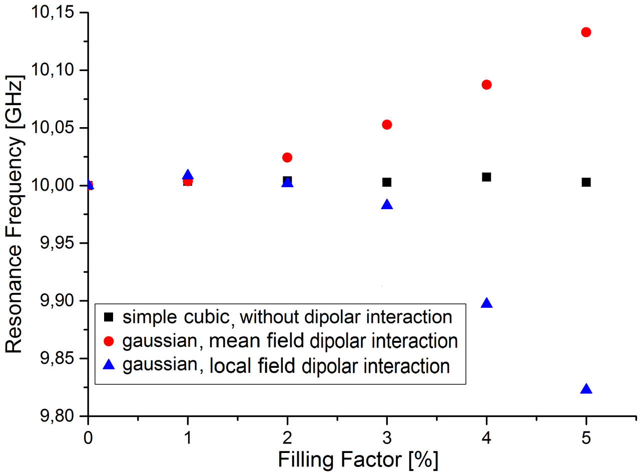

FIGURE 4.106 – *The resonance frequencies with $H_{eff} = const.$ are compared for the three regarded cases of a composite with a simple cubic inclusion lattice, i.e. without dipolar interaction, and a gaussianly disturbed lattice with a mean field approach and a local field distribution of dipolar interactions.*

First of all, with regard to figure 4.106, we want to analyze how a dependency of the resonance frequencies on the used microstructures and model assumptions is possible, when the case of $H_{eff} = const.$ is considered. For that purpose, we split off the the dipolar contribution from the total effective field

$$H_{eff} = H_{eff}^{wd} + \langle H_{dip} \rangle \tag{4.67}$$

where H_{eff}^{wd} denotes the effective field without static dipolar fields. Please note that $\langle H_{dip} \rangle$ denotes the spatial mean value of the dipolar fields in the whole sample while $\overline{H}_{dip}$ marks the average dipole fields surrounding the inclusions. Due to self-consistency (compare to equation 2.50) in the case of $H_{eff} = const.$,

$$\langle H_{dip} \rangle = 0 \tag{4.68}$$

is valid. Splitting

$$\begin{aligned} \langle H_{dip} \rangle &= f \langle H_{dip} \rangle_p + (1-f) \langle H_{dip} \rangle_m && (4.69) \\ &= f \langle H_{dip} \rangle_p + (1-f) \left(\overline{H}_{dip} + \langle H_{dip} \rangle_{m*} \right) = 0, && (4.70) \end{aligned}$$

where indices p and m denote particle and matrix phase and $m*$ the reduced matrix phase without the regions surrounding the inclusions, it becomes obvious that self-consistency can be obeyed while fluctuations between different regions in the composite are permitted, as long as they cancel each other out. Regarding that resonance frequency of one inclusion j is determined by the effective local field surrounding it

$$H_{eff,j}^{loc} = \begin{cases} H_{eff}^{wd} = H_{eff} = const. & \text{(simple cubic, without dipolar interaction)} \\ H_{eff} + \overline{H}_{dip} & \text{(gaussian, mean field dipolar interaction)} \\ H_{eff} + H_{dip,j} & \text{(gaussian, local field dipolar interaction),} \end{cases} \tag{4.71}$$

the differences in figure 4.106 can be explained by different values of the magnetic field at the surfaces of the inclusions depending on the regarded microstructure and model. Very interestingly, we observe different, superposing effects which can be isolated in the regarded models: When placing the inclusions on a simple cubic lattice in the host matrix, and thereby eliminating the influence of dipolar interactions, we found a constant resonance frequency for every volume fraction under a constant external field. Accordingly, surrounding demagnetization fields do not influence the resonance frequency of the spherical inclusions.

Using representative composites with static properties of randomly generated microstructures in the large system limit and including the average dipolar field at the places of the inclusions, we found an increasing resonance frequency in the range of $f = 1$ % to $f = 10$ %. So, we identified the influence of the dipolar interaction as resonance frequency raising.

Contrary, when including local distributions of the dipolar fields, we found the resonance's tendency to shift to lower values in the range of $f = 1$ % to $f = 5$ % which is a consequence of the blurring of the resonance peak and the properties of the Polder model. Because this model is the one which respects most of the physical circumstances in this chapter, we conclude that the resonance frequency descends for the composite systems of interest with growing filling factor of the ferromagnetic inclusions when boundary effects are eliminated and the externally applied field remains constant.

Also in this case, we want to analyze the magnitudes of μ'_{stat} and μ''_{max}. For that purpose, we firstly examine if an assignment of these both values between the composite and the homogeneous material with the determined effective parameter M_{eff}, $H_{eff}^{loc}(H_{eff} = const.)$ and α_{eff} is possible by comparing the curves of μ' and μ''. The corresponding plots are shown in figure 4.107

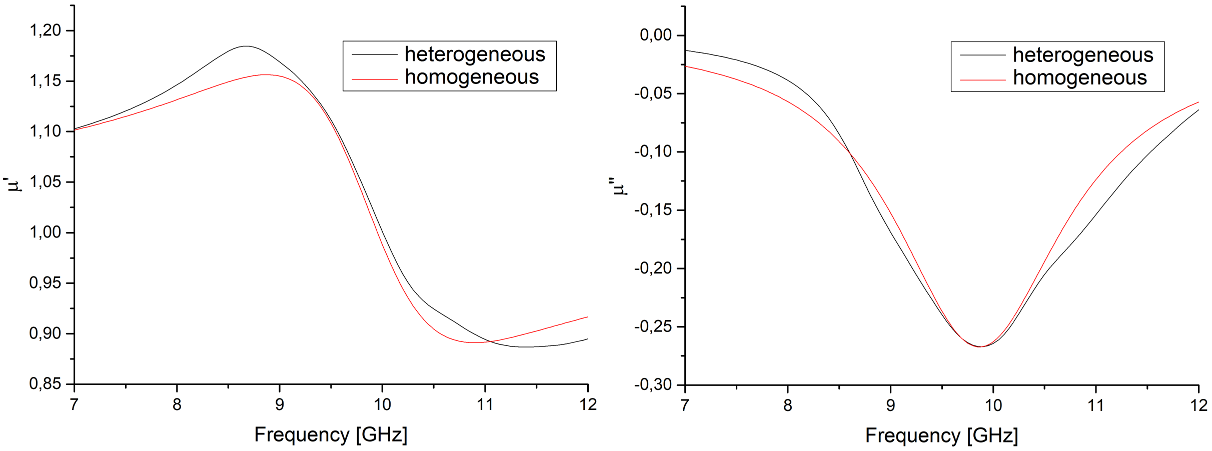

FIGURE 4.107 – *The real (left picture) and imaginary (right picture) part of* μ *of the composite with* $f = 5\ \%$ *and the homogeneous device of the same extensions with* $M_{eff} = 14\ 722\ \frac{A}{m}$, $H_{eff}^{loc}(H_{eff} = const.) = 279\ 053\ \frac{A}{m}$ *and* $\alpha_{eff} = 0.098$ *are plotted. In contrast to the effective magnetic field of the homogeneous samples regarded in figure 4.105,* $H_{eff}^{loc}(H_{eff} = const.)$ *is chosen instead of* H_{eff}*, leading to matching resonances.*

As already remarked in connection with figure 4.102, a perfect match between the permeabilities of the composite and the homogeneous medium can not be achieved anymore. Nevertheless, we notice that the values of μ'_{stat} and μ''_{max} agree despite of this. Accordingly, both values can again calculated by using equations 4.25 and 4.30 and the determined effective parameters M_{eff} and $H_{eff}^{loc}(H_{eff} = const.)$. Corresponding results are shown in figures 4.108 and 4.109 and compared to the outcomes of the previously considered models.

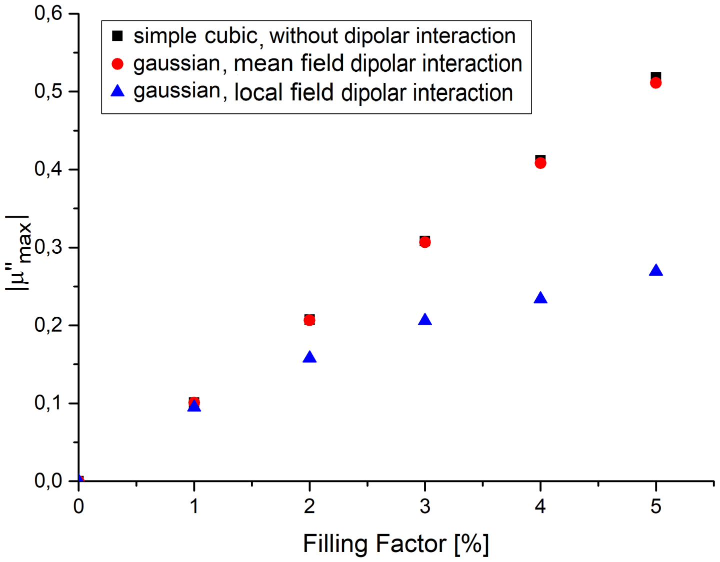

FIGURE 4.108 – *The values of* $|\mu''_{max}|$ *are plotted for the three different regarded models.*

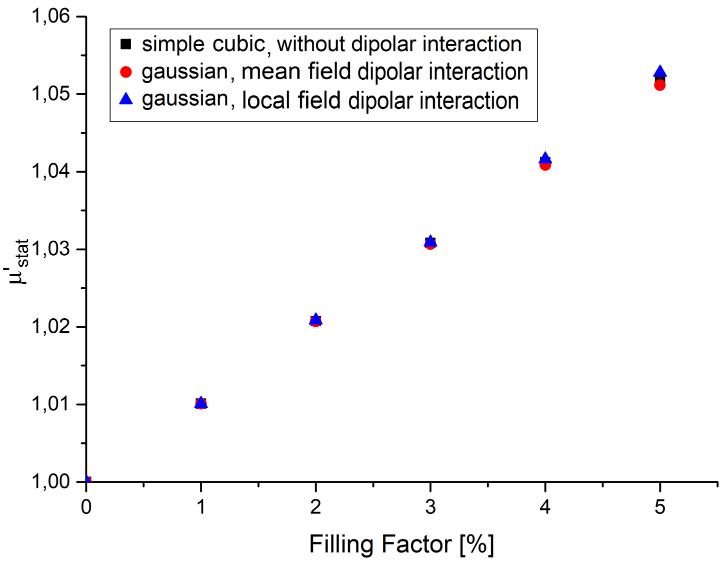

FIGURE 4.109 – *The values of μ'_{stat} are plotted for the three different regarded models.*

Comparing to the case of no dipolar interaction between the inclusions or a mean field approach with respect to the dipolar fields, we find lower values for $|\mu''_{max}|$ for an infinitely extended material in the present case. This tendency was already shown in figures 4.96-4.98 and is a consequence of the blurring of the individual resonance frequencies of the inclusions. Contrary, no significant deviations between the different models can be determined with regard to μ'_{stat}. The reason for this can be found by regarding equation 4.30: The values of $H_{eff}^{(loc)}(H_{eff} = const.)$ fluctuate only in the range of a few percent (see figure 4.103) while M_{eff} remains constant in all cases. Summarizing, we found the values of μ'_{stat} to be nearly independent from dipolar interactions. At this point, we again want to derive an analytic formula for the effective susceptibility tensor for the model of inhomogeneous field distributions inside the matrix. For that purpose, we have to analyze the three parameters M_{eff}, $H_{eff}^{loc}(H_{eff} = const.)$ and α_{eff}. Regarding the former one, we notice that the relation

$$\omega_m = \gamma M_{eff}(f) = \gamma M_s^{inc} \cdot \frac{f[\%]}{100} \tag{4.72}$$

is still valid, independent of the kind of dipolar interaction between the inclusions. Concerning the local effective magnetic field $H_{eff}^{loc}(H_{eff} = const.)$, we plot the determined values for different volume fractions and again perform a parabolic fit (see figure 4.110). This procedure yields the formula

$$H_{eff}^{loc}(H_{eff} = const., f) = (-244 \pm 97) f^2 \, \frac{\mathrm{A}}{\mathrm{m}(\%)^2} + (251 \pm 412) \frac{\mathrm{A}}{\mathrm{m}\%} f + 283950.5 \, \frac{\mathrm{A}}{\mathrm{m}}. \tag{4.73}$$

For damping parameters α_{eff}, linear fitting with the condition $\alpha_{eff} = 0.05$ for $f \to 0$ was already performed in picture 4.104, leading to

$$\alpha_{eff}(f) = \frac{(0.0092 \pm 0.0005)}{\%} f + 0.05. \tag{4.74}$$

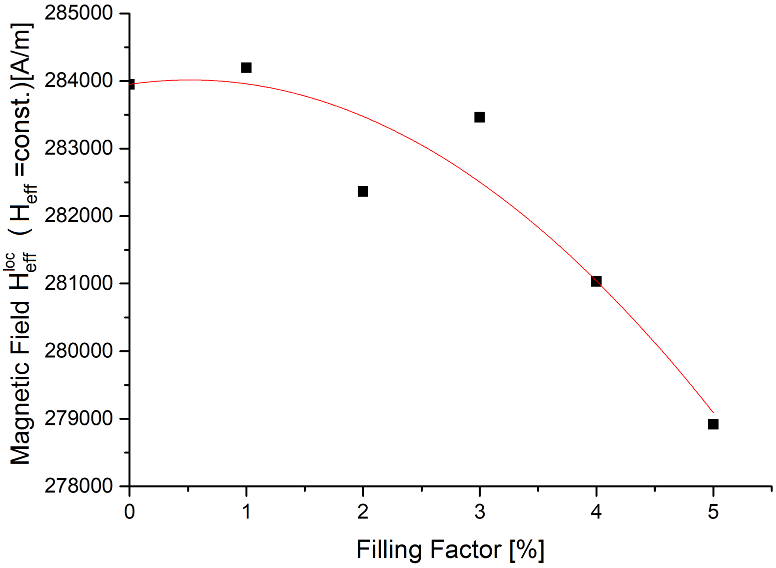

FIGURE 4.110 – *The local effective field in case of inhomogeneous field distributions inside the composite is parabolic fitted. Values shown here,* $H_{eff}^{loc}(H_{eff} = const.)$*, differ from the ones in figure 4.103,* $H_{eff}^{loc}(H_{inc} = const.)$*, by the demagnetization correction* $+\frac{1}{3}M_{eff}(f)$.

All together, we can insert these relations into Polder's model and calculate a homogeneous material approximation of the effective susceptibility tensor in the range of $f = 1$ % to $f = 5$ % which is done figures 4.111-4.113.

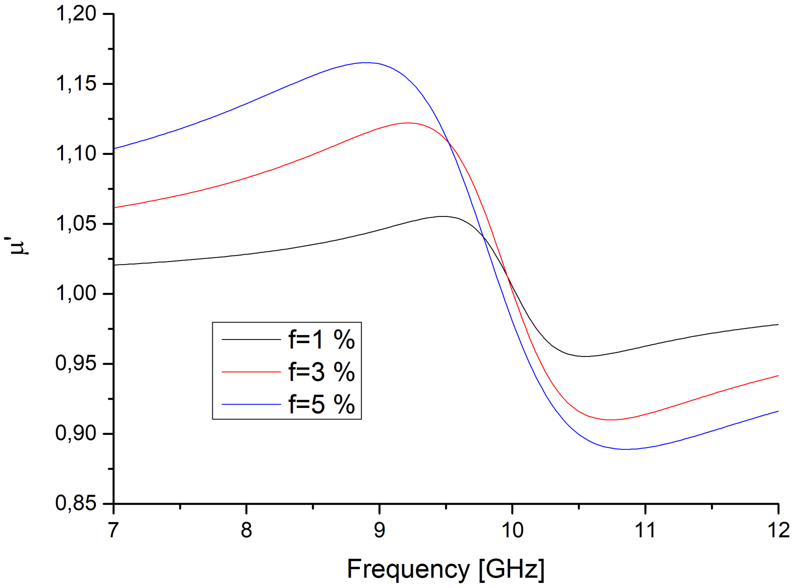

FIGURE 4.111 – *The real part of the diagonal entry of the permeability tensor for a homogeneous medium with the assigned effective parameters according to relations 4.72-4.74 is calculated for different volume fractions.*

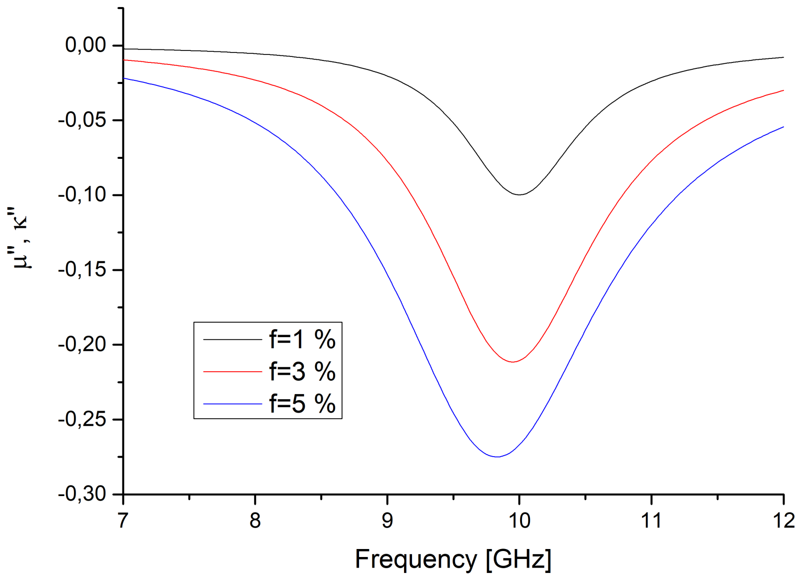

FIGURE 4.112 – *In an analog manner to figure 4.111, the imaginary parts of the diagonal and non-diagonal entries of the permeability tensor are shown.*

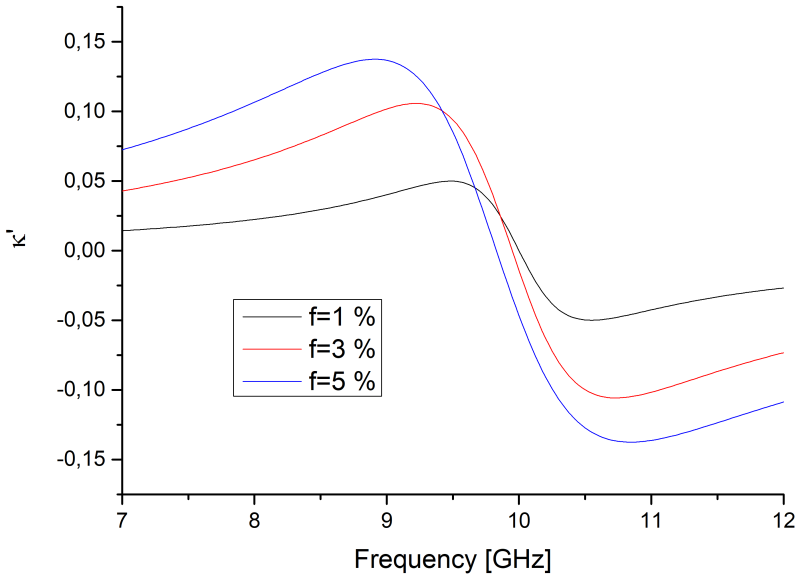

FIGURE 4.113 – *In an analog manner to figure 4.111, the real part of the non-diagonal entry of the permeability tensor is shown.*

In conclusion, we have found a set of analytic formulas which deliver the effective permeability tensor of homogeneous materials, which approximate the ferromagnetic behavior of the regarded composites in the regarded volume fraction range. Admittedly, the found relations only work for the parameter set of M_s^{inc}, H_{inc} and α at hand. It would be desirable to derive equations in which the dependencies on these magnitudes is explicitly highlighted. For achieving this, it is necessary to perform many further high-frequency simulations in the whole phase space of the regarded parameters, which can not be done in this work due to the large simulation times.

Up to there, we have analyzed the following models in this chapter:

1. Inclusions on a simple cubic lattice without static dipolar interaction
2. Inclusions with gaussian displacements without static dipolar interaction
3. Inclusions with gaussian displacements with static dipolar interaction in a mean field and a local field approach

Within this, the second model was only regarded in order to isolate the influence of the underlying microstructure. For completeness' sake, we now also regard composites in which inclusions are arranged on a simple cubic lattice, but the corresponding local effective magnetic fields are the same as for the gaussianly disturbed lattices. Comparing the susceptibilities of these composites with the results for the previously examined systems, we once again isolate the influence of different microstructures. Exemplarily, the outcomes for the composite with a filling factor of $f = 5$ % and the previously used parameters are shown in figure 4.114. For this result, we regarded the case of $H_{eff}^{loc}(H_{eff} = const.)$.

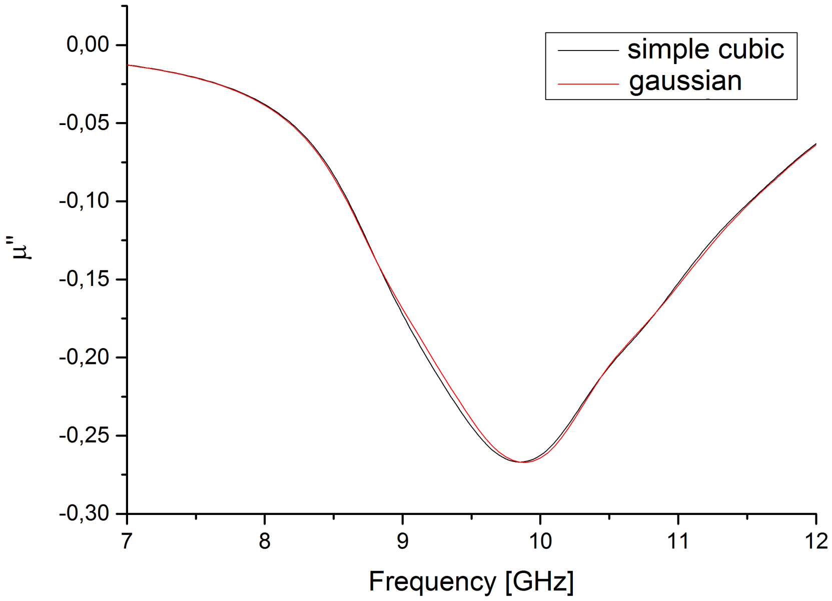

FIGURE 4.114 – *We compare the permeability of the composite with inclusions on a simple cubic lattice and on the gaussianly disturbed lattice with the same inhomogeneous field distributions in both cases for a filling factor of* $f = 5$ %.

Obviously, no significant differences can be observed. This result is in accordance with the previous finding (see section 4.3.2.1) that the regarded small changes in the microstructure do not meaningfully influence the composite's magnetic characteristics in the high-frequency simulations. Consequently, it can be followed that the exportation of the microstructure into the high-frequency simulation was not important and only the static magnetic fields surrounding the inclusions strongly influence the results.

In order to critically question the results gained in this section, one could ask if the assignment of composites to effective parameters of a homogeneous sample can also be done in another way: So far, we adjusted resonance frequencies by variation of the effective fields, the strengths of the resonance peaks via the saturation magnetizations and their width by the damping coefficients. Although this procedure is motivated by logical arguments, we also want to try another strategy: We keep effective magnetic field for every sample at a constant value of $H_{eff}^{loc} = 283952\ \frac{\mathrm{A}}{\mathrm{m}}$ (corresponding to a resonance frequency of $\frac{\gamma}{2\pi} H_{eff} = 10$ GHz for an infinite sample) and try to fix resonance curves by varying only saturation magnetization and damping coefficient. Within this, resonance frequency can be shifted towards higher values by increasing M_{eff}, due to demagnetization effects of the samples, while α can be used in order to tune the strength of the resonance peak. Indeed, this technique is successful for the composite with a volume fraction of $f = 1$ % and inhomogeneous field distribution because of the marginal frequency shift. Contrary, already for a composite with a filling factor of $f = 2$ %, linked with a more significant resonance shift towards lower values, an assignment without varying local effective magnetic field is not possible anymore (see figures 4.115 and 4.116).

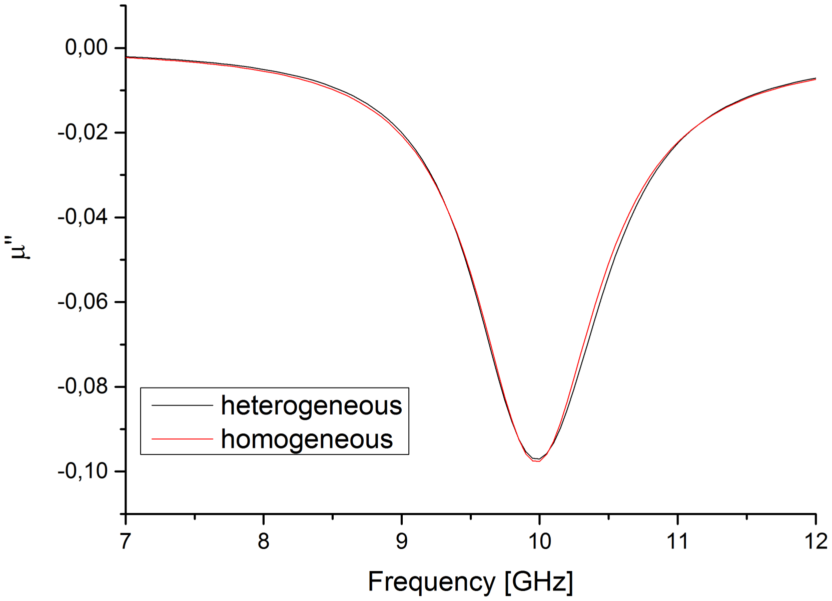

FIGURE 4.115 – *The resonance peak of the composite with a filling factor of* $f = 1$ % *and inhomogeneous field distribution is well reproduced by a homogeneous sample with parameters* H_{eff}^{loc} *corresponding to an unshifted resonance at* $\nu = 10$ *GHz (when eliminating boundary effects),* $M_{eff} = 2\ 944\ \frac{A}{m}$ *and* $\alpha_{eff} = 0.054$.

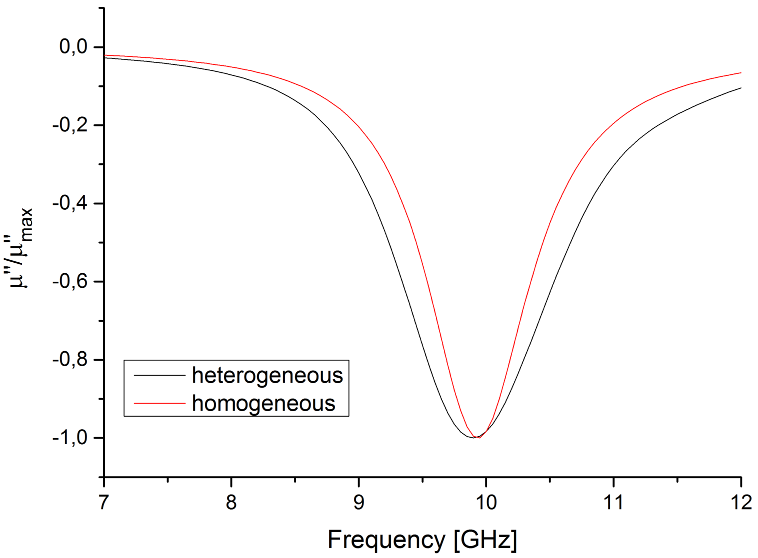

FIGURE 4.116 – *Even for* $M_{eff} = 80\ \frac{A}{m}$ *(approximately corresponding to* 1 *Gs), the resonance of the homogeneous sample appears at a slightly higher frequency as for the composite with a filling factor of* $f = 2\ \%$. *Effective local field is chosen again according to a frequency at* 10 *GHz for an infinitely extended sample and damping parameter as* $\alpha_{eff} = 0.05$. *Both curves where normalized to the maximum value of* $\mu''_{max} = |\mu''(\nu_{res})|$ *because of different orders of magnitudes of strength of the peak (homogeneous sample with* $M_{eff} = 80\ \frac{A}{m}$ *has a very weak peak) in order to highlight the different values of the resonance frequencies.*

For the purpose of highlighting that increasing saturation magnetization only allows shifts to higher frequencies while varying α_{eff} does not influence resonance frequency at all, we analyzed the resulting resonance peaks for a various set of parameters. Corresponding results are shown in figures 4.117-4.120.

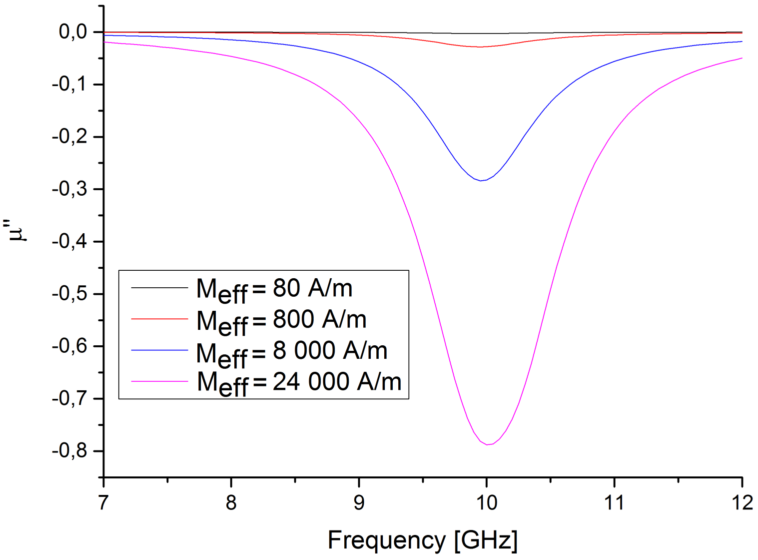

FIGURE 4.117 – *A homogeneous sample with the geometric extensions as the composite with* $f = 2\ \%$ *is analyzed with parameters* H_{eff} *corresponding to a constant resonance frequency of an infinitely extended sample at* $\nu_0 = 10$ *GHz and* $\alpha_{eff} = 0.05$ *while* M_{eff} *is varied. Picture shows absolute values of* μ'' *outlining the influence on the strength of the peak.*

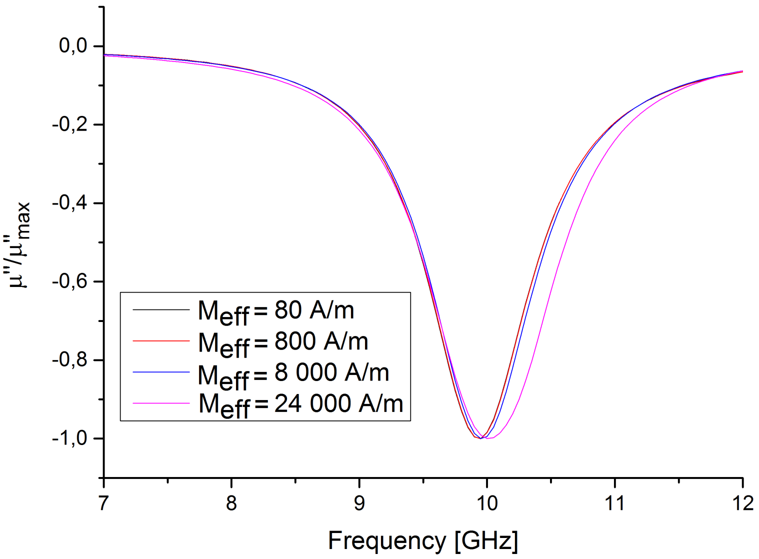

Figure 4.118 – *Curves from figure 4.117 are normalized to the maximum value of for each magnetization* $\mu''_{max} = |\mu''(\nu_{res})|$. *Obviously, resonance can only be shifted to higher frequencies, but a given minimum (which should be at* 10 *GHz, but is located at* 9.95 *GHz due to numerical errors) cannot be undershot by varying* M_{eff} *due to its restriction to non-negative values.*

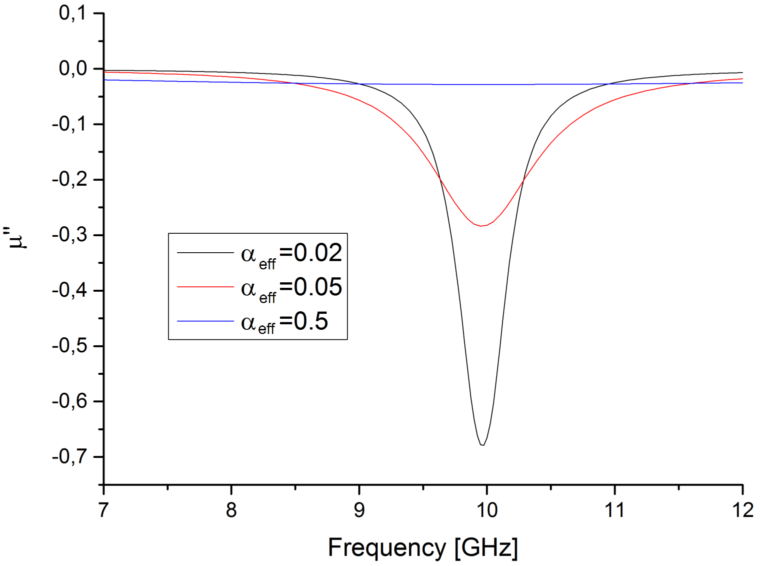

Figure 4.119 – *The same geometry with the same effective field as for results in figure 4.117 is under test, but saturation magnetization remains constant at* $M_{eff} = 8000\ \frac{A}{m}$ *while damping coefficient* α *is varied. Picture shows absolute values of* μ'' *and the damping parameter's ability of influencing the strength and the width of the resonance peak.*

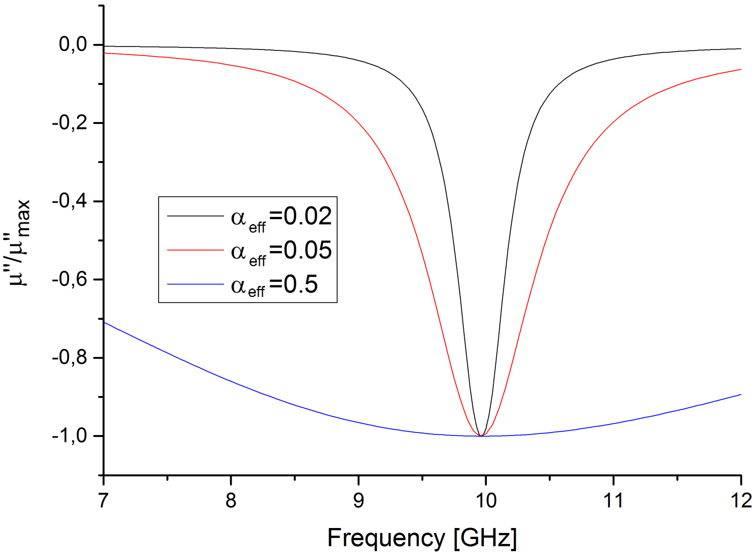

FIGURE 4.120 – *Curves from 4.119 are normalized to the maximum value of μ'', as in figure 4.118. As it can be seen, variation of damping coefficient does not influence resonance frequency.*

By this analysis, it was shown that an assignment between composite with dipolar interaction and homogeneous sample is not possible when keeping effective magnetic field at a constant value for different filling factors. Accordingly, the thesis of the resonance peaks shifting towards lower values when respecting inhomogeneous field distributions in the analyzed parameter range is supported.

4.3.2.4 Comparison with Arbitrary Random Insertion

In the previous sections, we used microstructures of composites with $N_{inc} = 27$ and $N_{inc} = 64$ which were generated with much effort compared to an arbitrary stochastic insertion of inclusions into the host matrix. In order to subsequently justify these method with regard to high-frequency simulations, we want to analyze the resonance curves of composites with such a completely random internal structure. For that purpose, we regard two devices with $N_{inc} = 64$ and a filling factor of $f = 1$ % and $f = 5$ %, shown in figure 4.121.

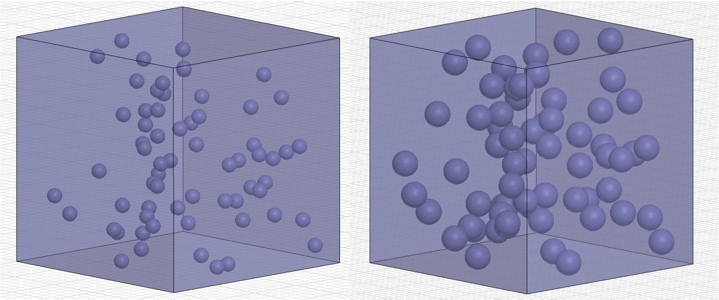

FIGURE 4.121 – *Two samples are generated by a completely stochastical insertion of inclusions without further restrictions but an exclusion of overlapping spheres. Left picture shows the composite with a volume fraction of $f = 1$ %, right picture $f = 5$ %.*

Again, we firstly neglect the influence of dipolar interactions in order to analyze the effect of the microstructure (compare to section 4.3.2.1). Corresponding resonance curves are shown and compared to results with gaussian displacements in figures 4.122 and 4.123.

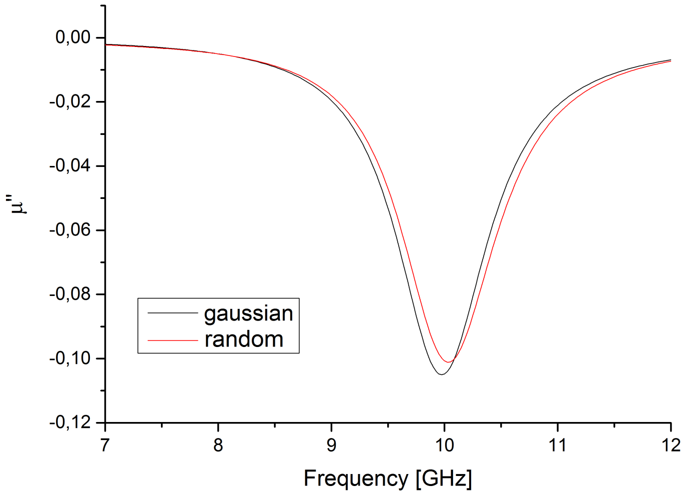

FIGURE 4.122 – *Picture shows μ'' for a sample with a filling factor of $f = 1\ \%$ and inclusions on a simple cubic lattice with gaussian displacements and purely randomly inserted inclusions. In this case, dipolar interactions between the spheres are neglected. Accordingly, all spheres hold the same internal magnetic bias of $H_{inc} = 183\ 154\ \frac{A}{m}$ while magnetization amounts $M_s^{inc} = 302\ 394.5\ \frac{A}{m}$ and damping coefficient $\alpha = 0.05$.*

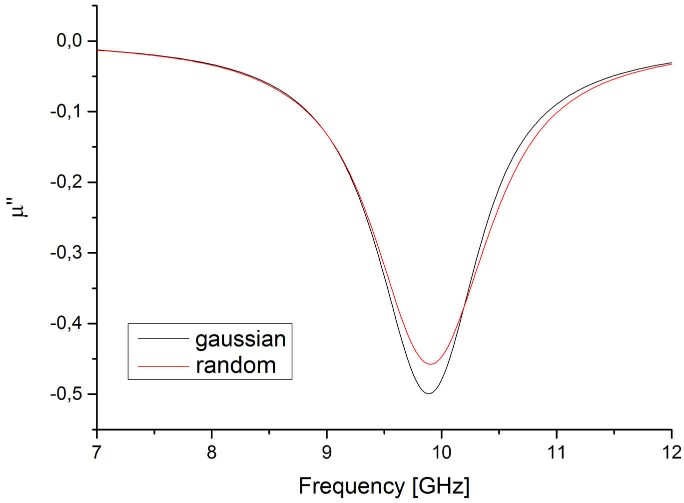

FIGURE 4.123 – *The same comparison as in figure 4.122 is done for a volume fraction of $f = 5\ \%$ with the same input parameters.*

Comparing with pictures 4.78 and 4.79, we notice more distincted deviations of the resonance curves with regard to the microstructure. Consequently, we have to search for new effective parameters of a corresponding homogeneous medium. The adaption of the resonance curves of the homogeneous by varying M_{eff} and $H_{eff}(H_{inc} = const.)$ to the respond of the heterogeneous composite is shown in figures 4.124 and 4.125.

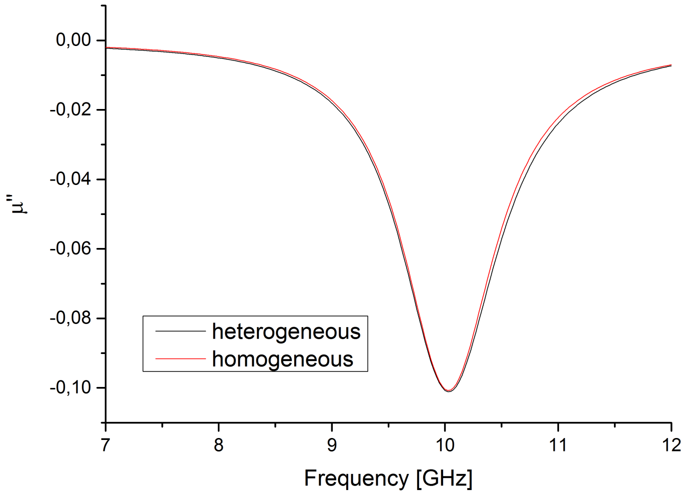

FIGURE 4.124 – *Considering the sample with* $f = 1$ %*, we determined* $M_{eff} = 2824 \frac{A}{m}$ *and* $H_{eff}(H_{inc} = const.) = 284\ 660 \frac{A}{m}$ *as adequate effective parameters of the homogeneous sample. Comparing with the previously found values for the composite with gaussian displacements of inclusions (*$M_{eff} = 2944 \frac{A}{m}$ *and* $H_{eff}(H_{inc} = const.) = 283\ 099 \frac{A}{m}$*), we notice slight differences.*

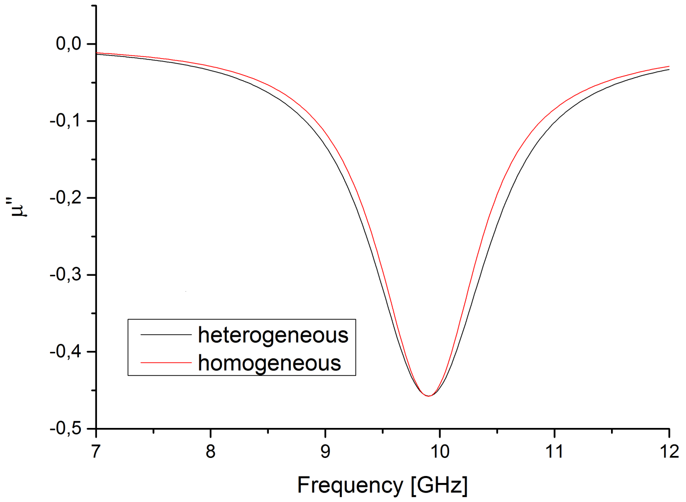

FIGURE 4.125 – *The same adaption as in figure 4.124 is done for a composite with a filling factor of* $f = 5$ %*. In this case, we find* $M_{eff} = 13\ 369 \frac{A}{m}$ *and* $H_{eff}(H_{inc} = const.) = 279\ 691 \frac{A}{m}$ *for the effective medium. For the composite with gaussian displacements, we previously determined* $M_{eff} = 14\ 722 \frac{A}{m}$ *and also* $H_{eff}(H_{inc} = const.) = 279\ 691 \frac{A}{m}$.

Using the found effective magnetization M_{eff}, we can again perform a demagnetization conversion to switch from $H_{inc} = const.$ to $H_{eff} = const.$ (see equation 4.20) and include the dipolar interactions between different spheres by respecting the inhomogeneous field distribution. Corresponding resonance curves are shown and compared with the results which were generated with the adaption method of the previous chapters in figures 4.126 and 4.127.

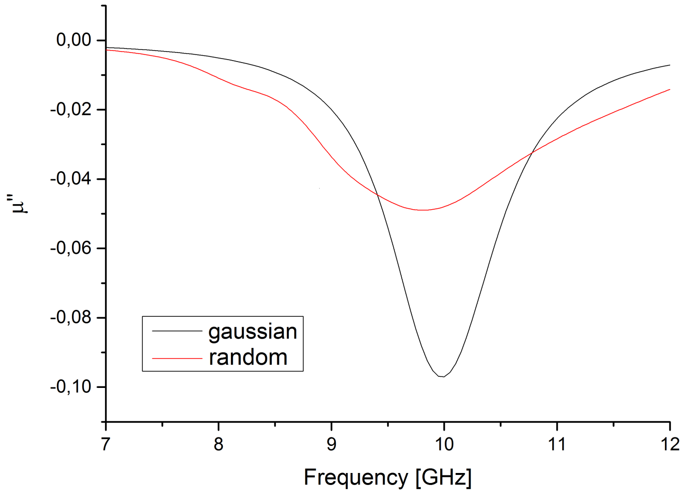

FIGURE 4.126 – *The both resonance curves of the composite with a volume fraction of* $f = 1~\%$ *and included dipolar interaction with spatial resolution. Red line shows results for the composite with purely random insertion of inclusions, black line displays the results for the method with* $H-$*field adaption with the help of gaussian displacements of inclusions.*

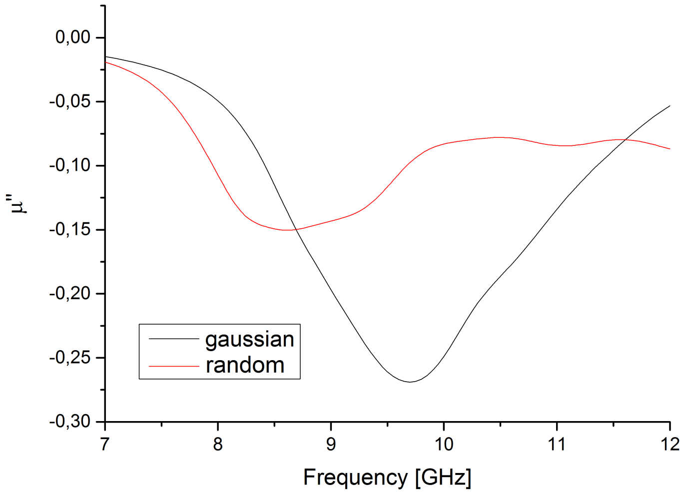

FIGURE 4.127 – *The same comparison as in figure 4.126 is done for a filling factor of* $f = 5~\%$.

Comparing these results with the ones already presented in section 4.3.2.3, we notice that the $H-$field adaption with the help of gaussian displacements is superior to the simply stochastic insertion method with regard to the supressing of artifacts due to the limited inclusion numbers: The resonance curves of composites with the stochastically inserted inclusions deviate much more from the typical shape of resonance curves in the Polder model and show a more blurred resonance peak. Accordingly, the invested effort in adapting the $H-$field distribution is an important tool in order to reduce the influences of the small systems' size and to enforce the trustworthiness of the corresponding results.

4.4 Comparison with Analytic Works

At this point, we want to compare the outworked numerical results to the analytically derived ones in previous works.
With regard to the work of Bregar [36] (see section 2.1), in which no frequency shift was predicted for different volume fractions of inclusions under a constant externally applied magnetic field when dipolar interactions are neglected, we obtain exact the same results: Arranging the inclusions on a simple cubic lattice and thereby eliminating dipolar interactions, resonance frequency remains constant while effective magnetization of the composites is given by $M_{eff} = M_s^{inc} \cdot \frac{f[\%]}{100\ \%}$.
Including dipolar interactions as in the second relevant work of Bregar [37] (see section 2.2), we distinguish two approaches, i.e. the averaging of the dipolar fields over all inclusions and applying the mean field on every included sphere on the one hand and the respecting of the spatial inhomogeneities of the dipolar fields on the other hand. In the later case, which is the most realistic model in this work, we also detected a decreasing resonance frequency for low volume fractions up to $f = 5\ \%$, as predicted in [37]. Although these results qualitatively agree with analytic predictions, quantitative deviations are obtained (see comparison of all models in figure 4.128). For clarity's sake, the different models are schematically sketched in figure 4.129

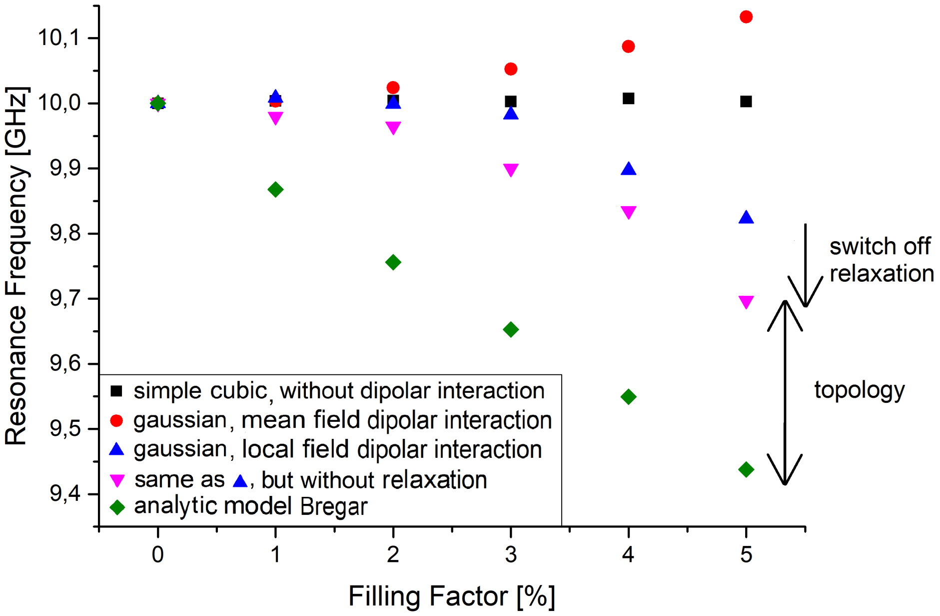

FIGURE 4.128 – *Figure 4.106 is expanded by the analytic prediction of Bregar [37] and numerical results in which no relaxation process of magnetic moments is taken into account.*

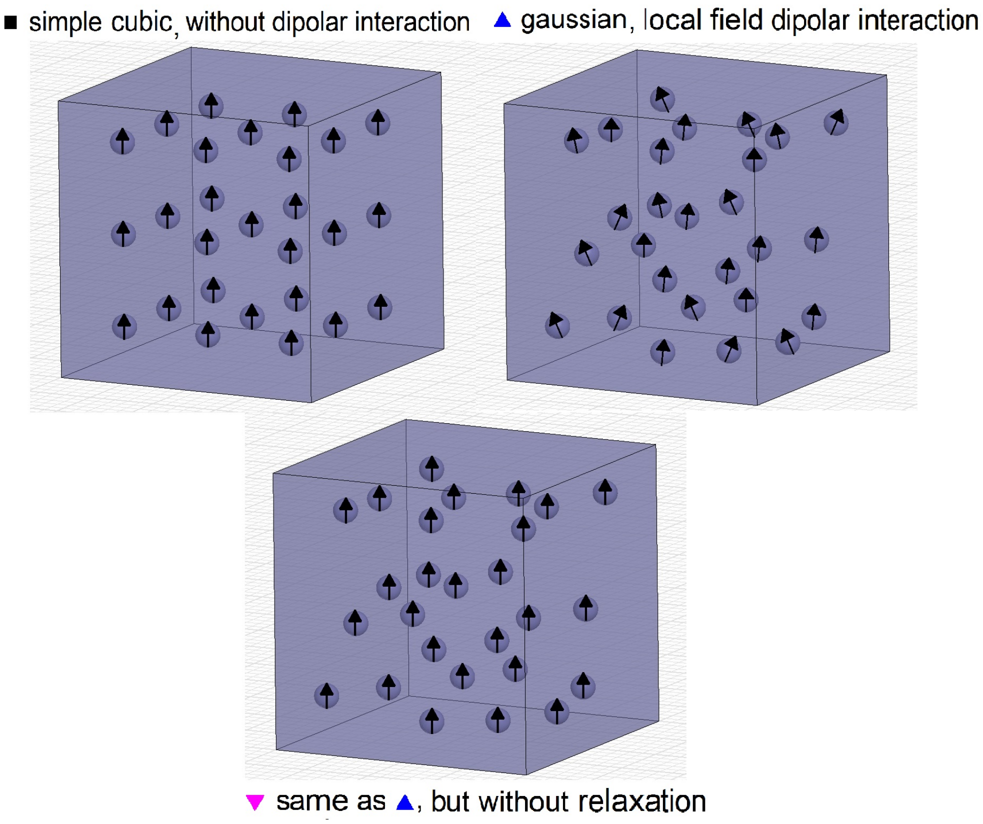

Figure 4.129 – *The corresponding models to three of the data sets shown in figure 4.128.*

Within our analyses, we noticed the raising of the averaged local field at the places of the inclusions to be a consequence of the relaxation process the of corresponding magnetic moments, which was numerically determined in static simulations. Due to the limits of analytic methods with regard to this manybody problem, the influence of this process is not regarded in the analytical model of Bregar [37]. Of course, this phenomenon also influences the results in which the inhomogeneity of the field is taken into account (blue triangles in figure 4.128). In order to examine the influence of this effect, we exclude the possibility of relaxation in our static simulation, i.e. local fields at the places of the inclusions are only once calculated, but no realignment of the moments is performed, and determine the effective parameters of such systems, when we respect these local fields (included as pink triangles in figure 4.128). As expected, results shift closer to the analytic prediction, but still not perfectly match. The main reason for this discrepancy can be found in the different topologies which are analyzed: While in [37], a structure leading to Bruggeman's mixing formula for the static case (see equation 2.54) is used for analytic calculations, which corresponds to an aggregate structure consisting out of spheres for both matrix and particle phase. As a consequence, polydispersity of these spheres is needed in order to reach a total filling factor of $f = 100$ %. As shown in section 4.3.1.3, polydispersity influences the distribution of the static dipolar fields.

Contrary, a cermet topology is numerically simulated (compare to figure 1.17) in this work. Accordingly, the presented results suggest that analytic predictions from [37] may be accurate for finely powdered samples, but overestimate the magnitude of the frequency shift for two-phase-composites in which monodispersal spherical inclusions

are homogeneously distributed in a continuous matrix.
Nevertheless, we want to compare our results for the adaption of the resonance peaks in our most complex model (corresponding to blue triangles in figure 4.128) to the prediction of Bregar [37] in figures 4.130-4.132.

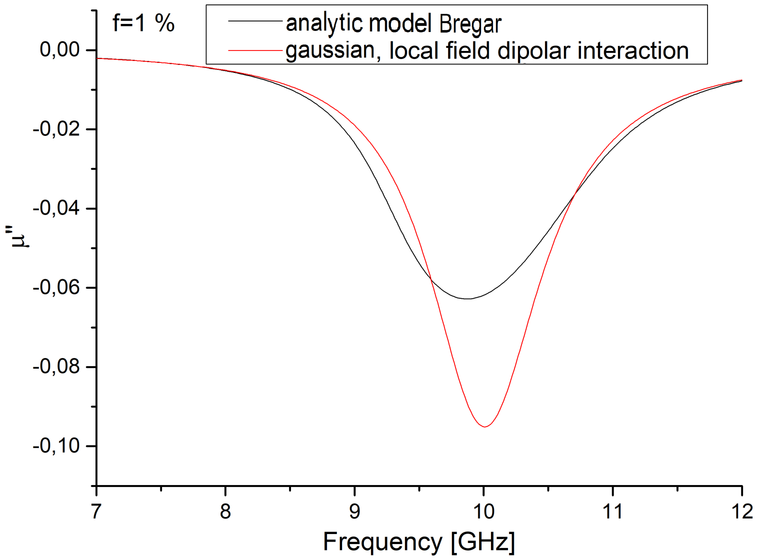

Figure 4.130 – *The resonance curve according to the analytic prediction from [37] and the results for the here presented model with inhomogeneously local dipolar interactions with relaxation. Filling factor amounts* $f = 1\ \%$.

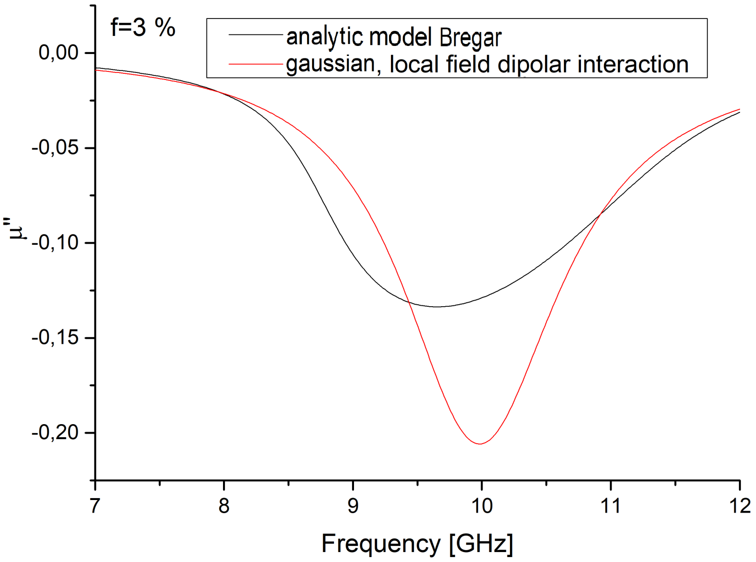

Figure 4.131 – *Same comparison as in figure 4.130 for a volume fraction of* $f = 3\ \%$.

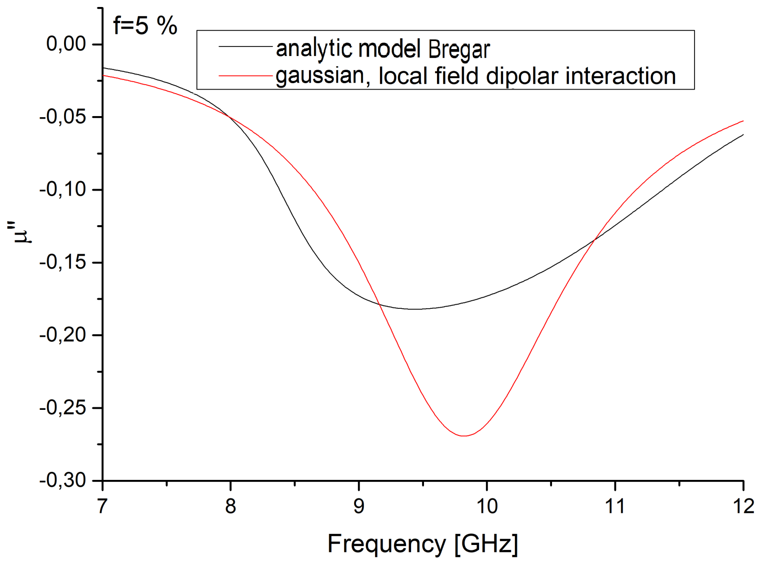

FIGURE 4.132 – *Same comparison as in figure 4.130 for a volume fraction of* $f = 5$ %.

In these graphs, we again observe qualitative accordance: For rising filling factors in this range, peaks shift towards lower resonance frequencies while broadening. Within this, strength of the peaks in the model of Bregar are more pronounced, which is separately analyzed in figure 4.133.

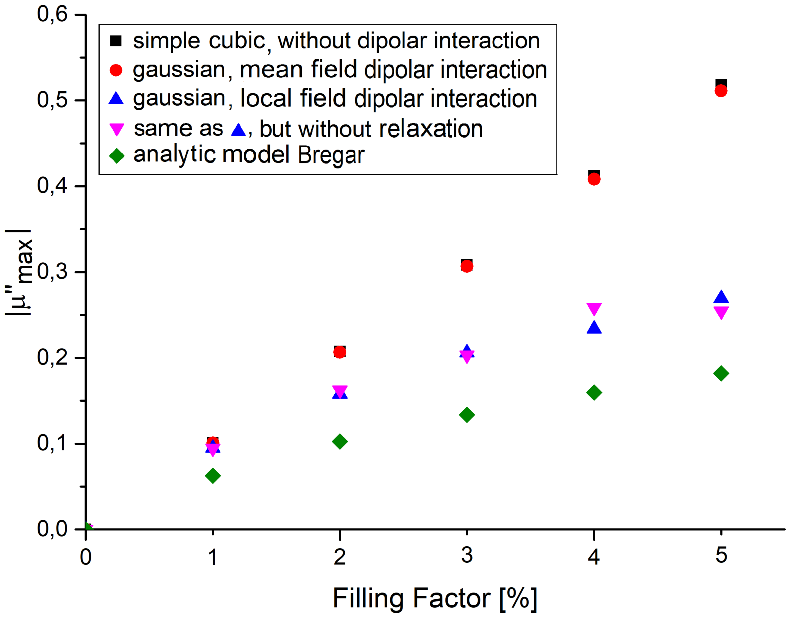

FIGURE 4.133 – *The maximum values of the resonance curves of the five regarded models as in figure 4.128 are plotted.*

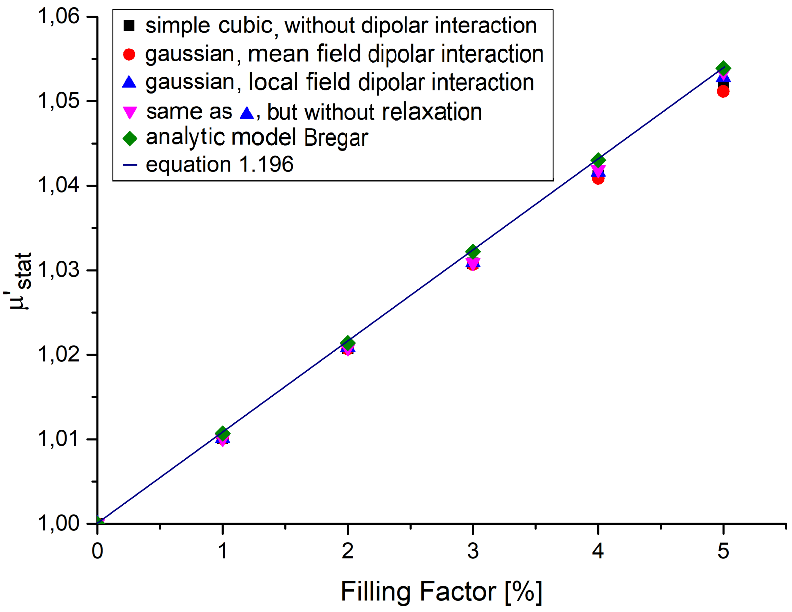

FIGURE 4.134 – *Figure 4.108 is expanded by Bregar' results and the regarded model with inhomogenenous fields without relaxation. Moreover, results according to equation 1.196 are drawn as line. The used parameters lead to a static particle permeability of* $\mu_{inc}^{stat} = 2.065$.

Obviously, the relaxation process does not influence the values of μ''_{max} as we learn from the matching of the results from the model without dipolar interaction (black squares in figure 4.133) and the mean field dipolar interaction (red circles) as well as from the regarding of the local fields with and without relaxation (blue and pink triangles). Only the widening of the peaks, caused by the inhomogeneous field distribution in the samples, reduces these values. As already remarked, this phenomenon is more distinct in Bregar's model.

Additionally, we also want to analyze the outcomings for the static permeability μ'_{stat}. As can be seen in figure 4.134, all results from this work and Bregar's analytic prediction, corresponding to Bruggeman's mixing formula, deliver almost the same results. Furthermore, values resulting from equation 1.196 are included, which are in accordance with the outcomings in the work of [36] (see equation 2.36), in which

$$\chi_{eff} = f\chi_{inc} \tag{4.75}$$
$$\Leftrightarrow \mu_{eff} = 1 + f\chi_{inc} \tag{4.76}$$
$$= (1-f) + f(1+\chi_{inc}) \tag{4.77}$$
$$= (1-f)\mu_m + f\mu_{inc} \tag{4.78}$$

is predicted. According to this, differences in the various models do not influence the static behavior of the composites due to the very small deviations from the parallel alignment of the magnetic moments. Consequently, discrepancies are restricted to the vicinity of the ferromagnetic resonance.

4.5 Chapter Summary

In this chapter, we investigated the magnetic response of infinitely extended composite materials with ferromagnetic inclusions in a non-magnetic matrix. For that purpose, we firstly dealt with preparatory work in which we examined the convergence of the ferromagnetic resonance curves with respect to various simulation and analysis parameters. In this context, we located inclusions on a simple cubic lattice in order to eliminate the dependence of the results on the present microstructure when comparing different samples. As a byproduct, this arrangement simplified the problem on hand because the neglection of dipolar interactions between the included ferromagnetic spheres is justified.

In order to analyze the behavior of samples with different volume fractions of inclusions, inclusion number and radius was kept constant ($N_{inc} = 27$ or $N_{inc} = 64$ with $r_{inc} = 0.0445$ cm or $r_{inc} = 0.0334$ cm, respectively) in order to avoid simulations' memory requirement to exceed the available resources while the geometric extensions of the host matrix were adjusted. In the following, the comparison between heterogeneous composite materials and homogeneous effective samples was used in order to eliminate the influences of boundary effects of the sample on the results and draw conclusions on geometry-independent material properties. During these examinations, a surprisingly high accordance of the resonance curves of the effective and the composite material has been detected.

Within the analysis of the results, a fundamental issue has to be obeyed: In experimental works, the static magnetic field, which is externally imposed on the samples, is kept constant in order to examine a possible resonance shift of the devices under test for different filling factors of ferromagnetic material. Contrary, in our simulation sequences, we have to define an internal magnetic bias of the ferromagnetic inclusions. Due to demagnetization effects at the boundaries between magnetic and non-magnetic domains in the composite, internal fields in the inclusions and the externally applied fields do not correspond to each other. Fortunately, this disagreement can be overcome by a demagnetization correction and the knowledge of the effective magnetization of the composite material which was already gained in previous simulation runs. Actually, the used proceeding for the demagnetization correction is a mean field approach, which, however, has been shown to be very accurate. In the here examined case of infinitely extended samples, no further demagnetization effects at the composite's outer boundaries have to be taken into account, leading to an equivalence of the effective field in the sample and the externally applied field. According to these approaches, it was shown that resonance frequency of samples with spheric inclusions on a simple cubic lattice, for which dipolar interactions can be neglected, is independent on the volume fraction of the ferromagnetic material and remains constant under a constant external static field.

In the following, we were interested in randomly generated microstructures. For that purpose, we firstly analyzed the influence of the assumptions in the static field calculations, which were necessary for a meaningful inclusion of dipolar interactions, and their convergence behavior with respect to inclusion numbers. Within this, it became obvious that large numbers of $N_{inc} \geq 5\,000$ are necessary in order to generate adequate field distributions inside the samples. Consequently, we had to develop a strategy in order to reproduce this behavior with much lower inclusion numbers to which we are restricted in the high-frequency simulations. The corresponding solution was found in the following procedure: Firstly, we again started with inclusions on a simple cubic lattice, but added randomly generated and gaussianly distributed vectors to their positions. Subsequently, the corresponding distribution of the local magnetic fields at the inclusions' centers is calculated and compared to the large system limit. Then, an error function is defined which delivers a quantitative tool in order to compare the deviation between the two distributions. Now, small systems are generated and the corresponding error function is calculated until it undershots a given treshold. Afterwards, the found microstructures and the calculated field distributions are used for analog simulation sequences as in the first section with inclusions on a simple cubic lattice. Here, three different models are examined: Firstly, we investigated the pure influence of the new microstructure by neglecting the additional appearing dipolar fields. By this, we showed that the regarded small displacements from the simple cubic lattice do not influence the results. Consequently, ferromagnetic resonance still remains constant in this case when externally applied field also remains constant. Secondly, we performed a mean field approach, meaning that the local distribution of the calculated dipolar fields was neglected, but the average field is considered to be present at the place of every inclusion. Repeating the comparison with homogeneous samples and the demagnetization correction, we showed the resonance frequency to increase with higher volume fractions of ferromagnetic material in the regarded parameter range. Thirdly, we also included the local field distribution into our high-frequency simulations, leading to an inverted behavior of the resonance frequency, which now shifts towards lower values for rising filling factors. This effect can be explained by the characteristics of the Polder model for ferromagnetic materials in usage. Especially, the counteracting behaviors of the last two models with included dipolar interactions highlight that the mean field approach leads to inverted and, consequently, wrong results. Despite these interesting outcomes, one has to admit the appearance of artifacts due to low inclusion numbers in high-frequency simulations which become more influential for higher filling factors. Accordingly, we must restrict to volume fractions up to 5 % in the simulations with the consideration of spatial resoluted field distributions. Thereby, results which are in qualitative accordance with previous analytic works are obtained. Reasons for deviations can be found in the effect of magnetic moment relaxation, calculated in static simulations in this work, but not accessible in analytic calculations, and the different considered topologies.

Summarizing, the results in this chapter delivered a fundamental insight into different effects which play important roles in the behavior of the resonance frequency of the composite material of interest.

Chapter 5

Examination of Finite Samples

In the previous chapter, we noticed that the measured permeabilities of samples strongly depends on their geometry (see figure 4.23). This influence was erased by the implementation of periodic boundary conditions in the static calculation of the inclusions' magnetic moments and comparison of the results of the dynamic simulation with homogeneous samples with identical extensions. Contrary, in this chapter, we want to gain further insights into the behavior of finite samples under various conditions in order to explain results drawn from real experiments in rectangular waveguides.

5.1 Homogeneous Inclusion Distribution

As a starting point, we investigate finite samples with homogeneously distributed spheres and firstly regard the calculation of the magnetic orientation of the inclusions when a static magnetic field is applied in $z-$direction. Accordingly, we switch off periodic boundary conditions in these simulation runs and, once again, increase inclusion numbers until convergence in the mean values of internal magnetic fields and their distribution is reached, as in section 4.3.1.1. As three different types of geometries we use a cubic sample with edge length $a_x = a_y = a_z = 1$ cm, a cuboid with halved length in propagation direction ($a_x = 0.5$ cm, $a_y = a_z = 1$ cm) and a cuboid with doubled length in propagation direction ($a_x = 2$ cm, $a_y = a_z = 1$ cm) and choose inclusions' diameter according to their number and the desired volume fraction f. Accordingly, matrix extensions do not vary with filling factor, as it was the case in the examination of infinite samples. Strength of the static magnetic field is chosen in such away that resonance of an isolated sphere occurs at $\nu_{res} = 10$ GHz, as before. Moreover, ferrite parameters are also identical to previous considerations, i.e. $M_s^{inc} = 302\ 394.5\ \frac{A}{m}$ and $\alpha = 0.05$. Convergence analysis is done for $f = 1\ \%$ and $f = 10\ \%$ for each of the three geometries, highlighting that a number of $N_{inc} \geq 10\ 000$ inclusions is sufficient in every case (see figures 5.1-5.8).

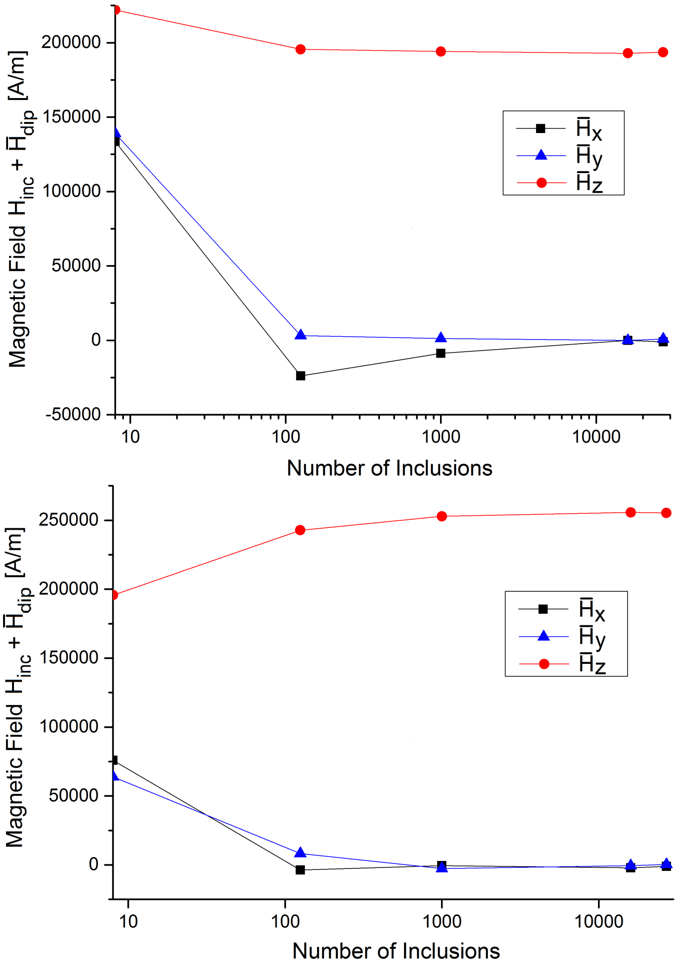

FIGURE 5.1 – *Convergence analysis of the mean values of the magnetic field components in the inclusions of the cubic sample. As before,* $\overline{H}_x$ *and* $\overline{H}_y$ *can be ignored comparing to* $\overline{H}_z$*.Top picture shows the case of* $f = 1$ %*, bottom* $f = 10$ %.

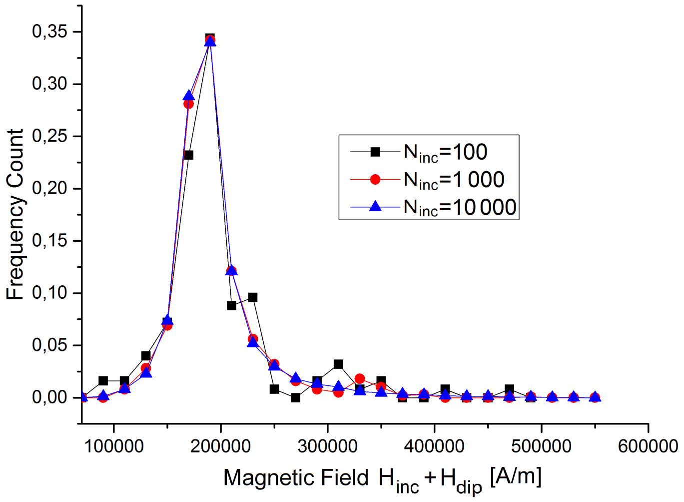

FIGURE 5.2 – *Convergence analysis of the distribution of the internal* $z-$*components of the magnetic fields inside the ferrite spheres in the cubic sample for different inclusion numbers. Picture shows the case of* $f = 1$ %.

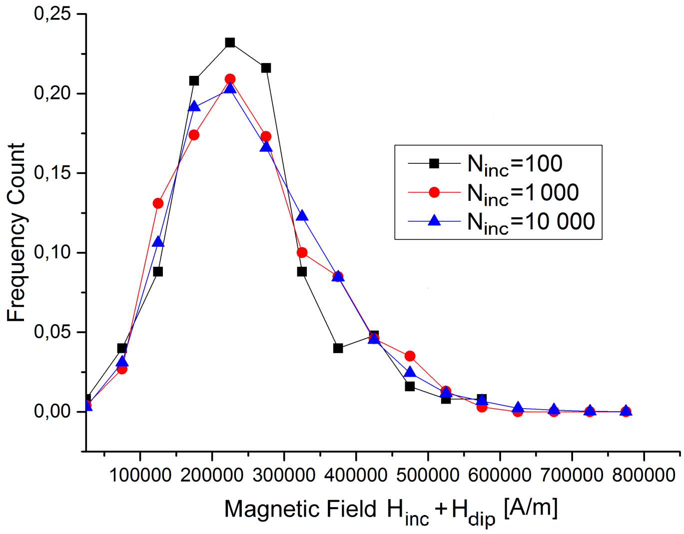

FIGURE 5.3 – *The same analysis as in figure 5.2 for a filling factor* $f = 10\ \%$.

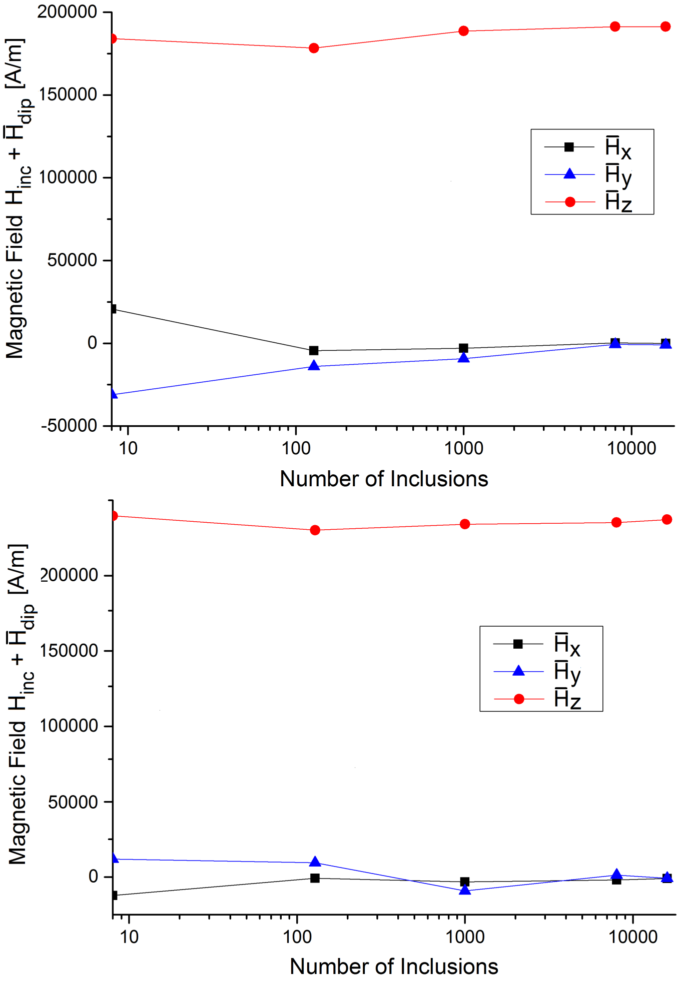

FIGURE 5.4 – *Convergence analysis of the mean values of the magnetic field components in the inclusions of the sample with doubled length. Top picture shows the case of* $f = 1\ \%$*, bottom* $f = 10\ \%$.

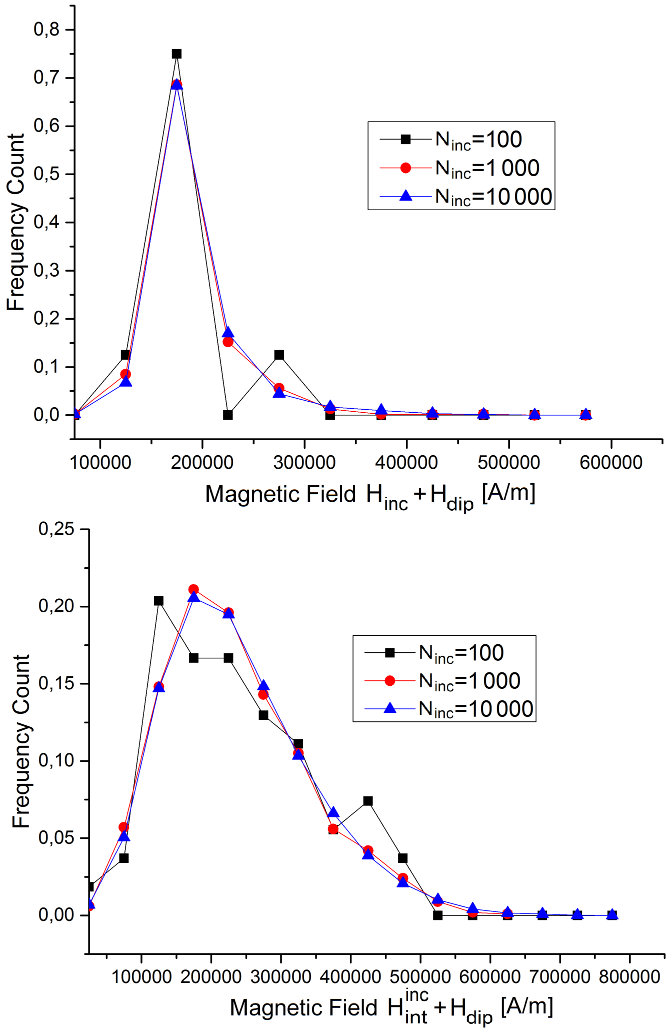

FIGURE 5.5 – *Convergence analysis of the distribution of the internal* $z-$*components of the magnetic fields inside the ferrite spheres in the sample with doubled length. Upper picture shows the case of* $f = 1$ %, *lower for* $f = 10$ %.

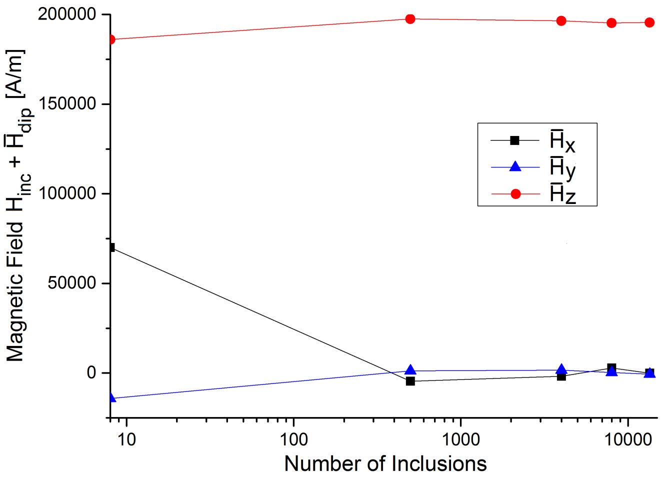

FIGURE 5.6 – *Convergence analysis of the mean values of the magnetic field components in the inclusions of the sample with halved length. Picture shows the case of* $f = 1$ %.

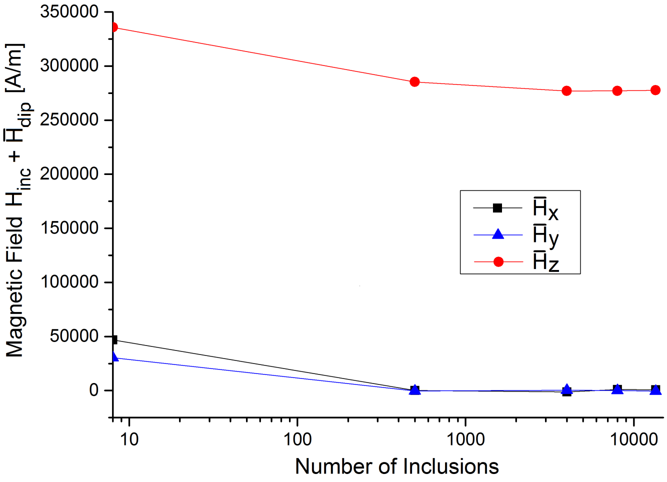

FIGURE 5.7 – *The same analysis as in figure 5.6 for a filling factor* $f = 10$ %.

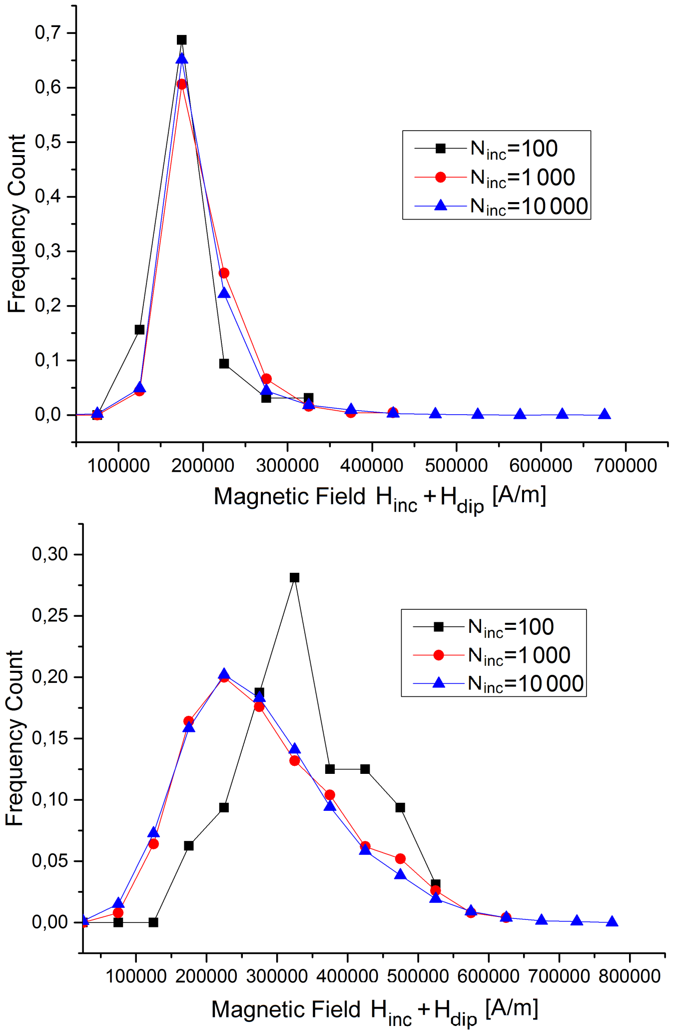

FIGURE 5.8 – *Convergence analysis of the distribution of the internal* $z-$*components of the magnetic fields inside the ferrite spheres in the sample with halved length. Top picture shows the case of* $f = 1$ %*, bottom* $f = 10$ %.

Accordingly, we use a sufficiently high number of $N_{inc} = 10\ 000$ randomly distributed inclusions and perform static simulation runs for each of the geometries in the given range of $f = 1\ \%$ to $f = 10\ \%$. Thereby, we determine the behavior for the mean values of the $z-$component of the magnetic field $\overline{H}_z$ at the places of the inclusions which is shown in picture 5.9 while we again neglect the components H_x and H_y, because $\overline{H}_z \gg \overline{H}_x, \overline{H}_y$ is still fulfilled.

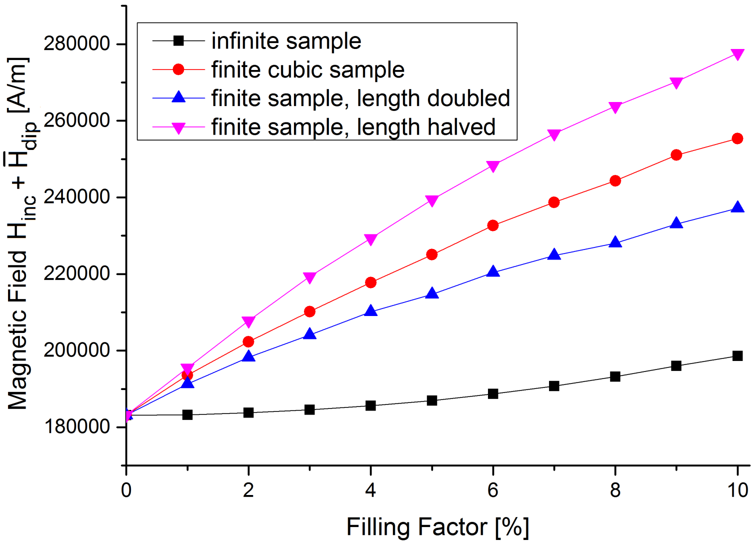

FIGURE 5.9 – *The mean values of the z-component of the magnetic field at the places of inclusions for different geometries. Obviously, the infinite sample produces the slowest increase with growing filling factor, while a reduced length enforces the magnetic field more compared to both other extensions of the finite device. This highlights the strong influence of the geometry on the results. Here, the case of $H_{int} = 183\ 154\ \frac{A}{m} = const.$ for all volume fractions is examined*

.

As in the previous chapter, we want to transfer these results into high-frequency simulations in HFSS and MOR. Once again, we have to reproduce the H-field distribution in the sample with much less spheres in the matrix due to the high memory consumption in HFSS. For the purpose of finding representative microstructures with low inclusion numbers and the static properties of the large system limit, the same strategy of $H-$field adaption is chosen as in section 4.3.1.2 while the volume fraction is chosen in the range of $f = 1\ \%$ to $f = 5\ \%$, for the same reason as in section 4.3.2.3.

In this context, the question appears if there are strong differences in the values of the magnetic field between core and periphery of the host matrix. In order to follow this issue, we firstly regard the internal magnetic fields of the inclusions which are placed in a cross section of thickness $a/5$ around $z = a/2$ parallely orientated to $x - y-$area (see figure 5.10). Within this, a again denotes the edge length of the cubic sample. Moreover, we divide this cross section into 20 circular sections (see picture 5.11), in which we regard the average magnetic field inside the inclusions. As in the former static simulations, we analyze composites with an inclusion number of $N_{inc} = 10\ 000$ in the following. Moreover, we examine the case of $H_{inc} = 183\ 154\ \frac{\mathrm{A}}{\mathrm{m}} = const.$ for different volume fractions.

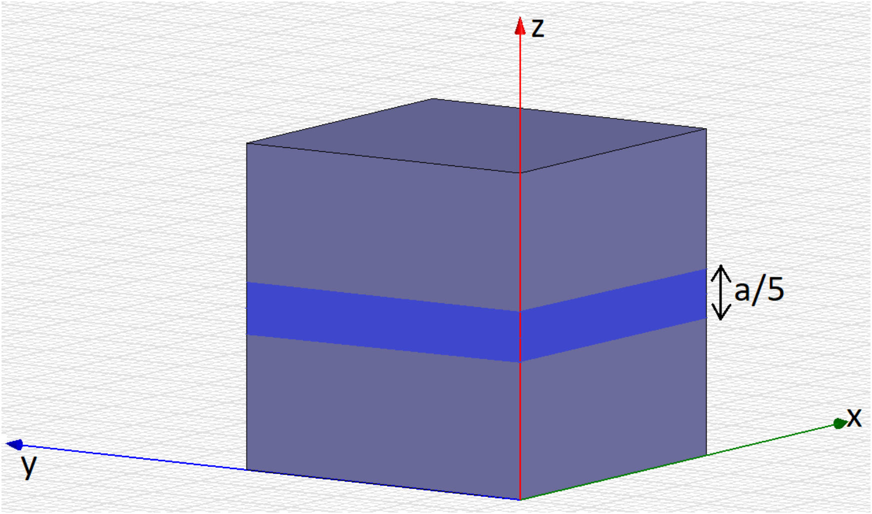

FIGURE 5.10 – *The internal magnetic fields of the inclusions in the blue cross section are analyzed in order to study boundary effects in the finite samples. For clarity's sake, no inclusions are drawn in the picture.*

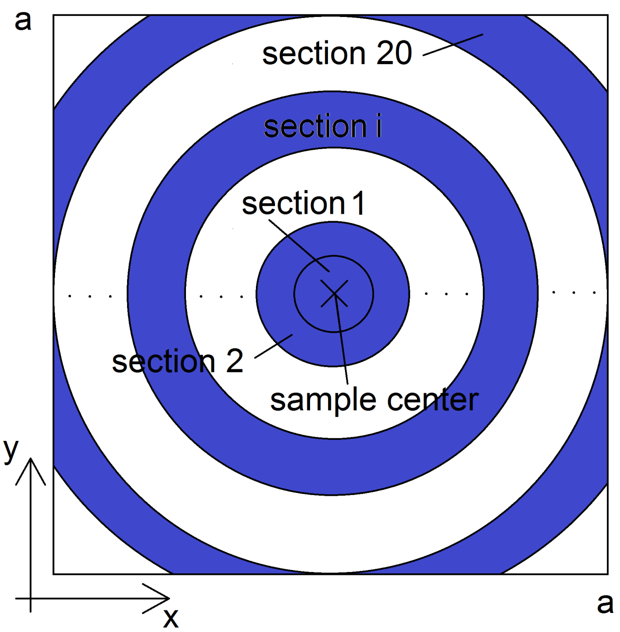

FIGURE 5.11 – *The observed cross section of the composite is again divided into* 20 *sections which are defined by the distance to the sample center. Areas outside of section* 20 *are small do not contain any inclusions. This schematic sketch is not true to scale.*

First of all, we analyze the $H-$field distribution in the shown cross section when spheres are arranged on a simple cubic lattice in order to gain first insight into this question. Corresponding results are shown in figure 5.12.

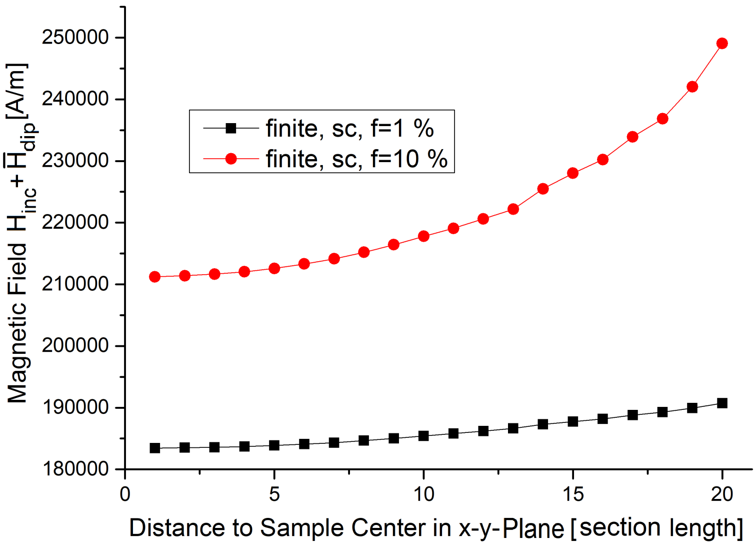

FIGURE 5.12 – *The cross section as shown in figure 5.10 is regarded for composites with a simple cubic lattice of inclusions with volume fractions of* $f = 1$ % *and* $f = 10$ %*. The distance from the midpoint of the considered area is divided into 20 sections in which field values are averaged.*

Within this, a strong dependence of the magnetic field on the position inside the matrix becomes obvious: Values are very high in the periphery of the sample, but decrease when approaching the core. An explanation for this phenomenon becomes obvious by repeating the calculations in equations 4.4-4.12 (corresponding to figure 4.16), but at the $x-z-$boundary of the sample, schematically illustrated in figure 5.13.

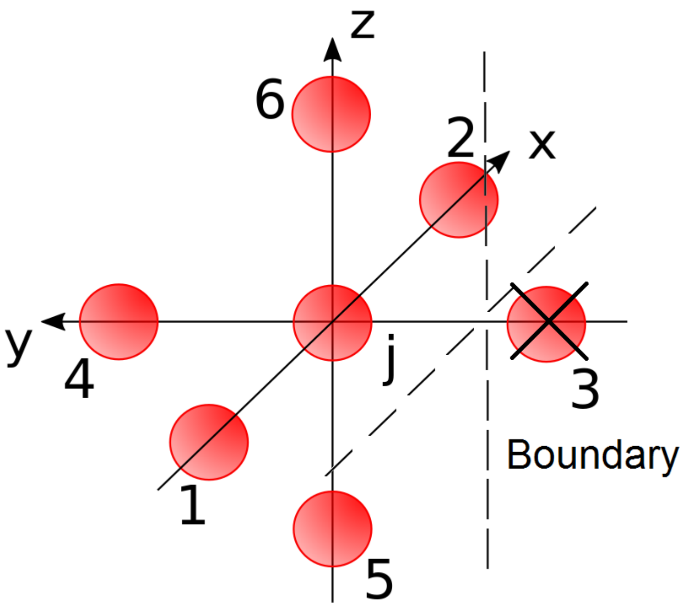

FIGURE 5.13 – *Figure 4.16 is slightly modified in order to explain the difference between the center and the periphery of a sample with aligned magnetic moments on a simple cubic lattice. Here, one of the boundaries of the sample which are parallely orientated to the* $x-z-$*plane is examined, leading inclusion* 3 *to drop out.*

In this regard, inclusion 3 is not integrated in the system, modifying calculations of the total dipolar field acting on inclusion j to:

$$\begin{aligned}
\sum_{i\in M_{ij}} \mathbf{H}_{ij} &= \mathbf{H}_{1j} + \mathbf{H}_{2j} + \mathbf{H}_{4j} + \mathbf{H}_{5j} + \mathbf{H}_{6j} \qquad (5.1)\\
&= \frac{1}{4\pi r_{nn}^2} \frac{3r_{nn}\mathbf{x}\left(p\mathbf{z}r_{nn}\mathbf{x}\right) - p\mathbf{z}r_{nn}^2}{r_{nn}^3} \qquad (5.2)\\
&+ \frac{1}{4\pi r_{nn}^2} \frac{-3r_{nn}\mathbf{x}\left(-p\mathbf{z}r_{nn}\mathbf{x}\right) - p\mathbf{z}r_{nn}^2}{r_{nn}^3} \qquad (5.3)\\
&+ \frac{1}{4\pi r_{nn}^2} \frac{-3r_{nn}\mathbf{y}\left(-p\mathbf{z}r_{nn}\mathbf{y}\right) - p\mathbf{z}r_{nn}^2}{r_{nn}^3} \qquad (5.4)\\
&+ \frac{1}{4\pi r_{nn}^2} \frac{3r_{nn}\mathbf{z}\left(p\mathbf{z}r_{nn}\mathbf{z}\right) - p\mathbf{z}r_{nn}^2}{r_{nn}^3} \qquad (5.5)\\
&+ \frac{1}{4\pi r_{nn}^2} \frac{-3r_{nn}\mathbf{z}\left(-p\mathbf{z}r_{nn}\mathbf{z}\right) - p\mathbf{z}r_{nn}^2}{r_{nn}^3} \qquad (5.6)\\
&= \frac{1}{4\pi r_{nn}^3}\left(-5p\mathbf{z} + 3p\mathbf{z} + 3p\mathbf{z}\right) \qquad (5.7)\\
&= \frac{1}{4\pi r_{nn}^3} p\mathbf{z}. \qquad (5.8)
\end{aligned}$$

Since the sum of the dipolar fields approaches zero in the center of such a composite (compare to result in equation 4.12), it is shown that dipolar fields become stronger in the periphery of slices parallel to the $x-y-$plane of these systems.

Performing the same analysis for finite composites with randomly inserted inclusions, results shown in figure 5.14 are obtained.

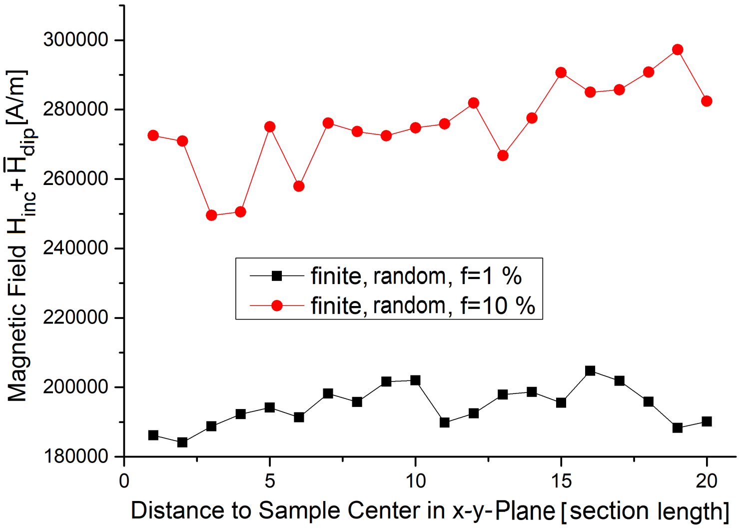

FIGURE 5.14 – *The same analysis as in figure 5.12 is done for a sample with a random inclusion insertion. A difference of around* 3 % *between the fields in the first and last section is observed for a filling factor of* $f = 10$ %.

In this case, an analog tendency for the fields to decrease in the inner device could be assumed, but is much less extended then in the previous case, which is a consequence of the not structured arrangement of the inclusions.

Not disregarding the anisotropy of the system, induced by the inclusions' internal magnetic bias pointing along the $z-$axis, we want to perform the same analysis for the $x-z-$direction. Results for finite samples with inclusions arranged on a simple cubic lattice or randomly inserted are shown in figures 5.15 or 5.16, respectively.

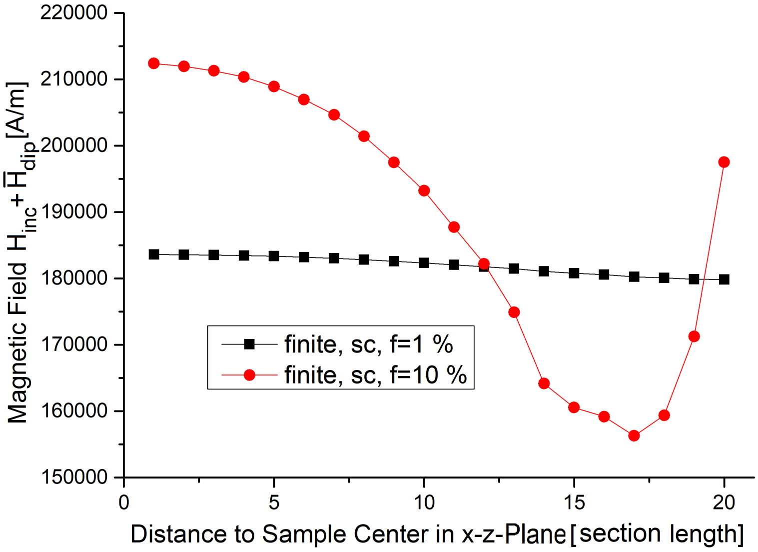

FIGURE 5.15 – *The same analysis for inclusions on a simple cubic lattice in a finite sample (compare to figure 5.12) is done in a corresponding slice of the composite parallel to $x-z-$plane.*

In this direction, we detect a shrinking of the dipolar fields when approaching from the core to the periphery, which can be again explained by an analog calculation to equations 5.1-5.8. Omitting the contribution of inclusion 5 or 6, as it is the case close to the sample boundaries parallel to $x-y-$direction, we obtain

$$\sum_{i\in M_{ij}} \mathbf{H}_{ij} = -\frac{1}{2\pi r_{nn}^3} p\mathbf{z} \tag{5.9}$$

which has the opposite sign as the former result (equation 5.8), explaining the reduced values of the fields.

But, in the outer periphery of the composite in $x-z-$direction, behavior is inversed, at least for a filling factor of 10 %. Here, we reach the vicinity of the corners of the quadratic slices of the composites in which two boundary areas are in proximitty. Following this, we can explain the rising of the magnetic field by omitting inclusions 2 and 6 in the common calculation, for example, delivering

$$\sum_{i\in M_{ij}} \mathbf{H}_{ij} = -\frac{1}{4\pi r_{nn}^3} p\mathbf{z} \tag{5.10}$$

which is reduced by a factor of 2 compared to the result in equation 5.9. In the data set coressponding to a filling factor of $f = 1$ %, interactions are simply too weak for

showing this inversion.
With regard to the analysis in the $x-y-$planes of the samples, such an inversion is neither detected in the simulations nor can be analytically predicted, when omitting inclusions 2 and 3 in the calculation, as it would be the case in one of the corresponding corners. This proceeding delivers

$$\sum_{i \in M_{ij}} \mathbf{H}_{ij} = \frac{1}{2\pi r_{nn}^3} p\mathbf{z} \tag{5.11}$$

and therefore an enforcement of the same tendency as detected in equation 5.8 instead of a reduction.

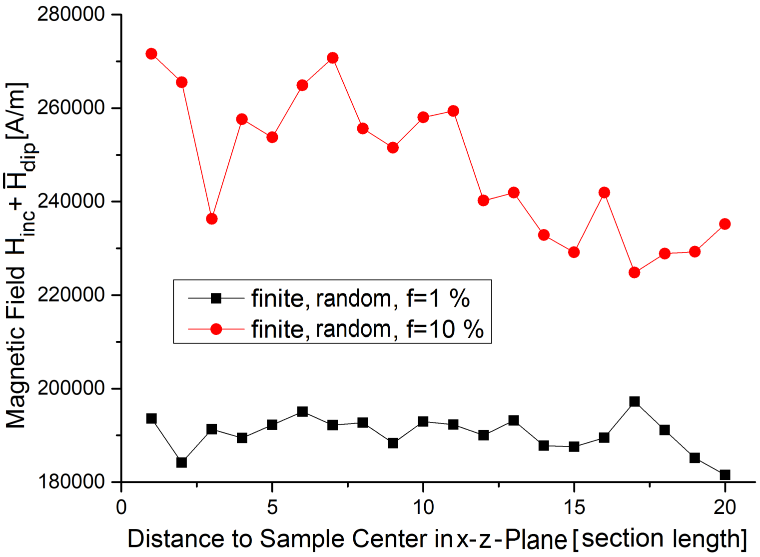

FIGURE 5.16 – *The same analysis for stochastically inserted inclusions in a finite sample (compare to figure 5.14) is done in a corresponding slice of the composite parallel to $x-z-$plane. Here, we observe a difference of around 14 % between the field values of the first and last section in the case of $f = 10$ %.*

Regarding the randomly generated composite (figure 5.16), we also detect a shrinking of the field magnitudes, but the disordered microstructure again produces statistically noise in the results.
For meaningfully answering the question if is is justified to neglect boundary effects within these procedures, we also analyze the cross section behavior of the magnetic field for infinite samples with random inclusion insertion, which is done in figures 5.17 ($x-y-$direction) and 5.18 ($x-z-$direction).

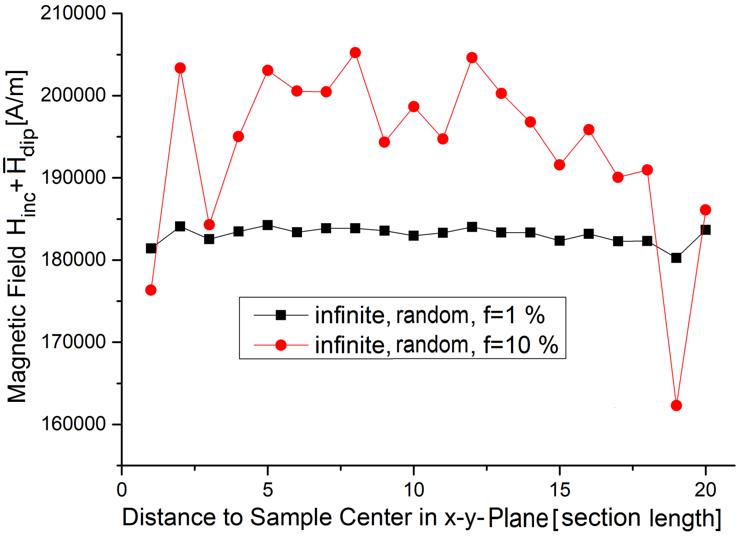

FIGURE 5.17 – *The same analysis in a cross section parallel to the* $x-y-$*plane as in figure 5.14 is done for a sample with periodic boundary conditions. Deviations in the range of* 22 % *between highest and lowest field values are observed for* $f = 10$ %.

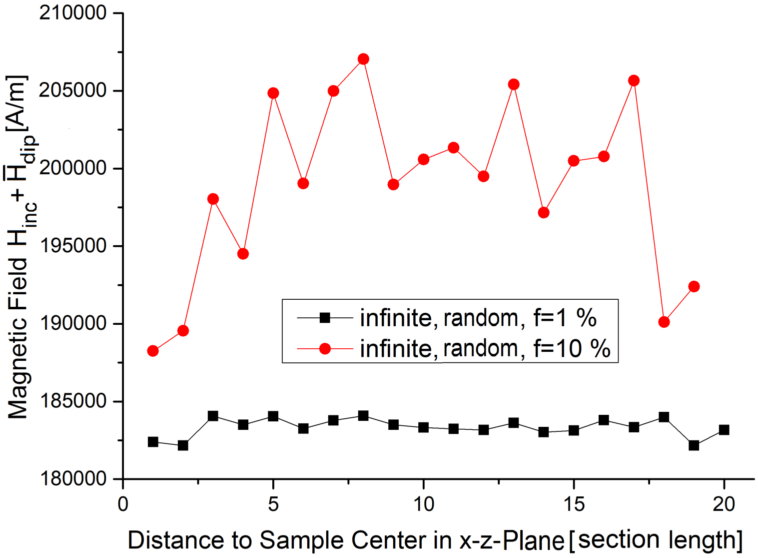

FIGURE 5.18 – *The same analysis in a cross section parallel to the* $x-z-$*plane as in figure 5.16 is done for a sample with periodic boundary conditions. Deviations in the range of* 9 % *between highest and lowest field values are observed for* $f = 10$ %.

Actually, the field values in the infinitely extended samples should be approximately constant, but are influenced by statistical deviations. Regarding the magnitude of these perturbations, 22 % in $x-y-$direction and 9 % in $x-z-$direction, we can expect the statistical errors for finite samples to be in the same order. Accordingly, it is justified to neglect the detected deviations between core and periphery (3 % in $x-y-$direction and 14 % in $x-z-$direction) in the regarded composites. Consequently, we reproduce the H-field distribution of all spheres in the large system limit by all inclusions of the low inclusion number microstructure without distinction between periphery and core of the composites.

Returning to the purpose of finding representative systems for high-frequency simulations, we must deviate from our former procedures in one point: In the previous chapter, we maintained the inclusions' radii and varyed the extensions of the matrix in order to generate different volume fractions. Now, it is desired to draw conclusions on the sample geometry for different filling factors. Accordingly, the matrix extensions of a considered geometry must kept constant and increasing volume fractions can be only realized by higher inclusion numbers or the choice of larger spheres. Again, limited memory capacity inhibits us from boosting the number of the included spheres.

Consequently, we are restricted to enlarge the diameters of the spheres whereby the following settings are chosen:

- Cubic sample: $N_{inc} = 64$ inclusions, radii from $r_{inc} = 0.0344$ cm ($f = 1$ %) to $r_{inc} = 0.0571$ cm ($f = 5$ %)
- Halved length sample: $N_{inc} = 32$ inclusions, radii from $r_{inc} = 0.0344$ cm ($f = 1$ %) to $r_{inc} = 0.0571$ cm ($f = 5$ %)
- Doubled length sample: $N_{inc} = 54$ inclusions, radii from $r_{inc} = 0.0445$ cm ($f = 1$ %) to $r_{inc} = 0.0762$ cm ($f = 5$ %)

Although these radii exceed the value of 0.0445 cm, for which convergence with respect to inclusions' size was detected in section 4.1, we have to accept this drawback due to lack of alternatives. But, as shown in figure 4.8, variations between $r = 0.0334$ cm and $r = 0.0668$ cm were very small and also influenced by the changed inclusion number ($N_{inc} = 8$ and $N_{inc} = 64$, see also equation 4.19 and the corresponding discussion). Because the minimal number of spheres in usage exceeds $N_{inc} = 8$ by a factor of four in the present case, this error source can be estimated as very small.

Summarizing, this procedure delivers sample structures which can be modeled in HFSS (shown in figure 5.19). The adaption of the $H-$field distribution is exemplarily shown for the case of the cubic sample with $f = 1$ % (see figure 5.20).

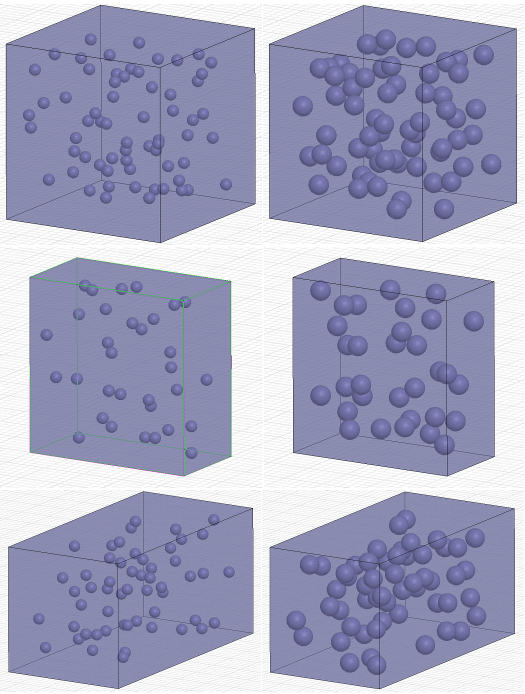

FIGURE 5.19 – *The three regarded sample geometries (top: cubic, middle: halved length, bottom: doubled length) with filling factors of $f = 1$ % (left) and $f = 5$ % (right). As it can be seen, different inclusion volume fractions are realized by changing the spheres' diameter in order to maintain the geometric extensions of the matrix. Compared to the arrangements in picture 4.62 for infinite devices, deviations from the initial simple cubic lattice are much more distinct. For the cubic sample, average dislocation from the initial simple cubic lattice amounts $\overline{\Delta x} = 3.26 r_{inc}$ with $r_{inc} = 0.0334$ cm for $f = 1$ % (infinite device: $\overline{\Delta x} = 1.33 r_{inc}$ with $r_{inc} = 0.00445$ cm) and $\overline{\Delta x} = 6.84 r_{inc}$ for $f = 5$ % with $r_{inc} = 0.0571$ cm (infinite device: $\overline{\Delta x} = 0.57 r_{inc}$ with $r_{inc} = 0.00445$ cm).*

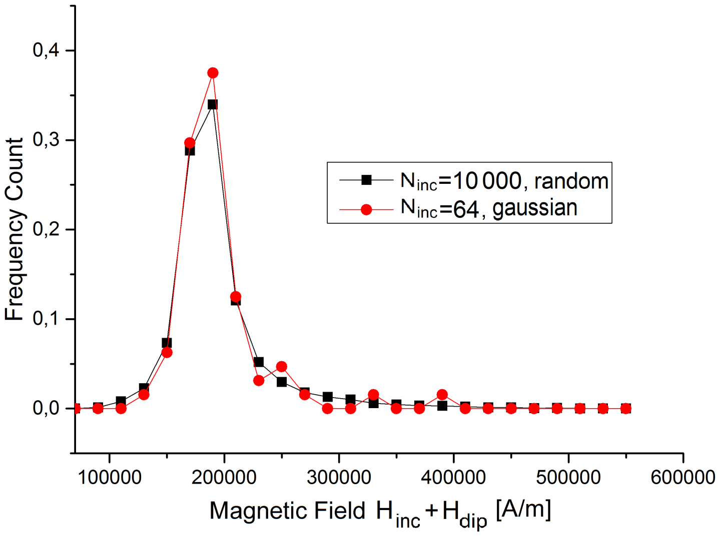

FIGURE 5.20 – *The $H-$field distribution must be adapted in order to reproduce the behavior of large systems containing $N_{inc} = 10\,000$ inclusions with the realizable inclusion numbers in HFSS. Here, the case of a cubic sample with $f = 1$ % and 64 inclusions is shown. Error function equals $\Delta = 0.0028$.*

This procedure is repeated for every geometry and every value of f between 1 % and 5 %. Using these results, we perform high-frequency simulations in HFSS. Within this context, we again have to be aware that internal magnetic biases were kept constant for different volume fractions, so far. Before simply adding $\frac{1}{3}M_{eff}(f)$ to them, according to equation 4.20, we have to check if it is still possible to assign effective values M_{eff} to homogeneous samples in such a way that they reproduce the resonance curves of the composites with the gained, new microstructures with high accordance. For that purpose, we once again switch off dipolar interactions between the inclusions and define identical internal magnetic biases leading an isolated sphere with $M_s^{inc} = 302\ 394.5\ \frac{\mathrm{A}}{\mathrm{m}}$ to resonate at $\nu_{res} = 10$ GHz (compare to section 4.3.2.1, $H_{inc} = 183\ 154\ \frac{\mathrm{A}}{\mathrm{m}}$). Then, we try to reproduce the corresponding resonance curves with homogeneous samples by variation of M_{eff} and $H_{eff}(H_{inc} = const.)$ while $\alpha = 0.05$ remains constant. Again, the performed adaptions, exemplarily shown for the three considered geometries and $f =$ 5 % in figures 5.21-5.23, show very good accordance when using the already determined values of M_{eff} and $H_{eff}(H_{inc} = const.)$ (data shown in figure 4.27), underlining that effective parameters of composites are still only marginally affected by the considered microstructures when neglecting dipolar interactions.

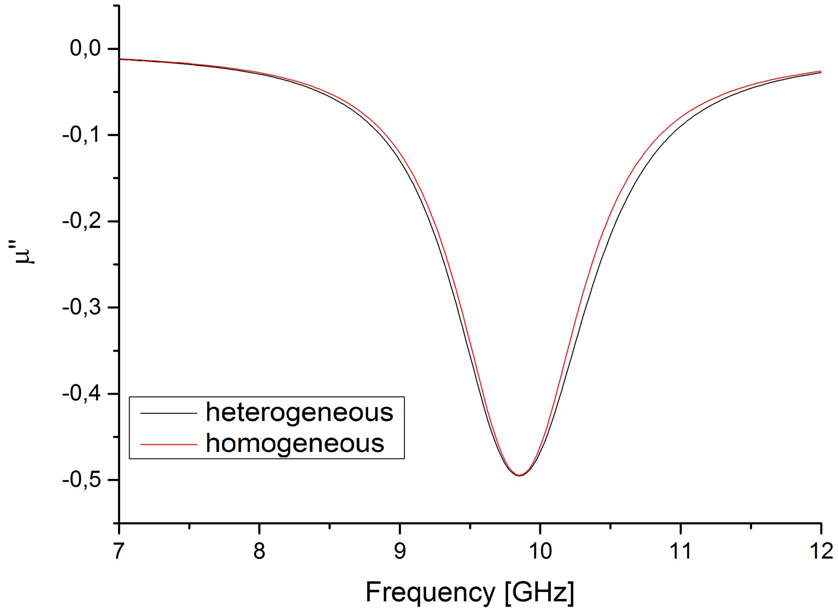

FIGURE 5.21 – *The comparison between the cubic samples consisting out of composite material with a filling factor of* $f = 5$ % *and the homogeneous sample with the already found values of* $M_{eff} = 14\ 722\ \frac{A}{m}$, $H_{eff}(H_{inc} = const.) = 279\ 125\ \frac{A}{m}$ *and* $\alpha = 0.05$ *shows good accordance.*

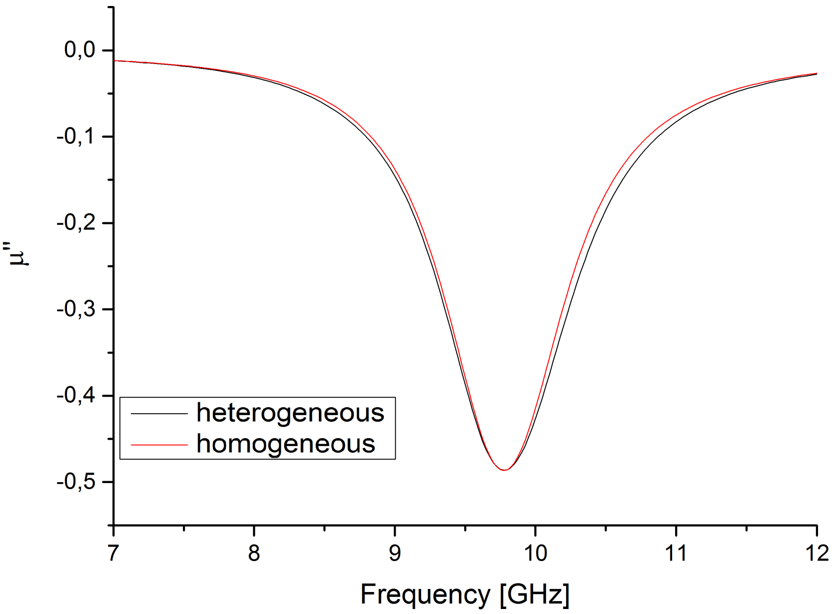

Figure 5.22 – *The results produced by samples with doubled length in wave propagation direction and a volume fraction of* $f = 5\ \%$ *are also very similiar. Input parameters are the same as for the results shown in figure 5.21.*

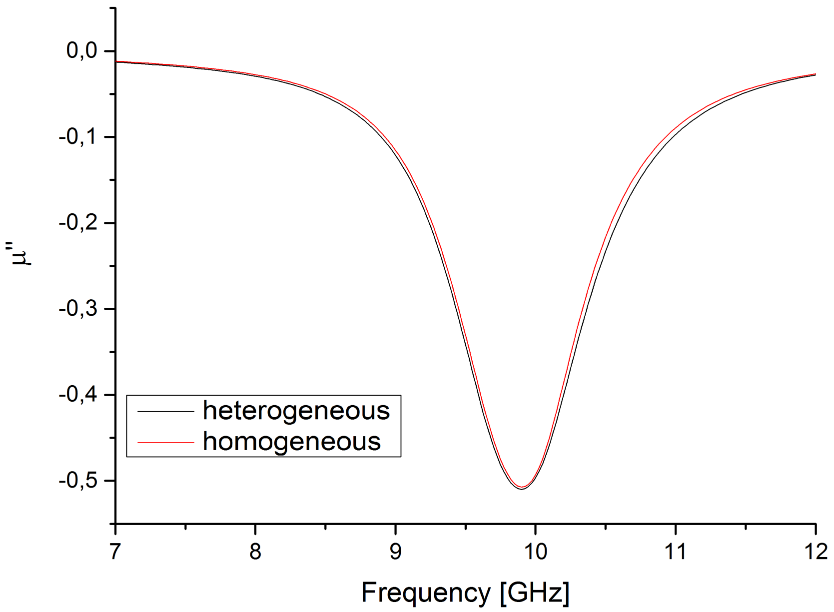

Figure 5.23 – *The adaption of the samples with halved length and* $f = 5\ \%$ *is shown. Input parameters are the same as for the results shown in figure 5.21.*

Accordingly, we can perform the demagnetization correction in order to keep the effective field in the composite constant, as before. Unfortunately, in contrast to the previously regarded infinitely extended samples, this effective field does not equal the externally applied field due to demagnetization fields of the whole composite devices, impeding a direct comparison the experimental works. Nevertheless, we analyze these systems under a constant effective field in the sample in order to detect impacts of

different properties of the composite on the permeability tensor.
In order to analyze the resonance behavior of the finite samples of interest, we use our most realistic model in which the local distribution of the dipolar fields is included and perform high-frequency simulations (compare to section 4.3.2.3). Then, we use the $S-$parameters gained from HFSS and MOR in order to determine the permeability tensors of the different samples. Corresponding results for μ'' are shown in figures 5.24-5.26.

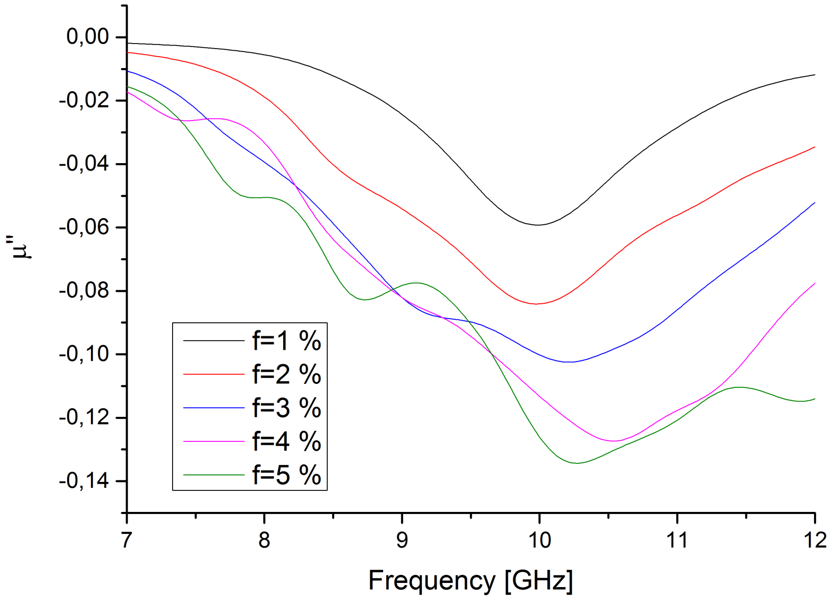

FIGURE 5.24 – *The gained resonance peaks of μ'' for different filling factors in the cubic sample when H_{eff} is kept constant for different filling factors.*

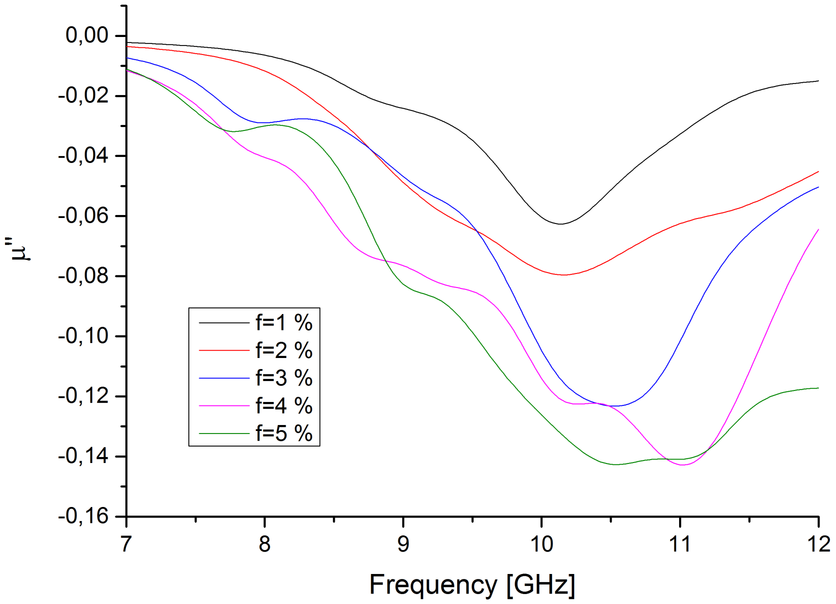

FIGURE 5.25 – *The same comparison as in figure 5.24 for the sample with halved length in wave propagation direction.*

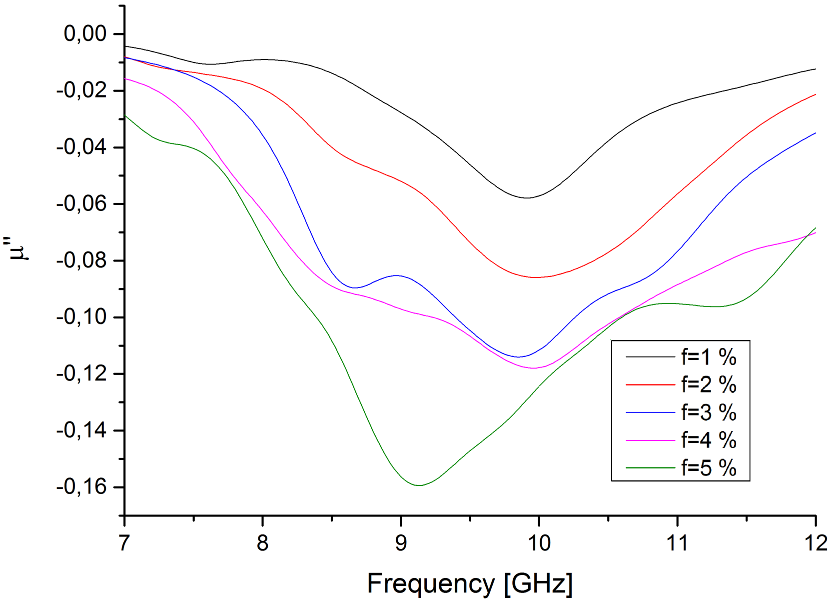

Figure 5.26 – *The same comparison as in figure 5.24 for the sample with doubled length in wave propagation direction.*

In this context, it is also interesting to compare the results for fixed values of f in dependence of the analyzed geometry. This is done in figures 5.27-5.29.

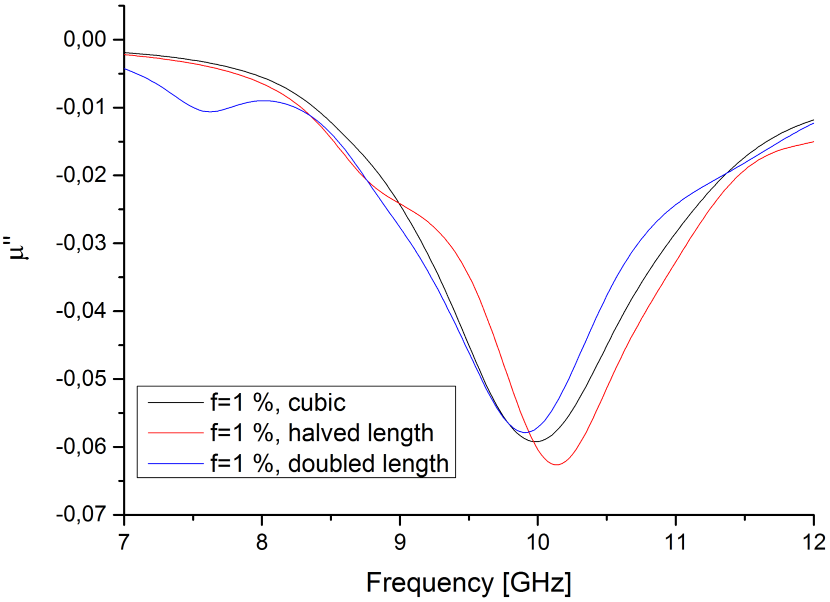

Figure 5.27 – *A comparison between the results of the three geometries for* $f = 1$ % *in the case of a constant value for* H_{eff}.

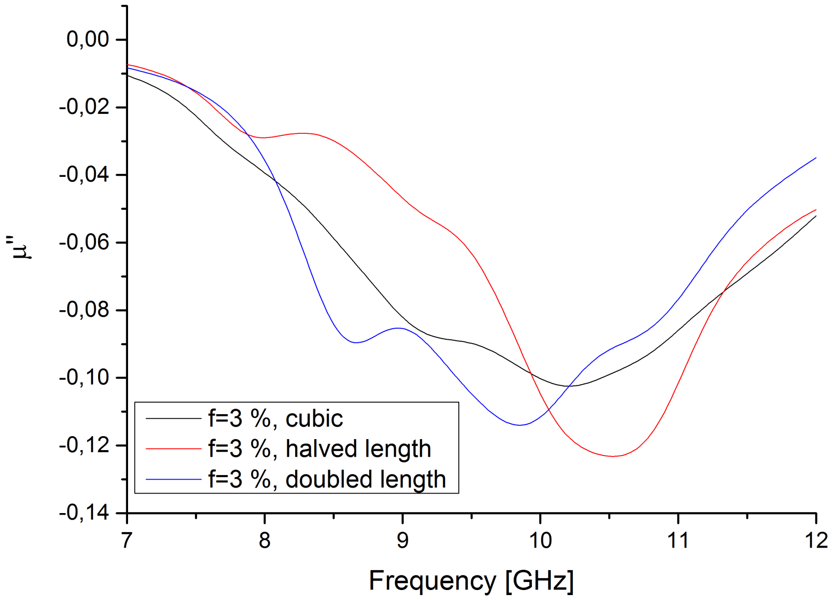

FIGURE 5.28 – *The same analysis as in figure 5.27 is done for a volume fraction of* $f = 3$ %.

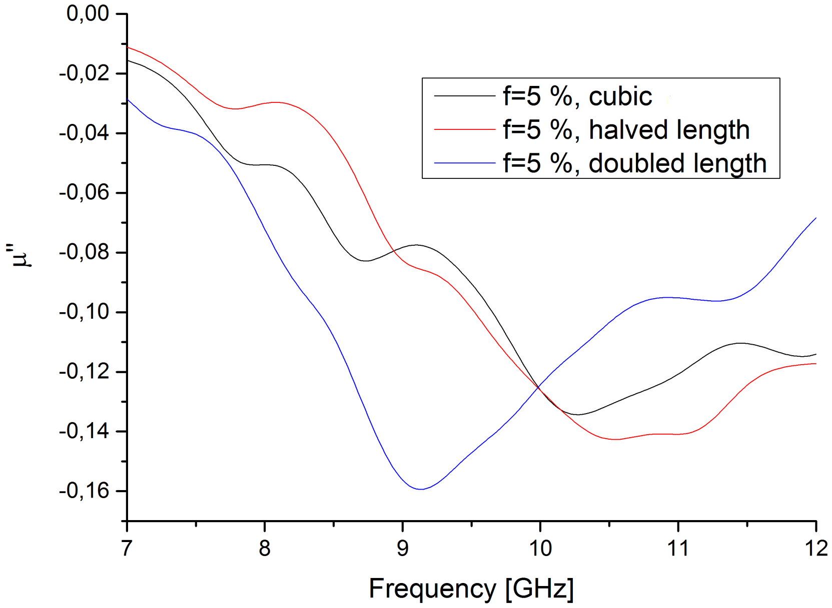

FIGURE 5.29 – *The same analysis as in figure 5.27 is done for a volume fraction of* $f = 5$ %.

From these graphs, several information can be drawn. Firstly, we notice that artifacts due to limited inclusion numbers are even more pronounced compared to the examination of infinite samples (compare with pictures 4.93-4.95). Of course, this effect complicates a senseful analysis. For the purpose of overcoming this problem, we regard several different microstructures for one geometry and one volume fraction, fulfilling our requirements with regard to the large system limit, and analyze the deviations between them. Corresponding results for $f = 1$ % and $f = 5$ % are shown in figures 5.30-5.35.

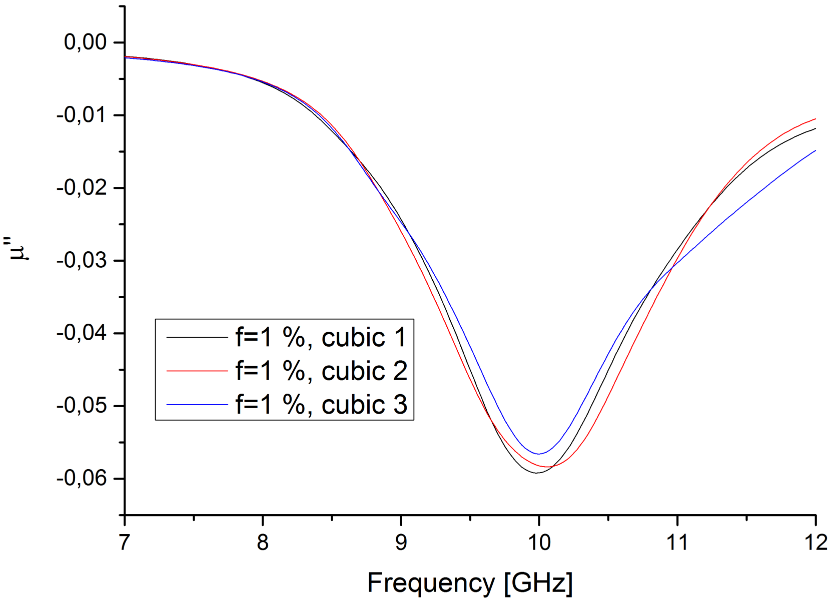

FIGURE 5.30 – *Three different microstructures in the cubic sample with* $f = 1\ \%$ *are under test. Obviously, resonance curves do not differ much and show almost the same resonance frequency.*

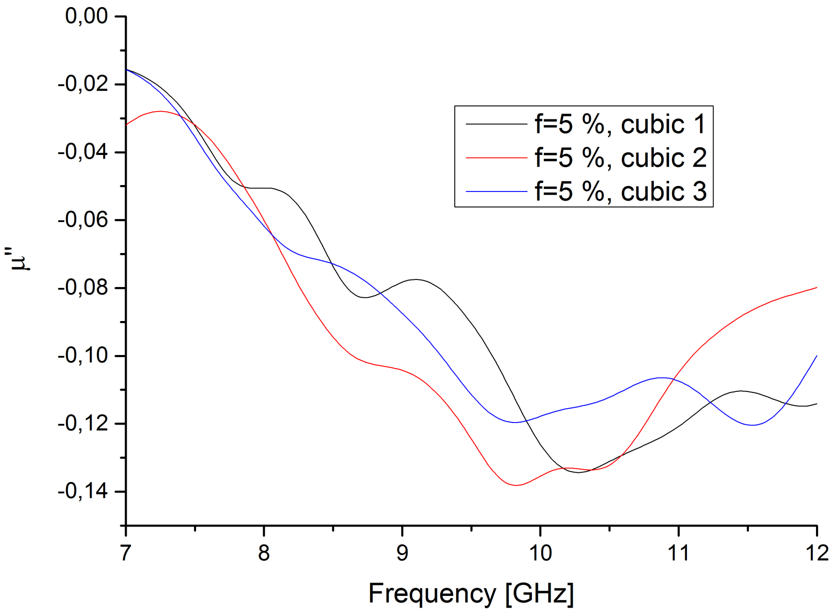

FIGURE 5.31 – *Comparing with the results in picture 5.30, deviations between different microstructures and artifacts, meaning the blurring of the peaks, become more distinct in the case of a filling factor* $f = 5\ \%$ *in the cubic sample. Especially the third simulation run (blue curve) shows almost two peak character as a result of the low inclusion number.*

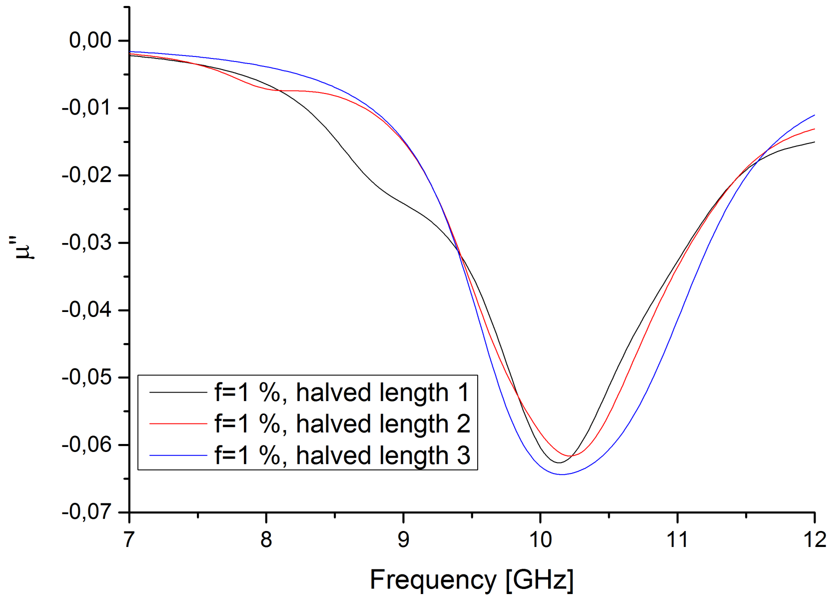

FIGURE 5.32 – *Comparable to the results for the cubic sample shown in figure 5.30, the sample with halved length and a volume fraction of* $f = 1~\%$ *also shows relatively stable resonance peaks.*

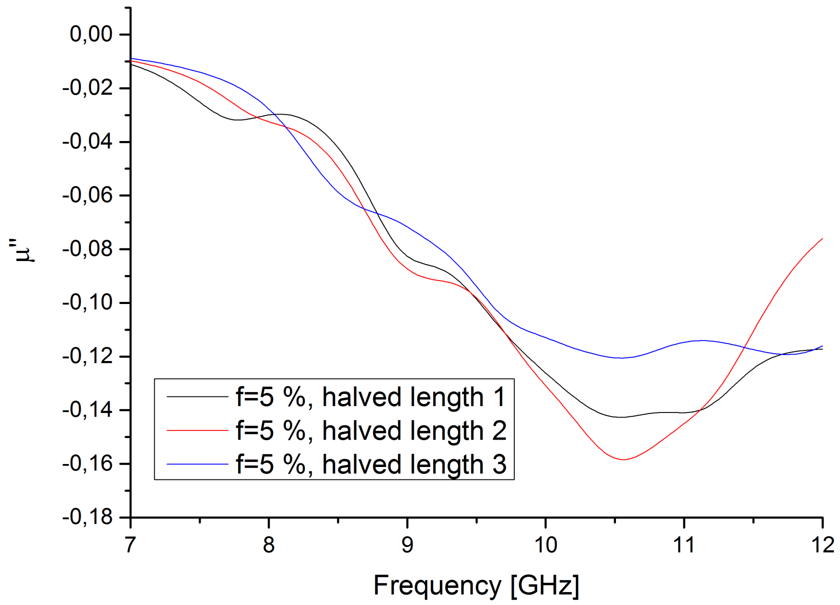

FIGURE 5.33 – *Increasing filling factor to* $f = 5~\%$ *in the sample with halved length, we notice the same tendencies as for the cubic sample (see figure 5.31): Artifacts in the form of additional hilltops arise and the resonance peaks become blurred.*

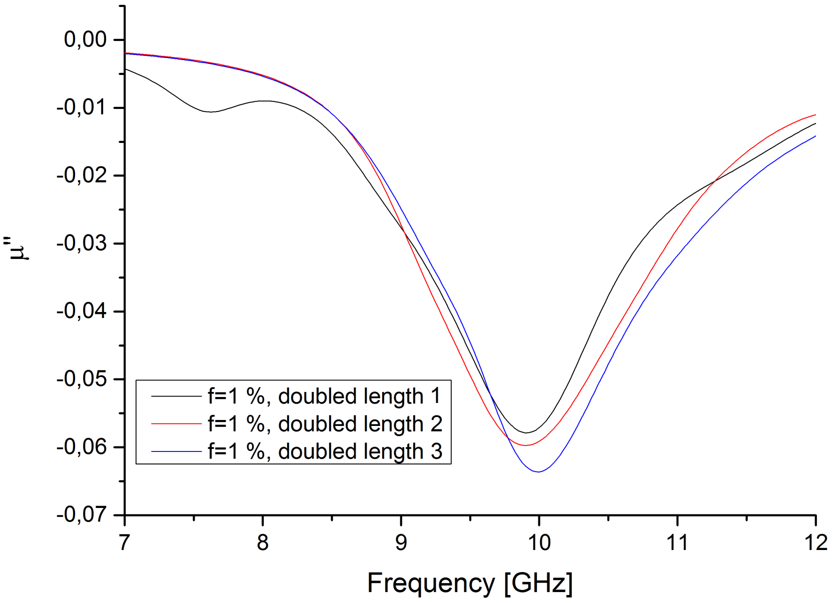

FIGURE 5.34 – *As in the previous samples, the device with doubled length also shows good agreement in the resonance curves for* $f = 1\ \%$.

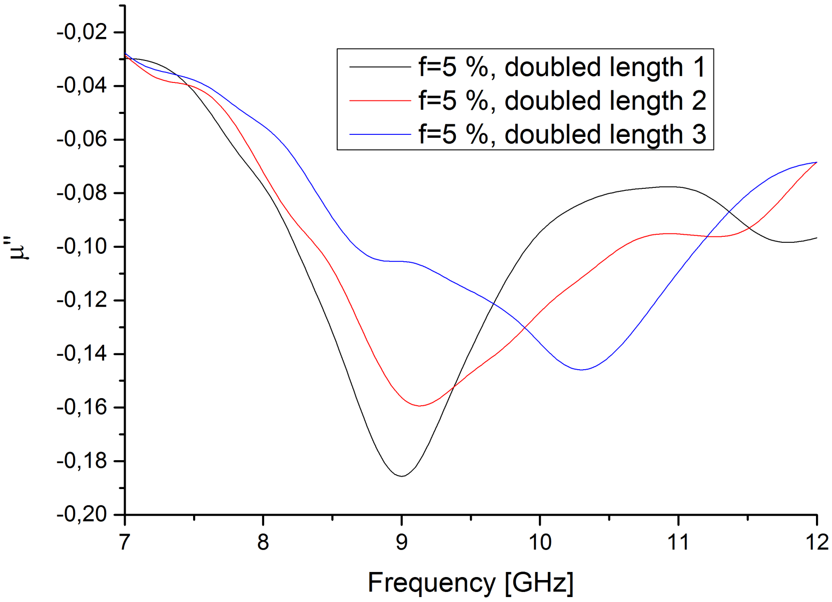

FIGURE 5.35 – *For the sample with doubled length and a volume fraction of* $f = 5\ \%$*, artifacts are less distinct then in the previous cases but there are also strong deviations between the different resonance frequencies.*

Secondly, we notice that resonance peaks move in dependence of geometry and inclusions' volume fraction. In order to draw meaningful conclusions, we average the resonance frequencies (meaning always the frequency point in which the maximum value of $|\mu''_{max}|$ is reached) of the three different microstructures and plot the results in dependence of the inclusions' volume fraction in picture 5.36. For clearness sake, it should be highlighted that in this case, no comparison to homogeneous samples with the same extensions is necessary, which was done in the previous chapter in order to get rid of demagnetization effects of the sample in the waveguide, because we are interested in the behavior of finite devices.

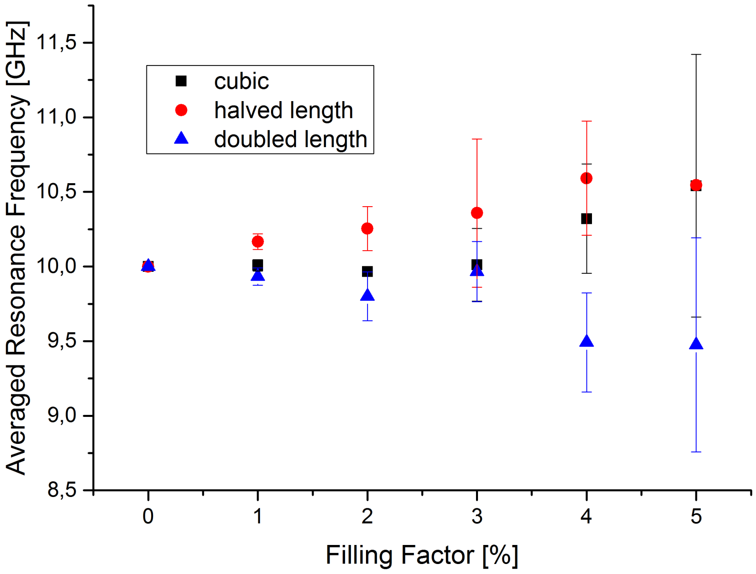

Figure 5.36 – *The averaged resonance frequencies of the three different regarded microstructures for each geometry and each value of filling factor f are shown. Error bars mark the standard deviations between the resonances of different microstructures. The magnitude of H_{eff} was maintained for every filling factor.*

Within the plot shown in figure 5.36 two results become obvious: Firstly, the standard deviations between different resonance frequencies of one type of sample (cubic, doubled length, halved length) increase with rising volume fraction of inclusions, which is seen as an artifact due to limited number of included spheres. It can be assumed that this effect would disappear if the large system limit would also be feasible in the high-frequency simulations. Despite of this drawback, the performed analysis delivers the tendencial behavior of the resonance frequencies under the condition $H_{eff} = const.$ which can be seen as qualitatively reliable: While the resonance of the finite cubic sample can be assumed as constant or slightly growing with increasing values of f, the device with halved length shows a rising resonance frequency. Contrary, the doubled length causes the resonance to tend towards lower values. In conclusion, a strong dependence of the resonance frequency behavior on the sample geometry is detected and should be considered in real experiments, in which always finite devices are under test. Accordingly, an experimenter, who is interested in geometry independent effective parameters of composite material, is recommended to obey the following recipe: First of all, the sample should be analyzed via the transmission and reflection method in a real experiment, delivering the effective permeability of the device in the waveguide. But, as shown in the present work, this result is influenced by geometry dependent effects as demagnetization in the waveguide and dipolar interaction between the inclusions. Therefore, a numerical simulation sequence, static and dynamic, of the experimental set-up with composite samples with the same geometric extensions as the device of the real experiment should be performed. In these simulations, the value for the effective field (differing from the experimentally applied external field) in the composite has to be varied until coincidence of the results is reached, while M_s^{inc} and α should be known as parameters of the included material. Afterwards, the parameter set should be used in static simulations with periodic boundary conditions. By this procedure, the geometry dependence due to the dipolar interaction of the inclusion is removed. Then, the results of this static simulation should be implemented in a high-frequency simulation of the composite. Finally, a further simulation sequence with homogeneous devices is necessary, in which input parameter are again varied until the results of the previous simulation is reproduced, in order to draw meaningful conclusions on the effective values of the composite material under test.

Moreover, we also want to gain isight into the origins of the detected frequency behavior. For that purpose, we firstly analyze the influence of the different geometries when using homogeneous materials with identical material parameters, i.e. the impact of demagnetization effects. The corresponding graphs are shown in figure 5.37 and show indeed a slight tendency for the resonance frequencies to behave according to $\nu_{res}^{double} < \nu_{res}^{cubic} < \nu_{res}^{halve}$, but which is quantitatively too weak comparing with results shown in figure 5.36.

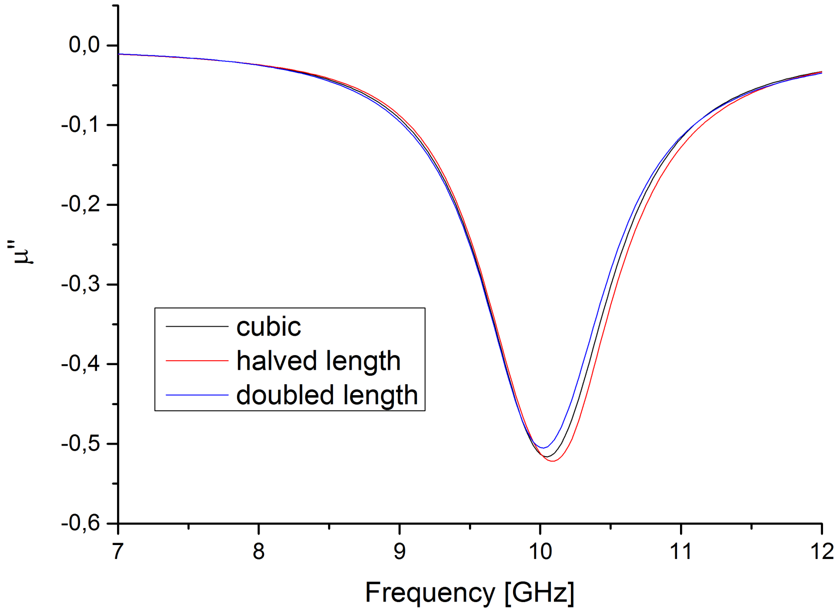

FIGURE 5.37 – *We regard the resonance curves of homogeneous samples with different geometries. Input parameters are* $\alpha = 0.05$, $H_{eff} = 283\ 952\ \frac{A}{m}$ *and* $M_{eff} = 14\ 722\ \frac{A}{m}$.

Accordingly, the explanation for the resonance behavior must be found in the characteristics of the dipolar interactions which are shown in figure 5.38

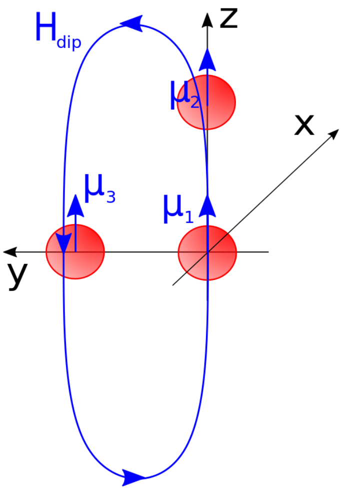

Figure 5.38 – *In order to explain the behavior of the magnetic fields in the inclusions and the resonance frequencies of the composites depending on the matrix geometry (see figures 5.9 and 5.36), we have to take a look at the form of the dipole field of one arbitrary inclusion (in the beneath picture placed at the coordinate system's origin and labeled with number one) and its influence on surrounding magnetic dipoles which all are parallely aligned in $z-$direction in our simulations, at first. While the dipole field caused by inclusion 1 is parellely aligned with the magnetic moment of inclusion 2 which is placed on the $z-$axis, the same dipole field antiparallely acts to the magnetic moment of inclusion 3 placed on the $y-$axis. Due to rotational symmetry of the dipole fields, the same effect appears for an inclusion located at the $x-$axis. Following this, included magnetic moments enforce each other when they are parallely aligned to their spatial connection vector, but counteract when the connection vector is orthogonally orientated. Consequently, a large extension of the sample in the direction of the dominant orientation of the magnetic moments, connected with many enforcing acting dipoles, compared to small extensions in the orthogonal directions leads to higher field values in the inclusions. Accordingly, the sample with halved length, for which extension in $z-$direction is twice as large as matrix size in $x-$direction, shows an increasing resonance frequency while the doubled length sample behaves the other way around.*

Beneath the resonance frequency, we also want to discuss the magnitudes of μ'_{stat} and μ''_{max} in the case of finite samples with a constant value of H_{eff}. Concerning the latter one, we can simply average the values of μ''_{max} over the results of the three different microstructures for each volume fraction (resonance curves shown in the graphs in 5.30-5.35 for the cases of $f = 1$ % and $f = 5$ %) because we are interested in the behavior of finite samples. Corresponding values for different geometries in dependence of volume fractions are shown in figure 5.39.

In this plot, we see that the values of μ''_{max} are nearly independent from the regarded geometry, in contrast to the resonance frequencies (see figure 5.36). With regard to an analysis of μ'_{stat}, we take a look at the found curves for μ' for different volume fractions and geometrix extensions shown in figures 5.40-5.45.

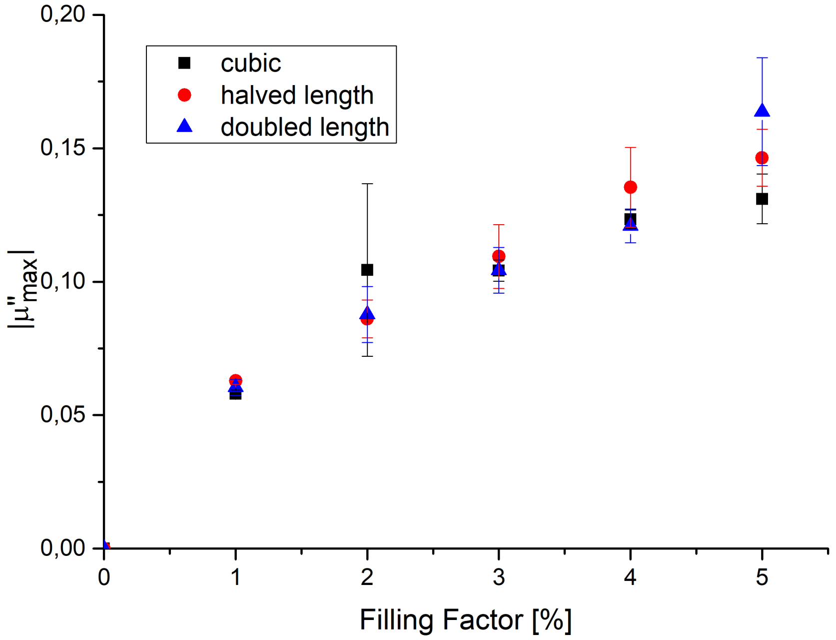

FIGURE 5.39 – *The values of* μ''_{max} *for the three different geometries and volume fractions in the range from* $f = 1$ % *to* $f = 5$ % *are averaged over the three regarded microstructures for every case. Error bars denote standard deviations. Magnitude of* H_{eff} *was kept constant.*

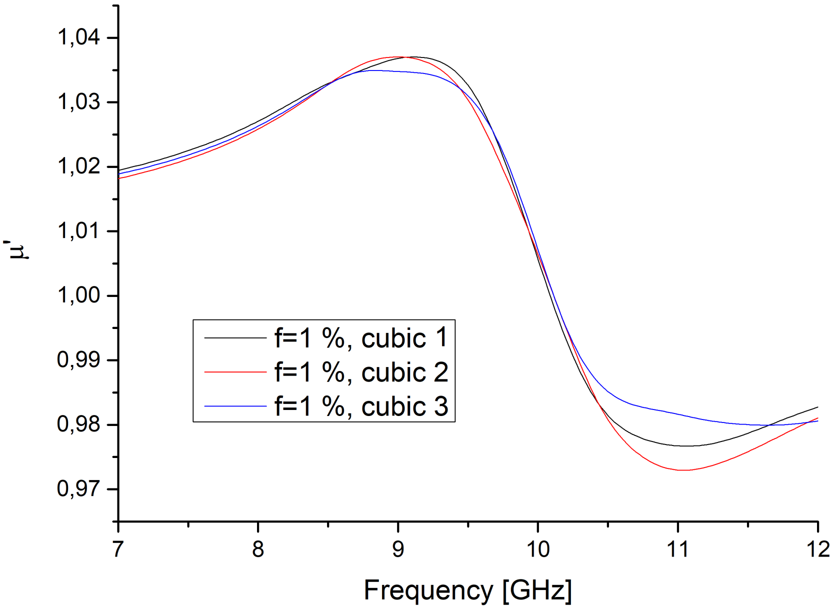

FIGURE 5.40 – *The curves for* μ' *for the three cubic samples with different microstructures and a volume fraction of* $f = 1$ %.

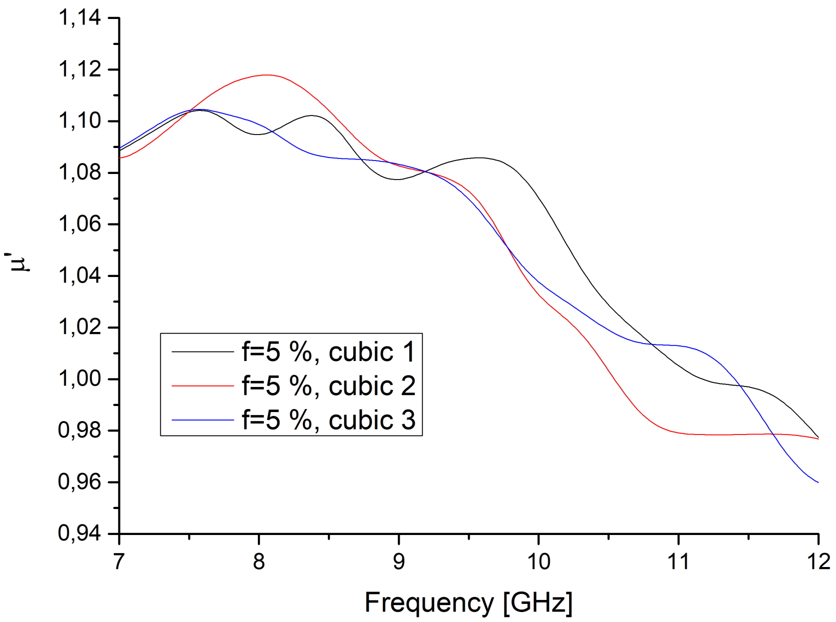

FIGURE 5.41 – *The curves for μ' for the three cubic samples with different microstructures and a volume fraction of $f = 5$ %.*

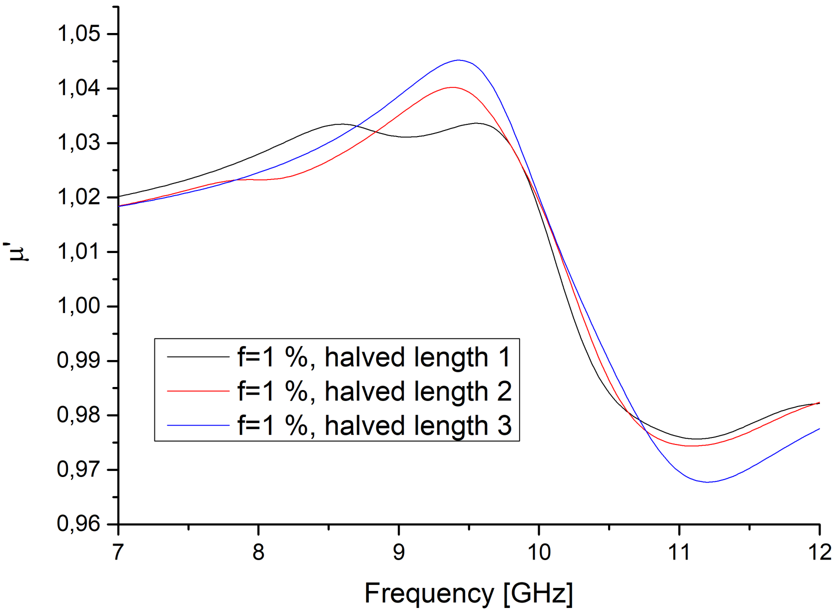

FIGURE 5.42 – *The curves for μ' for the three samples with halved length in propagation direction with different microstructures and a volume fraction of $f = 1$ %.*

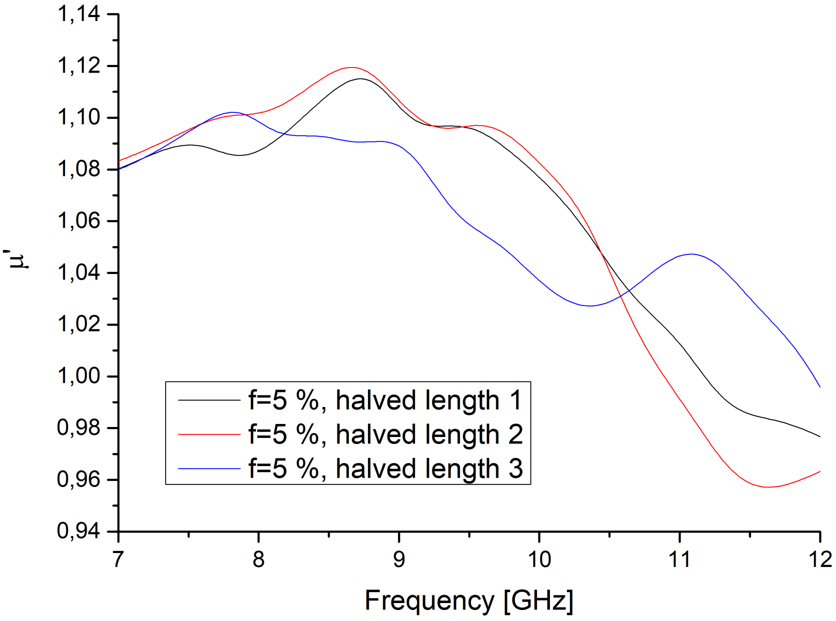

FIGURE 5.43 – *The curves for μ' for the three samples with halved length in propagation direction with different microstructures and a volume fraction of $f = 5$ %.*

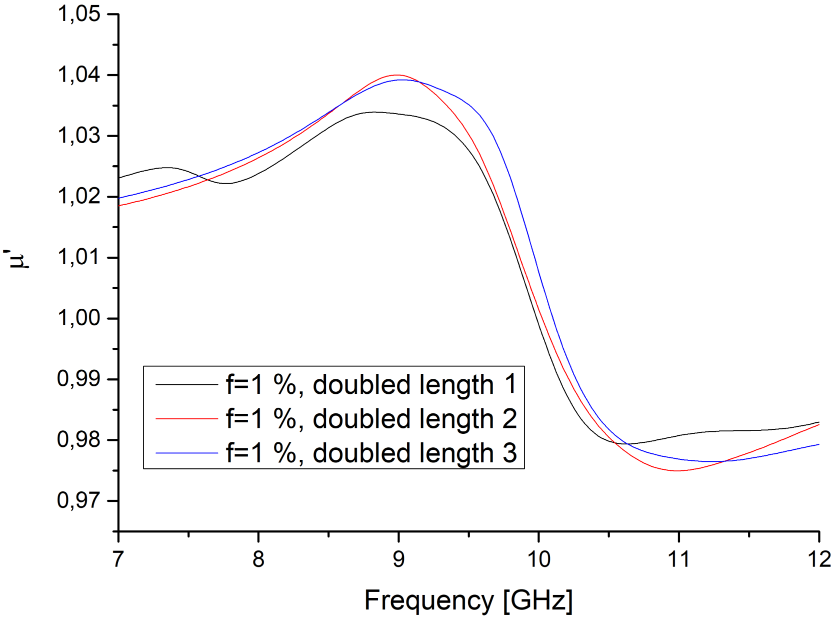

FIGURE 5.44 – *The curves for μ' for the three samples with doubled length in propagation direction with different microstructures and a volume fraction of $f = 1$ %.*

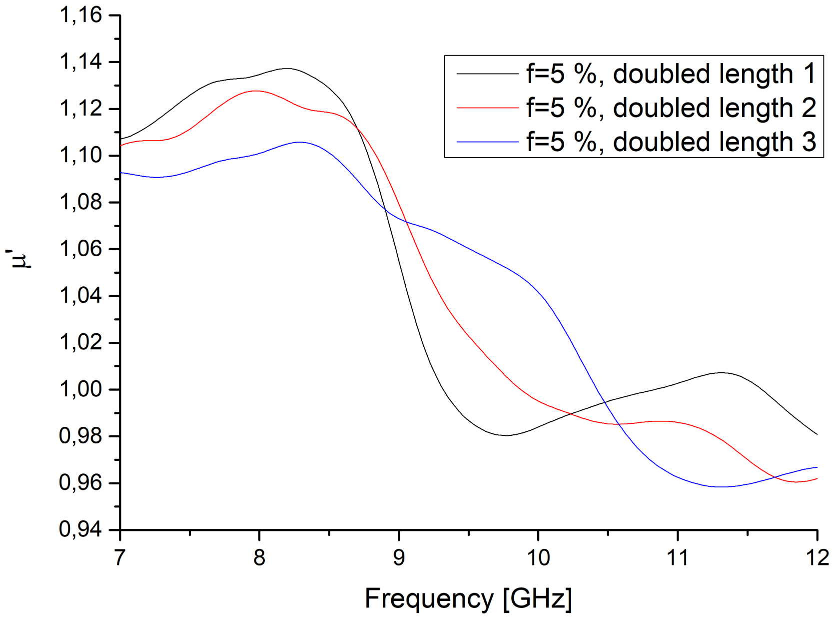

FIGURE 5.45 – *The curves for μ' for the three samples with doubled length in propagation direction with different microstructures and a volume fraction of $f = 5$ %.*

With respect to these outcomes, one has to admit two facts: Firstly, results for higher inclusion volume fractions (see figures 5.41, 5.43 and 5.45) are characterized by strong artifacts making a senseful analysis impossible. Secondly, even for low filling factors (see figures 5.40, 5.42 and 5.44), the values of μ'_{stat} can not be determined because the feasible frequency range in the experimental set-up with a rectangular waveguide has a lower boundary (compare to section 1.1.2.3). The later of these two problems could be overcome by the usage of a parallel plate waveguide, whose accessible frequency range is unlimited for low values. Unfortunately, the evaluation method in use by Quéffélec et al. does not apply for this type of waveguide. Accordingly, we are not able to gain deeper insight into the behavior of this magnitude in a direct manner.

However, also in this chapter, we want to derive an analytic formula for the effective susceptibility tensor in the case of $H_{eff} = const.$, which will also offer an opportunity for examining the magnitude of μ'_{stat}. For that purpose, we firstly average the results for μ'' for the different microstructures in order to reduce artifacts due to statistical errors and then try to find input parameter H^{loc}_{eff} and α_{eff} for equation 1.169 so that mean curves for every regarded volume fraction are well reproduced by Polder's formula. During this, we keep the same values for M_{eff} as in the previous sections, which is confirmed to be true for all geometries, as shown in figures 5.21-5.23. Corresponding adaptions are shown in figures 5.46-5.54.

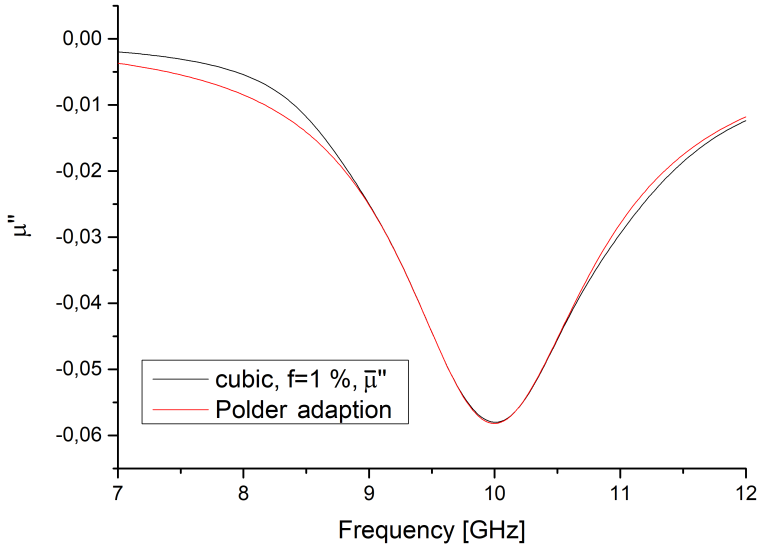

FIGURE 5.46 – *The three curves for μ'' and a filling factor of $f = 1\ \%$ of the cubic samples (see figure 5.30) are averaged. Afterwards, input parameter for Polder's formula are searched in order to obtain the highest accordance between the two curves. Here, parameter values $M_{eff} = 3023.9\ \frac{A}{m}$, $H_{eff}^{loc} = 283\ 900\ \frac{A}{m}$ and $\alpha_{eff} = 0.0915$ are in use. The case of $H_{eff} = const.$ is regarded.*

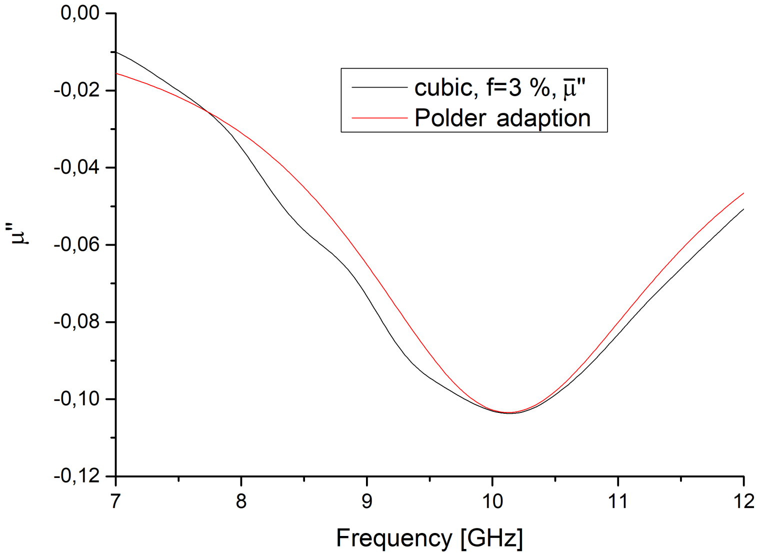

FIGURE 5.47 – *The same analysis as in figure 5.46 is done for a volume fraction of $f = 3\ \%$. Input parameters for Polder's equation are $M_{eff} = 9071.8\ \frac{A}{m}$, $H_{eff}^{loc} = 287\ 500\ \frac{A}{m}$ and $\alpha_{eff} = 0.1525$.*

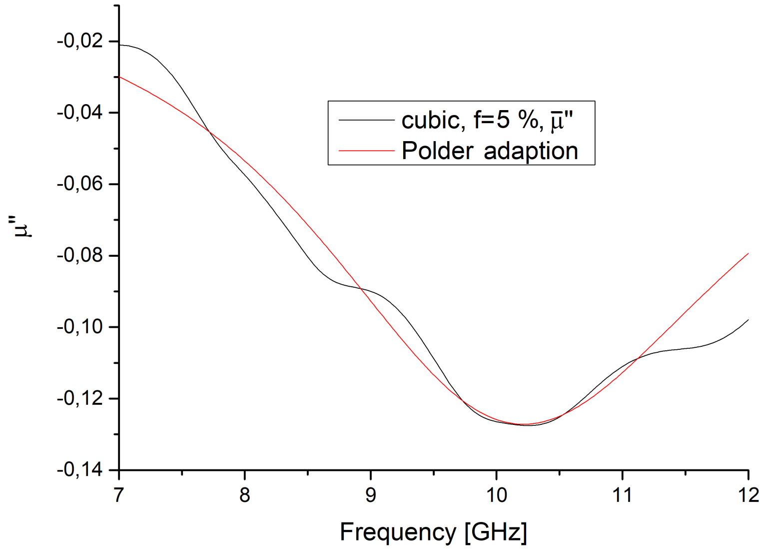

FIGURE 5.48 – *The same analysis as in figure 5.46 is done for a volume fraction of $f = 5\ \%$. Input parameters for Polder's equation are $M_{eff} = 15\ 119.6\ \frac{A}{m}$, $H_{eff}^{loc} = 290\ 000\ \frac{A}{m}$ and $\alpha_{eff} = 0.205$.*

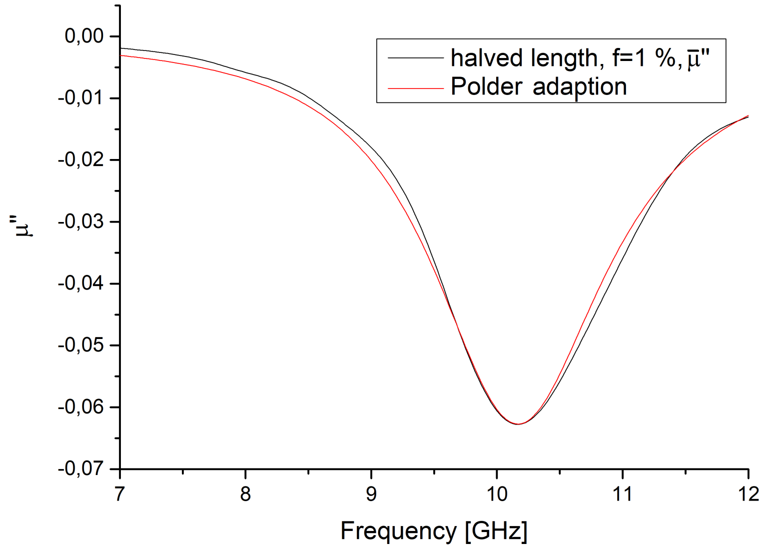

FIGURE 5.49 – *The three curves for μ'' and a filling factor of $f = 1\ \%$ of the samples with halved length (see figure 5.32) are averaged. Afterwards, input parameter for Polder's formula are searched in order to obtain the highest accordance between the two curves. Here, parameter values $M_{eff} = 3\ 023.9\ \frac{A}{m}$, $H_{eff}^{loc} = 288\ 700\ \frac{A}{m}$ and $\alpha_{eff} = 0.0835$ are in use. The case of $H_{eff} = const.$ is regarded*

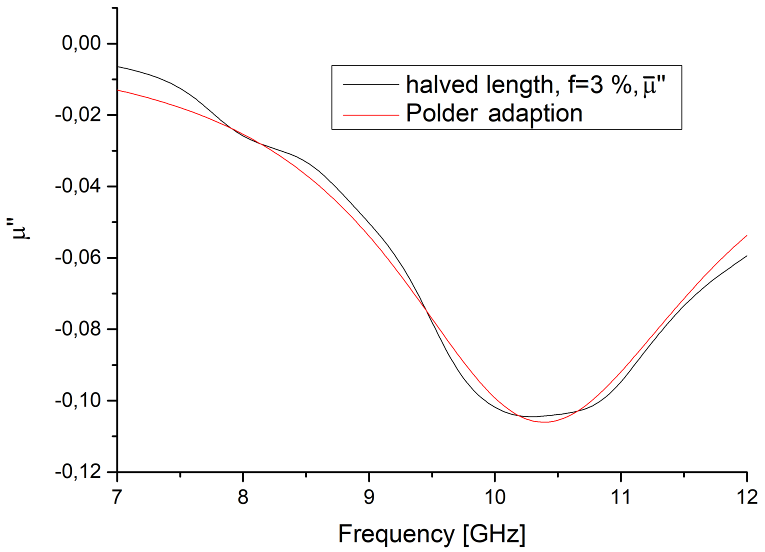

FIGURE 5.50 – *The same analysis as in figure 5.49 is done for a volume fraction of* $f = 3\,\%$. *Input parameters for Polder's equation are* $M_{eff} = 9\ 071.8\ \frac{A}{m}$, $H^{loc}_{eff} = 295\ 000\ \frac{A}{m}$ *and* $\alpha_{eff} = 0.145$.

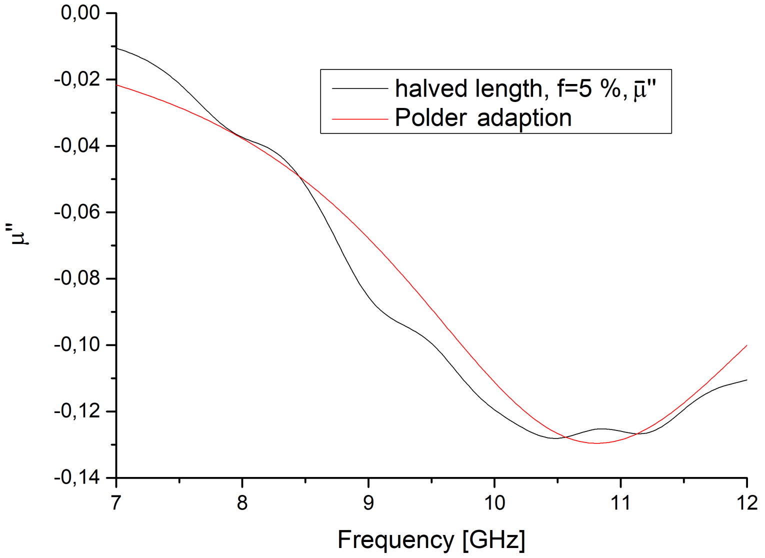

FIGURE 5.51 – *The same analysis as in figure 5.49 is done for a volume fraction of* $f = 5\,\%$. *Input parameters for Polder's equation are* $M_{eff} = 15\ 119.6\ \frac{A}{m}$, $H^{loc}_{eff} = 307\ 000\ \frac{A}{m}$ *and* $\alpha_{eff} = 0.19$.

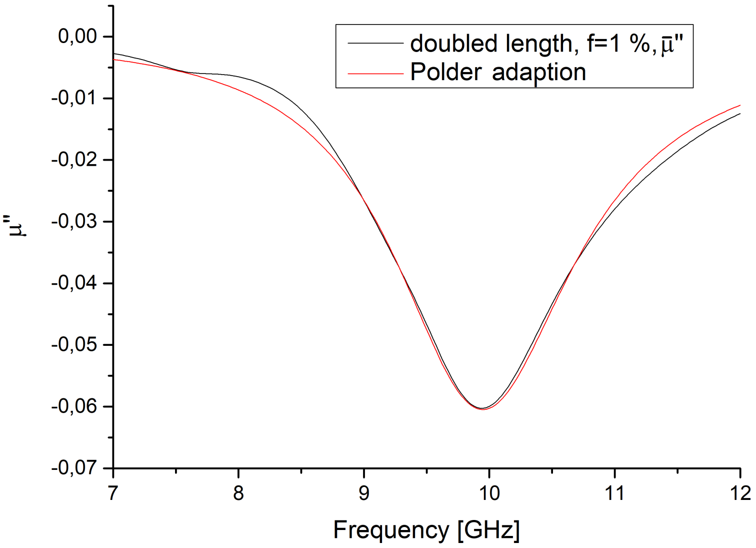

FIGURE 5.52 – *The three curves for μ'' and a filling factor of $f = 1$ % of the samples with doubled length (see figure 5.34) are averaged. Afterwards input parameter for Polder's formula are searched in order to obtain the highest accordance between the two curves. Here, parameter values $M_{eff} = 3\ 023.9\ \frac{A}{m}$, $H_{eff}^{loc} = 282\ 500\ \frac{A}{m}$ and $\alpha_{eff} = 0.0885$ are in use. The case of $H_{eff} = const.$ is regarded.*

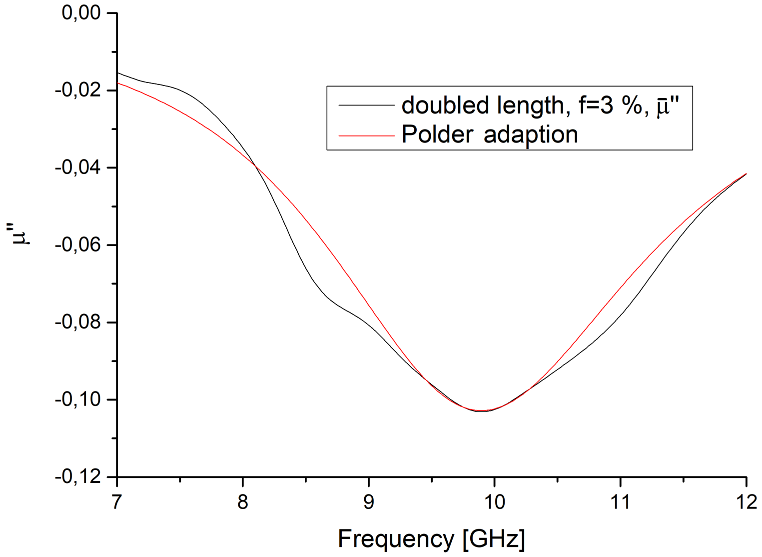

FIGURE 5.53 – *The same analysis as in figure 5.52 is done for a volume fraction of $f = 3$ %. Input parameters for Polder's equation are $M_{eff} = 9\ 071.8\ \frac{A}{m}$, $H_{eff}^{loc} = 281\ 000\ \frac{A}{m}$ and $\alpha_{eff} = 0.157$.*

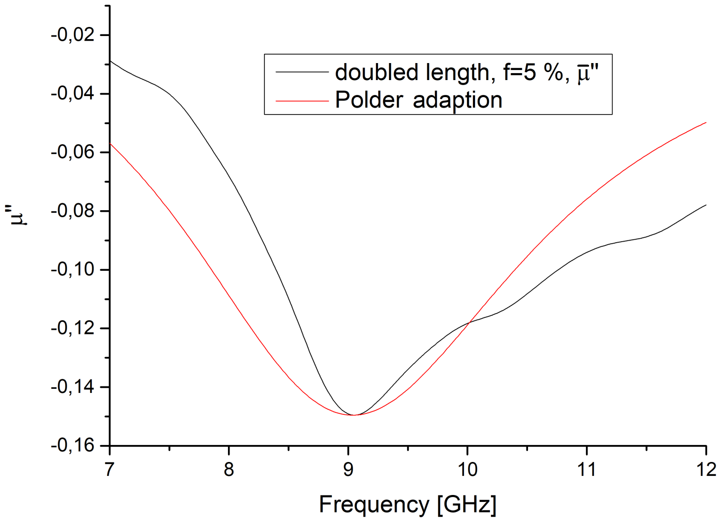

FIGURE 5.54 – *The same analysis as in figure 5.52 is done for a volume fraction of* $f = 5\ \%$. *Input parameters for Polder's equation are* $M_{eff} = 15\ 119.6\ \frac{A}{m}$, $H_{eff}^{loc} = 256\ 600\ \frac{A}{m}$ *and* $\alpha_{eff} = 0.197$.

These adaptions show good agreement for the cases of $f = 1\ \%$, but decreasing quality for higher filling factors, especially for the sample with doubled length (see figure 5.54). Nevertheless, we can assume that in the large system limit of $N_{inc} \to \infty$ the differences between the composite's resonance curves and the adaption with the help of Polder's model reduce. Under this assumption, we try to formulate equations for the effective susceptibility tensor in the case of the regarded finite samples. For that purpose, we plot the found effective parameters H_{eff}^{loc} and α_{eff} in dependence of the filling factor for every geometry in figures 5.55 and 5.56.

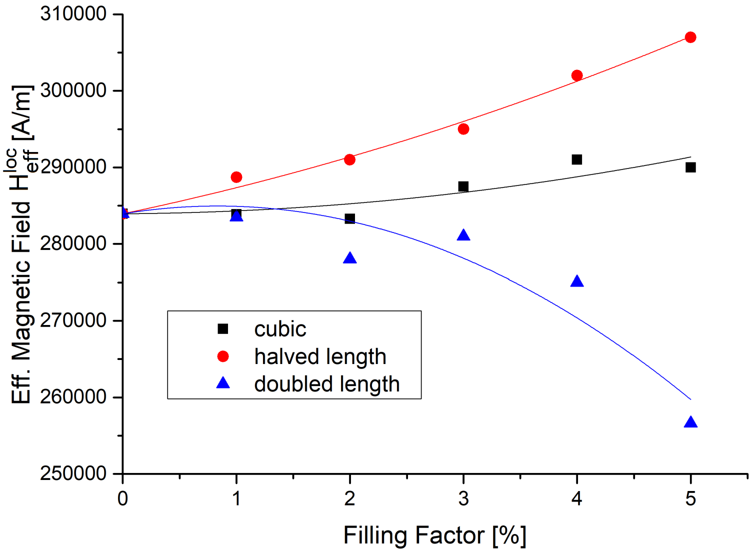

FIGURE 5.55 – *The found values for the local effective magnetic field* H_{eff}^{loc} *are plotted in dependence of the filling factor for every of the three regarded geometries and parabolic fitted. Thereby, we observe the same tendencies as for the averaged resonance frequency in figure 5.36. The case of* $H_{eff} = const.$ *is regarded.*

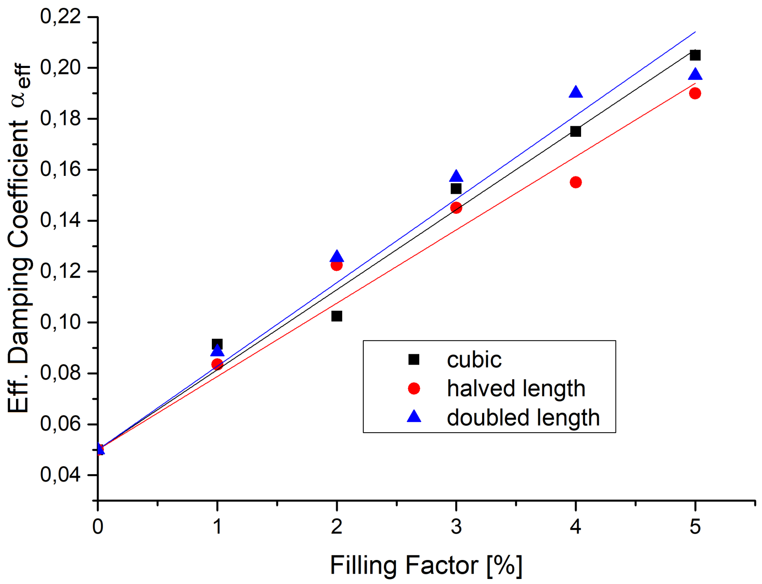

FIGURE 5.56 – *The determined values for the effective damping coefficient* α_{eff} *are plotted in dependence of the filling factor for every of the three regarded geometries and linear fitted.*

Parabolic fitting of the data set for the effective magnetic fields delivers (under the condition $H^{loc}_{eff}(f = 0\ \%) = 283\ 950.5\ \frac{\mathrm{A}}{\mathrm{m}}$)

cubic:

$$H^{loc}_{eff}(f) = (276 \pm 220)\ \frac{\mathrm{A}}{\mathrm{m}(\%)^2} f^2 + (100 \pm 931)\ \frac{\mathrm{A}}{\mathrm{m}\%} f + 283\ 950.5\ \frac{\mathrm{A}}{\mathrm{m}} \tag{5.12}$$

halved length:

$$H^{loc}_{eff}(f) = (305 \pm 123)\ \frac{\mathrm{A}}{\mathrm{m}(\%)^2} f^2 + (3103 \pm 518)\ \frac{\mathrm{A}}{\mathrm{m}\%} f + 283\ 950.5\ \frac{\mathrm{A}}{\mathrm{m}} \tag{5.13}$$

doubled length:

$$H^{loc}_{eff}(f) = (-1454 \pm 531)\ \frac{\mathrm{A}}{\mathrm{m}(\%)^2} f^2 + (2426 \pm 2241)\ \frac{\mathrm{A}}{\mathrm{m}\%} f + 283\ 950.5\ \frac{\mathrm{A}}{\mathrm{m}}. \tag{5.14}$$

Linear fitting of the data sets for the effective damping coefficients delivers (under the condition $\alpha_{eff}(f = 0\ \%) = 0.05$)

cubic :

$$\alpha_{eff}(f) = (0.031 \pm 0.001)\ \frac{f}{\%} + 0.05 \tag{5.15}$$

halved length :

$$\alpha_{eff}(f) = (0.029 \pm 0.001)\ \frac{f}{\%} + 0.05 \tag{5.16}$$

doubled length :

$$\alpha_{eff}(f) = (0.033 \pm 0.001)\ \frac{f}{\%} + 0.05. \tag{5.17}$$

Within this, we observe two phenomena:
Firstly, the local effective magnetic fields show the same tendencies as the resonance frequencies (see figure 5.36) which is no surprise due to the coupling of both magnitudes. This highlights again that dipolar fields in the matrix strongly depend on the sample geometry.
Secondly, we obtain values for the effective damping coefficient α_{eff} which seem to be independent of the device extensions and always show a linear relationship with regard to the volume fraction of the inclusions.
As already indicated, the performed adaptions are used for determining the values of $\mu'_{stat} = 1 + \frac{M_{eff}}{H^{loc}_{eff}}$. Corresponding results are shown in figure 5.57.

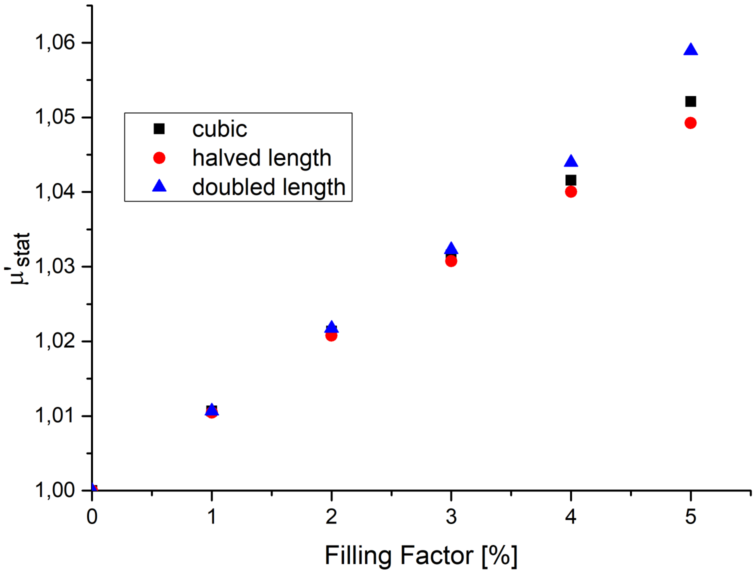

Figure 5.57 – *The magnitude of μ'_{stat} is analyzed for the three differentgeometric extensions.*

As can be observed, values of μ'_{stat} show a dependence on the sample geometry, which is a consequence of the different tendencies of the local effective field. Accordingly, μ'_{stat} is larger, when H^{loc}_{eff} is small.
Of course, the gained relations for the magnitudes of the local effective magnetic field, the damping coefficient and so on only apply for the material parameters of the ferrite inclusions and the magnetic field values in use. In order to derive general formulas, an analysis of the whole phase space of H_{inc}, M^{inc}_s and α would be necessary, which can not be delivered in this work.

5.2 Variation of Inclusion Density

After the analysis of finite samples with a homogeneous inclusion distribution in the previous section, we want to include a further aspect which could play an important role when experimentally examining real composites. Under the influence of gravity, buoyancy or other forces in the host matrix, it is possible that internal inclusion density becomes inhomogeneous what could be linked with an influence on the ferromagnetic resonance. In the following, we want to analyze this issue with the methods at hand. In order to perform a senseful examination of this topic, we have to define a model as simple as possible for an inhomogeneous inclusion distribution inside the matrix. For that purpose, we consider the finite cubic sample from the previous section with an edge length of $a_x = a_y = a_z = 1$ cm, $N_{inc} = 64$ (in high-frequency simulations), $f = 3$ % and divide it at $z = 0.5$ cm into two halves, an upper and a lower region. Afterwards, we distribute inclusions in such a way that in both regions different volume fractions are realized.

As before, we firstly have to analyze the static dipolar fields in these samples. Therefore, we once again analyze the convergence behavior of the average magnetic field at the centers of the inclusions and the field distributions in the large system limit for the sample in total and separately for the both regions. For this purpose, we regard the following filling factors in the both regions (first value valid for the upper region $z \geq 0.5$ cm):

- 3 % – 3 %
- 2.4375 % – 3.5625 %
- 1.5 % – 4.5 %
- 0.75 % – 5.25 %
- 0 % – 6 %

Within this, the first density distribution 3 % – 3 % does not have to be analyzed because it corresponds to the cubic composite with a homogeneous inclusion distribution which was under test in the previous section. Regarding the four other, results of the convergence analysis with regard to the average internal magnetic field and static field distributions are shown in figures 5.58-5.64 or 5.65-5.77, respectively. In these examinations, $H_{inc} = 183\,154\ \frac{\mathrm{A}}{\mathrm{m}} = const.$ is regarded.

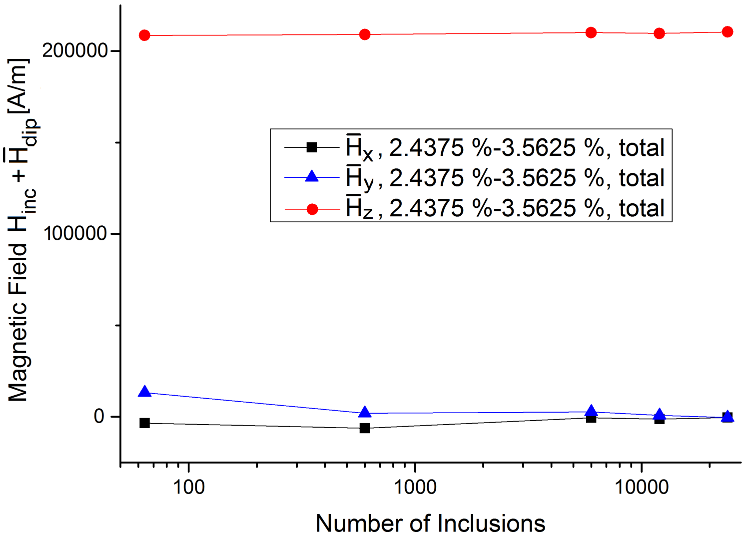

FIGURE 5.58 – *The components of the average magnetic field at the positions of the inclusions in dependence of the number of included spheres. Here, the complete sample with the filling factors* 2.4375 % *and* 3.5625 % *is regarded.*

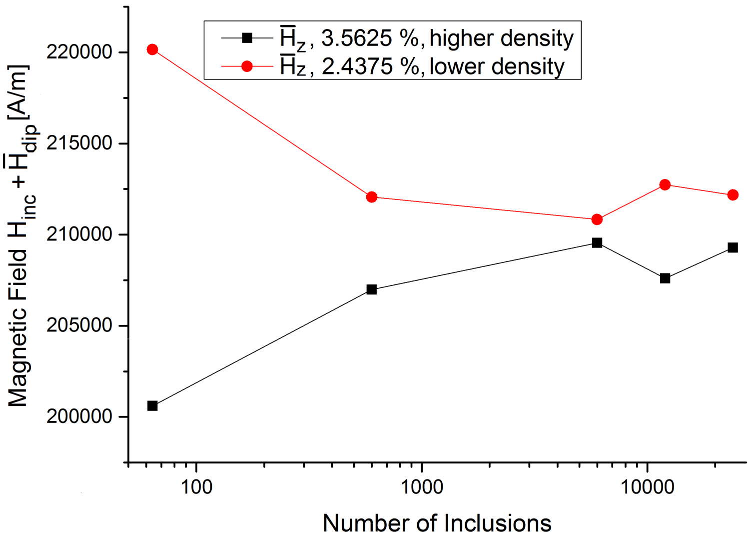

FIGURE 5.59 – *The* $z-$*components of the average magnetic field in dependence of the number of included spheres in the regions with* 2.4375 % *and* 3.5625 % *are compared to each other.*

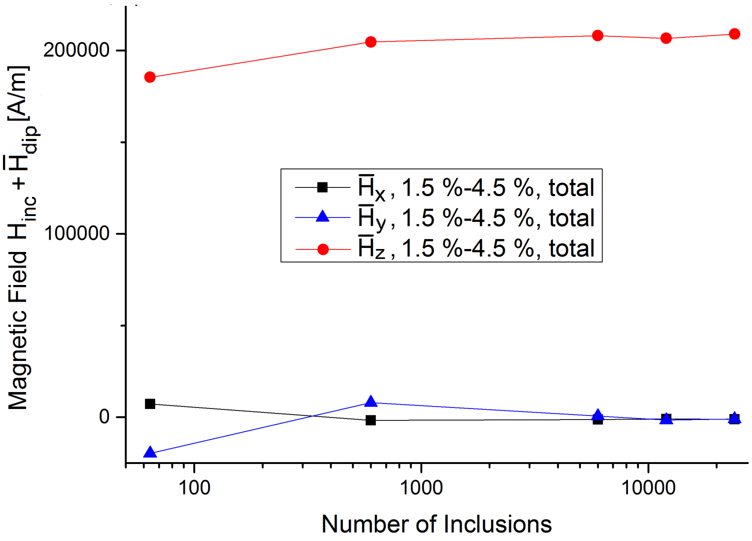

FIGURE 5.60 – *The convergence analysis of the magnetic field components is done for the whole device with the volume fractions* 1.5 % *and* 4.5 % *in both regions.*

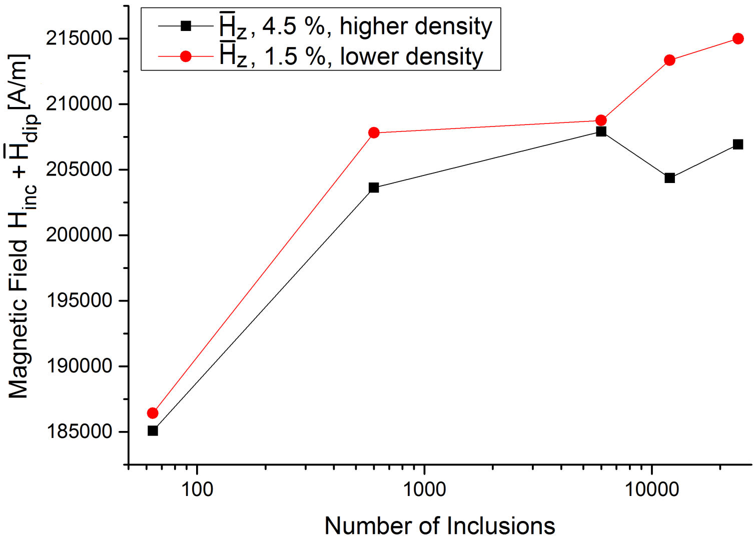

FIGURE 5.61 – *The $z-$components of the average magnetic field in dependence of the number of included spheres in the regions with $1.5\ \%$ and $4.5\ \%$ are compared to each other.*

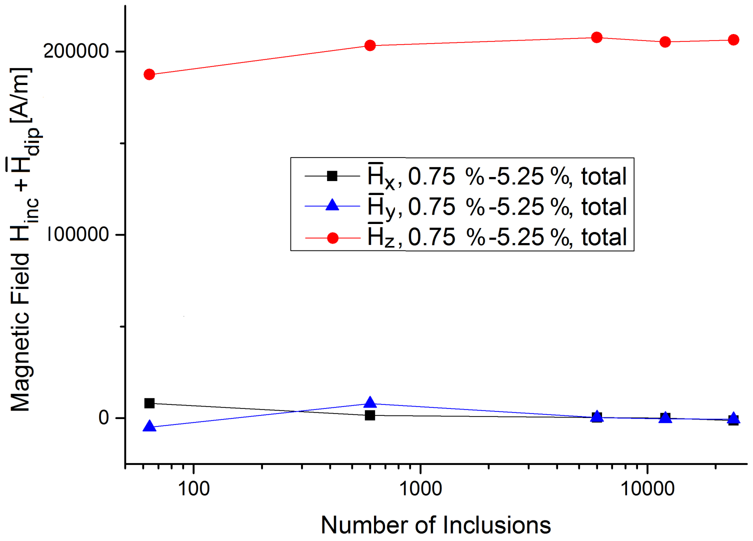

FIGURE 5.62 – *The convergence analysis of the magnetic field components is done for the whole device with the volume fractions $0.75\ \%$ and $5.25\ \%$ in both regions.*

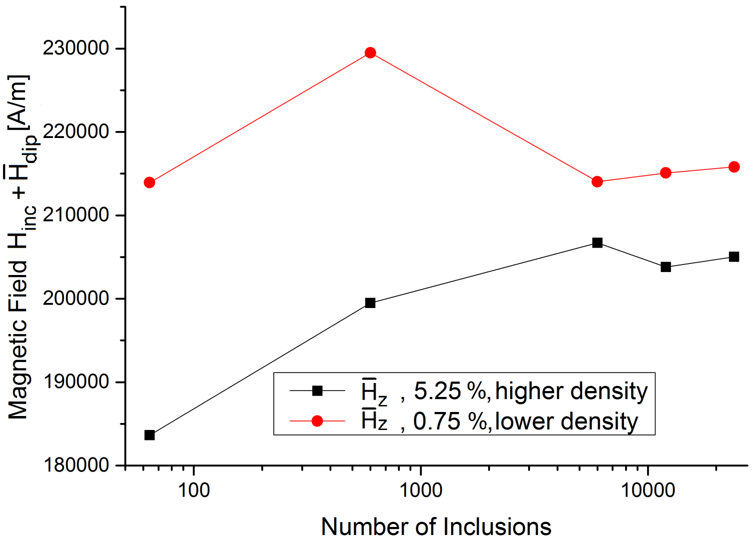

FIGURE 5.63 – *The* $z-$*components of the average magnetic field in dependence of the number of included spheres in the regions with* 0.75 % *and* 5.25 % *are compared to each other.*

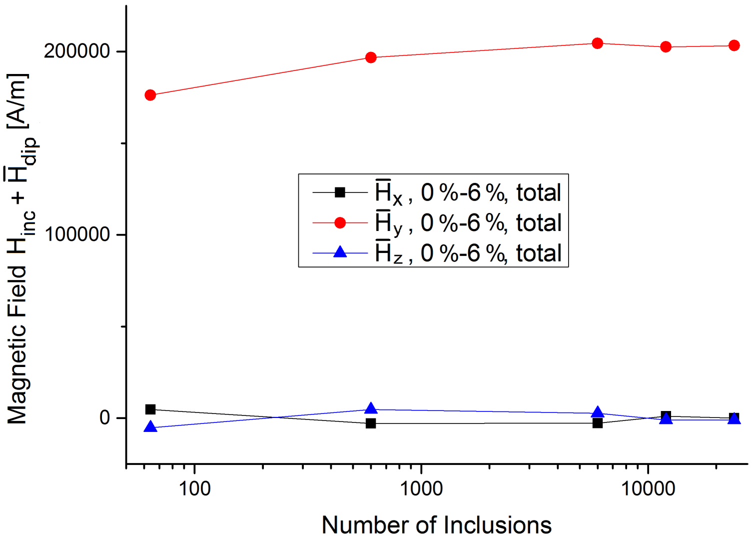

FIGURE 5.64 – *The convergence analysis of the magnetic field components is done for the device with the volume fractions* 0 % *and* 6 % *in both regions. Because inclusions are only placed in the high volume fraction region, a separated analysis of both regions does not contain further information.*

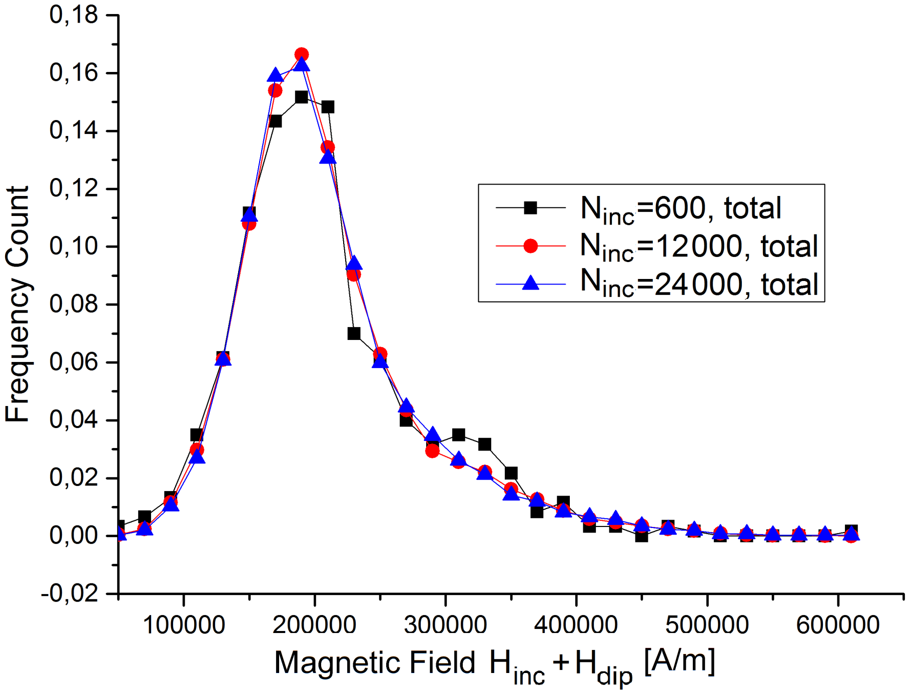

FIGURE 5.65 – *We regard field distributions for different inclusion numbers in the whole sample with an inclusion volume fraction of* 2.4375 % *in the upper region and* 3.5625 % *in the lower one. Curves for* $N_{inc} = 12\ 000$ *and* $N_{inc} = 24\ 000$ *are almost identical.*

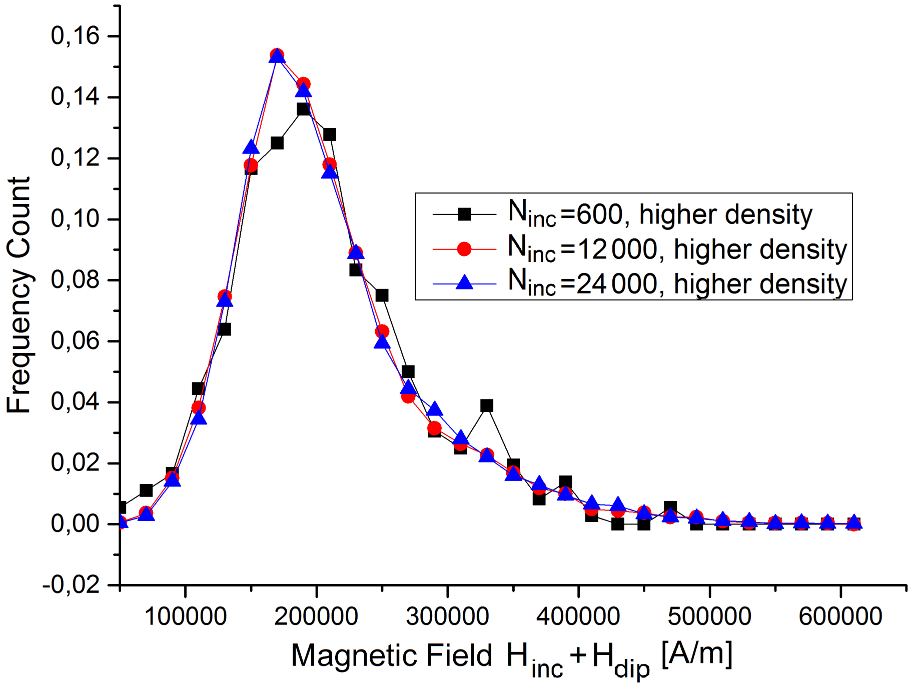

FIGURE 5.66 – *The same sample as analyzed in figure 5.65 is regarded, but only fields in the lower region with* $f = 3.5625$ % *are taken into account.*

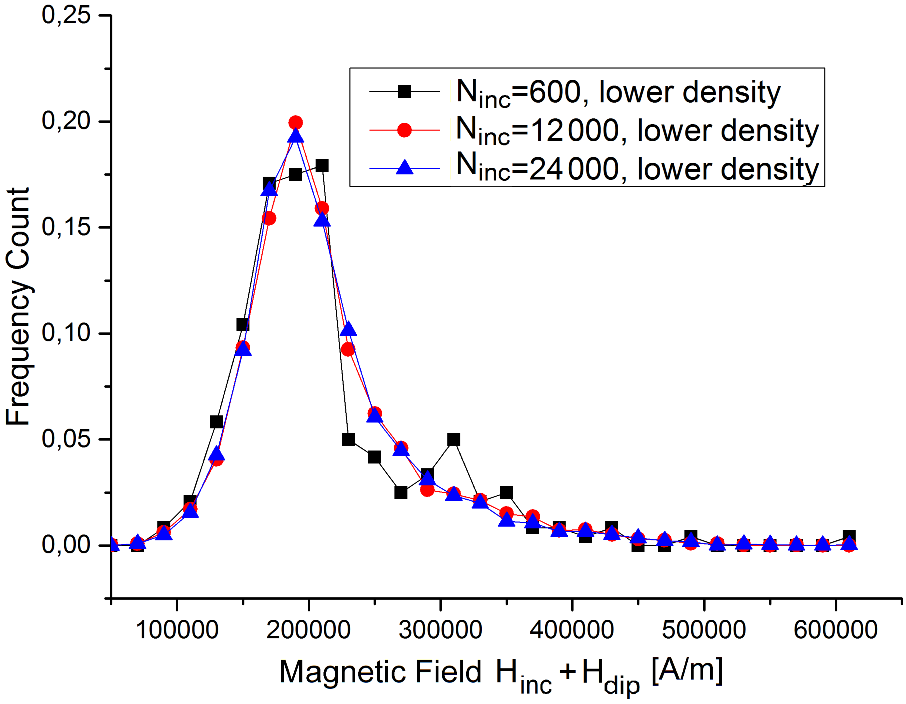

Figure 5.67 – *The same sample as analyzed in figure 5.65 is regarded, but only fields in the upper region with* $f = 2.4375$ % *are taken into account.*

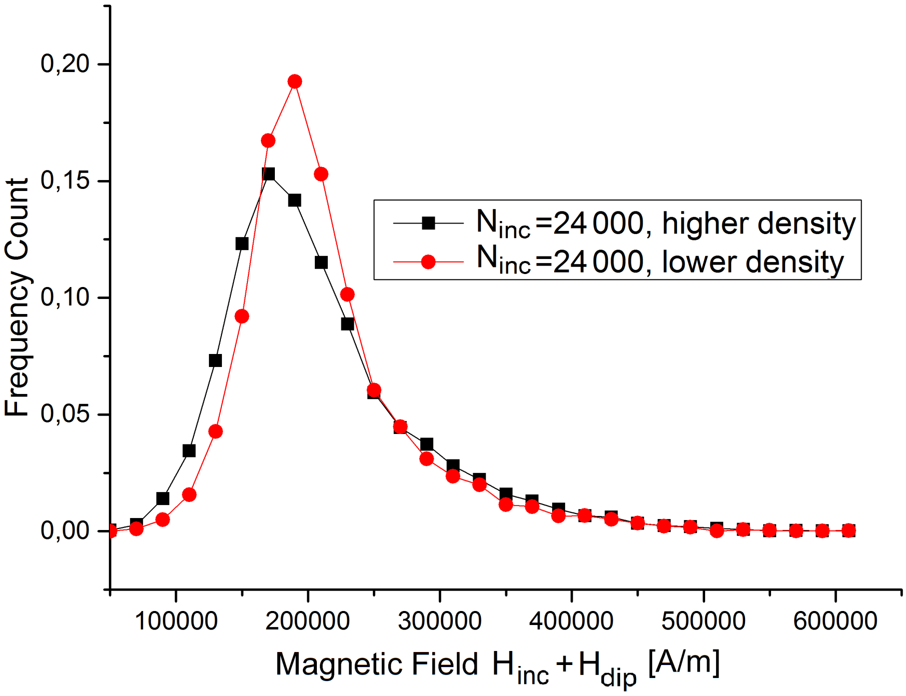

Figure 5.68 – *The comparison between the field distributions in the high and low density region for the sample with an inclusion volume fraction of* 2.4375 % *in the upper region and* 3.5625 % *in the lower one. Both distributions are normalized concerning the number of inclusions in the respective region.*

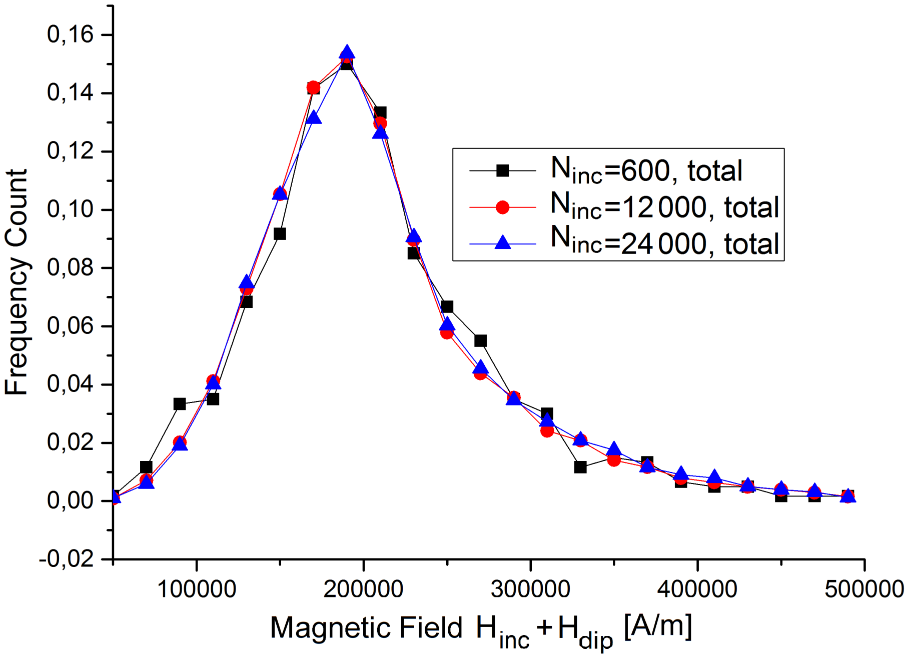

FIGURE 5.69 – *We regard field distributions for different inclusion numbers in the whole sample with an inclusion volume fraction of* $1.5\ \%$ *in the upper region and* $4.5\ \%$ *in the lower one. Curves for* $N_{inc} = 12\ 000$ *and* $N_{inc} = 24\ 000$ *are almost identical.*

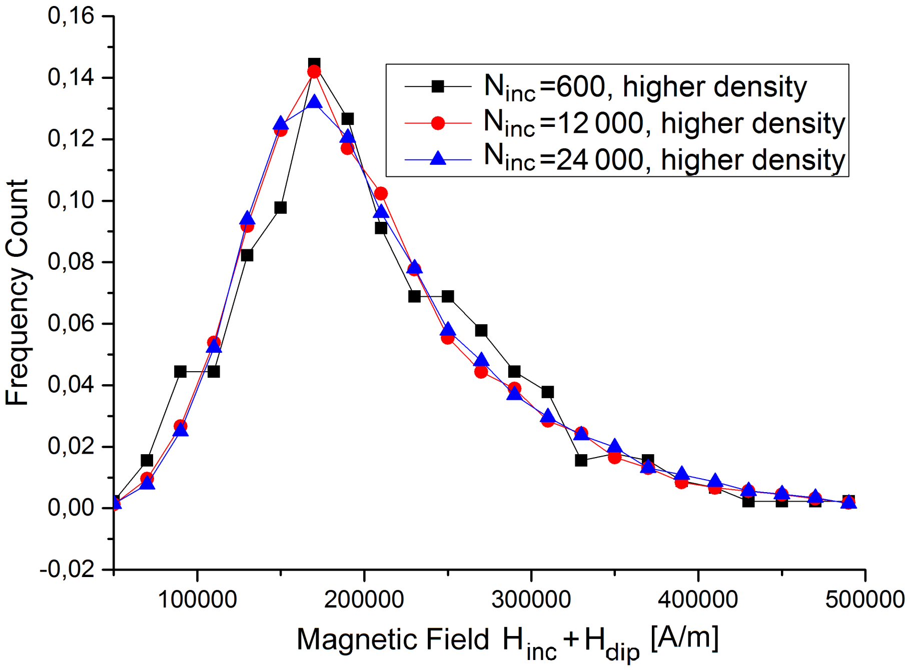

FIGURE 5.70 – *The same sample as analyzed in figure 5.69 is regarded, but only fields in the lower region with* $f = 4.5\ \%$ *are taken into account.*

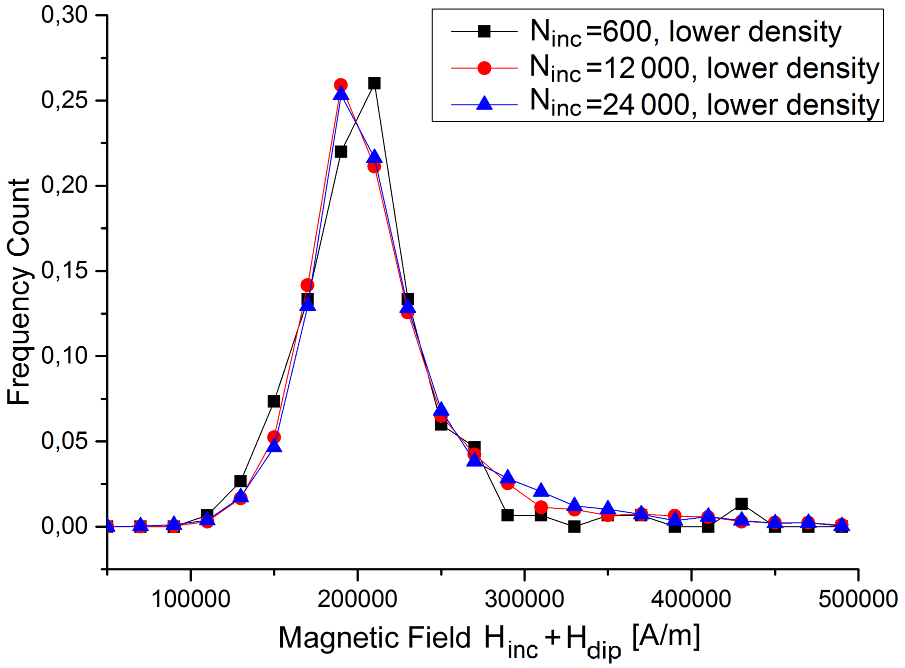

FIGURE 5.71 – *The same sample as analyzed in figure 5.69 is regarded, but only fields in the upper region with* $f = 1.5$ % *taken into account.*

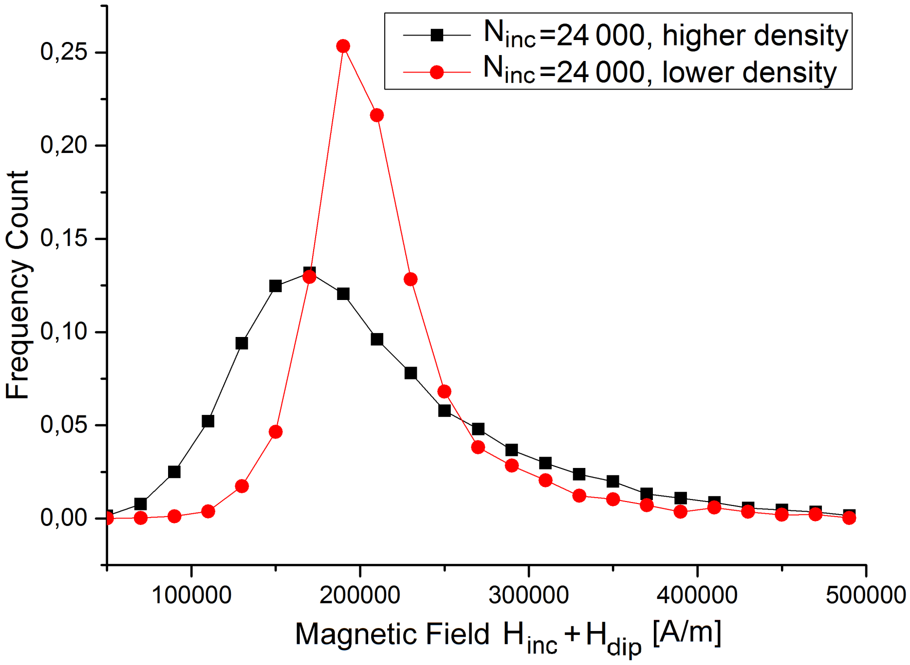

FIGURE 5.72 – *The comparison between the field distributions in the high and low density region for the sample with an inclusion volume fraction of* 1.5 % *in the upper region and* 4.5 % *in the lower one. Both distributions are normalized concerning the number of inclusions in the respective region.*

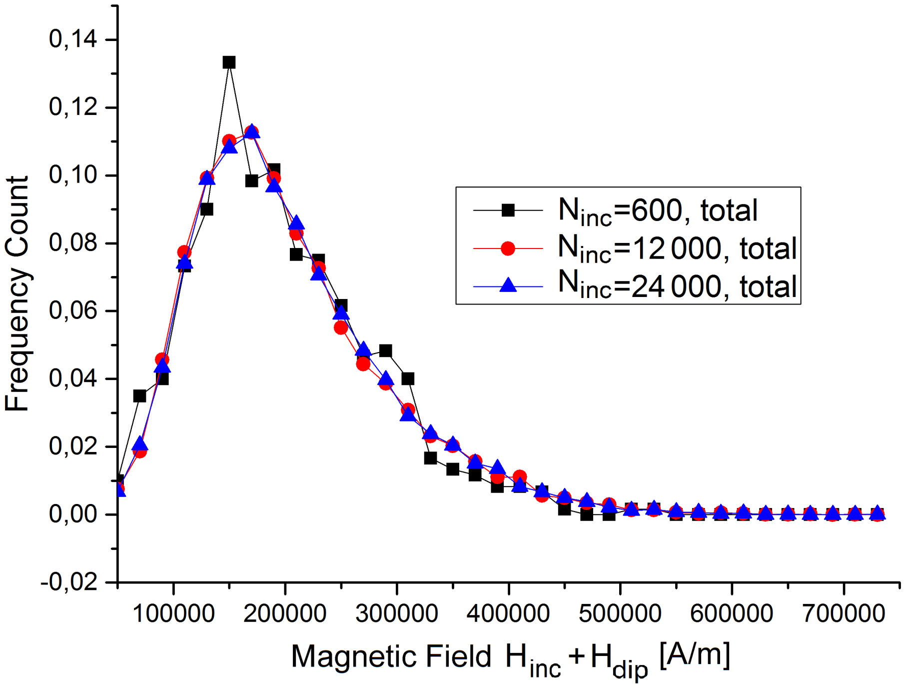

FIGURE 5.73 – *We regard field distributions for different inclusion numbers in the whole sample with an inclusion volume fraction of* 0.75 % *in the upper region and* 5.25 % *in the lower one. Curves for* $N_{inc} = 12\ 000$ *and* $N_{inc} = 24\ 000$ *are almost identical.*

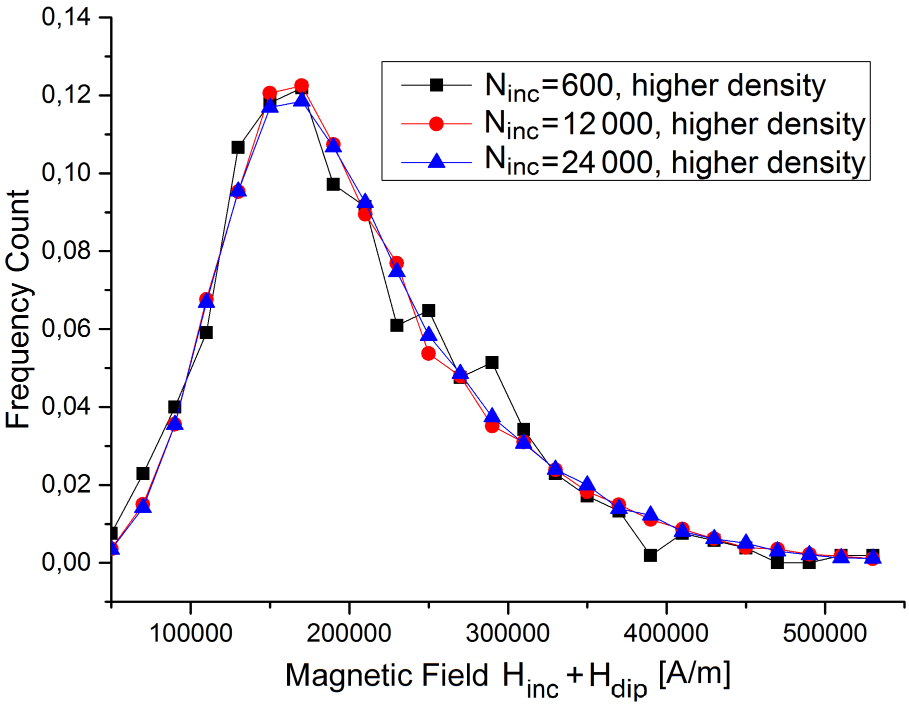

FIGURE 5.74 – *The same sample as analyzed in figure 5.73 is regarded, but only fields in the lower region with* $f = 5.25$ % *are taken into account.*

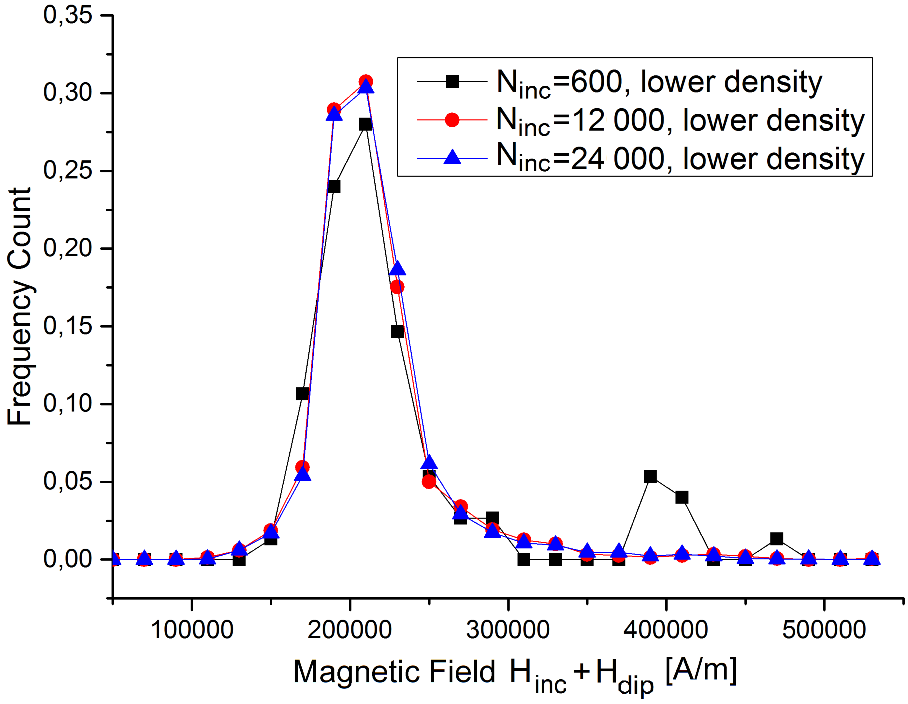

Figure 5.75 – *The same sample as analyzed in figure 5.73 is regarded, but only fields in the upper region with* $f = 0.75$ % *are taken into account.*

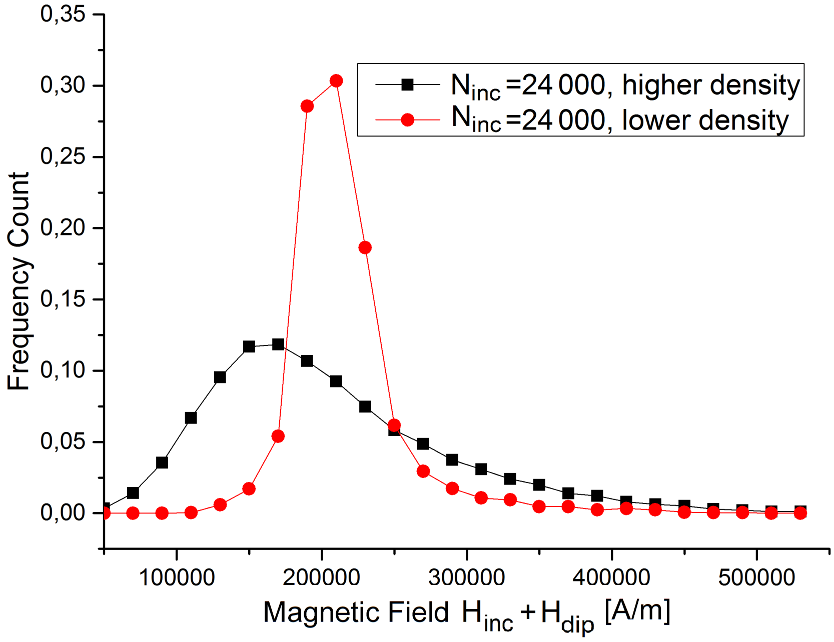

Figure 5.76 – *The comparison between the field distributions in the high and low density region for the sample with an inclusion volume fraction of* 0.75 % *in the upper region and* 5.25 % *in the lower one. Both distributions are normalized concerning the number of inclusions in the respective region.*

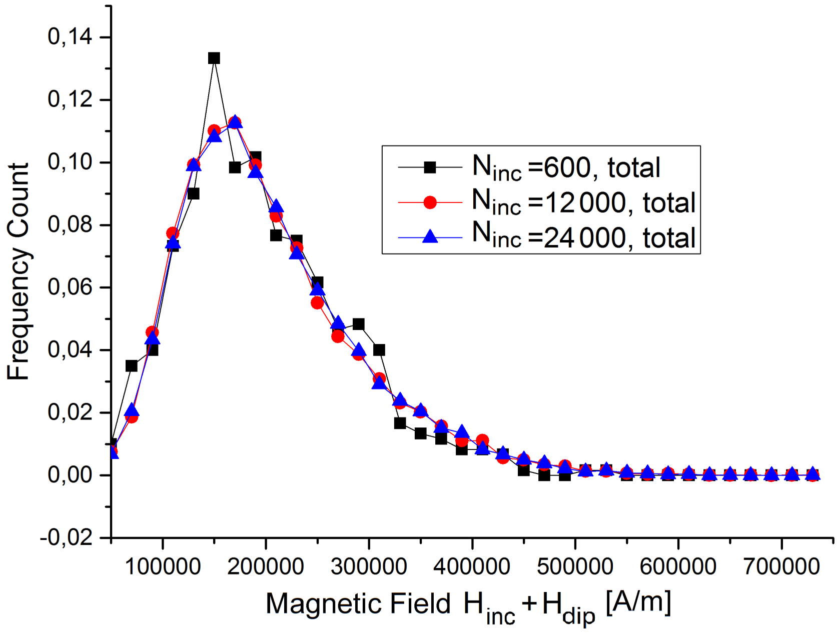

FIGURE 5.77 – *We regard field distributions for different inclusion numbers in the whole sample with an inclusion volume fraction of* $0\ \%$ *in the upper region and* $6\ \%$ *in the lower one. Curves for* $N_{inc} = 12\ 000$ *and* $N_{inc} = 24\ 000$ *are almost identical. Because inclusions are only placed in the high volume fraction region, a separated analysis of both regions does not contain further information.*

Again, we detect convergence behavior for $N_{inc} \geq 12\ 000$ in every case and in every density region and, thereby, gain knowlegde about the large system limit. As before, it is also justified to neglect the components of the magnetic field in $x-$ and $y-$direction because $\overline{H}_x, \overline{H}_y \ll \overline{H}_z$ is still always fulfilled. Furthermore, we observe that the average internal magnetic field in the inclusions in the region with the lower density is always stronger compared to the values in the high density region. Phenomenologically, this can be explained by again regarding the schematic sketch of the dipolar interaction in figure 5.38: Due to the orientation of the magnetic moments along $z-$axis, the inclusions' dipoles of the low and high density region (separated by $z = 0.5$ cm) enforce the magnetic fields at the positions of the inclusions in the other region. Consequently, the larger number of magnetic dipoles in the high density region creates stronger magnetic fields in the low density area than the other way around.

Moreover, the distribution in the low density region becomes sharper the higher the volume fraction difference grows while the distribution in the high density region becomes more blurred (see figures 5.68, 5.72 and 5.76). In order to compare the static behavior of the samples with different volume fraction differences, we regard the inclusions' average internal magnetic field component in $z-$direction, which is shown in figure 5.78 for the case of $H_{inc} = const.$.

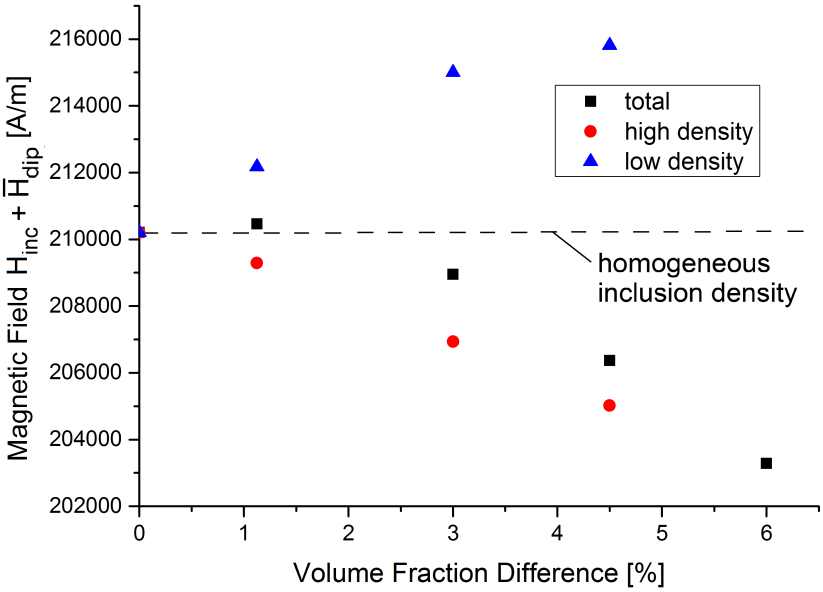

Figure 5.78 – *The average magnetic fields inside the inclusions are plotted in dependence of the differences between the filling factors of the upper and lower region of the device. Black squares rely on the total sample, red circles on the high density region and blue triangles on the low density region.* $H_{inc} = 183\ 154\ \frac{A}{m}$ *is valid in every simulation.*

In this graph, a clear tendency for the average magnetic field to shift towards lower values for higher differences of the volume fraction becomes obvious. For classifying the order of magnitude of this effect, we take a deeper look at the sample with a inclusions' volume fraction of 1.5 % in the low density and 4.5 % in the high density region, i.e. a volume fraction difference of 3 % and corresponding a relative deviation of 50 % with regard to the total filling factor of 3 %. While the average field shrinks by 0.8 % and the high density region field by 1.7 %, magnetic field in the low density area increases by 2.1 %. Contrary, a shift of the the average magnetic field by 1 % requires a volume fraction difference of 3.3 %, i.e. a filling factor of 1.35 % in the low density region and 4.65 %, meaning a relative deviation of 55 %, as interpolated from the shown data. Regarding the systematic errors of the static field simulation in the context of self-consisteny (see figure 4.57), this conclusions are qualitatively trustworthy due to accuracy with more than 99.7 %.

Nevertheless, due to the separation of the composite into two different regions with different properties, a two-peak character of the resonance curve could be assumed.

In order to transfer these results into high-frequency simulations, the found distributions are again used in order to reproduce the large system behavior with an inclusion number of $N_{inc} = 64$, with the same proceeding as before. Though, contrary to previous examinations, we also have to take care on the different volume fractions in both regions. For that purpose, we firstly define a simple cubic lattice in each region with inclusion numbers $N_{inc,up}$ and $N_{inc,low}$, according to the desired volume fractions, and afterwards add gaussianly distributed vectors to their position with the restriction that no inclusion can leave its region.

Again, adaption to $H-$field distribution works very well for the whole sample when trying enough different arrangements, as exemplarily shown for the volume fractions 0.75 % and 5.25 % in figure 5.79.

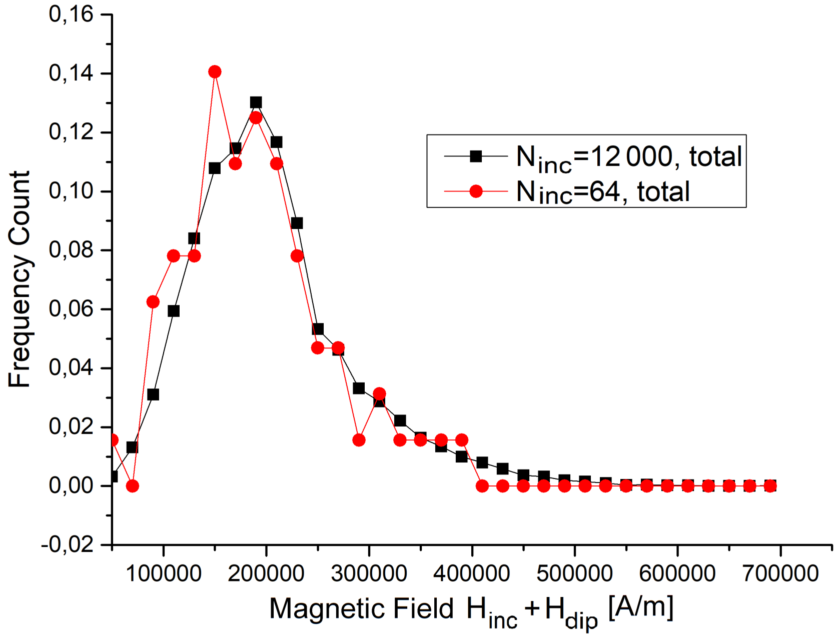

FIGURE 5.79 – *As before, adaption of the distribution of the magnetic field works very well for* $N_{inc} = 64$ *and the large system limit. In this case of volume fractions of* 0.75 % *and* 5.25 % *in the different regions, the defined error function takes the value of* $\Delta = 0.0035$.

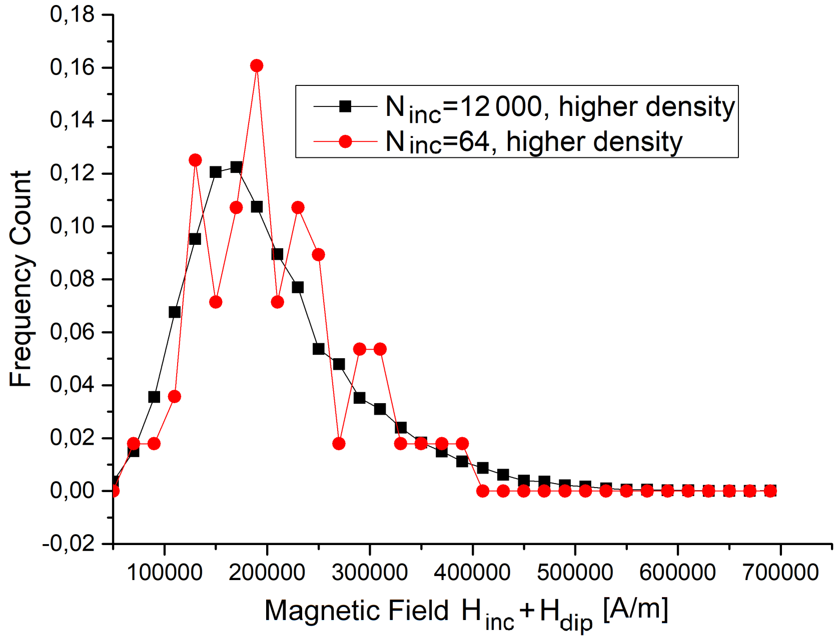

FIGURE 5.80 – *The same sample and microstructure as in figure 5.79 is regarded, but only inclusions in the high density region are taken into account.*

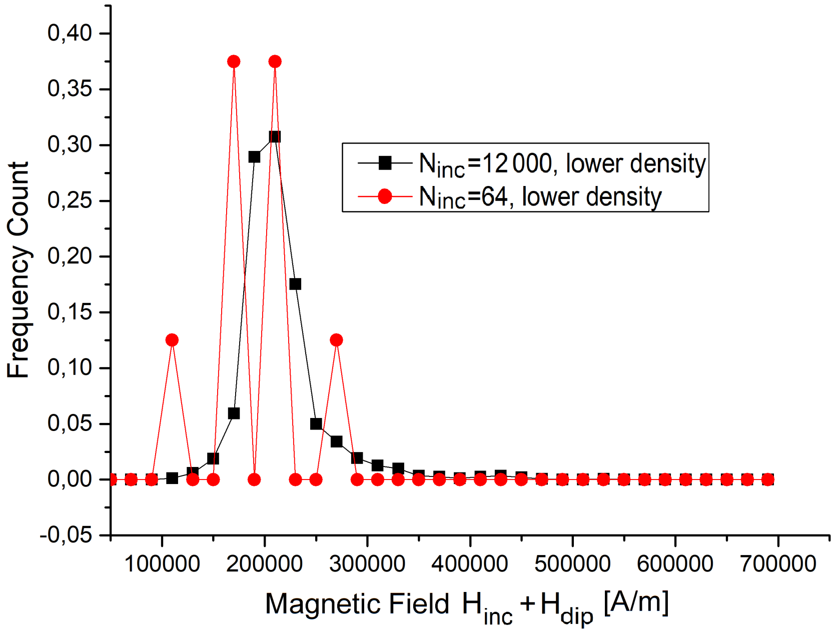

FIGURE 5.81 – *The same sample and microstructure as in figure 5.79 is regarded, but only inclusions in the low density region are taken into account.*

With regard to figures 5.80 and 5.81, one has to admit that adaption in the different regions is of lower quality. Nevertheless, the total distribution of the magnetic field and the density of inclusions in both regions is reconstructed by this representative system. Repeating this procedure for every desired contrast of filling factors, microstructures as shown in figure 5.82 are generated.

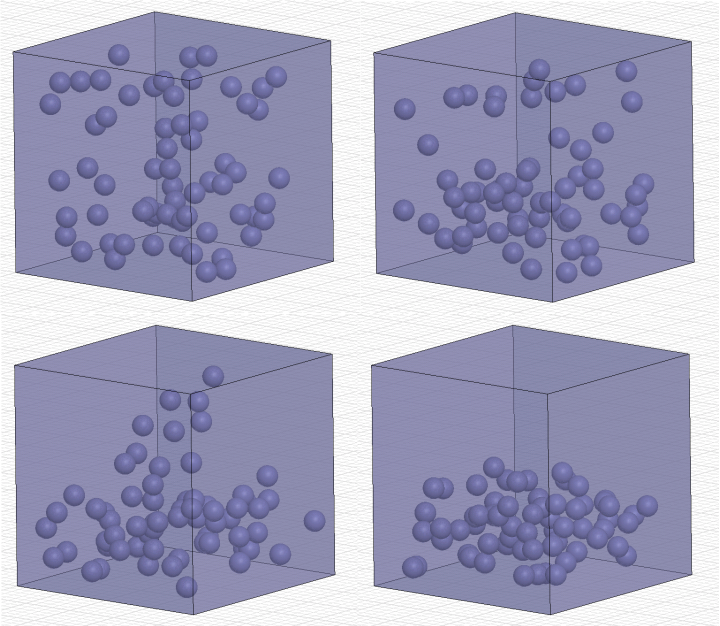

FIGURE 5.82 – *The devices under test for the inhomogeneous inclusion distributions. Top left picture shows the sample with the filling factor of* 2.4375 % *in the upper and* 3.5625 % *in the lower region. Analogically, top right shows the case of* 1.5 % *and* 4.5 %, *bottom left* 0.75 % *and* 5.25 % *and bottom right the case with an empty upper region and* $f = 6$ % *in the lower one.*

Accordingly, we use the shown devices for our high-frequency simulations in which we again include a demagnetization conversion in order to keep the effective field in the composite H_{eff} constant for different filling factors, as in the previous sections. Though, in the present case, we have to take in account that our sample is divided into two halves with different inclusion volume fractions. Accordingly, we use two different values for M_{eff} for the demagnetization correction (according to equation 4.20) for the inclusions in the upper and lower sample region. These values of M_{eff} are calculated by inserting the used volume fractions f into equation 4.13 which we drew from the corresponding linear fitting function. Afterwards, we calculate the entries of the effective Polder tensor with the same accuracy parameters as before, delivering the resonance peaks shown in figure 5.83. Within this plot, it becomes again obvious that the results are affected by artifacts in the form of minor additional hilltops. Accordingly, we again try to gain more insight by considering three different microstructures for every case. The corresponding resonance peaks are shown in pictures 5.84-5.87.

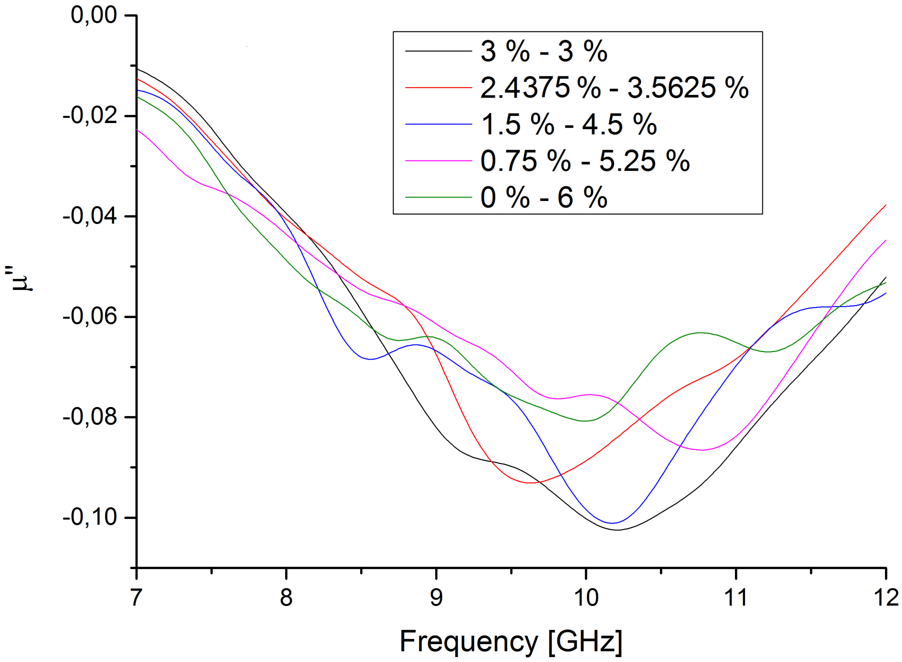

FIGURE 5.83 – *The resonance peaks resulting from different filling factor contrasts. The case of* $H_{eff} = const.$ *is examined.*

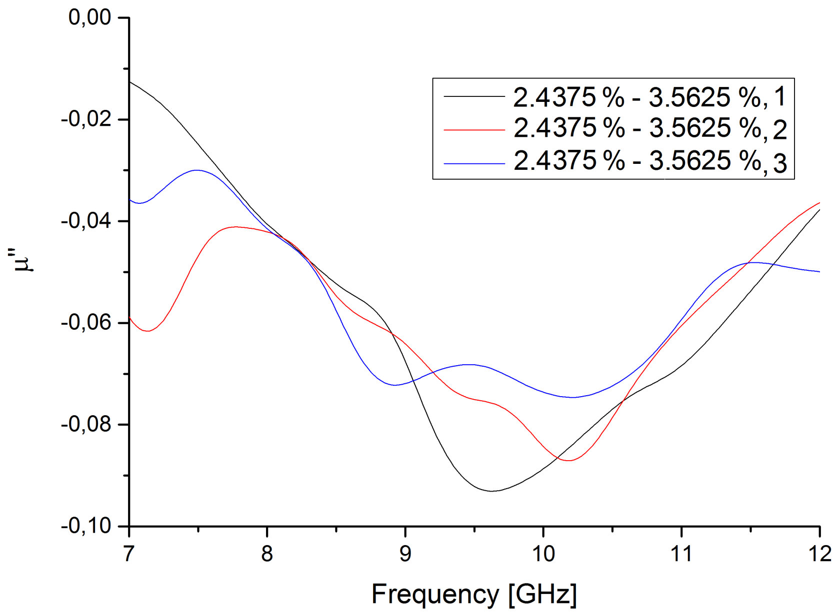

FIGURE 5.84 – *The resonance curves of three different microstructures fulfilling our requirements for the volume fractions of* 2.4375 % *in the upper and* 3.5625 % *in the lower region.*

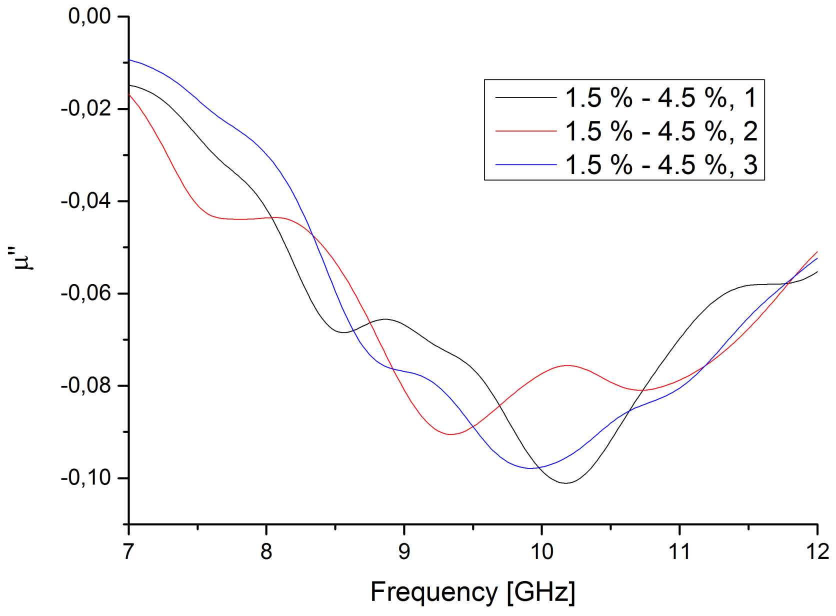

FIGURE 5.85 – *Same plot as in figure 5.84 for filling factors of* 1.5 % *and* 4.5 %.

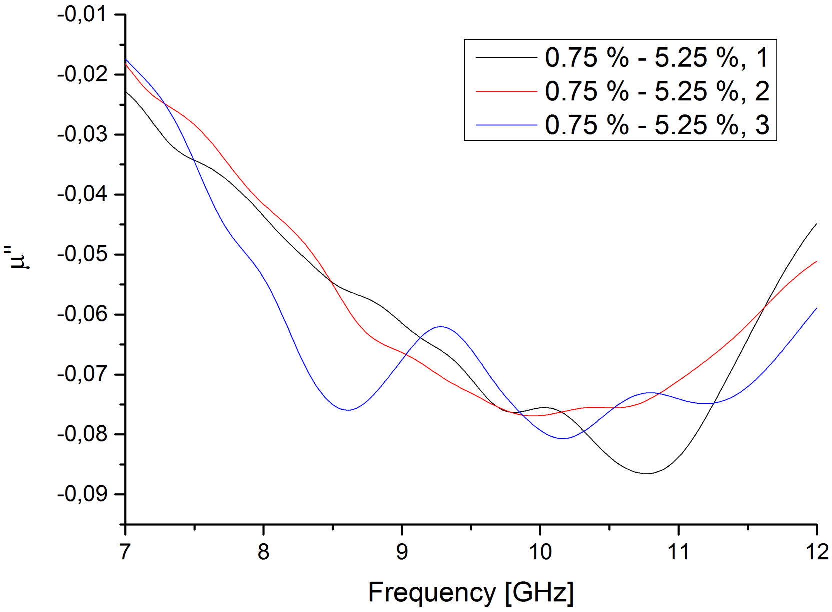

Figure 5.86 – *Same plot as in figure 5.84 for filling factors of* 0.75 % *and* 5.25 %.

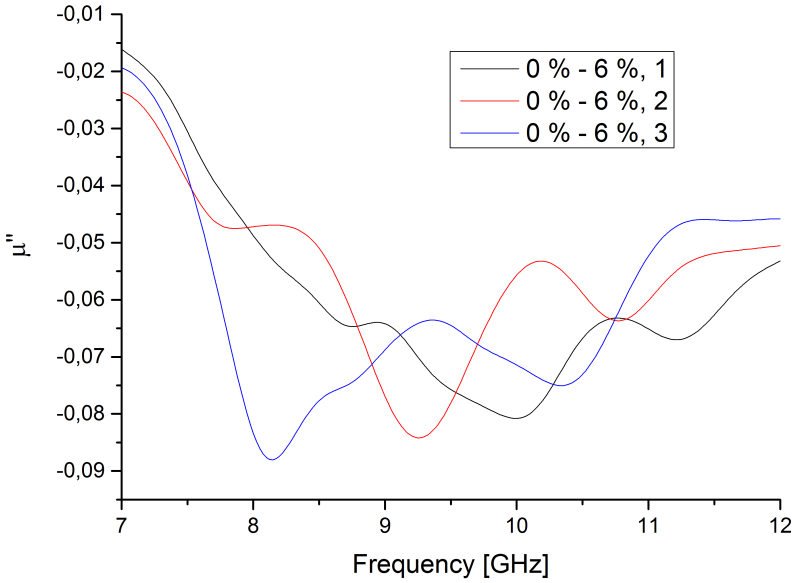

Figure 5.87 – *Same plot as in figure 5.84 for an empty upper region and* 6 % *in the lower region.*

These three different resonance curves for every case show very strong deviations between each other, highlighting that an inclusion number of $N_{inc} = 64$ in the high-frequency simulations is not sufficient in order to draw senseful conclusions for very large systems. Nevertheless, we tried to calculate an average resonance frequency for every regarded case, leading to results shown in figure 5.88.

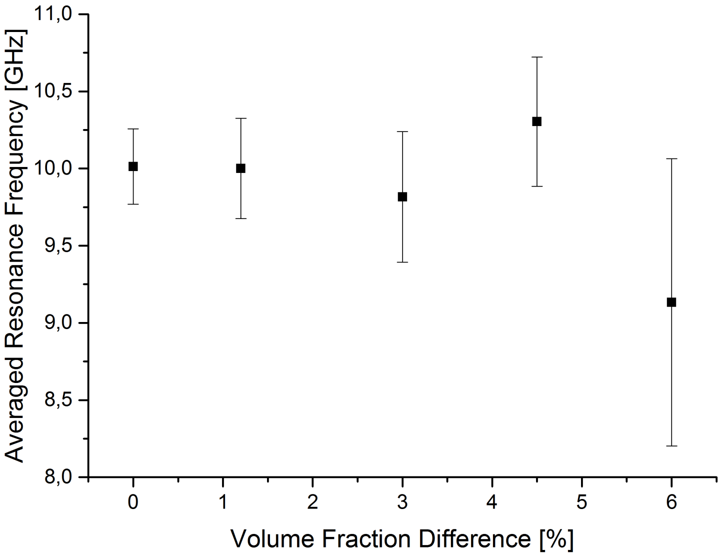

FIGURE 5.88 – *The resonance frequencies of the three different devices for every case are averaged and plotted in dependence of the difference of the volume fractions of the lower and upper region. Error bars denote standard deviations of the frequencies. Note that a zero volume fraction difference belongs to the cubic sample with a homogeneous inclusion distribution analyzed in the previous section and the value of* $6\ \%$ *relies on the sample with an empty upper half.* $H_{eff} = const.$ *is valid for every volume fraction difference.*

In contrast to data in figure 5.78, no unambiguous tendency can not be observed from the performed high-frequency simulations. This result implies that larger inclusion numbers in the high-frequency simulations are necessary in order to examine this issue in a meaningful manner. Furthermore, a growing of the standard deviation with increasing volume fraction difference can be observed which is a consequence of the blurring of the magnetic field distribution in the static simulations.

Concerning the magnitude of $|\mu''_{max}|$ we again simply average the values for the three different microstructures for every volume fraction difference with $H_{eff} = const.$ and plot the results in figure 5.89.

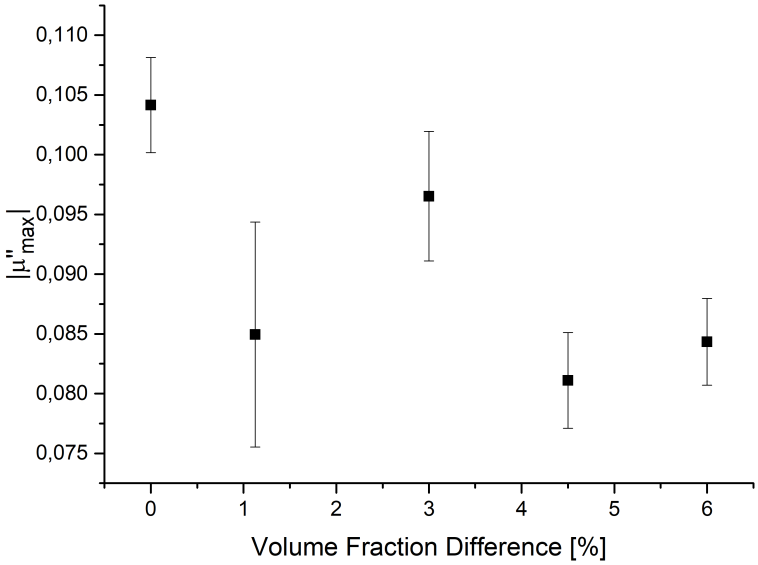

FIGURE 5.89 – *The averaged values of* $|\mu''_{max}|$ *are shown in dependence of the volume fraction difference in the case of* $H_{eff} = const.$.

This graph shows that the values of $|\mu''_{max}|$ are slightly decreasing with raising volume fraction difference, but quality of the results is too low in order to draw quantitative conclusions.

For the purpose of analyzing the magnitude of μ'_{stat}, we regard the curves for μ' for every microstructure of every volume fraction contrast in figures 5.90-5.93.

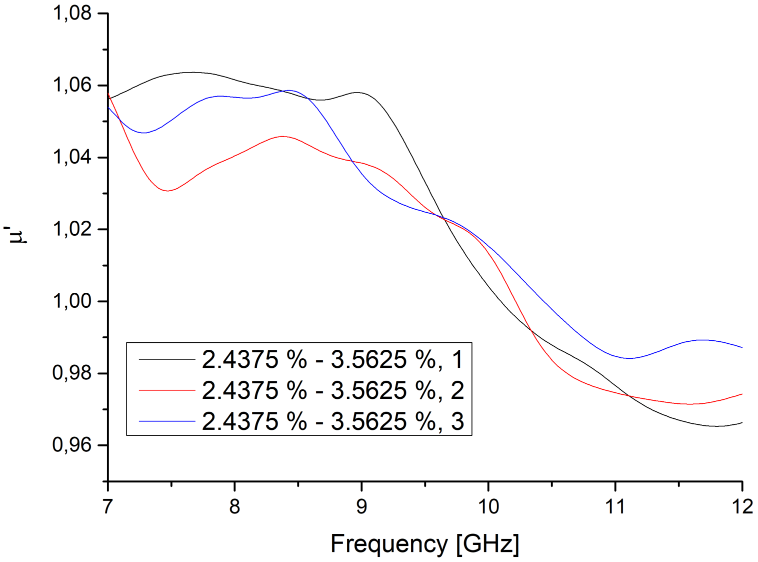

FIGURE 5.90 – *The results for* μ' *for the three microstructures with inclusion volume fractions of* $2.4375\ \%$ *and* $3.5625\ \%$ *in both regions.*

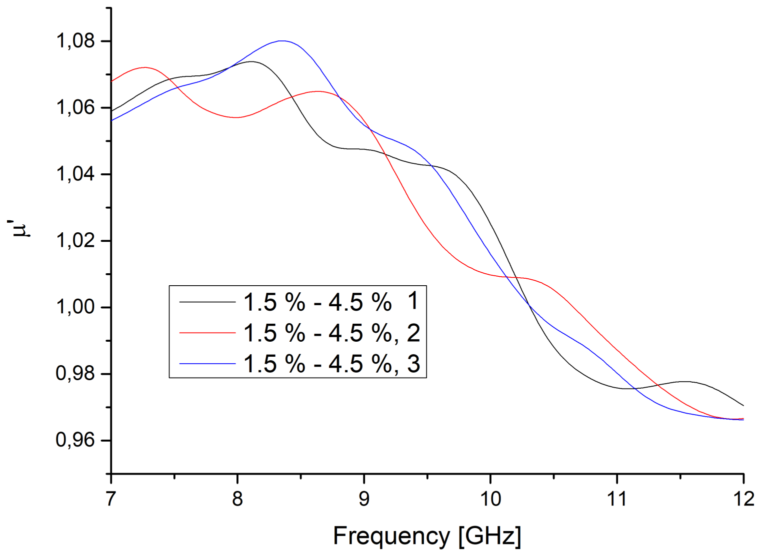

FIGURE 5.91 – *The same analysis as in figure 5.90 is done for volume fractions of* 1.5 % *and* 4.5 % *in both regions.*

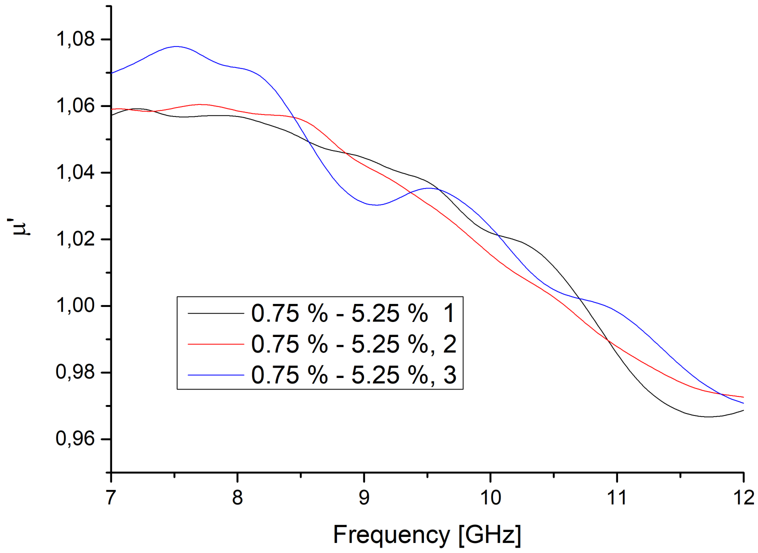

FIGURE 5.92 – *The same analysis as in figure 5.90 is done for volume fractions of* 0.75 % *and* 5.25 % *in both regions.*

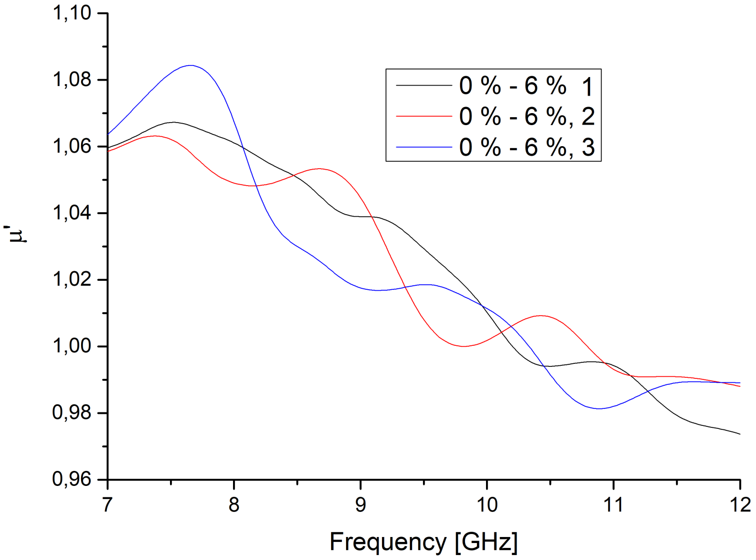

FIGURE 5.93 – *The same analysis as in figure 5.90 is done for volume fractions of* 0 % *and* 6 % *in both regions.*

Within these graphs, it becomes clear that a meaningful direct analysis is again not possible, due to the same reasons as in section 5.1: artifacts are distinct and the accessible frequency range is limited. Accordingly, we again firstly derice an analytic formula for the effectice permeability tensor in order to gain knowledge about the static behavior of μ'.

For the purpose of finding this relation in the case of $H_{eff} = const.$, we again average the three different resonance curves for every volume fraction contrast (see figure 5.94) and try to adapt these mean curves by variation of the input parameters H_{eff}^{loc} and α_{eff} in Polder's formula 1.169, while $M_{eff} = 9071.8\ \frac{\mathrm{A}}{\mathrm{m}}$ remains constant due to the constant filling factor of $f = 3$ % concerning the whole sample. Adaptions to the mean curves are shown in figures 5.95-5.98.

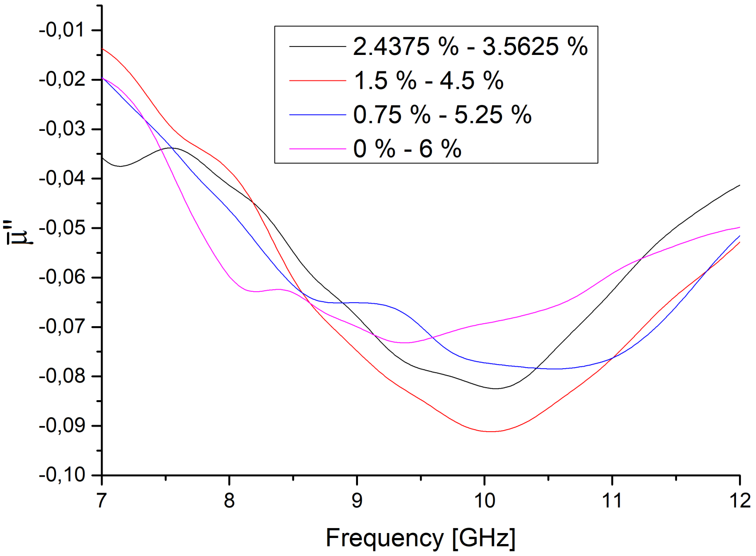

FIGURE 5.94 – *The results for* μ'' *for the three microstructures for every volume fraction contrast are averaged to the mean curves* $\overline{\mu''}$. *The effective field* H_{eff} *was maintained constant for every filling factor difference.*

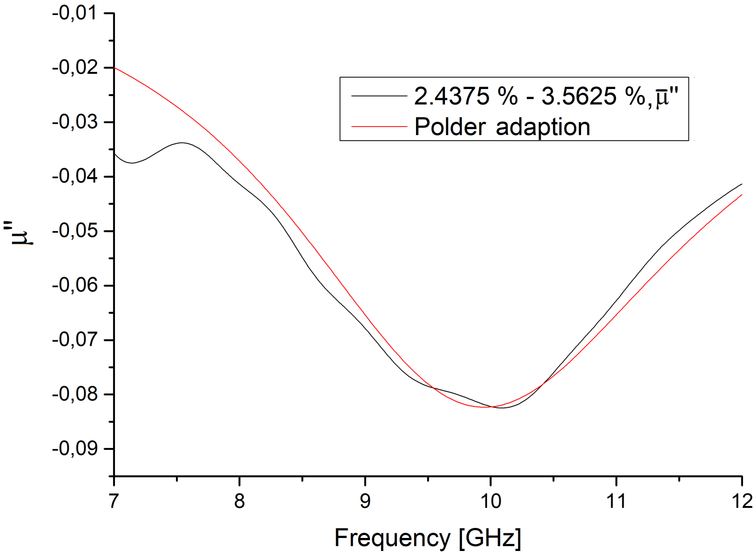

FIGURE 5.95 – *The mean curve for the volume fractions of* 2.4375 % *and* 3.5625 % *is adapted with the parameters* $H_{eff}^{loc} = 282\ 500\ \frac{A}{m}$ *and* $\alpha_{eff} = 0.195$.

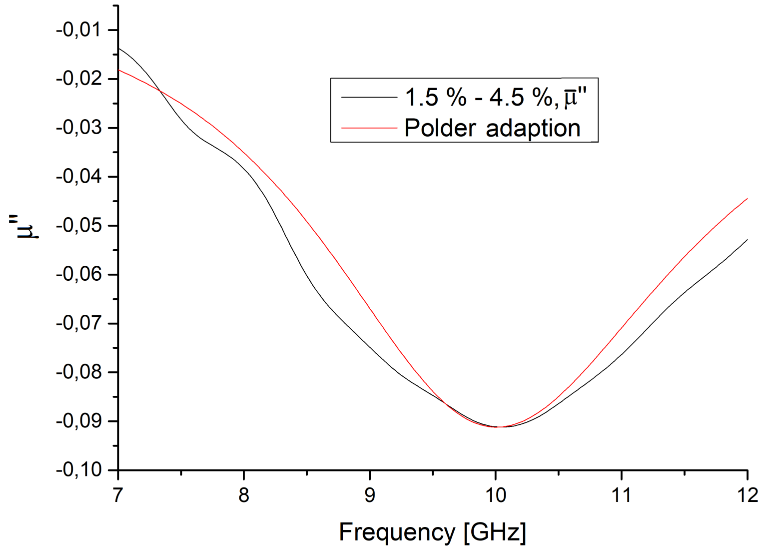

FIGURE 5.96 – *The mean curve for the volume fractions of* $1.5\ \%$ *and* $4.5\ \%$ *is adapted with the parameters* $H_{eff}^{loc} = 284\ 200\ \frac{A}{m}$ *and* $\alpha_{eff} = 0.175$.

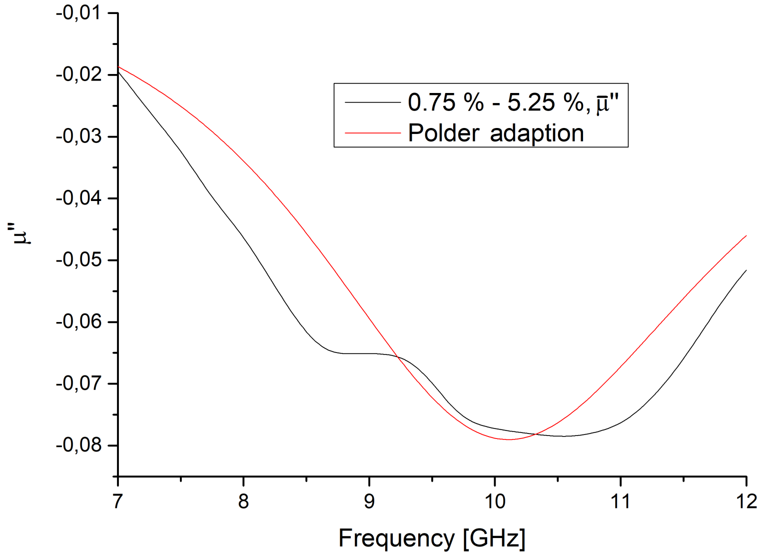

FIGURE 5.97 – *The mean curve for the volume fractions of* $0.75\ \%$ *and* $5.25\ \%$ *is adapted with the parameters* $H_{eff}^{loc} = 287\ 000\ \frac{A}{m}$ *and* $\alpha_{eff} = 0.2$.

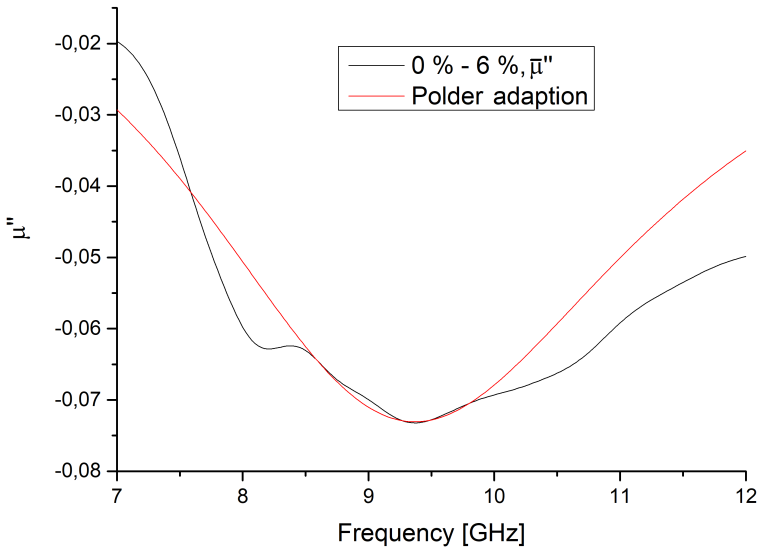

FIGURE 5.98 – *The mean curve for the volume fractions of* $0\ \%$ *and* $6\ \%$ *is adapted with the parameters* $H_{eff}^{loc} = 266\ 000\ \frac{A}{m}$ *and* $\alpha_{eff} = 0.2334$.

For further analysis, we plot the determined adaption parameters in dependence of the inclusions' volume fraction difference in figures 5.99 and 5.100.

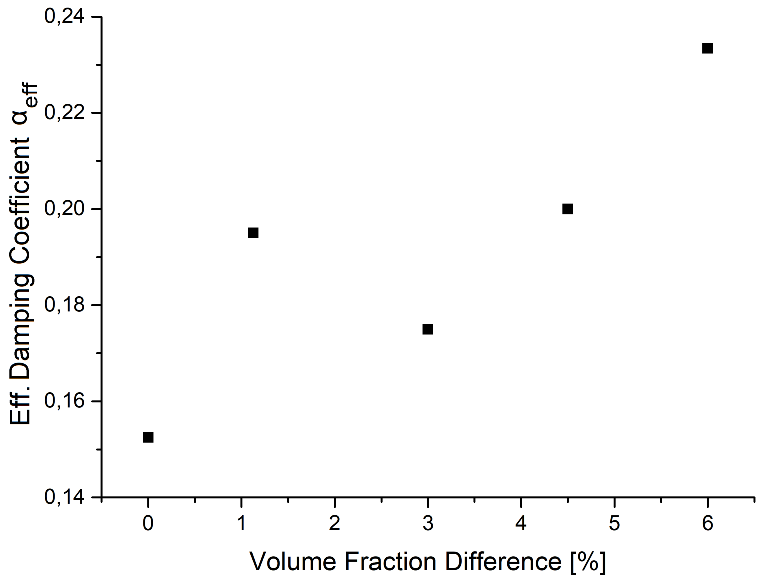

FIGURE 5.99 – *The effective damping coefficient* α_{eff} *from Polder adaption in figures 5.95-5.98 is plotted for the regarded volume fraction differences with* $H_{eff} = const.$ *in every case.*

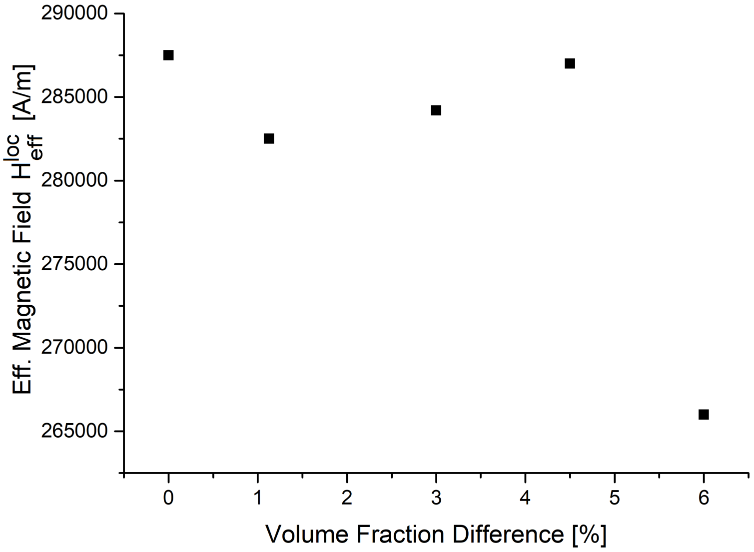

FIGURE 5.100 – *The effective magnetic field* H_{eff}^{loc} *from Polder adaption in figures 5.95-5.98 is plotted for the regarded volume fraction differences* $H_{eff} = const.$ *in every case.*

With regard to the damping coefficient α_{eff}, we find a growing of the values with increasing volume fraction difference, which is a consequence of the decreasing of $|\mu''_{max}|$ (see also figure 5.89) and the progressive blurring of the resonance peak. Considering the local effective magnetic fields, we again determine a similar behavior as for the resonance frequencies (see figure 5.88). But, unfortunately, no clear tendency can be drawn for the effective magnetic field from this graph, making a quantitative analysis impossible. For completeness sake, also the values for μ'_{stat} are again calculated from the derived effective parameters (see figure 5.101, also not showing an analyzable behavior.

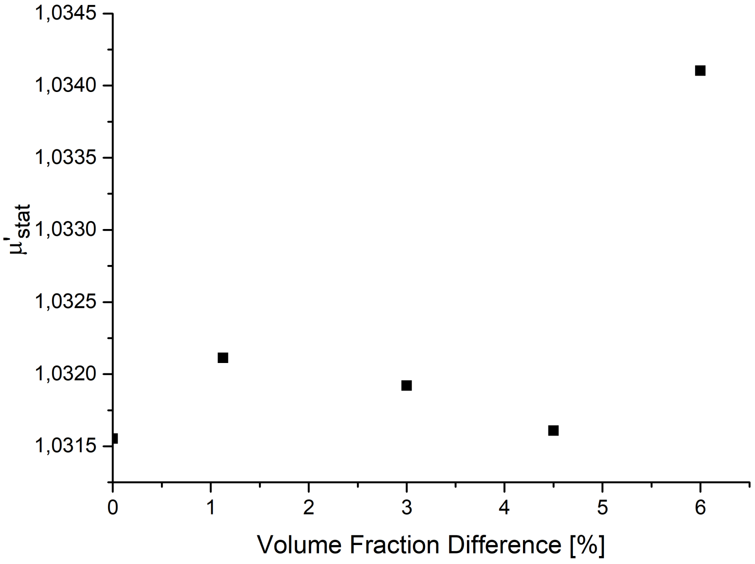

FIGURE 5.101 – *The magnitude of* μ'_{stat} *is analyzed for different volume fraction differences.*

Nevertheless, we want to find an accessible way in order to raise the quality of our results. Besides the increasing of the inclusion number, it is also possible that the implementation of periodic boundary conditions in the static simulations is a senseful step in order to improve the quantitative analyzability of the results because it could be helpful in order to reduce the blurring of the magnetic field distribution in the high density regions and, consequently, reduce the standard deviations of the resonance frequencies. Accordingly, we also want to examine the model of varied inclusion densities with periodic boundary conditions in the next section, even if it does not match to the chapter of finite samples.

5.3 Excursion: Variation of Inclusion Density with Periodic Boundary Conditions

In this context, we firstly have to find a meaningful realization of the periodic boundary conditions which is schematically drawn in figure 5.102. By this, we model an infinite sample which is divided into two inclusion density regions by the plane area parallely orientated to the $x-y-$plane at $z = 0.5$ cm.

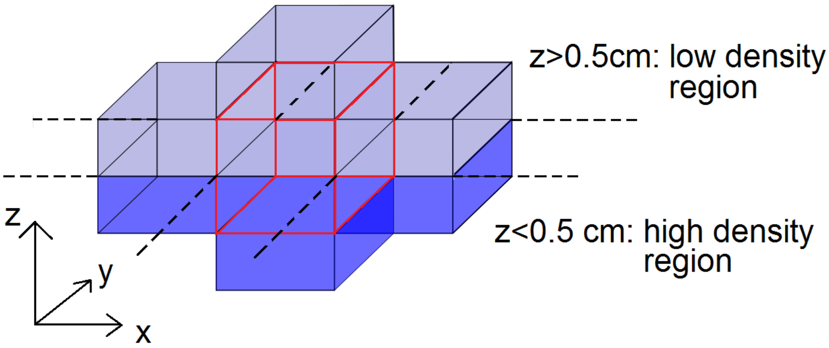

FIGURE 5.102 – *The implementation of the periodic boundary conditions is schematically shown. The actual sample is highlighted by red contours while light blue marks the low density region and dark blue the high density region. Picture shows how copies of these regions, of course with identical inclusion microstructures, are arranged in $x-$ and $z-$direction in order to generate the desired conditions. Naturally, the sample is also continued in $y-$ direction (and in the directions of the bisectings) in the same manner, which is omitted in the sketch for clarity's sake.*

With these boundary conditions, we repeat the analysis of the static magnetic fields for the same inclusion volume fractions as in the previous section. Corresponding results for the convergence behavior of the mean values of the magnetic field components (see figures 5.103-5.109) and the distributions (see figures 5.110-5.122) for the whole sample and separated according different density regions . There, we regard the case of $H_{inc} = 183\ 154\ \frac{\mathrm{A}}{\mathrm{m}} = const.$ for every volume fraction contrast.

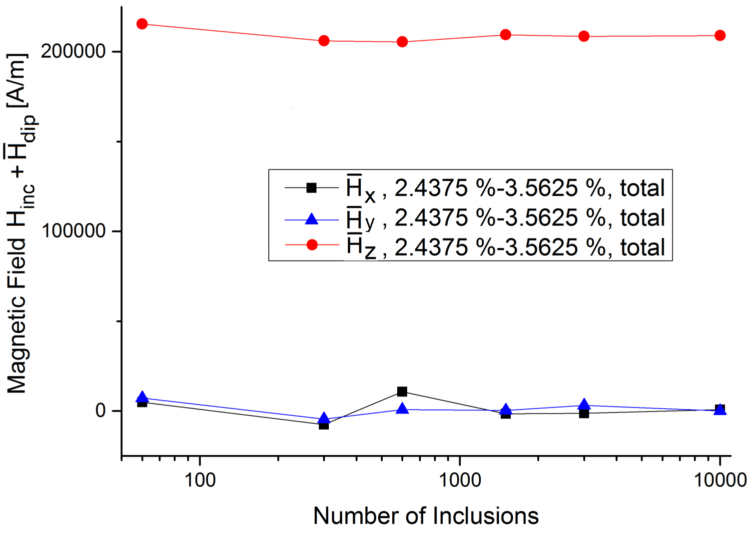

FIGURE 5.103 – *The components of the average magnetic field at the positions of the inclusions in dependence of the number of included spheres. Here, the complete sample with the filling factors* 2.4375 % *and* 3.5625 % *under periodic boundary conditions is regarded.*

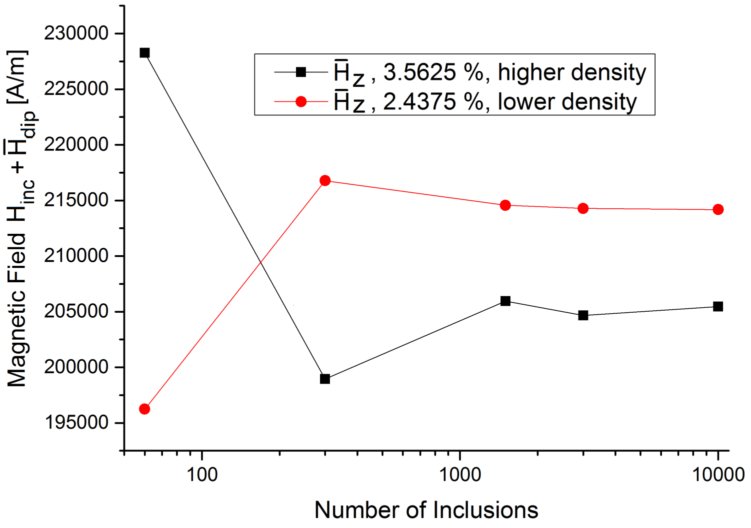

FIGURE 5.104 – *The $z-$components of the average magnetic field in dependence of the number of included spheres in the regions with* 2.4375 % *and* 3.5625 % *with implemented periodic boundary conditions are compared to each other.*

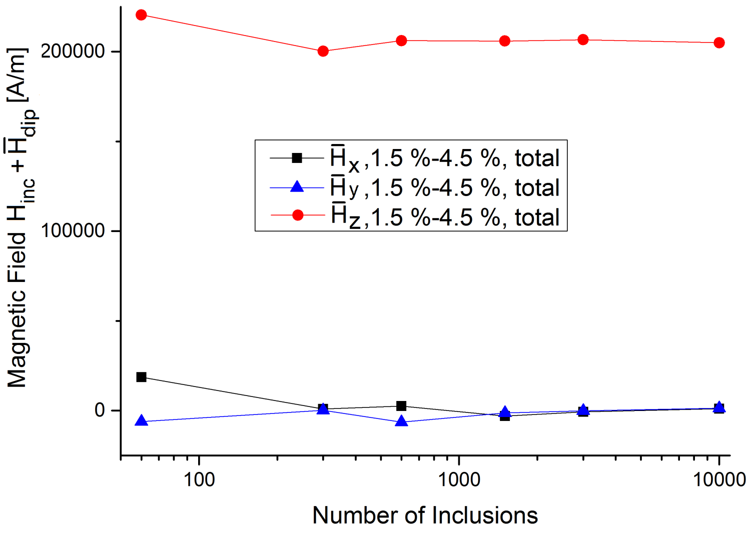

Figure 5.105 – *The convergence analysis of the magnetic field components is done for the whole device under periodic boundary conditions with the volume fractions* 1.5 % *and* 4.5 % *in both regions.*

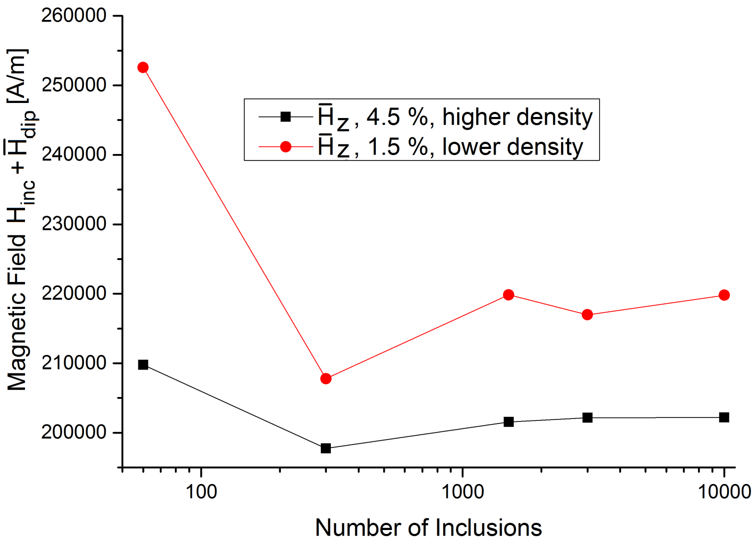

Figure 5.106 – *The* $z-$*components of the average magnetic field in dependence of the number of included spheres in the regions with* 1.5 % *and* 4.5 % *with implemented perdiodic boundary conditions are compared to each other.*

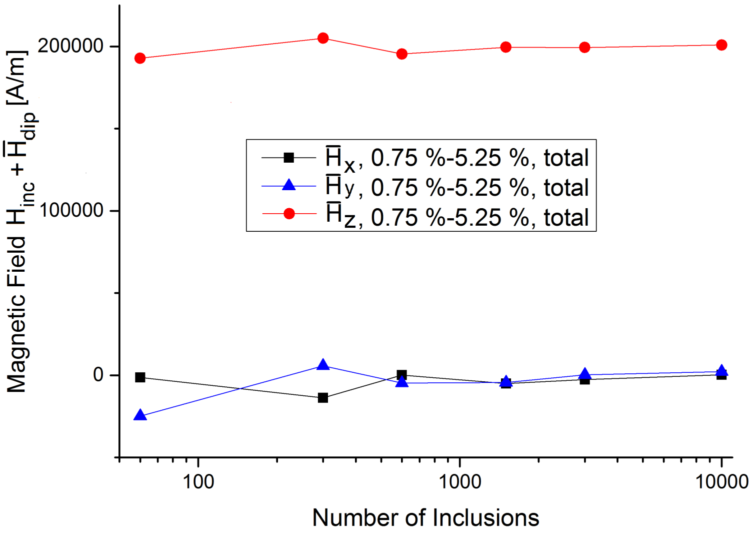

FIGURE 5.107 – *The convergence analysis of the magnetic field components is done for the whole device under periodic boundary conditions with the volume fractions* 0.75 % *and* 5.25 % *in both regions.*

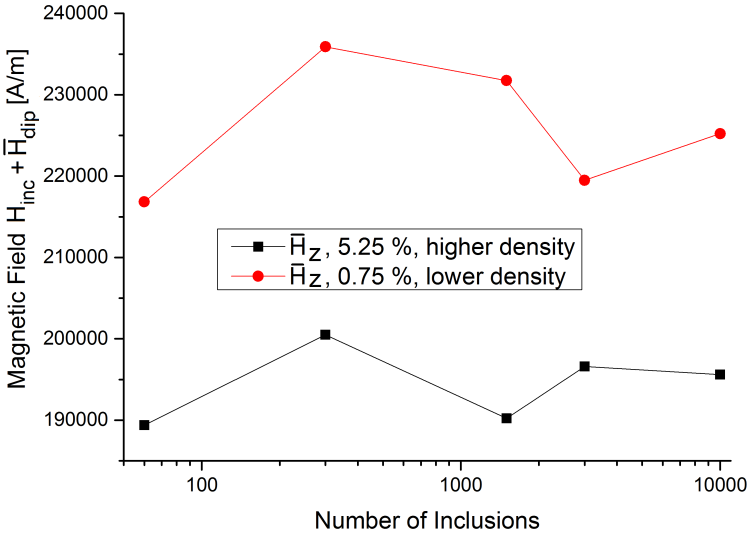

FIGURE 5.108 – *The* $z-$*components of the average magnetic field in dependence of the number of included spheres in the regions with* 0.75 % *and* 5.25 % *with implemented perdiodic boundary conditions are compared to each other.*

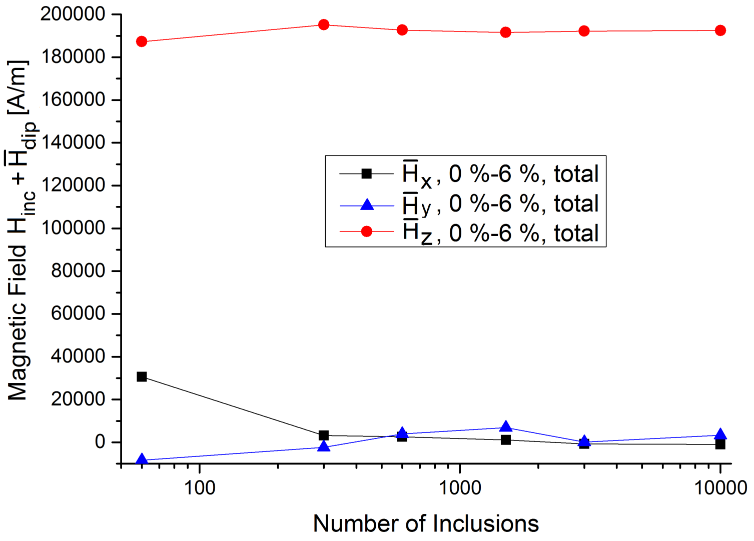

FIGURE 5.109 – *The convergence analysis of the magnetic field components is done for the whole device under periodic boundary conditions with the volume fractions* 0 % *and* 6 % *in both regions. Because inclusions are only placed in the high volume fraction region, a separated analysis of both regions does not contain further information.*

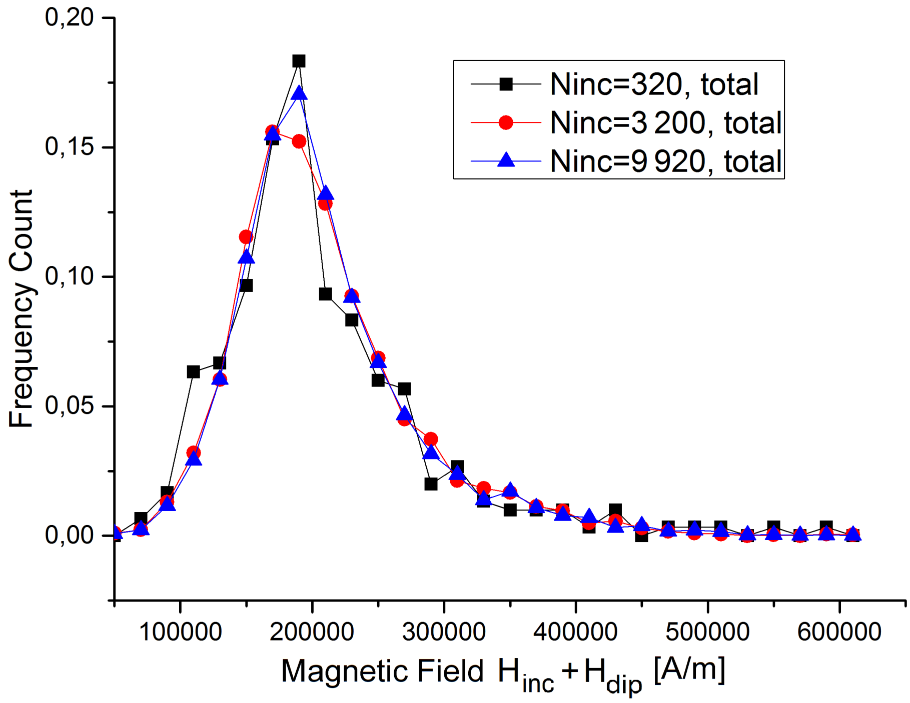

FIGURE 5.110 – *We regard field distributions for different inclusion numbers in the whole sample under periodic boundary conditions with an inclusion volume fraction of* 2.4375 % *in the upper region and* 3.5625 % *in the lower one.*

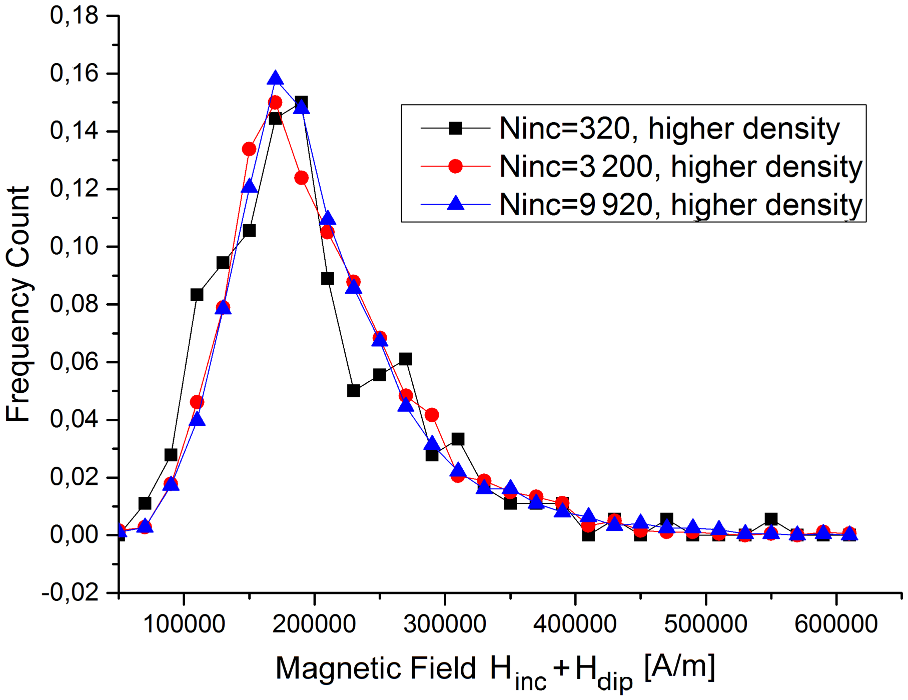

FIGURE 5.111 – *The same sample as in figure 5.110 is regarded, but only fields in the lower region with* $f = 3.5625$ % *are taken into account.*

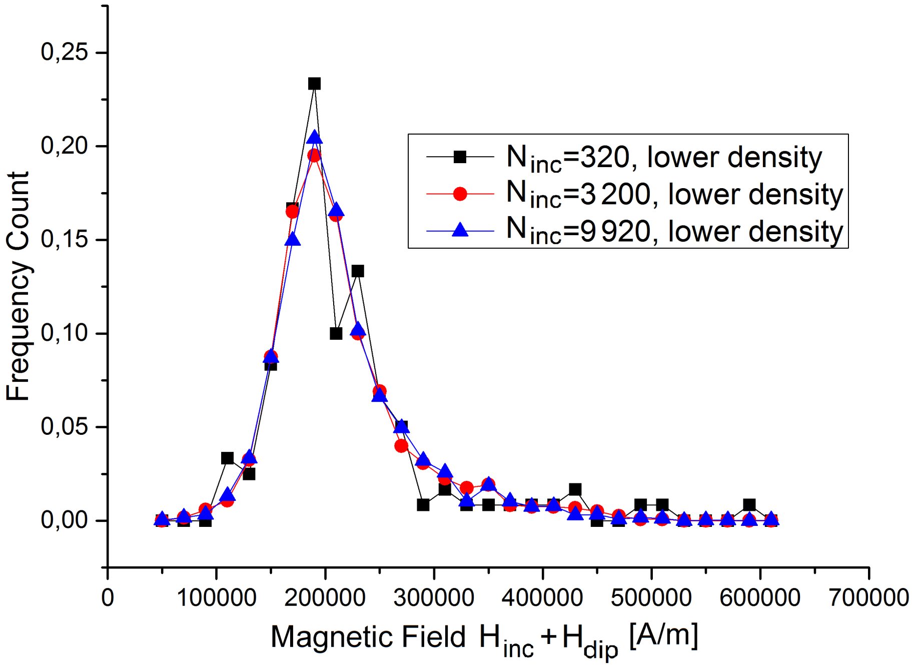

FIGURE 5.112 – *The same sample as in figure 5.110 is regarded, but only fields in the upper region with* $f = 2.4375$ % *are taken into account.*

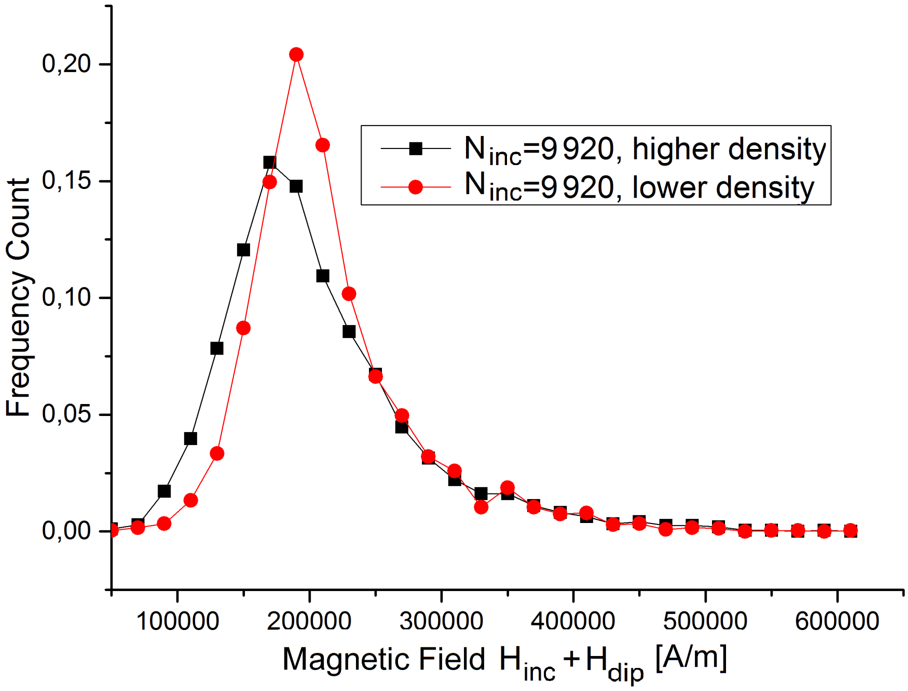

FIGURE 5.113 – *The comparison between the field distributions in the high and low density region for the sample with an inclusion volume fraction of* 2.4375 % *in the upper region and* 3.5625 % *in the lower one with periodic boundary conditions. Both distributions are normalized concerning the number of inclusions in the respective region.*

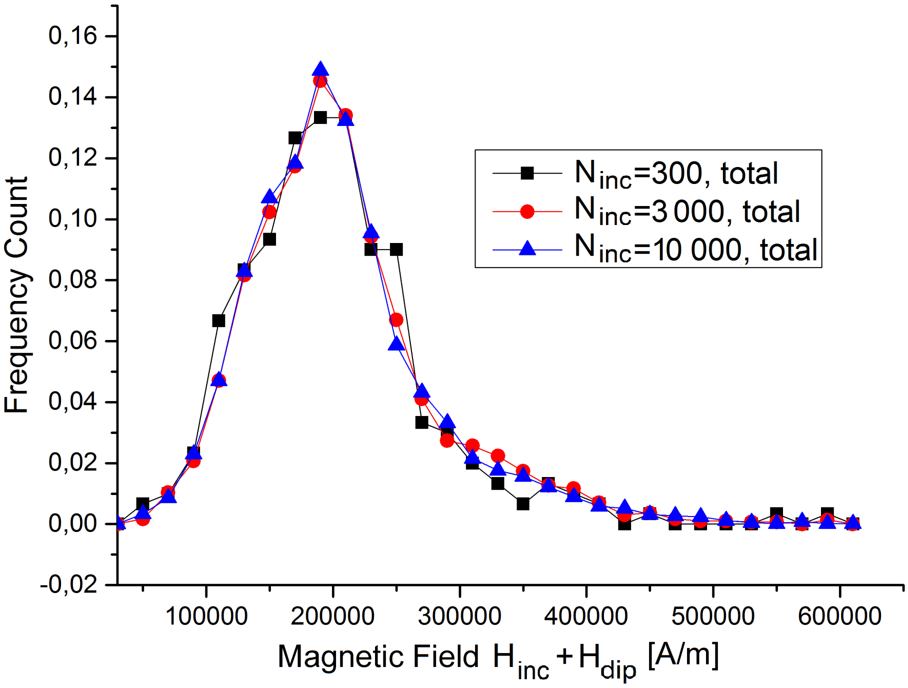

FIGURE 5.114 – *We regard field distributions for different inclusion numbers in the whole sample under periodic boundary conditions with an inclusion volume fraction of* 1.5 % *in the upper region and* 4.5 % *in the lower one.*

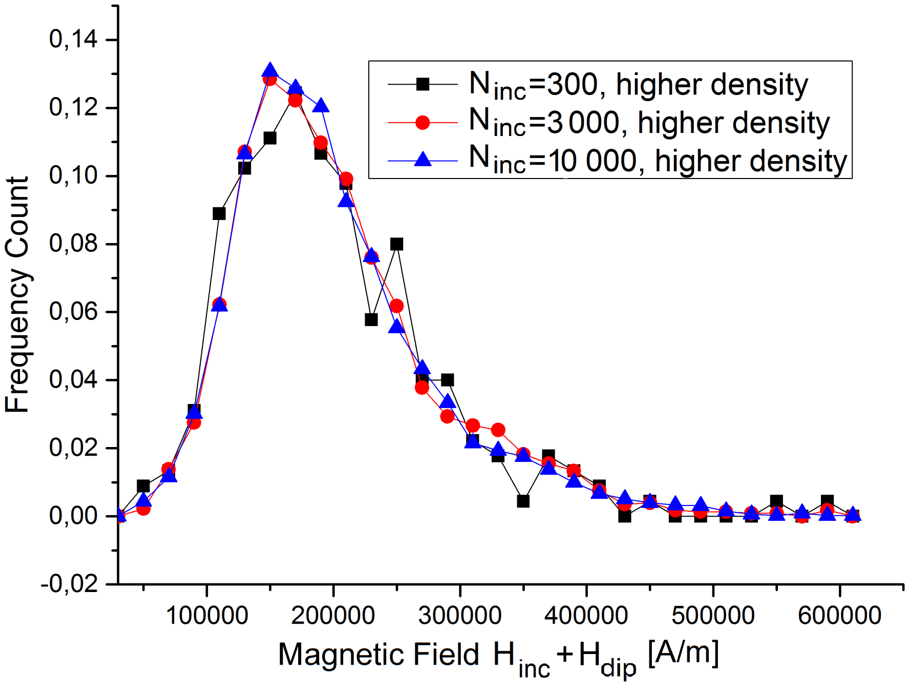

FIGURE 5.115 – *The same sample as in figure 5.114 is regarded, but only fields in the lower region with* $f = 4.5$ % *are taken into account.*

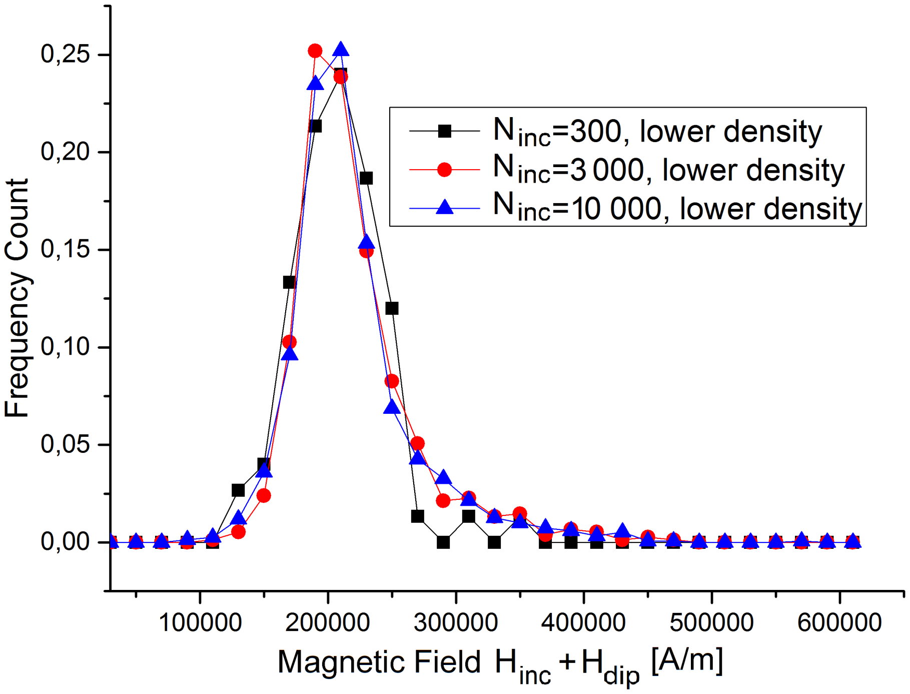

FIGURE 5.116 – *The same sample as in figure 5.114 is regarded, but only fields in the upper region with* $f = 1.5$ % *are taken into account.*

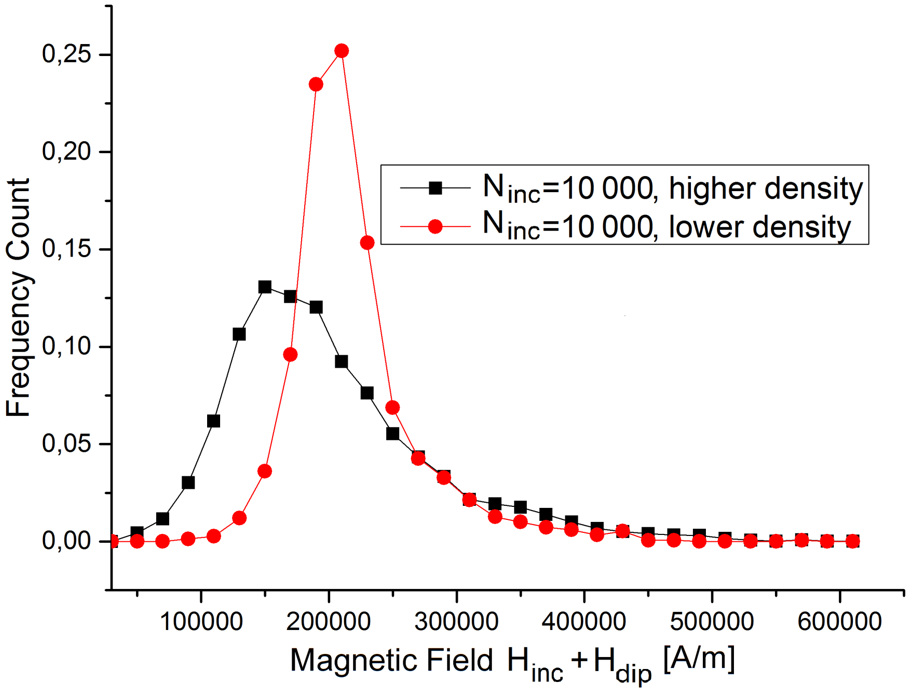

FIGURE 5.117 – *The comparison between the field distributions in the high and low density region for the sample with an inclusion volume fraction of* $1.5\ \%$ *in the upper region and* $4.5\ \%$ *in the lower one with periodic boundary conditions. Both distributions are normalized concerning the number of inclusions in the respective region.*

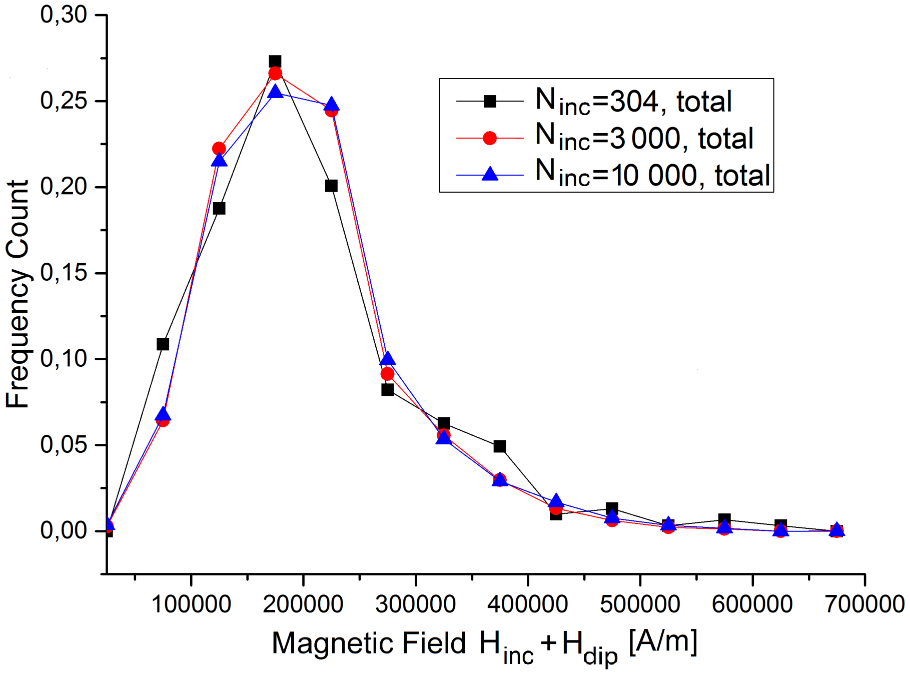

FIGURE 5.118 – *We regard field distributions for different inclusion numbers in the whole sample under periodic boundary conditions with an inclusion volume fraction of* $0.75\ \%$ *in the upper region and* $5.25\ \%$ *in the lower one.*

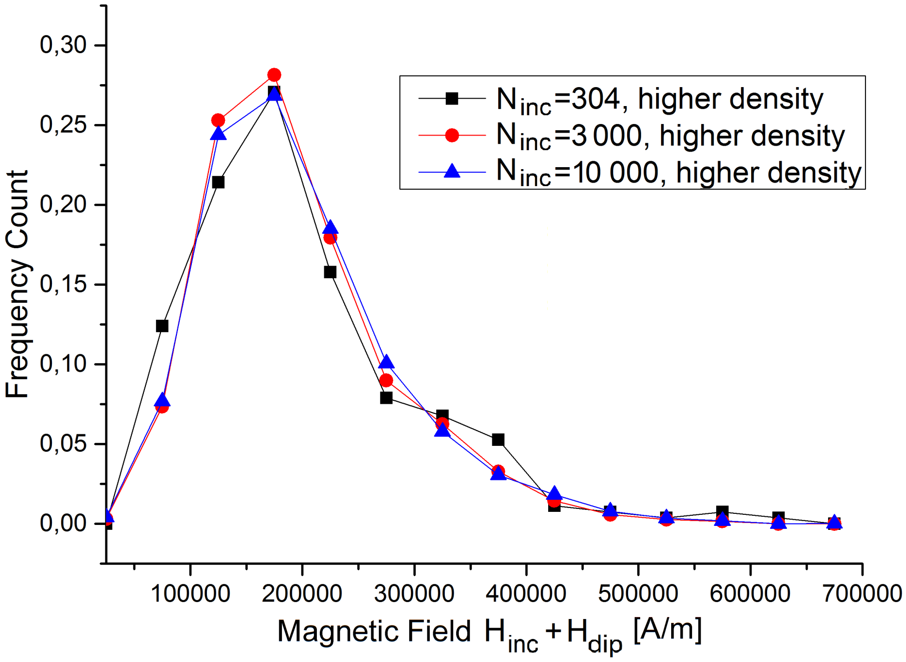

FIGURE 5.119 – *The same sample as in figure 5.118 is regarded, but only fields in the lower region with* $f = 5.25$ % *are taken into account.*

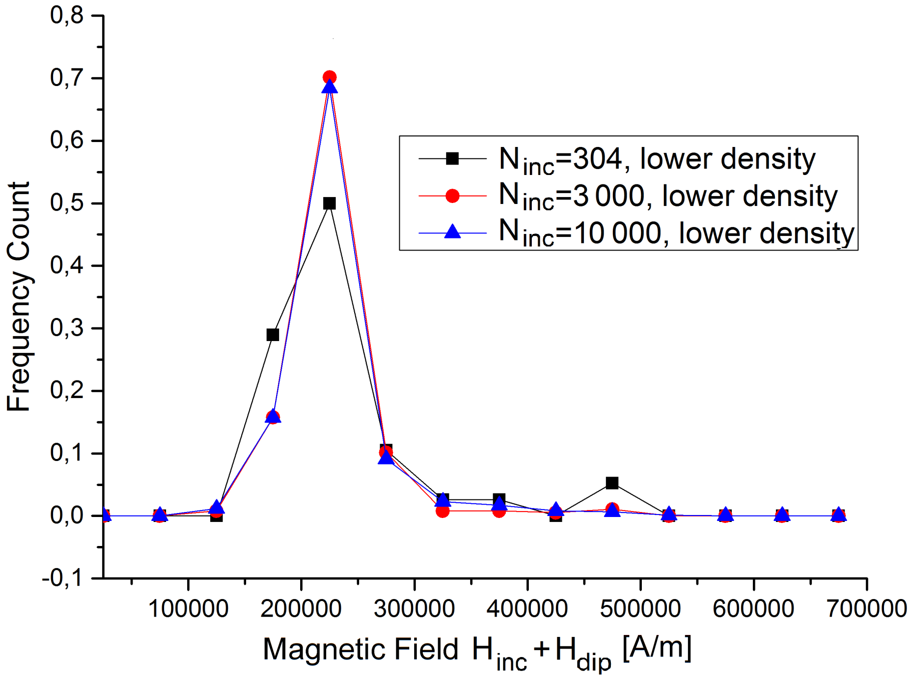

FIGURE 5.120 – *The same sample as in figure 5.118 is regarded, but only fields in the lower region with* $f = 0.75$ % *are taken into account.*

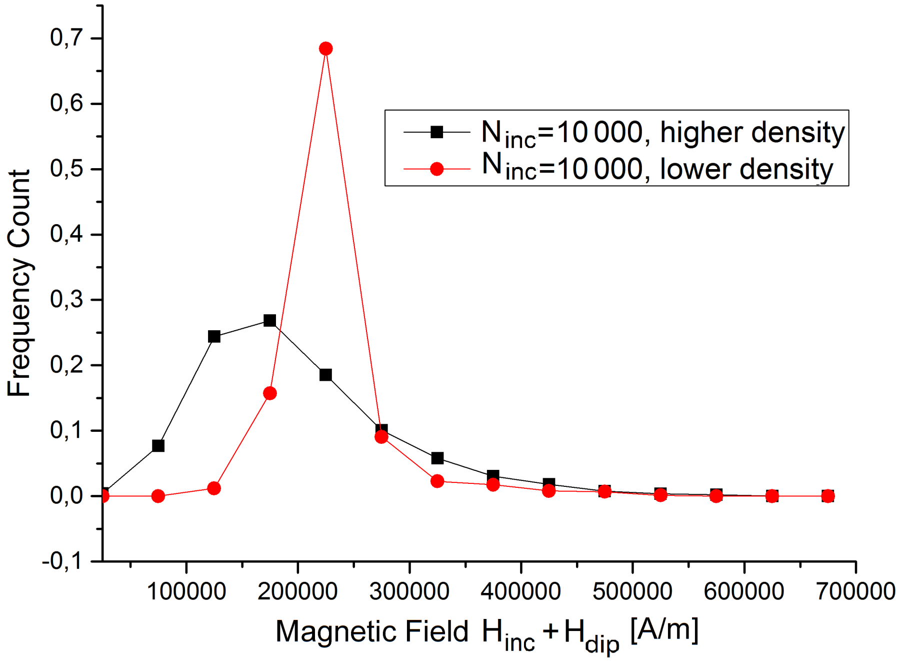

FIGURE 5.121 – *The comparison between the field distributions in the high and low density region for the sample with an inclusion volume fraction of* $0.75~\%$ *in the upper region and* $5.25~\%$ *in the lower one with periodic boundary conditions. Both distributions are normalized concerning the number of inclusions in the respective region.*

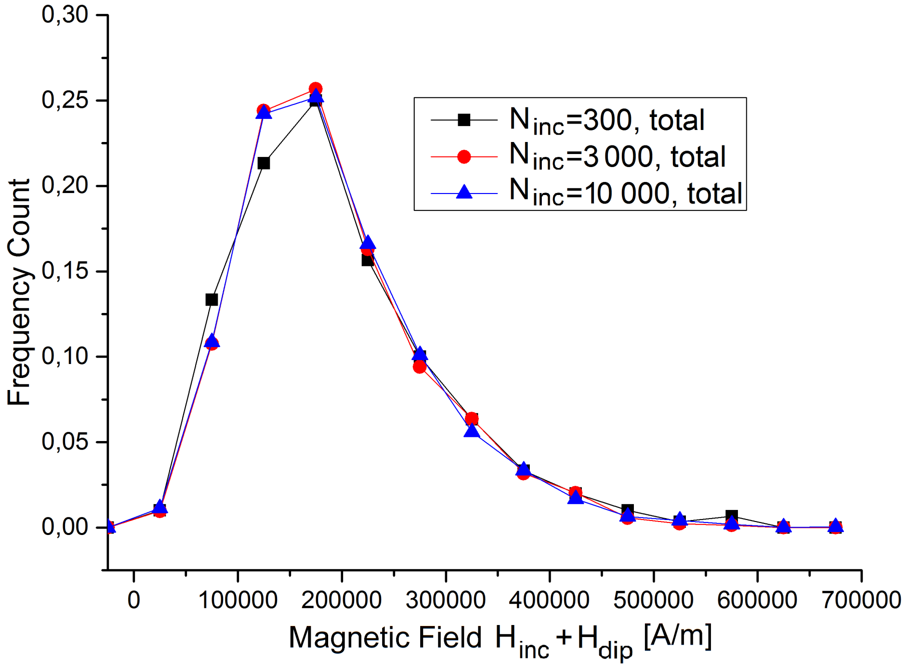

FIGURE 5.122 – *We regard field distributions for different inclusion numbers in the whole sample under periodic boundary conditions with an inclusion volume fraction of* $0~\%$ *in the upper region and* $6~\%$ *in the lower one.*

Once again, results converge when we use sufficiently large inclusion numbers in the whole sample, $N_{inc} \approx 10\ 000$ in this case, and we can still neglect the magnetic fields in $x-$ and $y-$direction. All other observations are qualitatively the same as for the finite samples in the previous chapter. The question is if the widening of the field distributions, especially in the high density region, was reduced by the implementation of the periodic boundary conditions. In order to examine this issue, we exemplarically compare corresponding distributions for the case of $f = 0.75\ \%$ in the low density region and $f = 5.75\ \%$ in the high density region in figures 5.123 and 5.124.
Unfortunately, we observe that the widening of the distributions was not reduced by the periodic boundary conditions and the results do not differ significantly. Consequently, better results compared to the previous chapter can not be expected, wherefore we dispense of further analysis of these models with high-frequency simulations. Nevertheless, we also want to compare the average magnetic field in the whole samples for different inclusion volume fractions differencs in both cases which is done in figure 5.125. Here, we recogneize small differences, which increase with the density contrast. In accordance with results plotted in figure 5.9, we again find lower values for the devices with periodic boundary conditions.

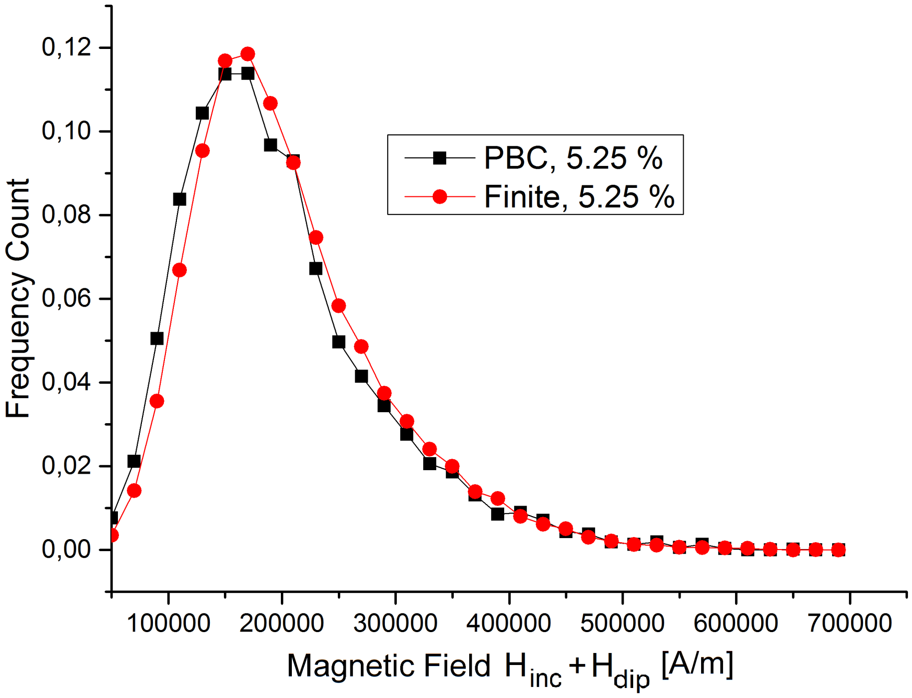

FIGURE 5.123 – *The magnetic field distributions in the high density region of the composite with inclusion volume fractions of* $0.75\ \% - 5.25\ \%$ *are compared for the case of a finite sample and with periodic boundary conditions.*

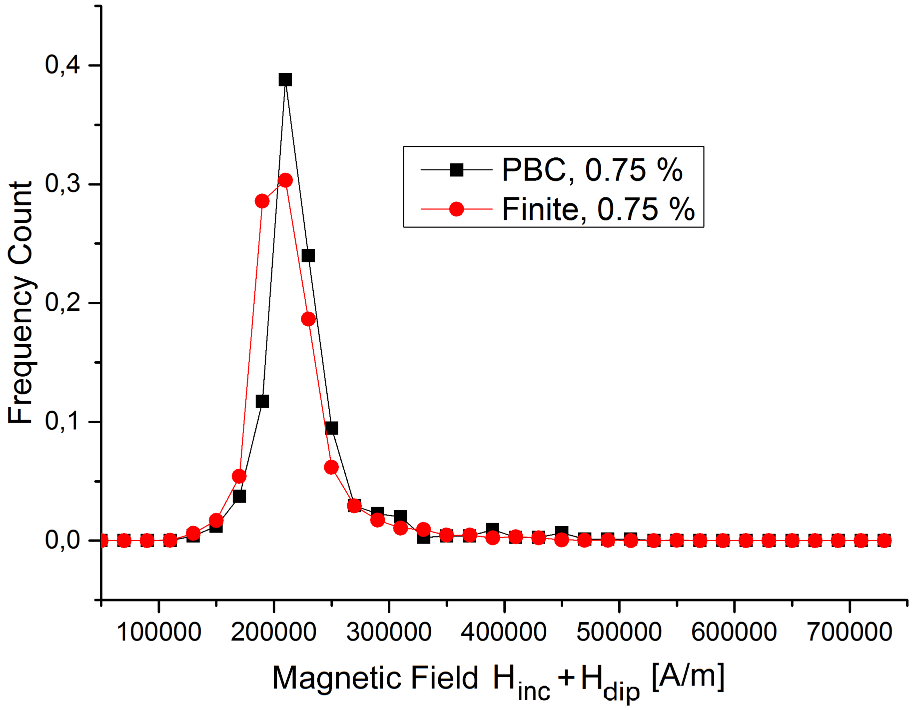

FIGURE 5.124 – *The magnetic field distributions in the low density region of the composite with inclusion volume fractions of* $0.75\ \% - 5.25\ \%$ *are compared for the case of a finite sample and with periodic boundary conditions.*

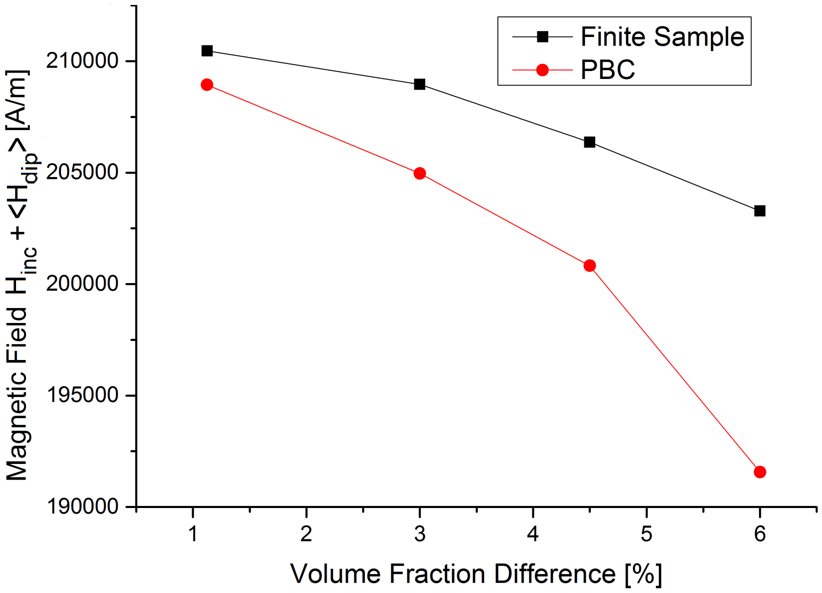

FIGURE 5.125 – *The average magnetic field at the places of all inclusions in the sample for different inclusion volume fractions in the cases of finite devices and samples with periodic boundary conditions are compared.* $H_{inc} = 183\ 154\ \frac{A}{m}$ *is valid for inclusion in every simulation.*

5.4 Chapter Summary

In contrast to the previous chapter, we were interested in finite samples in this part of the present work. For that purpose, we switched off periodic boundary conditions in the simulations of the static dipolar fields and increased the number of the randomly inserted inclusions until the large system limit was reached, as also previously done. Then, this limiting case was again reproduced by representative small systems with similar static properties in high-frequency simulations. During the evaluation of the corresponding results, strong artifacts related with the low inclusion number appeared. In order to reduce this statistical errors, we averaged the entries of the permeability tensor of interest over several simulation runs with different microstructures inside the sample. By this procedure, we improved the evaluability of the results.

In this context, we firstly analyzed the permeability tensor's dependence on the geometric extensions of the device under test. In contrast to examinations of infinitely extended samples in the previous chapter, the externally applied field and the effective field, H_{eff}, are not equal anymore due to demagnetization effects at the sample boundaries. Accordingly, further analysis referred only to the case of $H_{eff} = const.$ for every volume fraction.

Within this, we showed that different shapes of the sample can cause rising, constant and decreasing resonance frequencies, which is a very fundamental cognition. Especially when interpreting experimental measured permeability tensors, this knowledge must be considered. In order to draw meaningful conclusions from experiments on bulk material parameters for the equivalent homogeneous samples, a recipe is proposed in this chapter.

Furthermore, we also regarded inhomogeneous inclusion distributions inside the host matrix, which could be involuntarily caused through interactive forces like gravity or buoyancy in real samples. For analyzing this issue, we defined two zones in our sample with different filling factors of inclusions and applied the same prepatory work with regard to static field distributions on these systems. Afterwards, the corresponding small system devices were under test in high-frequency simulations. At this point, we recognized that artifacts due to the low inclusion numbers were very distinct and prevented a meaningful analysis. Even averaging of the results for different microstructures and the implementation of periodic boundary conditions, which were assumed to reduce statistical errors, were not capable to improve our results. Due to this problem, no significant conclusions can be drawn on systems with inhomogeneous inclusion distribution.

Chapter 6

Summary and Outlook

The main task of the present work was to gain knowledge on the properties of composites in the vicinity of the ferromagnetic resonance, consisting out of spherical inclusions of ferromagnetic material, which were dispersed in a non-magnetic host matrix. Thereby, the included spheres must fulfill the condition of the effective medium theory, meaning that they are small in comparison to the wavelength of the incoming high-frequent electromagnetic signal. With regard to this topic, many analytic approaches has been proposed over decades, as the mixing formulas by Maxwell-Garnett and Bruggeman, which try to calculate the composite's properties out of the components' material parameters. These fundamental theories, which suffer from different unphysical deficiencies, were taken up in the works of [36,37], in which several of these lacks were overcome. Therein, the authors mainly concentrate on a possible shift of the resonance frequency in dependence of the filling factor of the ferromagnetic material under a constant externally applied field. By an analytic approach, taking into account the tensorial character of the permeability of ferromagnetic materials and the influence of static magnetization of the included spheres, a shift of the resonance towards lower frequencies was derived for filling factors smaller than 30 % in a spherical or infinite sample, before tendency inverts and returns to values for homogeneous materials, again.

In this work, we tried to gain further insight into this topic by analyzing such composites with filling factors up to 10 % with the help of simulation methods, which is done in several steps. At first, we calculate static dipolar interactions between the magnetic moments of the included spheres in the large system limit, i.e. we require convergence of the distribution of the dipolar field values at the center of every inclusion with regard to their number N_{inc}. In these simulation, a relaxation of the magnetic moment to an equilibrium state is included while the condition of self-consistency is obeyed. Due to the high memory consumption in the high-frequency simulations, we can not examine these large systems, but we are able to find composites with low inclusion numbers ($N_{inc} = 27$ or $N_{inc} = 64$) reproducing the static field distributions in the limit of $N_{inc} \rightarrow \infty$. These systems with low inclusion numbers are then transferred into high-frequency simulations of transmission and reflection experiments in a rectangular waveguide performed with HFSS by Ansys and MOR by LTE. From the found $S-$parameters, we are able to calculate the effective permeability tensor of the composite under test with the help of the evaluation method developed in [45, 46]. These simulation steps are firstly excuted with a constant magnetic bias H_{inc} in every inclusion and for every filling factor in order to determine the effective magnetization of the composites under test. Afterwards, these determined values of M_{eff} are used for a demagnetization conversion between the internal field in the inclusions and the effective field H_{eff} in the composite. With this converted data, we analyze the shift of the ferromagnetic resonance, the strength of the resonance peak $|\mu''_{max}|$ and the static permeability μ'_{stat} with a constant value of H_{eff} in dependence of the volume fraction of included ferromagnetic material. Furthermore, we also derived formulas for the effective permeability tensor in the given parameter range.

Firstly, we concentrated on composites with infinite extensions, in which inclusions are arranged on a simple cubic lattice, as an elementary starting point of our examinations. Conditioned by this microstructure, we can neglect dipolar interactions between the ferromagnetic spheres, through which we are able to separate the influence of their static magnetization. Drawing conclusions on infinitely extended samples was possible by performing high-frequency simulations with homogeneous samples with the same shape whose material parameters were varied until their resonance curves match the ones of the corresponding composite. Due to the equivalence of the externally applied field and the effective field H_{eff} in case of infinite samples, we were able to analyze the resonance frequency under a constant external field, as experimentally relevant. As evaluation of the in-silico experiments showed, resonance frequency remains constant for every volume fraction of ferromagnetic material in this case.

In the next step, we analyzed infinitely composites with a random inclusion insertion, leading to significant dipolar interactions between the ferromagnetic spheres, which were firstly included in a mean field approach. Accordingly, we neglected the spatial inhomogeneity of the dipolar field and assumed the corresponding mean value $\overline{H}_{dip}$ for the place of every inclusion. As simulation sequences with a constant external field showed, this approach leads to rising resonance frequencies for the regarded range of filling factors. Further increasing complexity, we also took into account the spatial distribution of the dipolar fields. Consequently, every inclusion is supposed to a different magnetic field in our simulations, causing different permeabilities and resonance frequencies. Within this, we detected the tendency of the resonances to shift towards lower values under constant externally applied field. This phenomenon was detected as a consequence of the blurring of the resonance peaks and the implemented Polder model. Summarizing, we found two supposing and counteracting effects with regard to the shift of the resonance, from which the decreasing one is dominant. Especially, these recognition showed that a mean field approach for respecting the dipolar interaction leads to wrong results. Consequently, we concluded that the regarded infinitely extended composites show a decreasing resonance frequency when inclusions' volume fraction increases in the range from 0 % to 5 % while the external magnetic field remains constant. As it was shown in the performed high-frequency simulations, further increasing of the filling factor is connected with growing errors due to the low accessible particle number, leading to unreliable data.

In order to come closer to the results of real experiments, we also investigated finite samples with regard of the spatial inhomogeneity in the dipolar fields in our simulations. In contrast to infinitely extended samples, the externally applied and the effective field H_{eff} differ due to demagnetization effects at the sample boundaries in the waveguide. Accordingly, we kept only the value of H_{eff} constant for different filling factors.

In this context, we firstly analyzed the influence of the matrix geometry on the permeability and especially the resonance frequency. Therein, we recognized that we can create devices with increasing, constant and shrinking resonance frequencies by the variation of the host matrix's shape. An explanation for this behavior can be found in the form of the dipolar field of the magnetic moments and their interaction. During these simulation sequences, statistical errors and artifacts, caused by the more disordered microstructures in comparison to the composites corresponding to infinitely extended material systems, appeared which were reduced by taking the mean value of the effective permeabilities of different samples generated under the same conditions. Nevertheless, examination appeared only meaningful in the range to filling factors up to 5 % due to the enforcing of the artifacts with growing inclusion volume fractions, as before.

In the last simulation sequences of this work, we tried to analyze the influence of the inhomogeneous inclusion densities in the sample. Unfortunately, this examination was disturbed by even stronger artifacts due to the limited inclusion numbers in the high-frequency simulations, which could not be overcome with the methods at hand.

Considering forthcoming research, it would be very helpful to develop methods which allow higher inclusion numbers in high-frequency simulations in order to reduce statistical errors in the analysis of randomly generated systems. Besides a refining effect on the gained results, especially in the case of finite samples, this would open new opportunities with regard to further examinations: As it was already indicated in static simulations in the present work, polydispersity of the included spheres could have further influence on the composites behavior. Unfortunately, the accessible inclusion numbers are much too low in order to gain meaningful insight into this topic. Moreover, the issue of inhomogeneous inclusion distributions, which is tried to examine with the help of a simple model, offers much more interesting cases, as the accumulation of spheres, induced by attractive forces, or other special microstructures.

Furthermore, the usage of ellipsoid but spherical inclusions, with corresponding more complex demagnetization effects, could be an interesting topic of research.

Additionally, the examination of higher filling factors in every of the regarded or not-yet regarded cases is worthy to analyze because of the necessary existence of a returning point of the resonance shift behavior. For that purpose, further refinement of the static simulations, meaning the inclusion of higher magnetic moments and taking into account the spatial distribution of them, is necessary in order to generate trustworthy results.

Bibliography

---

[1] B. Viala, A. S. Royet, R. Cuchet, M. Aid, P. Gaud, O. Valls, M. Ledieu and O. Acher. RF planar ferromagnetic inductors on silicon. IEEE Trans. Magn. 40, 1999 (2004).

[2] P. M. T. Ikonen, K. N. Rozanov, A. V. Osipov, P. Alitalo, and S. A. Tretyakov. Magnetodielectric substrates in antenna miniaturization: Potential and limitations. IEEE Transactions on Antennas and Propagation, vol. 54, no. 11, pp. 3391-3399 (2006).

[3] B. K. Kuanr, D. L. Marvin, T. M. Christensen, R. E. Camleya, and Z. Celinski. High-frequency magnetic microstrip local bandpass filters. Appl. Phys. Lett. 87, 222506 (2005)

[4] K. H. Kim and M. Yamaguchi. Microwave absorption of integrated CoNbZr film on a coplanar waveguide. J. Appl. Phys. 99 (2006).

[5] O. Acher and S. Dubourg. Generalization of Snoek's law to ferromagnetic films and composites. Phys. Rev. B 77, 104440 (2008).

[6] O. Acher. Modern microwave magnetic materials: Recent advances and trends. Journal of Magnetism and Magnetic Materials 321 (2009) 2033-2034.

[7] L. K. H. Van Beek. Dielectric Behavior of Heterogeneous Systems. Progress in Dielectrics (1967).

[8] K. Chalapat et al. Ferromagnetic resonance in ϵ-Co magnetic composites (2014).

[9] D. Polder. On the theory of ferromagnetic resonance. The London, Edinburgh, and Dublin Philosophical Magazine and Journal of Science, 40 (1949).

[10] Bergmann-Schaefer. Lehrbuch der Experimentalphysik Band 2 Elektromagnetismus 9. Auflage (2006).

[11] Robert E. Collin. Field Theory of Guided Waves. Second Edition (1991).

[12] N. Marcuvitz. Waveguide Handbook (1965).

[13] D. M. Pozar. Microwave Engineering, Fourth Edition (2012).

[14] W. Demtröder. Experimentalphysik 2 - Elektrizität und Optik 2. Auflage (2002).

[15] D. J. Griffiths. Introduction to Electrodynamics. Cambridge University Press, 4th Edition (2017).

[16] W. Zinth and H. J. Körner. Optik, Quantenphänomene und Aufbau der Atome. Oldenburg Wissenschaftsverlag (2014).

[17] J. M. D. Coey. Magnetism and Magnetic Materials. Cambridge University Press

(2010).

[18] R. C. O'Handley. Modern Magnetic Materials - Principles and Applications (2000).

[19] B. Lax and K. J. Button, Microwave Ferrites and Ferrimagnetics. McGraw-Hill, New York 1962.

[20] G. W. Milton. The Theory of Composites. Cambridge Monographs on Applied and Computational Mathematics (2002).

[21] A. Sihvola. Electromagnetic Mixing Formulas and Applications. IET Electromagnetic Waves Series 47 (1999).

[22] T. C. Choy. Effective Medium Theory. Principles and Applications. Oxford Science Publications (1999).

[23] A. Niranjan and B. K. Padhi. On Magnetic analogue of Clausius-Mossotti equation. Department of Physics, Indian Institute of Technology, Delhi, New Delhi-110016, India(2013).

[24] J. C. M. Garnett. Colours in metal glasses and in metallic films. Philos. Trans. R. Soc. London A 203, 385-420 (1904).

[25] J. C. M. Garnett. Colours in metal glasses, in metallic films, and in metallic solutions II. Philos. Trans. R. Soc. London 205, 237-288 (1906).

[26] C. J. F. Böttcher. Theory of Electric Polarisation. (1952)

[27] D. A. G. Bruggeman. Berechnung verschiedender physikalischer Konstanten von heterogenen Substanzen I. Dielektrizitätskonstanten und Leitfähigkeiten der Mischkörper aus isotropen Substanzen. Annalen der Physik 5, pp. 636-659 (1935).

[28] S. Kirkpatrick. Percolation and Conduction. IBM Thomas J. Watson Research Center, Yorktown Heights, New York 10598 (1973).

[29] Z. Hashin, S. Shtrikman. A Variational Approach to the Theory of the Effective Magnetic Permeability of Multiphase Materials. Journal of Applied Physics 33, 3125 (1962).

[30] G. W. Milton. Bounds on the complex dielectric constant of a composite material. Applied Physics Letters (1980).

[31] D. J. Bergman. Exactly Solvable Microscopic Geometries and Rigorous Bounds for the Complex Dielectric Constant of a Two-Component Composite Material. Physical Review Letters, 44(19) (1980).

[32] D. J. Bergman. Bounds for the complex dielectric constant of a two-component composite material. Physical Review B, 23(6) (1981).

[33] D. J. Bergman. Rigorous Bounds for the Complex Dielectric of a Two-Component Composite. Annals of Physics, 138 (1982).

[34] R. Pelster. Bounds for local and average microwave absorption in heterogeneous systems. Journal of colloid and interface science, 318(2) (2008).

[35] B. Hallouet. Mikrostruktur und effektive Eigenschaften von dielektrischen und magnetischen Kompositen: das inverse Problem (Dissertation, 2013).

[36] V. B. Bregar and M. Pavlin. Effective-susceptibility tensor for a composite with ferromagnetic inclusions: Enhancement of effective-media theory and alternative ferromagnetic approach. Journal of Applied Physics 9, 6289 (2004).

[37] V. B. Bregar. Effective-medium approach to the magnetic susceptibility of composites with ferromagnetic inclusions. Physical Review B 71, 174418 (2005).

[38] J. D. Jackson. Classical Electrodynamics 3rd edition (1999).

[39] P. H. Lissberger and P. W. Saunders. Optical and magneto-optical properties of thin film cermets. Thin Solid Films, 34 (1976) 323-333.

[40] D. R. McKenzie, R. C. McPhedran. Exact modelling of cubic lattice permittivity and conductivity. Nature Vol. 265 (1977).

[41] H. Goldstein. Classical Mechanics (Addison-Wesley, Reading, 1980).

[42] W. B. Weir. Automatic Measurement of Complex Dielectric Constant and Permeability at Microwave Frequencies. Proceeding of the IEEE, Vol. 62, No. 1, January 1974.

[43] A. M. Nicolson. Broad-band microwave transmission characteristics from a single measurement of the transient response. IEEE Transactions on Instrumentation and Measurement (Volume: 17, Issue: 4, Dec. 1968).

[44] A. M. Nicolson and G. F. Ross. Measurement of the Intrinsic Properties of Materials by Time-Domain Techniques. IEEE Transactions on Instrumentation and Measurement, Vol. IM-19, No. 4, November 1970.

[45] P. Quéffélec, M. Le Floc'h and P. Gelin. Nonreciprocal Cell for the Broad-Band Measurement of Tensorial Permeability of Magnetized Ferrites: Direct Problem. IEEE Transactions on Microwave Theory and Techniques, Vol. 47, No. 4, April 1999.

[46] P. Quéffélec, M. Le Floc'h and P. Gelin. New Method for Determining the Permeability Tensor of Magnetized Ferrites in a Wide Frequency Range. IEEE Transactions on Microwave Theory and Techniques, Vol. 48, No. 8, August 2000.

[47] J. Baker-Jarvis, E. J. Vanzura and W. A. Kissick. Improved Technique for Determining Complex Permittivity with the Transmission/Reflection Method. IEEE Transactions on Microwave Theory and Techniques, Vol. 38, No. 8, August 1990.

[48] S. W. Yun, M. J. Lee and I. S. Chang. Analysis of step discontinuities on planar dielectric waveguide containing a gyrotropic layer. IEEE Transactions on Microwave Theory and Techniques, Vol. 37, March 1989.

[49] D. E. Muller. A method for solving algebraic equoations using an automatic computer. Mathematic Tables and Aids to Computation, Vol.10, 1956.

[50] P. Lampariello and R. Sorrentino. The ZEPLS program for solving characteristics equoations of electromagnetic structures. IEEE Transactions on Microwave Theory and Techniques, Vol. MTT-23, No. 8, May 1975.

[51] M. Leroy. On the Convergence of Numerical Results in Modal Analysis. IEEE Transactions on Antennas and Propagation, Vol. AP-31, No. 4, July 1983.

[52] R. Mittra ans S. W. Lee. Analytical Techniques in the Theory of Guided Waves

(1971).

[53] D. Marcuse. Coupled-mode theory for anisotropic optical waveguide. Bell Syst. Tech. J., vol. 54, pp. 985-995, May 1975.

[54] R. B. Wilson. A Simplicial Method for Convex Programming. PhD thesis, Harvard University, 1963.

[55] J. Nocedal and S. J. Wright. Numerical Optimization. Springer Series in Operations Research. Second Edition (2006).

[56] K. Schittkowski, Y. Yuan. Sequential Quadratic Programming Methodes. June 2010.

[57] Y. Zhu and A. Cangellaris. Multigrid Finite Element Methods for Electromagnetic Field Modeling. IEEE Press Series on Electromagnetic Wave Theory, 2006.

[58] V. De La Rubia, U. Razafison, Y. Maday. Reliable Fast Frequency Sweep for Microwave Devices via the Reduced Basis Method. IEEE Transactions on Microwave Theory and Techniques, Institute of Electrical and Electronis Engineers, 2009, 57 (12(1)), pp. 2923-2937.

[59] Y. Konkel, O. Farle, A. Kohler, A. Schultschik, R. Dyczij-Edlinger. Adaptive Strategies for Fast Frequency Sweeps. COMPEL - The international journal for computation and mathematics in electrical and electronic engineering, Vol. 30 Issue: 6, pp.1855-1869 (2011).

[60] User's guide - High Frequency Structure Simulator. Ansoft Corporation (2005).

[61] M. F. Hansen and S. Morup. Models for the dynamics of interacting magnetic nanoparticles. Journal of Magnetism and Magnetic Materials 184, 262-274 (1998).

Danksagung

Zunächst möchte ich mich an dieser Stelle bei Herrn Prof. Dr. Rolf Pelster bedanken, der die vorliegende Arbeit ermöglicht und in zahlreichen Diskussionen zu ihrem Gelingen beigetragen hat. Durch seine freundliche, hilfsbereite Art und seine stets offene Tür ermöglichte er durchweg ein äußerst angenehmes Arbeitsklima, welches nicht als selbstverständlich anzusehen ist.

Ferner gilt mein Dank Herrn Prof. Dr. Romanus Dyczij-Edlinger, der die Software seines Lehrstuhls großzügigerweise zur Verfügung gestellt hat, ohne die eine Bearbeitung des Themas dieser Arbeit nicht möglich gewesen wäre. Auch er stand stets als Ansprechpartner bei fachlichen Problemen zur Verfügung und hat somit entscheidend auf die Entstehung dieser Arbeit eingewirkt.

Außerdem bedanke ich mich bei allen aktuellen und ehemaligen Mitarbeitern der beiden Arbeitsgruppen Pelster und Dyczij-Edlinger für den stets freundschaftlichen Umgang. Besonders erwähnen möchte ich dabei Dr. Klaus Schappert und Dr. Rolf Baltes, mit denen ich über Jahre hinweg ein Büro in den jeweiligen Gruppen geteilt habe. Zusammen mit Dr. Béatrice Hallouet standen alle drei stets für fachliche Diskussionen zur Verfügung, wofür ich mich noch einmal gesondert bedanken möchte.

Nicht unerwähnt lassen möchte ich an dieser Stelle natürlich meine Eltern, die mir durch ihre Unterstützung den Weg zu einer Ausbildung geebnet haben, die die vorliegende Arbeit überhaupt erst möglich gemacht hat.